Intraseasonal circulation on the Western Antarctic Peninsula Shelf with implications for shelf-slope exchange

Darren Craig McKee

Submitted in partial fulfillment of the
requirements for the degree of
Doctor of Philosophy
in the Graduate School of Arts and Sciences

COLUMBIA UNIVERSITY

2019

ABSTRACT

Intraseasonal circulation on the Western Antarctic Peninsula Shelf with implications for shelf-slope exchange

Darren Craig McKee

The continental shelf on the western side of the Antarctic Peninsula is a region of substantial climate and ecosystem change. The Long Term Ecological Research project at Palmer Station has been sampling and studying the shelf ecosystem and physical environment since 1990. This dissertation seeks to improve our understanding of the subtidal and intraseasonal (hereafter defined together as 3-100 days) circulation on the neighboring continental shelf and is particularly motivated by the aims of the project to understand (1) how lateral transports of scalar parameters such as heat affect the vertical stratification and (2) how coastal canyon heads are linked to the larger-scale shelf circulation and why they are such ecologically productive environments. In this dissertation we study: (1) the origin and mixing of mesoscale eddies as agents of heat transport and stirring; (2) the spatial coherence of shelf-scale barotropic velocity fluctuations, their origin through flow-topography interaction with Marguerite Trough Canyon, and their associated heat transports; and (3) the wind-driven dynamics of the long-shore flow manifested through coastal trapped waves and their ability to both induce upwelling at a coastal canyon head and to modulate isopycnal depth at the continental shelf-break. This work takes an observational approach, utilizing the rare and expansive data set afforded by the long-term

sampling program including shipboard CTD and ADCP profiles, moored current meter time series, and CTD profiles from an autonomous underwater vehicle.

Table of Contents

List of Tables

List of Figures

Acknowledgments

First, I would like to thank my advisor, Doug Martinson, for his encouragement and support – both scientific and otherwise – throughout this process. These attributes were manifested in long evenings in front of the whiteboard and critique of many drafts, but also through steady supply of sugar, caffeine, and stories. His trust in my abilities allowed me to play a major role in the design of field campaigns and to collect the data needed for this dissertation. I am also indebted to Rich Iannuzzi who, in addition to being our group's instrumentation and data wizard, served equally important roles as guru and life coach.

I benefited greatly from dialog with my other committee members, Arnold Gordon and Xiaojun Yuan. Arnold, with his seemingly limitless knowledge of the global ocean, always forced me to ask 'so what?' and to think about the implications of my findings. Xiaojun provided context for my work and helped me develop the ideas of remote wind forcing in chapter 4 with her expertise in polar oceanography and atmospheric teleconnections.

I was privileged with the opportunity to conduct this research as part of the Pal LTER team. This wonderful cast of characters (including everyone among the principal investigators, support staff, technicians and crew aboard the ARSV *Laurence M. Gould*, and students) has been a wellspring of intellectual curiosity and creativity. In particular, I would like to thank: Oscar Schofield for his enthusiasm and for giving me control of one of his gliders for an entire field season, yielding the data set that led to chapter 2; Hugh Ducklow for giving me so many opportunities to go to sea (perhaps too many!); and finally Naomi Manahan for conducting mooring operations when I was not at sea (and for providing sass and good humor when I was). Practically speaking, I was partially supported by Palmer LTER Award NSF PLR-1440435.

A number of other people at Lamont contributed either directly to this work or to simply making this seemingly endless endeavor somewhat more tolerable. To name a few, Ginny DiBlasi-Morris is always cheerful and keeps the Oceanography ship on course. Brendan and Orawan Buckley always had time for conversation on trips to the frog pond. Mark Cane shared his wisdom as only he can and taught me about equatorial waves (which aren't all that different from continental shelf waves after all). Bruce Huber taught me about mooring design and ADCP's and was inspirational in his attention to detail and his patience. Larry Rosen, our former Socratic gadfly, kept me on my toes with his unannounced discourse and provided a wealth of esoteric knowledge along the way. Finally, Ryan Abernathey had useful insights regarding mixing in chapter 2.

Without doubt, though, the greatest acknowledgments are due to my family – my parents and my sister, Kali – who had the undue burden of putting up with me over the years. They were supportive in ways too numerous to mention, were always there for me without hesitation, and are a major reason this work was seen to completion.

1) Introduction and Background

Section 1.3.2.2 and figure 1.2 were published in:
Gille, S.T., D.C. McKee, and D.G. Martinson, 2016: Temporal changes in the Antarctic Circumpolar Current: Implications for the Antarctic continental shelves. *Oceanography*, **29(4)**, 96-105, doi:https://doi.org/10.5670/oceanog.2016.102.

1.1) Introduction

The continental shelf on the western side of the Antarctic Peninsula (WAP) is a region of substantial climate and ecosystem change (Cook et al. 2016; Ducklow et al. 2007; Martinson et al. 2008; Meredith and King 2005; Schmidtko et al. 2014; Stammerjohn et al. 2008, 2012; Turner et al. 2013, 2016). The Long Term Ecological Research project at Palmer Station (Pal LTER) has been sampling and studying the WAP shelf since 1990 (Smith et al. 1995). This dissertation seeks to improve our understanding of the subtidal and intraseasonal (hereafter defined together as 3-100 days) circulation on the WAP shelf and is particularly motivated by the aims of the Pal LTER project to understand (1) how lateral transports of scalar parameters such as heat affect the vertical stratification and (2) how coastal canyon heads are linked to the larger-scale shelf circulation and why they are such ecologically productive environments. In this dissertation we study: (1) the origin and mixing of mesoscale eddies as agents of heat transport and stirring; (2) the spatial coherence of shelf-scale barotropic velocity fluctuations, their origin through flow-topography interaction with Marguerite Trough Canyon, and their associated heat transports, and (3) the wind-driven dynamics of the long-shore flow manifested through coastal trapped waves and their ability to both induce upwelling at a coastal canyon head and to modulate isopycnal depth at the continental shelf-break. While numerical models have been absolutely vital for testing the plausibility of physical phenomena in the region (Dinniman et al. 2011, 2012; Dinniman and Klinck 2004; Graham et al. 2016; St-Laurent et al. 2013; Thoma et al.

2008) and informing the field campaigns undertaken here, all hypotheses must eventually be ground-truthed with observations. Thus, this work takes an observational approach, utilizing the rare and expansive data set afforded by the Pal LTER program including shipboard CTD and ADCP profiles, moored current meter time series, and CTD profiles from an autonomous underwater vehicle.

In this introductory chapter we begin in section 1.2 by presenting an overview of the physical environment on the WAP which points to the important role played by shelf-slope exchange of warm subpycnocline waters. Shelf-slope exchange is discussed in section 1.3 by describing various potential exchange processes and assessing our current state of understanding. In section 1.4 we present an overview of the Pal LTER program with particular emphasis paid to the theme of lateral connections and vertical stratification that motivates this study, culminating in what has been termed the canyon hypothesis. Finally, in section 1.5 we provide an overview of the three research chapters to follow.

1.2) The physical environment of the WAP

1.2.1) Overview

The continental shelf on the WAP broadly contains the regions spanning Drake Passage to the north and the Bellingshausen Sea shelf to the southwest (figure 1.1). The hydrography and circulation span two very different regimes separated approximately by the southern terminus of the Bransfield Strait. The Bransfield Strait features a cyclonic gyre (Zhou et al. 2006) which circulates cold waters from the Weddell Sea (Gordon and Nowlin 1978). The influence of cold Weddell Sea waters is confined to the vicinity of the Strait, possibly due to the sharp potential vorticity barrier at its southwestern boundary imposed by its western boundary current (Zhou et

al. 2006) or by the steep bathymetry crossing the shelf to the south (Moffat and Meredith 2018), or due to the divergence in the climatological winds from coastally upwelling to the north and coastally downwelling to the south of Anvers Island. On the other hand, the southern region of the WAP – which is the focus of this work – is under strong influence of Circumpolar Deep Water (CDW) that is upwelled within the Antarctic Circumpolar Current (ACC) and brought into close proximity of the continental shelf by the topographically unobstructed flow of the southern boundary of the ACC in its vicinity.

While the CDW spans a range of properties, it is historically separated into two end-members with distinct origins: Upper Circumpolar Deep Water (UCDW) is defined by a temperature maximum (and oxygen minimum) and Lower Circumpolar Deep Water (LCDW) is defined by a salinity maximum (Gordon 1971). This is partly because, while the Ekman divergence over the ACC leads to the upwelling of CDW around the continent, the deep waters of the different basins have different properties. The UCDW is more easily identified by its low oxygen signature (since the temperature maximum is sometimes subdued). It originates in the very old deep waters of the Pacific and Indian Oceans and is found approximately between neutral surfaces γ^n = [27.95 – 28.15 kg m^{-3}] (Whitworth et al. 1998) which corresponds to depths of ~200-600 m south of the Polar Front. The LCDW salinity maximum can be traced to North Atlantic Deep Water in the Atlantic sector and the water mass approximately spans the neutral surfaces γ^n = [28.18 – 28.27 kg m^{-3}] (Orsi et al. 1999). The lower isoneutral of CDW is the densest that is completely circumpolar around Antarctica and approximately corresponds to the 0 ºC isotherm which sometimes defines the upper boundary of Antarctic Bottom Water (AABW). Flow of CDW generally follows ACC streamlines except in the downstream vicinity of topographic features which generate strong eddy activity that transports the water southward and

upward along isopycnals (Tamsitt et al. 2017), towards the Antarctic shelf-break. With the southern boundary of the ACC generally coincident with the southernmost extent of UCDW (Orsi et al. 1995), it is apparent that UCDW is available immediately adjacent to the WAP shelf (figure 1.2).

1.2.2) Hydrography and subinertial circulation on the WAP

1.2.2.1) Hydrography

The subpycnocline layer of the mid-shelf region of the WAP consists of a modified variety of CDW (mCDW) (Klinck 1998; Martinson et al. 2008; Smith et al. 1999). Above that is a remnant winter mixed layer water (Winter Water; WW) that was formed at the freezing point during sea ice production the previous winter. The diffusive balance between the remnant WW and the underlying CDW maintains the permanent pycnocline, whose stratification is quite weak and more comparable to deep ocean stratification elsewhere (Howard et al. 2004). The CDW end-member is episodically replenished via shelf-slope exchange, yielding an effectively limitless source of heat. Because wintertime formation of sea ice mixes the water column downwards and entrains heat from the permanent pycnocline, the perpetual resupply of subpycnocline heat prevents overturn and maintains water column stability, even in winter (Martinson 1990).

Specifically, it is the UCDW that dominates hydrography on the WAP shelf (Klinck et al. 2004; Martinson et al. 2008; Smith et al. 1999). The LCDW, on the other hand, is found within troughs (Klinck et al. 2004; Moffat et al. 2009) and may mix with the UCDW at the shelf-break (Smith et al. 1999). The mCDW is formed by mixing UCDW diapycnally with overlying WW and isopycnally with laterally adjacent shelf waters, yielding an attenuation in end-member properties as water traverses the shelf from slope to coast (figure 1.3). Near the slope the

temperature maximum is distinctly at mid-depth (~300 m) whereas at the coast and within canyons it is found deeper in the water column, often at the bottom. Above the WW in summertime is a surface mixed layer containing Antarctic Surface Water (AASW), separated from the WW by a much stronger seasonal pycnocline. The depth and properties of the surface mixed layer vary regionally and interannually and are affected by insolation, wind-mixing, and freshwater input from both sea ice and glacial melt (Carvalho et al. 2016; Meredith et al. 2017). A canonical temperature profile and *T*/*S* diagram are shown in figure 1.3.

1.2.2.2) Circulation

The large-scale (hundreds of kilometers) subinertial circulation on the WAP can largely be attributed to the large-scale wind field. There is a strong northeastward flowing current (Shelf-Break Jet; SBJ) along the inner continental slope associated with the southern boundary of the wind-driven ACC and with the overlying wind stress curl upwelling. The coastal winds are generally coastal-downwelling south of the Bransfield Strait, yielding a broad, southwestward Coastal Current (CC). The baroclinic component of the CC is seasonally enhanced by a cross-shelf density gradient induced by near-surface meltwater (Moffat et al. 2008). The shelf-break flow associated with the ACC's southern boundary and its turbulence leads to a complex set of braided and/or meandering jets (Savidge and Amft 2009; Stern et al. 2015) that may be coincident with or distinct from the ACC southern boundary at different latitudes or at different times. The prevailing cyclonic circulation associated with the SBJ and the CC is well captured in fields of geopotential anomaly as calculated from ship surveys (Martinson et al. 2008) as well as in Eulerian-mean absolute currents from a database of shipboard ADCP profiles (Savidge and Amft 2009).

On smaller scales (tens of kilometers) the flow is largely barotropic, which has the consequence of supporting cyclones over canyons and anticyclones over banks. This has been revealed by isolated moorings (Martinson and McKee 2012; Moffat et al. 2009) and regional models (Dinniman et al. 2011; Dinniman and Klinck 2004) and even by surface drifters (Beardsley et al. 2004), the latter confirming an expression of the bathymetry at the surface. Canyons are effective at channeling CDW towards the coast (Klinck et al. 2004; Martinson et al. 2008). On even smaller scales (< 10 km), mesoscale eddies are important components of the circulation (Couto et al. 2017; Graham et al. 2016; McKee et al. 2019; Moffat et al. 2009) and of the tracer variance (Eveleth et al. 2017). A schematic of the circulation on the WAP is shown in figure 1.1.

A crucial aspect of the WAP circulation is the dominance of energetic, short-duration currents that break up the large-scale, linear barotropic f/H circulation and deliver CDW from the slope onto the continental shelf and provide a significant source of available heat. Studies reveal delivery generally occurs with temporal frequency ~1 event / week (Martinson and McKee 2012; Moffat et al. 2009) and generally occurs at certain topographically preferred locations such as curved isobaths (Dinniman and Klinck 2004) and canyons such as Marguerite Trough (Couto et al. 2017; Dinniman et al. 2011; Graham et al. 2016; Martinson and McKee 2012; McKee et al. 2019; Moffat et al. 2009). CDW delivery is observed to have different vertical structure and overall efficacy in eddy-resolving regional models (Graham et al. 2016), suggesting that multiple processes are responsible. Shelf-slope exchange is discussed in more detail in section 1.3.

1.2.3) Climate change on the WAP and the role of ocean heat

The WAP is undergoing substantial climate change. One physical variable that demonstrates this most clearly is sea ice. The sea ice in the region containing the WAP and

Bellingshausen Sea is decreasing as rapidly as the sea ice in the Arctic, yielding a season that has decreased in length by 3.3 months between 1979-2011 (Stammerjohn et al. 2012). The changes in sea ice season on the WAP can be attributed to changes in the meridional wind: stronger warm northerly winds in spring drive an earlier retreat and a subsequent delayed advance (Stammerjohn et al. 2008). These changes in meridional wind are, in part, associated with changes in the Southern Annular Mode (SAM) (Thompson and Wallace 2000), the leading mode of atmospheric variability in the Southern Hemisphere representing a strengthening of the polar vortex, which demonstrated a trend towards a more positive state since the 1970's (Marshall 2003). The SAM has a strong non-annular component that projects onto the Amundsen Sea Low in the southeastern Pacific and demonstrates strong interannual variability, modulating winds, sea ice, and air temperatures on the WAP (Lefebvre et al. 2004; Stammerjohn et al. 2008) and modulating the high-latitude response to the El Niño Southern Oscillation (ENSO) (Fogt et al. 2011; Stammerjohn et al. 2008), which also projects onto sea level pressure in the southeast Pacific and affects meridional wind and general storminess there (Yuan 2004).

Associated with the major sea ice changes on the WAP is a strong wintertime atmospheric warming (Turner et al. 2013). Much of this wintertime warming can be attributed to changes in the sea ice cover whereby the longer ice-free period yields a longer period of time for the wind-driven mixing of heat across the pycnocline (Dinniman et al. 2012) and for the warming of the ocean surface by insolation (Meredith and King 2005; Stammerjohn et al. 2012), both of which contribute to a further delay in the autumn sea ice advance. There is some evidence that the warming trend has weakened or reversed since 1999 due to changes in the mid-latitude jet and low pressure over Drake Passage, the latter advecting cold air from the Weddell Sea, even though the more persistent cyclonicity and stronger polar front jet in the same time

period would tend to be associated with warmer, low ice conditions on the WAP (Turner et al. 2016).

While ice edge advance and retreat are largely wind-driven, subpycnocline ocean heat can control their timing under weak winds, and, regardless of wind strength, ocean heat dominates the control of ice production (Saenz et al. 2018). Stammerjohn et al. (2012) estimate that the observed surface ocean temperature increase of 0.04 ºC yr^{-1} (Meredith and King 2005) distributed over a typical seasonal mixed layer thickness (25 m; Martinson et al. 2008) would not supply enough heat to account for the observed trend in sea ice delay, making it necessary to invoke subpycnocline heat. Ocean heat is also directly relevant in the distribution of melt rates of marine-terminating glaciers. Glaciers under the influence of the cold Bransfield Strait waters are either advancing or stable whereas those under the influence of warm CDW are retreating (Cook et al. 2016). Both the changes in sea ice and in glacial melt are modulating the freshwater balance of the WAP water column (Meredith et al. 2017).

Clearly, subpycnocline ocean heat has important implications for sea ice, glacial ice, and atmospheric temperature changes on the WAP. The shelf waters at the seafloor of the WAP have warmed and shoaled in recent decades (Martinson et al. 2008; Schmidtko et al. 2014). Many of the same changes in the wind that are affecting the sea ice field are attributed to the warming of continental shelf waters around the continent. In particular, a shift to a more +SAM state has the effect of shifting the westerlies farther south. This has the effect of reducing the effect of the polar easterlies and their associated coastal downwelling, thus isopycnal depths associated with UCDW shoal at the shelf-break and bring warmer water to shelf depth (Spence et al. 2014). While such a process does happen, this is a deceptively simple view of cross-isobath

transport of CDW. A more detailed overview of shelf-slope exchange is presented in the next section.

1.3) Shelf-slope exchange

1.3.1) The shelf-slope exchange problem

To understand why shelf-slope exchange is difficult to achieve it is illustrative to revisit the Taylor-Proudman theorem. Approximating the Antarctic coast as aligned in the zonal direction, suppose that the large-scale flow around the continent is steady and in geostrophic balance:

$$fu = -\frac{1}{\rho}\frac{\partial p}{\partial y}, \qquad -fv = -\frac{1}{\rho}\frac{\partial p}{\partial x}. \tag{1.1}$$

If we differentiate these relations in x and y, respectively, and neglect the planetary vorticity gradient (which is much smaller than the topographic vorticity gradient associated with the steep continental slope; $\beta_{topo} = f\alpha/H \sim 9 \times 10^{-9}$ (ms)$^{-1}$, $\beta_{planetary} \sim 1 \times 10^{-11}$ (ms)$^{-1}$), we are left with:

$$-\left(\frac{\partial u}{\partial x} + \frac{\partial v}{\partial y}\right) = \frac{\partial w}{\partial z} = 0. \tag{1.2}$$

Therefore, if the vertical velocity is zero at the upper boundary then it must be zero everywhere. And, if the vertical velocity is zero at the seafloor then there can be no flow across isobaths since

$$w = -\mathbf{u}\cdot\nabla H = 0. \tag{1.3}$$

Taking this a step further, substituting the thermal wind balance into the steady continuity equation reveals the further restriction that the velocity vector is everywhere parallel to the shear vector:

$$-u\frac{\partial v}{\partial z} + v\frac{\partial u}{\partial z} = \mathbf{u}\times\frac{\partial \mathbf{u}}{\partial z} = 0. \tag{1.4}$$

Thus, the flow is steered by bathymetry at all depths. This is a statement of the Taylor-Proudman theorem.

In order to generate cross-isobath flow, then, we need to consider processes that violate the major assumptions that led to the theorem. For example, we should consider processes that introduce time dependence (e.g., mesoscale eddying, transient wind forcing), nonlinearity (e.g., momentum advection, flow-topography interactions), and/or friction (e.g., surface or bottom Ekman layers). Any such process is innately difficult to quantify since cross-isobath flow will be secondary to the long-shore geostrophic balance, however, they are made even more difficult to observe and model by the unique physical environment of the Antarctic margins. The high latitude (large f) and weak stratification (small N) make the relevant length scales very small (for example, the first deformation radius $L_1 = NH/f \sim 5$ km on the WAP shelf). Additionally, the small N emphasizes bathymetric control, and small-scale canyons and troughs are generally poorly mapped.

1.3.2) Potential exchange processes and our current state of understanding

Here we outline some physical processes that may be relevant for the cross-slope delivery of UCDW onto the WAP shelf and summarize our current state of understanding. As will be revealed in the following discussion, there are three unique traits to the long-shore flow along the WAP slope that render exchange probable: (1) Close proximity of the southern ACC boundary; (2) weak or absent Antarctic Slope Front; (3) wide, eastward flowing SBJ.

1.3.2.1) Mesoscale eddies

In addition to the southern ACC boundary being located in close proximity to the continental shelves of West Antarctica, the Antarctic Slope Front (ASF; Gill 1973) that occupies much of the perimeter of the Antarctic margins is generally weak or absent along the WAP

(figure 1.4). Because mesoscale eddies can transfer water across the slope wherever isopycnals are continuous between the shelf and the open ocean, this means a wide range of mid-depth isopycnals have uninterrupted access to the continental shelf. All that remains is an instability process that can generate eddies to stir the cross-slope gradient along isopycnals.

Mesoscale eddies draw from the large-scale available potential energy (baroclinic instability) and/or the large-scale mean kinetic energy (barotropic instability). Various classical problems in geophysical fluid dynamics (e.g., the so-called Eady, Charney, and Phillips problems) and observations (e.g., Stammer 1998) demonstrate that baroclinic instabilities tend to form coherent structures on the order of the first deformation radius ($L_1 = NH/f$). This length scale can be interpreted physically in various equivalent manners: (1) the scale beyond which flows have more available potential energy than kinetic energy; (2) the scale at which rotational effects become important; (3) the ratio of the gravity wave speed to the Coriolis parameter. We use the term mesoscale to refer to variability with scales on the order of L_1.

Because instabilities depend on sign changes of the potential vorticity gradient (Pedlosky 1987), in accordance with modified Eady theory, for prograde currents (isopycnals slope in the same sense as isobaths) the topographic potential vorticity barrier associated with the bottom slope is generally destabilizing to a point but then strongly stabilizing with the relevant parameter being the ratio of the isopycnal slope to the bottom slope (Blumsack and Gierasch 1972; Isachsen 2011). While this would tend to suppress baroclinic instability on the steep continental slope of the WAP, interior potential vorticity gradient sign changes associated with strong shears in the shelf-break jet may still promote instabilities (Isachsen 2011). Eddy fluxes around the continent are highly dependent on a variety of parameters, including the isopycnal

slope and bottom topography and are thought to be highly localized geographically (Stewart et al. 2018; Stewart and Thompson 2015).

The importance of the mesoscale on the WAP has been argued for by theoretical means (Stewart and Thompson 2015), demonstrated in high-resolution numerical models (Graham et al. 2016; St-Laurent et al. 2013), and observed (Couto et al. 2017; Martinson and McKee 2012; McKee et al. 2019; Moffat et al. 2009). Warm-core, subpycnocline, primarily anticyclonic eddy-like features have been found within several tens of kilometers from the shelf-break, particularly in the vicinity of Marguerite Trough, and are steered along isobaths. The hydrographic properties of the eddies indicate an injection of UCDW as it is found on the continental slope and their length scale is as large as or slightly larger than the first baroclinic Rossby radius.

Most prior observational studies have focused on the role of the eddies in isolating warm slope water and transporting it onto the continental shelf, similar to the role played by lens-like eddies (e.g., Meddies; Ruddick and Hebert 1988). However, the cascades associated with geostrophic turbulence yield a much more gradual spectral roll-off for potential enstrophy and tracer variance compared to that of density, meaning that energy-containing, low-mode baroclinic instabilities effectively stir and twist tracer gradients along isopycnals into increasingly small-scale *T*-*S* features that must be density compensated (Smith and Ferrari 2009). Mesoscale eddies are the focus of chapter 2, where we will show that their effect is two-fold as they both isolate and transport pure UCDW from the slope onto the shelf but also stir the cross-slope gradient along isopycnals, generating density-compensated *T*-*S* variance.

1.3.2.2) Flow-topography interaction

The slope and deep continental shelves of Antarctica are everywhere incised by glacially carved submarine canyons and troughs. The WAP in particular is characterized by two major

canyon systems (figure 1.1): Marguerite Trough to the south, leading to Marguerite Bay south of Adelaide Island, and Palmer Deep canyon to the north near Anvers Island. In particular, Marguerite Trough appears to have a profound impact on both the mean and intraseasonal variability of flow on the inner shelf between the two islands.

Theories for flow interaction with a canyon suggest that when a right-bounded flow in the southern hemisphere (as is the SBJ against the WAP) impinges upon a submarine canyon, cyclonic vorticity is introduced into the water flowing over the canyon, steering the flow up-canyon along the downstream wall (Allen et al. 2001; Allen and Hickey 2010; Kämpf 2006, 2007). Canyons effectively decrease the dynamically relevant length scale of the flow which increases the Rossby number and allows up-canyon flow to cross isobaths and upwell onto the shelf-proper at a location shoreward of the impinging current. Once on the shelf, vortex compression will steer the flow again seaward in the downstream direction, generating an anticyclonic counterpart to the canyon cyclone. When the incident flow is slow (or reversed), the cyclonic vortex generated at the canyon mouth remains in place and the SBJ passes by largely unaffected (Waterhouse et al. 2009). However, if the flow is sufficiently strong, the cyclonic vortex is swept shoreward to occupy the entire canyon and cross-isobath flow out of the canyon is enhanced by nonlinear effects.

In the Southern Ocean, this mechanism produces eastward flowing currents with associated intruding flow along the eastern walls of canyons. These conditions are met along the WAP and Bellingshausen Sea, as well as in parts of the Amundsen Sea. Even in the western Amundsen Sea where surface currents are westward, an eastward undercurrent exists at canyon depths (Walker et al. 2013), which should permit the process. In the Amundsen and Bellingshausen Seas and along the WAP, CDW delivery within canyons is both observed

(Assmann et al. 2013; Martinson and McKee 2012; Schofield et al. 2013; Wåhlin et al. 2013; Walker et al. 2013) and modeled (Dinniman et al. 2011; Dinniman and Klinck 2004; Graham et al. 2016; St-Laurent et al. 2013; Thoma et al. 2008). Using an isopycnic-coordinate model, Thoma et al. (2008) found that enhanced westerlies led to more cross-shelf transport of CDW, but they were not able to deduce the underlying process. Dinniman et al. (2011) used a 4-km resolution configuration of the Regional Ocean Modeling System (ROMS) model to find that the cross-canyon CDW dye flux was correlated to the inner-slope transport, which in turn was correlated to the along-slope wind fluctuations in the weather band. In a later study, Dinniman et al. (2012) found that enhanced westerlies led to more total cross-shelf transport of CDW. Interestingly, the greater transport of CDW was not associated with greater basal melting for the deeper ice shelves because the stronger winds additionally drove stronger cross-pycnocline mixing of CDW heat to the atmosphere (presently, cross-pycnocline mixing of heat is believed to be rather weak; Howard et al. 2004). Wåhlin et al. (2013) and Assmann et al. (2013) also found eastward wind at the shelf-break to be important in the exchange, observing depth-independent fluctuations at weather-band frequencies along the eastern wall of the canyon that correlated with the eastward wind. Carvajal et al. (2013) used the same mooring data as Wåhlin et al. (2013) and found that using higher spatial resolution synthetic aperture radar winds improved the statistical correlation with the subsurface currents. They also suggested that sea ice cover may mitigate the ocean's ability to respond to higher frequency events. In most of these studies, delivery was found to be, at least in part, episodic, and coherency of CDW transport with wind stress was found at various time scales.

In addition to the advective process, canyons may channel mesoscale CDW-core eddies towards the coast (Moffat et al. 2009). In an idealized numerical model study with a

baroclinically unstable zonal current flowing along a continental slope cross-cut by a submarine trough, St-Laurent et al. (2013) found that canyons yield intrusions of CDW by the advective-driven canyon upwelling process but also by channeling CDW eddies into the canyon. They found that the dominance of one mechanism over the other is dependent on whether the jet was wide enough to straddle the canyon (yielding mean flow-topography interaction) or held offshore (yielding wave-topography interaction). Each process could yield a similar shoreward heat flux. It is not currently known how or if winds may alter the proximity of the shelf-break current or by how much the current's proximity varies, though their model jet widths varied by 12 km. The wide width of the SBJ in the vicinity of Marguerite Trough (Graham et al. 2016) may partly explain why that canyon has such a profound impact on the shelf circulation downstream.

While canyons are clearly significant for fostering cross-shelf transport, they cannot provide the only means of exchange, because intrusions of CDW are also observed in both westward flowing currents (e.g., Ross Sea) and in regions without canyons. In their 4-km resolution ROMS model study, Dinniman and Klinck (2004) found that intrusion sites are generally correlated with isobath curvature: for sufficiently high Rossby number, in locations where isobaths curve into the shelf-break current the flow is unable to adjust to the changing topography and nonlinear momentum advection carries the current onto the shelf.

The effects of Marguerite Trough canyon on the WAP circulation at intraseasonal time scales are considered in chapter 3.

1.3.2.3) Ekman transports

The stress imparted by the seafloor on a slope current yields a net transport to the right of the flow in the Southern Hemisphere. For right-bounded barotropic currents, this has the effect of pumping CDW upwards onto the continental slope. Because the water column is stratified,

the upwelling process advects buoyancy, which, after an adjustment time, generates a lateral density gradient and associated geostrophic current within the Ekman layer that exactly cancels the barotropic flow at the seafloor. Setting the long-shore flow at the seafloor to zero has the effect of halting the Ekman transport, yielding an arrested Ekman layer.

Arrested Ekman layers have been observed in the regions of the Amundsen Sea slope under the influence of the eastward flowing ACC, but not the westward limb of the Ross Gyre (Wåhlin et al. 2012). The shoreward transports that those authors obtained by integrating over the Ekman layer and along the slope are comparable to those induced by a neighboring submarine canyon (Walker et al. 2007). Bottom Ekman transports on the WAP have recently been implicated in a modeling study by Spence et al. (2017) who suggest that an enhanced eastward flow in response to a barotropic sea surface height drop induced by a coastal Kelvin wave yields a shoreward transport of CDW in a bottom Ekman layer. They argue that the response is particularly strong on the WAP owing to the steep bottom slope.

While the conditions on the WAP are certainly conducive to the process, CTD casts on the WAP reveal that bottom Ekman layers do not generally penetrate very far onto the shelf and reveal that the water that is transported up-slope within these layers is generally the saltier and denser LCDW. In contrast to this, the hydrography of the WAP is dominated by the warmer and more buoyant UCDW (Martinson et al. 2008; Smith et al. 1999) and observations (Martinson and McKee 2012; Moffat et al. 2009) and regional model simulations (Graham et al. 2016) of shelf-slope exchange suggest that the temperature signal associated with weather-band fluctuations is mid-depth-intensified, not bottom-intensified. While bottom Ekman layers do likely play some role in shelf-slope exchange on the WAP (e.g., perhaps providing a mixing

pathway with UCDW at the shelf edge to yield mCDW), we choose to focus on other processes more consistent with the dominance of UCDW.

1.3.2.4) Coastal trapped waves

A critical parameter for flow-topography interaction and bottom Ekman layer transport is the magnitude (and direction) of the flow along the inner slope. Most prior studies cited above find good correlation between this quantity and the long-shore wind stress but generally do not indicate any underlying dynamical link between the two or the scale of the wind systems that are correlated to the flow. Antarctica is a unique environment in that its uninterrupted coastline provides a circumpolar waveguide in both the atmosphere and ocean. Therefore, there is the plausibility for the current along the WAP slope to feel the influence of energetic, low-wavenumber, long-shore wind stress from remote locations. It has long been known (Aoki 2002; Kusahara and Ohshima 2009) that tide gauges around the continent demonstrate a circumpolar-coherent response in sea surface height at periods longer than about 10 days and that this coherent variability modulates Drake Passage transport via barotropic dynamics (Hughes et al. 2003).

Additionally, finite-wavenumber variability in the long-shore wind has been shown to influence coastal sea surface variability at shorter time scales via barotropic shelf waves (Kusahara and Ohshima 2009), although thus far authors have only considered fluctuations in sea surface height and not whether or not such fluctuations are transmitted to the velocity field. Coastal trapped waves are the natural response of shelf currents to long-shore wind stress (Gill 1982): As the long-shore wind stress induces an Ekman transport across the shelf, the associated vorticity perturbation causes the disturbance to propagate with the coast to its left in the southern hemisphere. Coastal trapped waves are dispersive and their modal properties depend on both

bottom slope and stratification, however in the limit of vanishing stratification they become barotropic shelf waves (Huthnance 1978) and in the low-frequency, low-wavenumber limit relevant for intraseasonal variability they are approximately nondispersive (Gill and Schumann 1974). Wind-driven variability in the long-slope barotropic transport and its relation to flow-topography interaction has not been sufficiently studied to this point but represents a potentially significant way to generate energetic currents along the WAP shelf. In addition to modulating the long-shore flow at the shelf-break, coastal trapped waves may modulate pycnocline depth at or near the continental slope, which can set the properties of the water that is transported onshore (Griffin and Middleton 1986). Coastal trapped waves are the focus of chapter 4 and both of the above potential impacts are studied.

1.3.2.5) Tides

The role played by tides in shelf-slope exchange on the WAP has long been neglected. This could be in part because tidal energy on the WAP is thought to be relatively weak compared to other Antarctic shelves (e.g., Beardsley et al. 2004). A more cynical view, though, would argue that they have been neglected because the regional models that have informed much of our knowledge of WAP circulation have not included their forcing (Dinniman et al. 2011; Dinniman and Klinck 2004; Graham et al. 2016). Tides have been shown to lead to cross-slope transfer of CDW in the Ross Sea by modulating isotherm depth at the shelf-break (Kohut et al. 2013). Tidal-forced short coastal trapped waves along the continental slope may have a strong shoreward component (Middleton et al. 1987). Tides may also yield exchange via rectification of a periodic flow. A recent study (Stewart et al. 2018) considers for the first time a circum-Antarctic model at 1/48º resolution that both resolves eddies and includes tidal forcing. They find that while eddies yield a strong shoreward heat flux over the slope, tides yield a shoreward

heat flux over the shelf-proper. An interesting result is that the tidal transport is largely compensated by a mean transport, which is probably due to a tidal or eddy momentum flux convergence. Tides are not considered in this work and are filtered out of all time series when applicable.

1.4) The Pal LTER program

1.4.1) Project overview

The Pal LTER has been studying the pelagic marine ecosystem on the western Antarctic Peninsula shelf since 1990 (Smith et al. 1995). The overarching goal of the project is to obtain a comprehensive understanding of the Antarctic seasonal sea-ice influenced ecosystem south of the Antarctic Polar Front. This includes understanding: (1) Physical forcing of the ecosystem from climate scale wind variability to local sea ice and ocean properties; (2) Trophic interactions from phytoplankton through zooplankton up to top predators (penguins and whales); and (3) biogeochemical cycling. An implicit assumption is that all levels of the marine ecosystem are dependent on the temporal variability of sea ice. This includes components as disparate as the phenology of primary production and the foraging patterns and survival of top predators. As discussed in section 1.2, the duration and timing of the annual sea ice cycle is rapidly changing, with both a decreasing trend and substantial interannual variability.

The physical oceanography aspect of the project is most interested in the interplay between lateral transports and vertical stratification across myriad spatial ($L_1 \sim 5$ km through CTW wavelengths $\sim 10^3 - 10^4$ km) and temporal (subtidal through decadal) scales. This includes shelf-slope exchange processes as discussed in section 1.3 and processes of vertical and lateral mixing. Cross-slope delivery and mixing of heat, in particular, is of interest, owing to the

links between ocean heat and sea ice growth and thickness (e.g., Martinson 1990; Saenz et al. 2018), as well as to the links between ocean heat and glacial melt (Cook et al. 2016) and thus trace metal release (Annett et al. 2017) and near-surface stratification (Meredith et al. 2017).

1.4.2) Lateral connections and vertical stratification

In the current iteration of the Pal LTER a major theme of research emphasizes lateral connections and vertical stratification. As was stated in the proposal, since vertical water column stratification determines bottom-up controls on WAP ecosystem dynamics, the project seeks to answer the question: what are the effects of lateral transports (sea ice, glacial meltwater, offshore heat and nutrients, iron) on local stratification, and how do they drive changes in the ecosystem? A guiding component of this theme has been what is termed the "canyon hypothesis", motivated by the observation that canyons foster a productive food web at their heads (Schofield et al. 2013). Ecological hotspots on the WAP shelf, identified, in part, in terms of locations of permanent Adelie penguin breeding sites and increased phytoplankton biomass, are coincident with the heads of submarine canyons (Ducklow et al. 2007; Fraser and Trivelpiece 1996; Schofield et al. 2013). Over the head of Palmer Deep, the food web consists of one or more seasonal phytoplankton blooms (Kim et al. 2016) which is grazed by Antarctic krill, who serve as the major prey source for penguins and other top predators. The foraging behavior of Adelie penguins is influenced by variability in krill aggregation properties and biomass, which are related to the circulation (Bernard and Steinberg 2013).

Compared to the shallower adjacent shelf, canyons have reduced sea ice, elevated sea surface temperature, elevated chlorophyll, and an elevated abundance of diatoms, which are often indicative of a bigger bloom (Kavanaugh et al. 2015). Because UCDW is rich in macronutrients (and moderately so in micronutrients), it was generally assumed that an important

ecological role for the canyons was their ability to funnel UCDW towards the coast (e.g., Prézelin et al. 2000). On the contrary, more recent work suggests that the role of the canyon is more so its induced circulation and stratification at its head as opposed to the tracers within the channeled flow.

Carvalho et al. (2016) used repeat glider flights across the head of Palmer Deep canyon to reveal that a fundamental control on phytoplankton blooms is the mixed layer depth: blooms are associated with a shallower mixed layer depth, and shallower mixed layer depths are associated with lower salinity water (due to glacial or sea ice melt). They found that macronutrients were not initially limiting, which is consistent with the findings of Kim et al. (2016). Both the regulatory role of warm water in limiting sea ice growth (Saenz et al. 2018) and the mechanical upwelling induced by along-axis flow can place a bottom-up control on the mixed layer depth in near-shore environments.

Kohut et al. (2018) deployed an ocean observing system consisting of gliders, moorings, and HF radar over Palmer Deep and found that residence times associated with advection by surface currents are about 1-2 days, which is shorter than phytoplankton doubling time growth rates. This led them to conclude that Palmer Deep serves as more of a conveyor belt whereby the canyon head accumulates phytoplankton biomass due to horizontal advection as opposed to fostering local growth due to upwelling conditions.

Trace metals such as iron are critical for biological blooms and are generally limiting on the WAP shelf, particularly near the shelf edge. Correlations between meteoric water inputs and dissolved and particulate iron concentrations suggest a glacial meltwater origin for iron along the WAP coast and near the canyon head with larger concentrations at near-shore canyon heads

compared to the mid-shelf, particularly the northern shelf (Annett et al. 2017). Thus, the UCDW is not thought to be the primary iron source to the ecosystem.

In summary, lateral advection along the axis of the canyon may: (1) mechanically induce upwelling of warm water that keeps sea ice thin and attenuates mixed layer properties from below; (2) transport phytoplankton biomass towards the canyon head as it is episodically 'flushed'; (3) resuspend or retain trace elements whose primary origin is at the coast. A major gap in our understanding that we hope to address is whether or not circulation at the canyon head can be related to circulation on the inner shelf, to exchange processes at the shelf-break, and, ultimately, to wind forcing, both local and remote.

1.4.3) Oceanographic sampling

This work primarily utilizes observational data collected through the Pal LTER. Relevant to this work, the Pal LTER employs annual summertime cruises (1993-present) to sample the shelf study area, which encompasses a grid to the west of the peninsula from the coast to a couple hundred kilometers offshore, spanning slightly north of Anvers Island down to slightly north of Alexander Island (figure 1.5). The grid includes a set of regular stations nominally spaced 100 km in the 'grid line' direction (long-shore, x) and 20 km in the 'grid station' direction (cross-shore, y). All locations use the LTER coordinate system and are given as GGG.SSS where GGG is the grid line (units of kilometers) and SSS the grid station (units of kilometers) with origin 000.000 at ~69.0 ºS, ~73.6 ºW, near Alexander Island. All grid stations on the 200-600 lines were occupied through January 2008 whereas now only a subset of stations is sampled, complemented by various process study sites. At each station the ship collects a full-depth conductivity-temperature-depth (CTD) profile. From 1993-1997 these were collected with a Sea-Bird SEACAT system. Since 1998 (and for deep stations in 1996-1997) these have been

collected with a Sea-Bird 911+ CTD system, with dual pumped sensors in use since 1999. In addition, since 2000 the vessel used by the project (ARSV *Laurence M. Gould*) collected velocity profiles from its hull-mounted RDI 150 kHz narrowband instrument.

Since 2007, station data are supplemented with data from an array of moored current meters, which provide very high temporal resolution data coverage, and with data from an autonomous underwater vehicle, which provides very high spatial resolution data coverage and real-time adaptive sampling. The two platforms are leveraged to maximize their strengths. Several year-long moored current meter records are used to quantify subtidal and intraseasonal variability and to elucidate dynamics of shelf-slope exchange processes and barotropic waves. On the other hand, the Teledyne-Webb Slocum glider (Schofield et al. 2007) is used to sample the mesoscale eddy field on the WAP, to track an eddy, and to quantify its heat loss.

Instrumentation, sampling strategies, and sampling procedures are described in much greater detail in the individual research chapters as the relevant data sets are introduced. However, to provide an overview of the long-term nature of the Pal LTER sampling, we plot a few variables relevant for shelf-slope exchange in figure 1.6. The figure highlights (1) that there is not a simple relationship between subpycnocline heat content (figure 1.6b) and either depth-averaged current (which transports the heat, figure 1.6a) or near-bottom upwelled isopycnal at shelf edge (which sets source water properties, figure 1.6d), and (2) that mooring site 300.100 is representative of the properties of the southern shelf.

1.5) Outline and goals

Most broadly speaking, the aim of this work is to enhance our understanding of the circulation on, and cross-isobath delivery of UCDW to, the WAP inner shelf over the region

spanned by the Pal LTER grid, roughly between Adelaide and Anvers Islands (the boxed region in figure 1.1). This is a region where marine-terminating glaciers are thinning (Cook et al. 2016) and where the biological hotspot of Palmer Deep canyon is found (Schofield et al. 2013). More specifically, we focus on subtidal through intraseasonal variability in the circulation and seek to understand the dynamics of mesoscale eddies and flow-topography interaction as agents of cross-isobath delivery of UCDW. The intraseasonal time scale, which in this study is defined to span the ranges commonly referred to as the intraseasonal along with the weather band (3-100 days), represents a band for which there is a major gap in our understanding of circulation and shelf-slope exchange, owing in part to the sparseness of observations in space and time. A parallel goal is to understand how the UCDW mixes laterally and vertically to dictate WAP stratification. Few estimates of heat flux exist (e.g., Howard et al. 2004), diffusivities are poorly constrained (Howard et al. 2004; Klinck 1998; Klinck et al. 2004; Martinson et al. 2008), and almost nothing is known of relevant mixing processes.

With knowledge that flow-topography interaction is dependent on the long-shore flow speed and direction as discussed in section 1.3, we also seek to understand to what extent the shelf-break flow is barotropic and what sets its magnitude. This work is particularly motivated by the canyon hypothesis of the Pal LTER, where we test the idea that canyons serve as an effective way to link very disparate length scales. We speculate that large-scale, low-waveumber variability in the long-shore wind stress modulates the barotropic transport along the WAP slope whereby along-axis flow is transmitted to coastal canyon heads such as that of Palmer Deep.

The approach taken is observational, providing and analyzing a rare and unique set of data from various observing platforms (principally moored current meters and an autonomous underwater vehicle) that should serve to ground-truth simulations from regional models and

predictions from climate models that cannot resolve all processes at the relevant spatial scales. The chapters are organized as follows.

Chapter 2 examines the origin and attenuation of UCDW-core mesoscale eddies on the WAP shelf in the vicinity of Marguerite Trough. This chapter centers around a novel data set collected by a Slocum glider in which the AUV first flew directly through several warm-core eddies on the shelf, quantifying their statistics, and then identified and tracked an eddy over ~4 days in order to quantify its heat loss. It is shown that the vertical structure, radius, and separation of the eddies is consistent with a first mode baroclinic instability of the shelf-break current upstream. Concurrent shipboard CTD and ADCP data are used to diagnose the responsible mixing processes and to parameterize vertical and lateral diffusivities. Several explanations for observed thermohaline layering are considered and, while none are conclusive, the most likely candidate appears to be quasigeostrophic stirring by the eddy itself. The observed rate of heat loss of the eddy is corroborated by a diffusion model initialized with the eddy's initial hydrographic properties and informed by the parameterized diffusivities. A fundamental conclusion is that the eddies predominately lose heat laterally and downwards which preserves subsurface heat.

Chapter 3 presents the first shelf-scale observational view of intraseasonal variability in the WAP mid-shelf circulation as measured by an array of current meters that spans the two layers of the water column in the vertical, ~427 km in the long-shore dimension, and samples continuously for up to a year in length. Through EOF analysis of those records we identify a pattern that explains over half of the total variance and that remains the same across years regardless of which current meters were sampling. The pattern is related to the long-shore wind in accordance with barotropic dynamics and is qualitatively consistent with flow-topography

interaction with a canyon. An analysis of kinetic energy spectra supports the interpretation that the shelf-break current is diverted shoreward at the location of the canyon and generates substantial counterclockwise energy at periods shorter than ~10 days as the flow is compressed by a downstream bank. Surprisingly, the circulation is generally incoherent with the subpycnocline heat content, except at periods of ~40-50 days, which dominate the velocity variability.

Chapter 4 builds upon the results of chapter 3 by seeking to understand what sets the long-shore velocity fluctuations at the shelf-break that drive the spatially coherent shelf circulation pattern. In this chapter we test the hypothesis that, much like coastal sea surface height, the long-shore current can be described as a sum of a circumpolar-coherent wavenumber zero mode and one or more barotropic shelf waves. We use reanalysis surface stress integrated along wave characteristics around the continent to predict the long-shore current from the shallow water equations in the long-wave limit and compare the result to the observed barotropic current as measured by the moored current meters with good accuracy. An important distinction from previous studies is the importance of mode 2 waves in the velocity signal. In this chapter we explain the 40-60 day variability identified in the previous chapter as being due in part to strong fluctuations in the coherent mode at this period but also to the second mode wave. After diagnosing the wind-driven dynamics we discuss some of their implications for shelf-slope exchange. We show that episodic, bottom-intensified wintertime warming at a location inshore of Palmer Deep canyon is related to the predicted sea surface height signal at the location of the canyon, confirming that canyons are able to funnel large-scale, remote wind forcing down to small topographic scales via coastal trapped barotropic dynamics. This provides a potential mechanism for the canyon hypothesis of the Pal LTER and is consistent with the suggestions of

Kohut et al. (2018) that Palmer Deep acts as more of a conveyor belt of biomass rather than an incubator.

In chapter 5 we synthesize our findings and provide some recommendations for future work. Particular attention is paid to consider to what degree the processes identified on intraseasonal time scales may scale up to explain interannual or trend-like variability in the region and to what degree the processes identified here are generalizable to other regions around the continent.

Figures

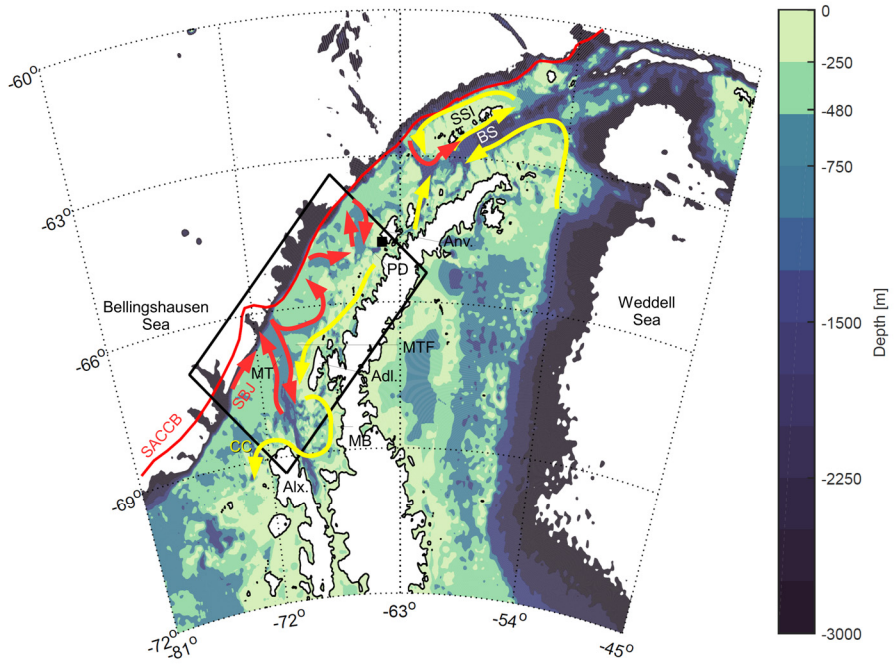

Figure 1.1: Overview of circulation on the central and the Bransfield Strait regions of the WAP as inferred from observations, modified from figure 1 of Moffat and Meredith (2018). Generally speaking, currents in red are northeastward, warm, and originate in the ACC at the continental slope whereas currents in yellow are southwestward, colder, and originate either in the Weddell Sea or via buoyancy effects due to near-shore freshwater input. Palmer Station is indicated with a black square and the Pal LTER sampling grid is indicated as a black rectangle. The acronyms are: SACCB = Southern ACC Boundary (the 0.35 dyn m contour from Orsi et al. 1995), SBJ = Shelf-Break Jet, CC = Coastal Current, MT = Marguerite Trough, MTF = Marguerite Trough Fork, MB = Marguerite Bay, PD = Palmer Deep, BS = Bransfield Strait, Adl = Adelaide Island, Anv = Anvers Island, Alx = Alexander Island, and SSI = South Shetland Islands.

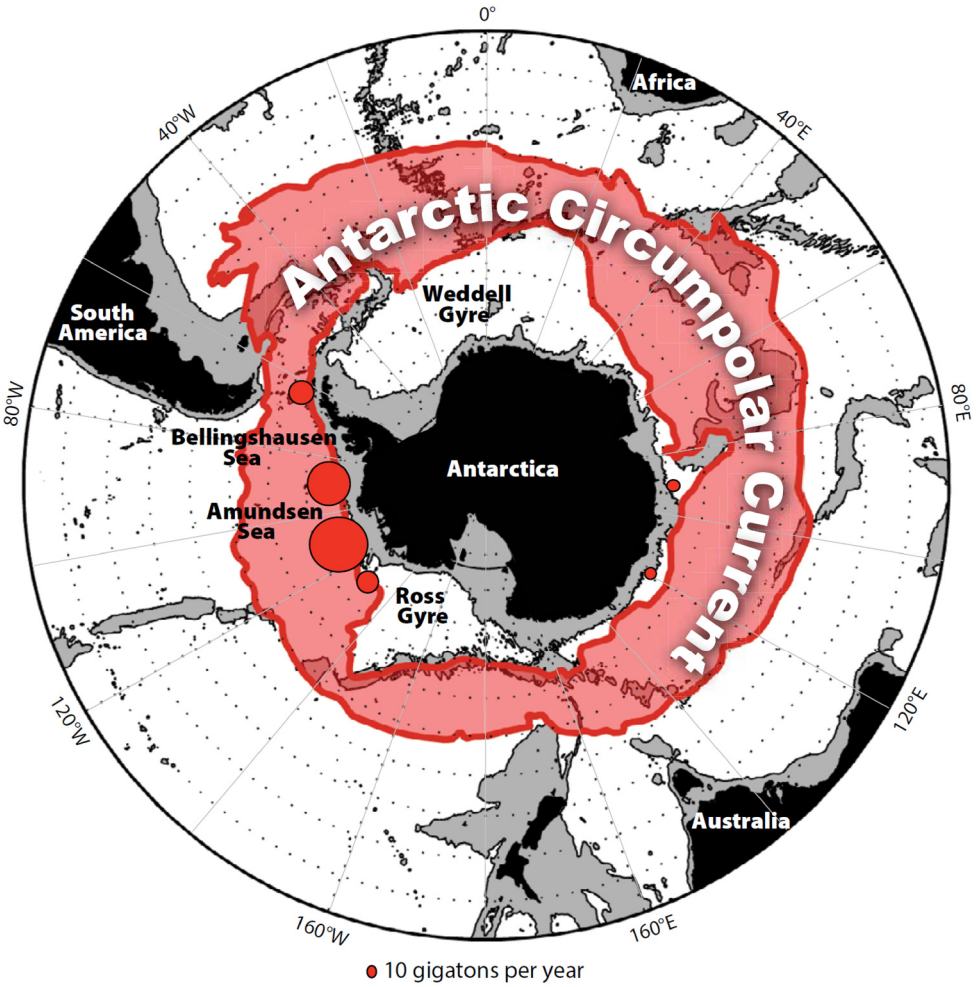

Figure 1.2: Mean position of the ACC frontal features (pink, bounded by red lines at northern and southernmost streamlines that pass through Drake Passage). Red circles indicate regions of significant ice mass loss from the Antarctic continent, as found by Rignot et al. (2008). The northern latitude boundary is 30ºS, and latitudes are marked with dotted lines at 5º increments. Grey shading indicates bathymetry shallower than 3000 m, and black indicates land. Figure reproduced from Gille et al. (2016) (their figure 2).

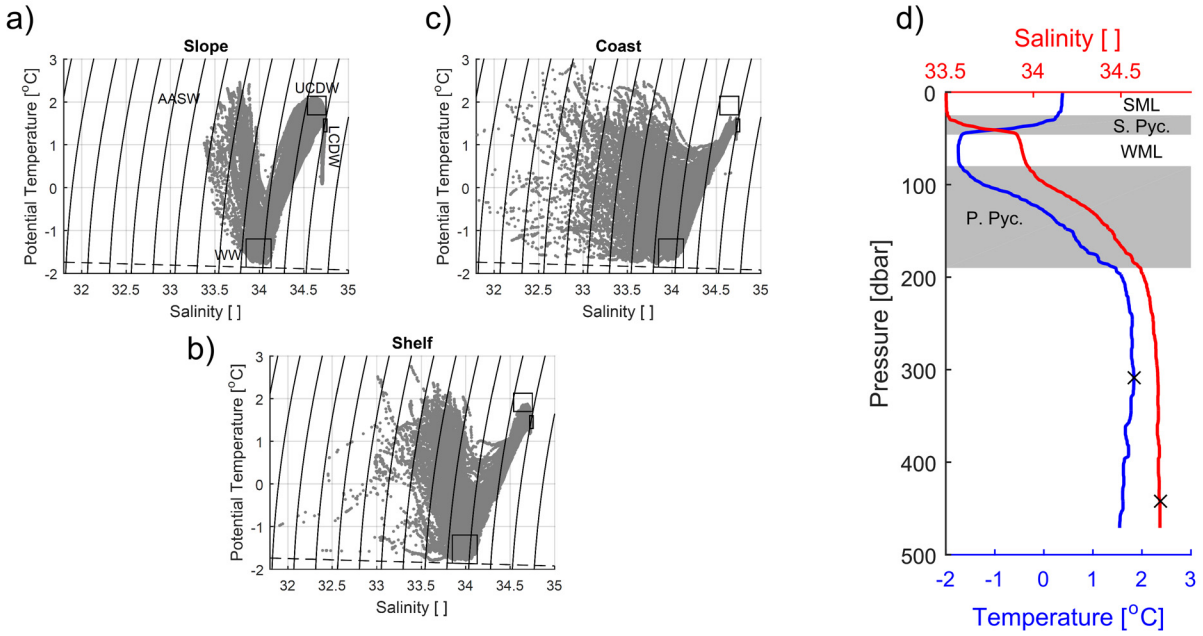

Figure 1.3: Overview of WAP area hydrography and stratification. **(a)** Temperature-salinity diagram for all Slope station CTD casts on the Pal LTER grid collected between 1999-2008 between the 200 and 600 grid lines. Potential density isopycnals spaced every 0.2 kg m^{-3} are indicated with solid lines and the surface freezing point is indicated with a dashed line. The boxes for UCDW and WW use the definitions of Martinson et al. (2008) meant to be representative of open-ocean ACC values. The box for LCDW uses the temperature range of Klinck (1998). The lower salinity bound is his suggested value of 34.72 although the upper bound was arbitrarily chosen as 34.76. **(b)** and **(c)** are as in (a) except for the Shelf and Coast regions, respectively. **(d)** Representative profiles of temperature and salinity (site 300.100 year 2004). The depth ranges of the seasonal mixed layer (SML), seasonal pycnocline (S. Pyc.), remnant winter mixed layer (WML), and permanent pycnocline (P. Pyc.) are identified as in Martinson and Iannuzzi (1998) and are labeled and alternately shaded. The temperature and salinity maxima are identified with black x's.

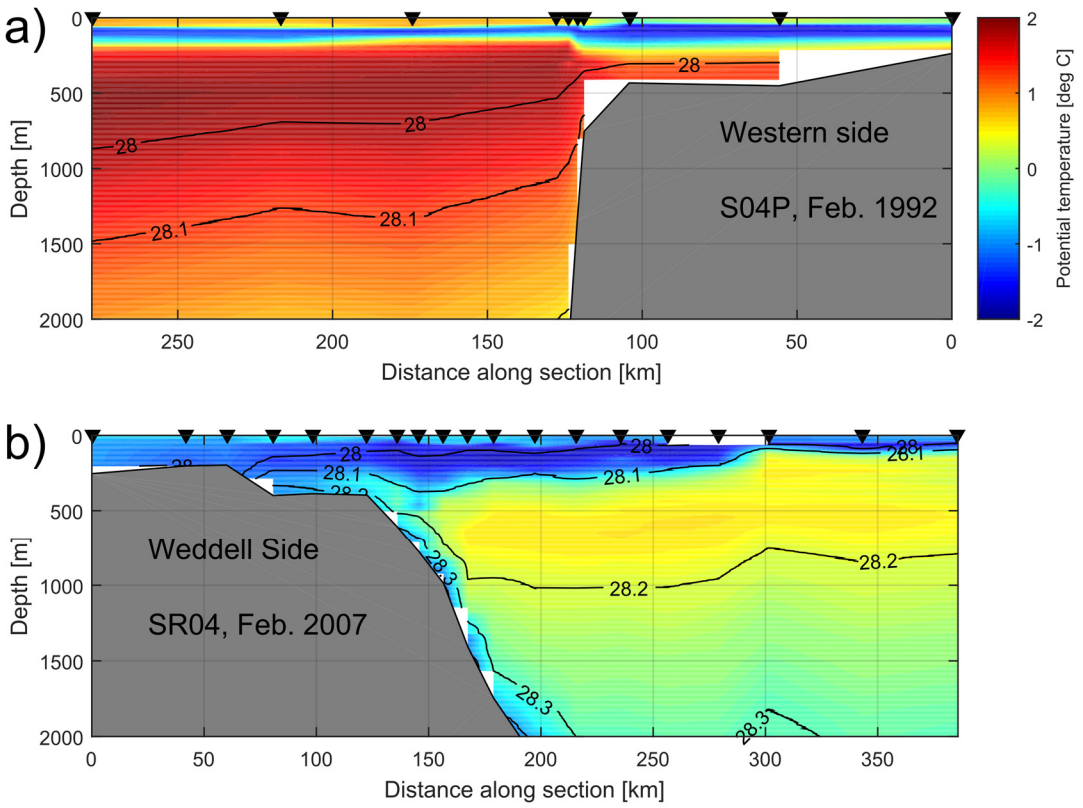

Figure 1.4: Cross-slope sections of neutral density and temperature across **(a)** the western WAP slope (along WOCE Hydrographic Program (WHP) transect S04P, February 1992) and **(b)** the Weddell Sea Slope (along WHP transect SR04, February 2007). The color contours for temperature and the line contours for neutral density are the same in each panel. Only the upper 2000 m of each section are shown.

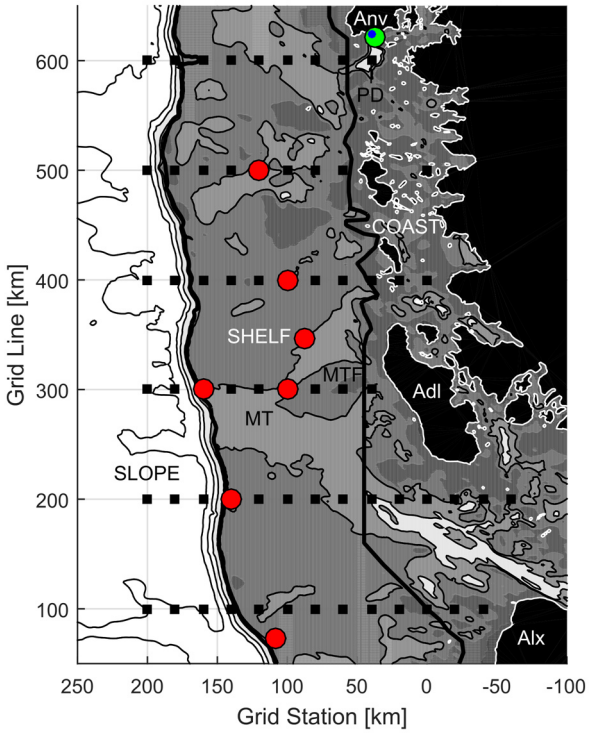

Figure 1.5: Overview of the Pal LTER sampling grid. The domain corresponds to the rectangle in figure 1.1. Most locations in this document use the Pal LTER coordinate system and are given as GGG.SSS where GGG is the grid line (units of kilometers) and SSS the grid station (units of kilometers). Origin 000.000 is at ~69.0ºS, ~73.6ºW, near Alexander Island. The nominal shipboard stations are spaced every 20 km in the Grid Station coordinate, are spaced every 100 km in the Grid Line coordinate, and are shown here as black squares. Bold black lines separate the Shelf regime from the Coast and Slope regimes. Current meter mooring sites are shown as red circles and the single thermistor-only mooring site is shown as a green circle. The location of Palmer Station is indicated with a blue dot at the southern edge of Anvers Island. Bathymetry is contoured every 500 m between -3000 m and -1500 m and is then contoured at -750 m, -480 m, and -250 m. Bathymetry is shaded between -1500 and -750 m, between -750 and -480 m, between -480 and -250 m, and between -250 and 0 m. The bathymetric features and islands labeled are as in figure 1.1.

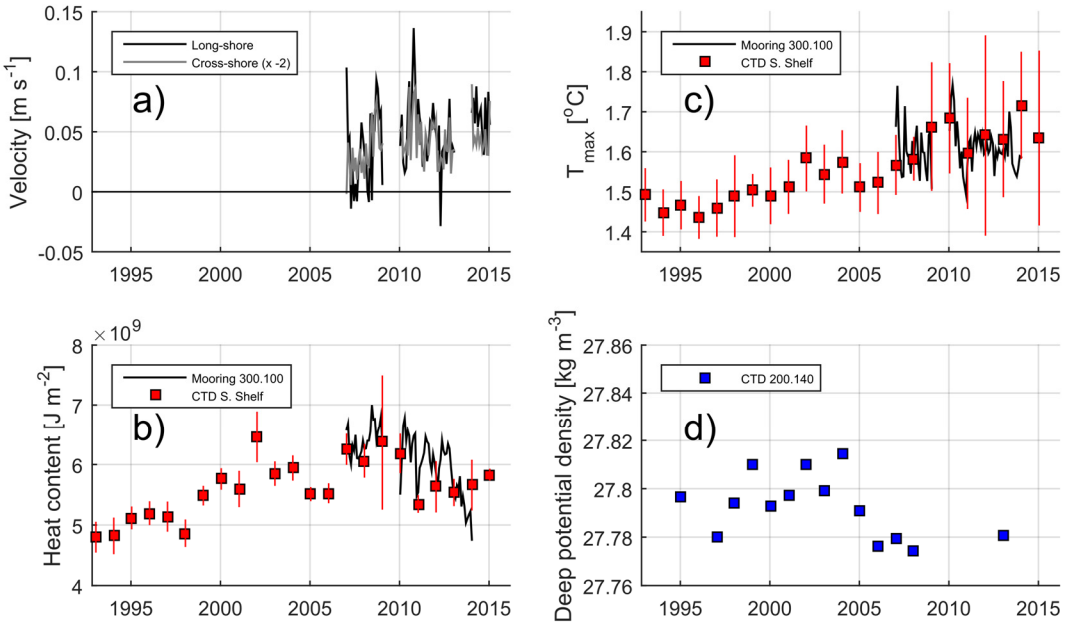

Figure 1.6: Overview of some long-term Pal LTER data sets relevant for shelf-slope exchange. **(a)** Monthly-average long-shore (black) and cross-shore (grey, scaled by -2) depth-averaged velocity components at mooring site 300.100, which samples UCDW diverted onto the shelf from the ACC, towards the north at the Marguerite Trough Fork. **(b)** Subpycnocline heat content from mooring 300.100 (black line) and from the cruise-average of all Southern Shelf CTD casts (between the 200 and 400 lines) for each January cruise. Mooring data are monthly averages. Error bars on CTD data represent two standard errors. **(c)** Exactly as in (b) but for the temperature maximum. **(d)** Potential density at 400 m for the CTD cast taken at 200.140 on each January cruise. 200.140 is at the shelf edge in ~420 m depth.

2) Origin and attenuation of mesoscale structure

Published along with Appendix A as:
McKee, D.C., D.G. Martinson, and O. Schofield, 2019: Origin and attenuation of mesoscale structure in Circumpolar Deep Water intrusions to an Antarctic shelf. *J. Phys. Oceanogr.*, **49(5)**, 1293-1318, 10.1175/JPO-D-18-0133.1.

Abstract:

Cross-isobath transport of Upper Circumpolar Deep Water (UCDW) provides a major source of heat to the Antarctic continental shelves. Adaptive sampling with a Slocum glider revealed that the UCDW regularly intrudes onto the western Antarctic Peninsula shelf within mesoscale eddies, and a linear stability analysis of the shelf-break current upstream confirmed eddy length scales and vertical structure are consistent with the baroclinic instability of the current. The properties of the most unstable mode are insensitive to current orientation but sensitive to bottom slope in accordance with modified Eady theory. Once on the shelf, the eddies' core properties mix with ambient shelf water to form modified CDW (mCDW). Concurrent shipboard CTD and ADCP data are used to diagnose the responsible mixing processes and highlight the importance of thermohaline intrusions. The genesis mechanism of the interleaving layers cannot be confirmed, however a simple analytic model suggests the upper limit contribution of advection by internal waves cannot account for the observed temperature variance unless the cross-eddy temperature gradient is large. Data-adaptive sampling of an eddy with the glider revealed it lost heat across two isopycnals and a fixed radius at a rate of 7×10^9 J s^{-1} over 3.9 days. This rate is corroborated by a diffusion model initialized with the eddy's initial hydrographic properties and informed by the heat fluxes parameterized from the shipboard data. The results suggest eddies predominately lose heat laterally and downward, which preserves subsurface heat for melting of marine-terminating glaciers.

2.1) Introduction

The west Antarctic Peninsula (WAP) is bordered by the Antarctic Circumpolar Current (ACC) which flows along the continental slope. Below the surface layer, the ACC advects a warm mass of Circumpolar Deep Water (CDW) with significant heat content relative to the *in-situ* freezing point. The CDW spans a range of properties, though Gordon (1971) distinguishes between an upper (UCDW) and lower (LCDW) variety defined by temperature and salinity maxima, respectively. The southern boundary of the ACC is defined as the southernmost presence of UCDW (Orsi et al. 1995) and, unique compared to the rest of Antarctica, near the WAP the ACC flows immediately adjacent to the shelf-break, making UCDW readily available to the shelf (figure 2.1).

The WAP is undergoing rapid climate change and the ocean is a primary heat source, particularly in winter when there is no direct radiative forcing. The marginal seas of West Antarctica are warming (Schmidtko et al. 2014) and the increase in heat content along the WAP margin has been attributed to a warming of the UCDW T_{max} (Martinson et al. 2008). Cook et al. (2016) confirm an oceanic role in glacier retreat along the WAP by demonstrating an asymmetry in glacial advance/retreat: southern marine-terminating glaciers that have access to warm subpycnocline waters are retreating whereas northern glaciers under the influence of much colder Bransfield Strait waters are not. More and/or warmer CDW has also left its imprint on the atmosphere. The northern portion of the WAP is undergoing rapid winter warming (Turner et al. 2013), presumably related to lighter sea ice cover venting ocean heat to the atmosphere. The reduced sea ice cover, in turn, may be related to changes in the winds and their effect on UCDW delivery and mixing across the pycnocline (Dinniman et al. 2012).

The myriad consequences of UCDW heat have made the exchange of CDW with the WAP shelf an active area of research (Klinck 1998; Smith et al. 1999; Klinck et al. 2004; Dinniman and Klinck 2004; Moffat et al. 2009; Dinniman et al. 2011, 2012; Martinson and McKee 2012; Spence et al. 2014, 2017; Graham et al. 2016; Couto et al. 2017), which is summarized in a recent review by Moffat and Meredith (2018). Various processes have been implicated in driving the cross-isobath transport of CDW onto the WAP shelf, each of which may dominate on different time and/or space scales. The importance of the mesoscale has been argued for by theoretical means (Stewart and Thompson 2015), demonstrated in high-resolution numerical models (St-Laurent et al. 2013; Graham et al. 2016; Stewart et al. 2018), and observed (Moffat et al. 2009; Martinson and McKee 2012; Couto et al. 2017). Warm-core, subpycnocline, primarily anticyclonic eddy-like features have been found within several tens of kilometers from the shelf-break, particularly in the vicinity of Marguerite Trough, and are steered along isobaths. The hydrographic properties of the eddies indicate an injection of UCDW as it is found on the continental slope and their length scale is as large as or slightly larger than the first baroclinic Rossby radius, which near the shelf-break is about 5 km. Decorrelation lengths of physical and geochemical scalars on the WAP shelf are also about 5 km (Eveleth et al. 2017), suggesting mesoscale eddies may dominate tracer stirring. The eddies' large heat content relative to surrounding waters indicates a potentially large onshore heat flux. For example, in numerical models, cumulative onshore heat transport is reduced by as much as 50% when model grid spacing is increased from 1 to 2 km (St-Laurent et al. 2013).

Still, very little is known about the origin of the eddies. Their core hydrographic properties and stratification suggest an origin along the continental slope and their observation along isobaths suggests they are, at least in part, advected within the mean flow. Consistent with

the former, an idealized numerical model with a continental slope straddled by a jet similar to that observed along the WAP suggests that the jet soon becomes unstable and a Rossby wave containing alternating warm anticyclones and cold cyclones emerges (St-Laurent et al. 2013). Additionally, it is important to understand the processes that attenuate the mesoscale variability and work towards setting the larger-scale shelf stratification. Once UCDW intrudes onto the shelf it mixes to become modified CDW (mCDW), but attempts to understand UCDW transformation have been based on shelf-integrated budgets and have been process-independent (Klinck 1998; Smith et al. 1999; Klinck et al. 2004).

In this study we seek to both understand the origin of mesoscale eddies observed on the WAP shelf and then identify and quantify the major processes responsible for their heat loss. Our focus is on the southern grid region of the Palmer Long Term Ecological Research project (Pal LTER; Smith et al. 1995) and in particular the vicinity of Marguerite Trough as this is a region of frequent eddy activity, is close in proximity to the shelf-break jet that we hypothesize generates the eddies, and contains well-defined bathymetric pathways by which to steer the eddies. We primarily use data from a novel Slocum glider survey designed to sample a known pathway for CDW exchange, documenting gradients along the axis of advection for any eddies encountered along the way, and then identify and track an eddy in real time through data-adaptive sampling. This allows, for the first time, high-spatial and temporal resolution transects directly through some of these eddies and a real-time quantification of the attenuation of their core properties. We supplement this with shipboard CTD and ADCP data used to quantify the mixing processes in the WAP environment around and within the eddies and to diagnose the instability that generates the eddies. Ultimately, we simulate the evolution of the eddy as

documented by the glider with a simple diffusion model informed by our parameterized mixing processes.

2.2) Data and observations

The principal data set used in this study is a set of temperature and salinity profiles collected by a Teledyne-Webb Slocum glider (Schofield et al. 2007) equipped with an unpumped Sea-Bird CTD. Slocum gliders traverse the water column (to 1000 m) in a sawtooth pattern by changing their buoyancy, traveling with average horizontal speed of 0.35 m s^{-1}. There is a hysteresis effect apparent in the up versus down traces that we correct by applying the thermal lag correction of Garau et al. (2011). We also empirically correct for a salinity bias by regressing glider-recorded salinity against ship-recorded salinity, each averaged in subpycnocline temperature bins, for five stations that were occupied by both platforms (maximum temporal separation of 12 days). To facilitate analysis, all corrected up and down traces are binned into 1-m profiles whose latitude, longitude, and time coordinates are taken as the average of all intraprofile samples.

The glider was deployed at Palmer Station at the head of Palmer Deep Canyon (PD) and traveled downgrid before reaching grid station 400.100 (see figure 2.2 for grid convention and physical setting), at which point it began the first of two phases of sampling. In the first phase, the glider flew against the mean current within the anticyclonic cell extending out of Marguerite Trough in order to sample any eddies being advected across the shelf and to identify lateral gradients in their properties. In the second phase, after reaching station 290.115 within Marguerite Trough, it waited to come across an eddy in order to track it in real time. The sampling strategy and basic observations of each of these stages are described below.

2.2.1) Glider survey – Advective Path

2.2.1.1) Sampling strategy

The Advective Path (highlighted in figure 2.2) refers to the anticyclonic cell extending out of Marguerite Trough that carries upwelled UCDW to the northern portion of the grid. This path was confirmed to carry UCDW by Martinson and McKee (2012) and its width and central location were inferred from the depth-averaged currents and CDW dye transport in Dinniman et al. (2011; their currents superimposed on our figure 2.2). Because the width of the current is about the same as the expected diameter of the eddies we were confident that by flying straight through it we would be able to cross any existing eddies traversing the shelf. Nominal glider profile spacing is 1 km, which should afford several profiles through each eddy.

2.2.1.2) Eddy characteristics

As the glider flew upstream (downgrid), it encountered five eddies imbedded within the subpycnocline T_{max} layer. We define a mCDW temperature profile as the along-isopycnal average of all profiles whose T_{max} is < 1.55 ^{o}C and then compute heat content per unit area Q of the eddy profiles relative to this mCDW profile by differencing the two and integrating between σ_{shal} = 1027.64 kg m^{-3} and σ_{deep} = 1027.76 kg m^{-3}. We use neighboring mCDW as our reference profile because we are interested in how the eddies mix with their surroundings. We choose these isopycnals since (1) they encompass a positive temperature anomaly within eddies, (2) σ_{shal} is relatively stable within the permanent pycnocline, and (3) σ_{deep} is near, but does not intersect, the bottom. Series of temperature, salinity, heat content per unit area, and geostrophic current at 280 dbar relative to the bottom are shown in figure 2.3, with the eddies labeled A-E (geographic locations of eddies A-E shown in figure 2.2). Fundamental statistics for each eddy developed and discussed below are given in table 2.1.

To quantify the dimensions, gradients, and heat content of these eddies, we obtain an analytical representation for the eddy in terms of a Gaussian function that is fit to the data via nonlinear regression. Specifically, we identify intraeddy profiles via positive heat content and assign them an along-eddy coordinate χ along an axis determined via orthogonal regression of profile grid line against grid station. This allows inversion of the following model

$$Q(\chi) = Q_{\max} \exp\left(-\left(\frac{\chi - \chi_0}{R} \right)^2 \right) \tag{2.1}$$

for core heat content per unit area $Q_{\max}$, center χ_0, and radius R. Implicit in this model is the assumption of axisymmetry, which we maintain throughout the paper. Our model is similar to those used by other authors (Couto et al. 2017), however we fit the function to integrated heat content as opposed to along-isopycnal temperature anomalies since integration smooths over some of the locally high temperature variance that can reduce the quality of fit. The total eddy heat content is given by the radial and azimuthal integrals of Q:

$$Q_{\text{tot}} = 2\pi \int_{\chi_0}^{\chi_0 + R} (\chi - \chi_0) Q(\chi) \, d\chi \, . \tag{2.2}$$

It is important to note that radii (and heat content) determined from this method are underestimates because the glider may not be going straight through the eddy (they are half chord lengths) but also because the glider is deliberately flying against the mean flow which is advecting the eddy through the glider during sampling. Therefore, we provide an additional measure of eddy size as half the along-track distance spanned by intraeddy profiles (R_{TD}), which tends to be slightly larger.

The cores of the eddies contain as much as 5.5 x 10^8 J m^{-2} relative to the reference profile. In *T-S* space, the properties of these eddies are consistent with UCDW. Particularly so, eddy C contains water disjoint from neighboring water, consistent with UCDW as found

upstream on the continental slope and indicating warm-core isolation. The upstream eddies A-C are narrower than their downstream counterparts D-E, having radii $R \sim 3$ km ($R_{TD} \sim 5$ km) compared to $R \sim 7$ km ($R_{TD} \sim 9$ km). Eddies D-E are broader than the upstream eddies but do not have a substantially smaller heat content per unit area and in fact tend to have more total heat. The large discrepancy in upstream versus downstream total heat content might be more reflective of a sampling bias (offset trajectory through eddy center and stronger head current encountered through eddies A-C) as opposed to an actual difference in heat content.

The injection of UCDW into the shelf water column means that the eddies are associated with a downward deflection of isopycnals and anticyclonic shear (figure 2.3). The deflection of isopycnals is largest in the weakly stratified portion of the water column at and below the T_{max}, which leads to a cross-track geostrophic velocity signal. To quantify this, we evaluate the geostrophic current at 280 dbar relative to the bottom. We choose this depth as it is the approximate depth of the moored current meters used by Martinson and McKee (2012) upstream where they found the largest eddy signal. A composite over all of the eddies (figure 2.4) reveals a well-defined signature of anticyclonic rotation centered about a warm core, similar to the composites of Moffat et al. (2009).

We measure temperature gradients at the eddy boundaries via a least squares approach. We define $\partial T/\partial z\big|_{top}$ by regressing a straight line to the portion of the temperature profile spanning 10 m above and below the depth of σ_{shal} and then averaging the slopes laterally across all profiles within $\chi_0 \pm R$. We define $\partial T/\partial z\big|_{bot}$ similarly, considering the region 40 m above and below the depth of σ_{deep}. To estimate $\partial T/\partial r\big|_R$, we fit a straight line on each isopycnal to the temperature value at the profile nearest to $\chi_0 \pm R$ and up to two values on either side of that profile and then average the slopes between σ_{shal} and σ_{deep} and across both hemispheres. Owing

to the nature of glider sampling, for the same reasons radius estimates are underestimates, lateral gradient estimates are overestimates. Vertical gradients are similar for all eddies while lateral gradients are larger for the three upstream eddies.

2.2.2) Glider survey – Tracking Stage

2.2.2.1) Sampling strategy

We conducted transects along a 'fence' perpendicular to the eastern wall of Marguerite Trough (figure 2.2, blue line) to find an eddy and then track it via real-time adaptive sampling. Given the local Rossby radius (~5 km), the mean flow speed, an assumption that eddies are advected within the mean flow, and the lateral deviation of the mean flow, we determined that the fence should be 15 km wide and that it should be surveyed back to back in a 24 h period, which is within the operational constraints of the glider. During sampling, profiles were inspected for a $T_{max} \geq 1.8$ ºC as evidence of a UCDW-core eddy and, if found, trajectories were forecast by integrating along both the vector of 24-h mean glider depth-averaged currents and along a streamline fit to the Dinniman et al. (2011) model time-depth averaged currents, both of which generally agreed within one Rossby radius. We encountered an eddy shortly after initiating sampling and crossed it five times over 4 days. The trajectory followed the eastern wall of Marguerite Trough, consistent with the eddy-like features observed by Moffat et al. (2009).

2.2.2.2) Eddy characteristics

We define a local reference profile in the same manner as before and subtract it in order to obtain Q. Analogous to the Advective Path, sections of data are shown in figure 2.5. However, unlike in that stage, we are not confident that we consistently crossed the eddy via a chord length. Connecting spatial end-members of threshold T_{max} along a line perpendicular to

isobaths leads to an estimated mean diameter of 8.5 km, similar to the eddies observed on the Advective Path. There is, in general, a decrease in heat content per unit area over time. Anticyclonic shear is less apparent beyond the first few crossings, and the vertical structure of temperature and salt anomalies is much more complicated. We will quantify the heat loss of this eddy in section 2.5.

2.2.3) Shipboard data

2.2.3.1) Pal LTER CTD and SADCP

Shipboard data are used to supplement the glider data and to apply mixing parameterizations. CTD profiles are collected as part of the standard sampling on the annual cruises to the WAP each austral Summer since 1993 and are currently (since 1999) collected with a dual-pumped Sea-Bird 911+ CTD system (see Martinson et al. 2008 for details). The standard grid locations are indicated as black squares in figure 2.2. The entire grid was occupied until 2008 whereas now only a subset of stations is occupied (nominally one coastal, shelf, and slope station per grid line), though this is generally complemented by various process-study CTD casts at nongrid locations that are not plotted but are utilized here.

Processed, high-resolution (5 min in time, 8 m in vertical) velocity profiles from the ARSV *L. M. Gould*'s hull-mounted RDI 150 kHz narrowband instrument were obtained from the Joint Archive for Shipboard ADCP (SADCP). The 150 kHz instrument provides velocity profiles good to about 300 m (depending on weather and sea state) when the vessel is on station. For mixing parameterizations we need concurrent shear and stratification profiles, so only the overlapping portion of the database is used (Januaries 2000-15; SADCP installed in mid-1999). For those applications, the hydrographic data are bin-averaged onto the same 8-m grid of the velocity data. Stratification and shear are computed as first differences on the 8-m grid as

$N^2 = -\frac{g}{\rho}\frac{\Delta\rho}{\Delta z}$ and $S^2 = \left(\frac{\Delta U}{\Delta z}\right)^2 + \left(\frac{\Delta V}{\Delta z}\right)^2$. For bins with very weak stratification ($N^2 < 1 \times 10^{-6}$ s^{-2}), N^2 is set to a constant value (1×10^{-6} s^{-2}).

2.2.3.2) Casts on Advective Path

We draw special attention to 5 CTD casts collected in January 2014 along the Advective Path that was sampled by the glider the year prior (triangles in figure 2.2). These casts fortuitously sampled one or more eddies and indicate substantial interleaving structure, particularly in the pycnocline (figure 2.6). The layering connects cores of injected slope-type UCDW to the surrounding cooler pycnocline. These data are used to assess the importance and origin of thermohaline intrusions into the eddies.

2.2.3.3) S04P casts across continental slope

We suspect the eddies are generated along the continental slope. To diagnose the structure and stability of the shelf-break current upstream of Marguerite Trough we use CTD data from the WOCE S04P cruise in February 1992 ('x' symbols in figure 2.2). Though it is possible that the hydrographic structure over the continental slope has changed in the long interim period, we use these data as they provide a high spatial resolution transect across the slope, slightly finer than the 2011 reoccupation of the line. The stations are 'moved' from their original location to the 200 line by tracing the isobath at the actual station location to the 200 line, a small correction (a few kilometers). Neutral density is computed using the Jackett and McDougall (1997) software and profiles of neutral density, temperature, and salinity are filtered with a third-order Butterworth filter with width 100 dbar to remove noise and filter out Charney-type instabilities. We choose to do this because surface-trapped Charney-type instabilities do not convert significant available potential energy (APE) to eddy kinetic energy (EKE) compared to the pycnocline-level instabilities we are seeking (Smith 2007). Geopotential anomaly is

calculated from the smoothed temperature and salinity profiles and is linearly extrapolated to handle bottom triangles. Both neutral density and geopotential anomaly are mapped with a Gaussian weighting function to a two-dimensional grid across the slope using the WOCE global climatology vertical grid (Gouretski and Koltermann 2004) and uniform 5-km horizontal spacing.

2.3) Origin of mesoscale structure

2.3.1) QG model and background state

To understand the theoretical characteristics of eddies on the WAP, we begin by diagnosing the stability of the shelf-break current upstream of where UCDW intrudes onto the shelf. We follow the inviscid quasigeostrophic model of Smith (2007), assuming a local, slowly-varying mean stratification N and horizontal flow $\mathbf{U}$ depending only on z. Assuming plane-wave solutions $\Re\left\{\hat{\psi}(z)\exp\left[i\left(kx+ly-\omega t\right)\right]\right\}$ where $\hat{\psi}$ is the complex amplitude of the perturbation streamfunction, ω the complex perturbation frequency, and $\mathbf{k} = (k, l)$ the wavevector, the linearized quasigeostrophic equations in geographic coordinates lead to the eigenvalue problem

$$\left.\begin{aligned}
&\left(\mathbf{k}\cdot\mathbf{U}-\omega\right)\left(\Gamma-\mathbf{k}\cdot\mathbf{k}\right)\hat{\psi} = -\left(k\frac{\partial Q}{\partial y}-l\frac{\partial Q}{\partial x}\right)\hat{\psi} && -H<z<0\\
&\left(\mathbf{k}\cdot\mathbf{U}-\omega\right)\frac{\partial\hat{\psi}}{\partial z} = \left[k\left(\frac{\partial U}{\partial z}-\frac{N^2\alpha^y}{f}\right)+l\left(\frac{\partial V}{\partial z}+\frac{N^2\alpha^x}{f}\right)\right]\hat{\psi} && z=-H\\
&\left(\mathbf{k}\cdot\mathbf{U}-\omega\right)\frac{\partial\hat{\psi}}{\partial z} = \left(k\frac{\partial U}{\partial z}+l\frac{\partial V}{\partial z}\right)\hat{\psi} && z=0
\end{aligned}\right\}. \qquad (2.3)$$

Here, $\Gamma = \frac{\partial}{\partial z}\left(\frac{f^2}{N^2}\frac{\partial}{\partial z}\right)$ is the potential vorticity stretching operator and $\alpha^{x,y}$ are the bottom slopes. We caution that the assumption of a linearly growing wave in a stable background state

that is steady in time is highly idealized. Surely interactions with the evolving turbulence field of the ACC are relevant for the dynamics of the shelf-break flow. Nevertheless, we suspect that the regularity of the eddies and their common statistical metrics (figures 2.3, 2.4; Moffat et al. 2009; Couto et al. 2017) demonstrate that there is a preferential length scale and vertical structure for instabilities in this environment.

The background state is defined by the gridded stratification and geostrophic velocity profiles at grid location 200.150. This site is chosen as it is located midway across the slope and the geostrophic shear there agrees well with climatological SADCP shear. The current is assumed to flow parallel to isobaths, specifically at an angle of 40º north of east. The local bottom slope is calculated by fitting a 2D plane to all ETOPO1 bathymetry data (Amante and Eakins 2009) within a radius of 0.25º about the grid location.

One assumption of this model is that the background state varies slowly in the horizontal. Since there is clearly lateral shear in the shelf-break current, we need to justify excluding the potential of barotropic instability. For a generic, mixed baroclinic-barotropic instability, the contribution to the growth rate from baroclinic instability scales as $\sigma_{BC} \sim \frac{fL}{ND}\left|\frac{\partial U}{\partial z}\right|$ and the contribution from barotropic instability scales as $\sigma_{BT} \sim \left|\frac{\partial U}{\partial y}\right|$ (Pedlosky 1987). For these data, the latter is one order of magnitude smaller than the former ($\sigma_{BC} \sim 13$ day^{-1}, $\sigma_{BT} \sim 2$ day^{-1}). This is corroborated by Stern et al. (2015) who found baroclinic instability to grow much faster than barotropic instability in their QG model of a similar shelf-slope configuration, though their model was fully turbulent and not limited to the linear growth stage.

2.3.2) Most unstable mode

The equation is discretized as in Smith (2007) and solved for a range of wavenumbers. For each wavenumber, the most unstable mode is that with the largest imaginary part of ω. We find the overall most unstable mode to have an inverse wavenumber $|\mathbf{k}_{\max}|^{-1}$ = 4.4 km and growth rate 0.4 day^{-1} (figure 2.7). Over the wavenumber space evaluated, this is both the global and only local maximum. The mode's vertical structure is characterized by nonzero amplitude below the permanent pycnocline in the CDW depth range with a maximum at about 600 m and a secondary maximum at about 350 m. Specifically, this depth range spans the water column presence of UCDW ($T \geq 1.7$ ºC) and LCDW ($S = S_{\max}$) within the four profiles across the slope. The instability appears to be qualitatively similar to a Phillips type instability (Phillips 1954) for the following reasons: 1) vertical structure seems to be dictated by interior sign changes in the potential vorticity gradient, 2) ~33º phase shift within the amplitude-maximum indicates APE release there, and 3) horizontal scale obeys $L \approx (N/f)h_{\text{pycnocline}} \approx 5$ km.

Overall these findings are in very good agreement with the glider observations over the Advective Path (figure 2.3). First, the vertical structure of the mode is concentrated within and below the permanent pycnocline, which is where the eddies exist. Second, the observed diameters of eddies A-C upstream and average crest-to-crest separation are ~ 8.3 km (averages of $2R$ and $2R_{\text{TD}}$) and 22.3 km, respectively, which are comparable to the theoretical diameters $2|\mathbf{k}_{\max}|^{-1}$ = 8.8 km and crest-to-crest separation $2\pi|\mathbf{k}_{\max}|^{-1}$ = 27.8 km for eddies spun off an unstable Rossby wave. Temperature anomalies relative to mCDW and geostrophic currents provide some evidence for a cold cyclone between eddies B-C, though in general, only warm anticyclones tend to be found on the shelf. The eddies D-E downstream on the path are broader than A-C but have a similar separation. With the caveat that this is a linear model, note that the

wavelength implies delivery of (365 days) x $u|\mathbf{k}_{max}|/2\pi$ = 57 - 114 eddies per year (for typical shelf currents of 0.05 or 0.10 m s^{-1}) which could account for the totals observed by Moffat et al. (2009) and Martinson and McKee (2012).

2.3.3) Roles of bottom slope and current orientation

Exploring the parameter space of bottom slopes and current orientations allows us to simultaneously understand the sensitivity of the most unstable mode's structure and growth rate to these parameters and to understand how generalizable these results are to other regions around Antarctica. Using the same geostrophic shear and stratification profiles, we repeat the above analysis for all bottom slopes between -0.15 and +0.15 at increments of 0.01 and for all current orientations between 0º (zonal) and 90º (meridional) counterclockwise from east at 10º increments and examine changes in the growth rate, wavevector, and structure of the most unstable modes. Evaluating positive and negative bottom slopes effectively allows consideration of both prograde (isopycnals slope in same sense as bathymetry; e.g., WAP) and retrograde (isopycnals slope in opposite sense as bathymetry; e.g., Ross Sea) jets.

Figure 2.8 shows the growth rate and inverse wavenumber of the most unstable mode over the entire parameter space. The orientation of the current has essentially no effect on the instability. This is likely because the planetary beta effect is so small at this latitude that potential vorticity gradients are dominated by the stretching term and bottom slope. Indeed the topography plays a large role in determining the strength and properties of the most unstable mode. It is found that negative bottom slopes are stabilizing while increasing positive bottom slopes are destabilizing to a point and then stabilizing. Blumsack and Gierasch (1972) demonstrate that the relevant parameter for the stability problem under QG scaling is not the bottom slope itself but rather the ratio of the bottom slope to the isopycnal slope, $\delta \equiv \alpha/s$. In

the QG model of Smith (2007) that we use, the bottom slope only enters the problem as a boundary condition in the bottom layer's potential vorticity gradient. When the bottom slope exceeds the slope of the 1028.0 kg m^{-3} neutral surface, the potential vorticity gradient vanishes in the lower layer which has the effect of suppressing the growth rate in accordance to the Charney-Stern criteria (Pedlosky 1987). Nevertheless, this does not change the fact that there are still sign changes in the interior potential vorticity gradient and therefore instability persists where $\delta > 1$ or $\delta < 0$ (Isachsen 2011). These regions of weaker instability with inverse wavenumbers of 4-5 km all have similar vertical structure as the most unstable mode obtained in the realistic scenario analyzed earlier.

The fastest growing modes for prograde currents with relatively flat bottoms ($0 \leq \delta \leq 1$) are qualitatively consistent with Eady modes for the following reasons: 1) they have amplitude maxima at both ~350 m and near the bottom; 2) they have an inverse wavenumber $L \approx NH/1.6f$ ≈ 9.4 km, probably since the weakly varying N is dynamically similar enough to the uniform N of Eady's model. These modes have a pronounced spike at ~350 m near the UCDW temperature maximum and, in regions with a flatter bottom slope than the WAP, could also be expected to contribute to exchange of CDW. The region between $-2 \leq \delta < 0$ represents a sort of transition between the Eady-type modes and the Phillips-type modes. They have smaller length scales (~2 km) and are bottom-boundary trapped. This trend fits the qualities described by Blumsack and Gierasch (1972) for increasingly negative slope parameter, namely decreasing length scale and boundary trapping.

2.4) Attenuation of mesoscale structure

Having identified a plausible origin for the UCDW eddies, we here consider the processes responsible for their decay. Box inversions of steady heat budgets on the WAP point to diapycnal mixing between overlying remnant winter mixed layer Winter Water (WW) and a constantly replenished CDW layer as the maintenance of the permanent pycnocline. For some context, using a steady advective-diffusive balance, Klinck et al. (2004) place an upper bound on the vertical (lateral) diffusivity of heat at 7.7×10^{-4} m^2 s^{-1} (1600 m^2 s^{-1}) in the limit of no lateral (vertical) mixing. In an earlier study, Klinck (1998) used seasonal changes in water properties and a similar integrated budget to find a vertical (lateral) diffusivity of heat as 1×10^{-4} m^2 s^{-1} (37 m^2 s^{-1}). Martinson et al. (2008) used interannual variability of WW heat content and assumed a UCDW replenishing time to suggest a vertical diffusivity of 8.5×10^{-5} m^2 s^{-1}. Our study, however, focuses on how the properties of the subpycnocline 'box' are set by the mixing of advected parcels of UCDW, within which the vertical and lateral gradients are quite different from those used in mean-shelf balances.

2.4.1) Shear-driven instability

Shear-driven instability is thought to be important in maintaining the permanent pycnocline and is thought to yield larger heat fluxes on the WAP than double-diffusive instabilities (Howard et al. 2004). Regarding sources of shear, internal tides are likely not important but near-inertial waves may be. Howard et al. (2004) suggest the semidiurnal tide is weak, as is the stratification, making baroclinic conversion unlikely. Further, Beardsley et al. (2004) use rotary spectral analysis of drifter velocity to show power in the semidiurnal band is two orders of magnitude less than that in the near-inertial. In general, we might expect that vertical mixing should be elevated over seamounts or within cross-cutting canyons. At

seamounts, internal waves with frequency at the critical slope may be generated whereas in canyons internal waves may become trapped and focused towards the canyon head (Gordon and Marshall 1976).

Because we do not have microstructure measurements within eddies or on the surrounding mid-shelf, our approach is to use SADCP and CTD data to estimate diffusivities, temperature gradients, and heat fluxes across the permanent pycnocline, which we define globally to be between 98 and 250 m. We exclude grid stations below the 000 grid line as the hydrography there is very different (very deep and cold remnant winter mixed layers). Note that winter mixing by entrainment of the thermocline during brine rejection is not considered here, but is important in the annual heat budget (Martinson and Iannuzzi 1998).

2.4.1.1) General shear-driven instability

The method of Pacanowski and Philander (1981, hereafter PP81) computes a diffusivity $K_z(z)$ as a function of the Richardson number, with the idea being that when shear overcomes stratification, instability and mixing result. This method was developed for steady currents in equatorial ocean models and assumes nothing about the underlying sources of shear. Nevertheless, it has been applied to the WAP (Howard et al. 2004) and to other high latitude environments (Dewey et al. 1999). For every 8-m binned CTD cast we have we pair it with all concurrent on-station SADCP profiles and compute a time-averaged Richardson number $\overline{\mathrm{Ri}} = \left\langle N^2 / S^2 \right\rangle$. Because this is essentially a space-time averaged Ri based on finite-differenced data, it is best interpreted as a probabilistic measure of potential instability at space (and time) scales lower than the differencing (and averaging) scales. The PP81 parameterization is

$$K_z = 10^{-5} + \frac{5\times10^{-3} + 10^{-4}\left(1+5\overline{\mathrm{Ri}}\right)^2}{\left(1+5\overline{\mathrm{Ri}}\right)^3}\ \mathrm{m^2 s^{-1}} \qquad (2.4)$$

and a vertical heat flux can then be calculated at each depth as

$$Q_f = \rho_0 c_p K_z \, \partial T / \partial z \, . \tag{2.5}$$

2.4.1.2) Internal wave parmeterizations

Various authors have modeled the energy transfer through the steady Garrett-Munk (GM; Garrett and Munk 1975) internal wave vertical wavenumber spectrum via nonlinear interactions down to dissipation scales and turbulence production by scaling the GM shear spectrum by observed shear variance (e.g., Gregg 1989, hereafter G89). By assuming a steady turbulent kinetic energy balance and assuming a constant mixing efficiency ($\Gamma = 0.2$), one can then estimate a diffusivity coefficient from parameterized dissipation via the relation $K_z = \Gamma \varepsilon / N^2$. We use a modified version of the G89 parameterization, which is:

$$K_z(z) = K_0 \frac{\left\langle S^4 \right\rangle}{\left\langle S_{\mathrm{GM}}^4 \right\rangle} h\left(\mathrm{R}_\omega\right) j\left(f, N\right). \tag{2.6}$$

In this expression, $\left\langle S^4 \right\rangle$ is the 8-m SADCP shear squared, multiplied by 2 (correcting for the finite-difference filter; Gregg and Sanford 1988), and then squared again and averaged in time; $\left\langle S_{\mathrm{GM}}^4 \right\rangle$ is the GM shear spectrum (with local scaling parameters for the WAP shelf; see Appendix A) integrated up to a cutoff wavenumber $\beta = 0.2\pi$ rad m^{-1}, squared, and then multiplied by 2 (assuming Gaussian statistics); and $K_0 = 5.6 \times 10^{-6}$ m^2 s^{-1} is a nominal diffusivity for the underlying internal wave spectrum (see Appendix A). The functions h and j are corrections added later and are not part of the original G89 model.

First, $h(\mathrm{R}_\omega)$ is a polynomial function of R_ω, the N^2-normalized shear-strain variance ratio, which is designed to adapt the model to non-GM wave fields with different aspect ratios and frequency content:

$$h(\mathrm{R}_\omega) = \frac{3(\mathrm{R}_\omega + 1)}{2\sqrt{2}\mathrm{R}_\omega\sqrt{\mathrm{R}_\omega - 1}}. \quad (2.7)$$

The GM spectrum has $R_\omega = 3$ ($h = 1$), and larger values of R_ω indicate elevated importance of near-inertial waves. Most of the open ocean has $R_\omega \sim 7$ (Kunze et al. 2006), and values in the Southern Ocean are generally between 8 and 12 (Naveira-Garabato et al. 2004; Thompson et al. 2007). Calculating shear and strain spectra for each cast as in Kunze et al. (2006), we find $R_\omega = 9$ ($h = 0.42$) averaged over the LTER grid, and, owing to the difficulty involved in estimating strain, we use that constant value for all casts.

The second term $j(f, N)$ is a correction for latitude arising because the rate at which waves are Doppler shifted depends on the ratio of their horizontal and vertical wavenumbers, which depends on Coriolis frequency f (Gregg et al. 2003):

$$j(f, N) = \frac{f\mathrm{acosh}(N/f)}{f_{30}\mathrm{acosh}(N_0/f_{30})}. \quad (2.8)$$

This dependence was in the scaling used by G89, but he held $f\mathrm{acosh}(N/f)$ to be constant. We use a typical latitude for the WAP (66.5 ºS) for all casts. After developing a diffusivity profile, a heat flux profile is calculated from equation 2.5.

2.4.1.3) Results and interpretation

Fundamental results are presented in the form of profiles of N^2, S^2, and K_z averaged over the Shelf region (see figure 2.2 for regional boundaries) in figure 2.9. In general, S^2 decreases more slowly with depth than does N^2, becoming nearly white below the pycnocline and yielding diffusivities that increase with depth. To confirm that the apparently unusual behavior of S^2 with depth is real, we compare the SADCP shear at station 200.140 to the shear calculated from a set of 6 moored current meter records at that site (corrected for finite differencing following Gregg and Sanford 1988 using local GM scaling). The current meter shear (bold blue line) and SADCP

shear (thin black line) at site 200.140 agree remarkably well, suggesting that, at least at this site, the large shear variance (and hence the large diffusivities) at depth is real (figure 2.9b).

While the SADCP shear variance represents an integral across all frequencies, we can band-pass filter the current meter observations between [f, N_0] to retain only shear in the internal wave band. Doing so (dashed blue line in figure 2.9b) suggests that the internal wave band shear profile has the same shape as the total shear profile but that SADCP shear might be overestimating internal wave shear by a factor of ~1.6. Because we cannot evaluate this relation at other sites, we do not attempt to make any correction for non-internal wave shear. The histogram of $\langle S^2 \rangle / \langle S^2_{\mathrm{GM}} \rangle$ in the pycnocline depth range (figure 2.9e) suggests observed shear variances are generally a factor of 2-3 greater than GM. Spectra of shear and strain in the pycnocline confirm that $R_\omega = 9$ is a good fit on the WAP shelf (figure 2.9d) and reveal an elevated importance of near-inertial waves in comparison to a standard GM spectrum.

Both the G89 and PP81 diffusivities increase with depth for reasons discussed above. Diffusivity values in the permanent pycnocline are small ($< 10^{-5}$ m^2 s^{-1}), so much so that the asymptotic lower limit of the PP81 method renders it inapplicable there (figure 2.9c). Although the two methods agree better deeper in the water column, all further analyses will exclusively consider the G89 parameterization. The shear (figure 2.9b) and diffusivity (figure 2.9c) profiles are presented as means with the shaded region enclosing two standard errors, where both the means and standard errors are computed on log-transformed data. Owing to the large number of stations sampled, uncertainty in the mean is small.

To get a sense of how diffusivity and vertical heat fluxes vary regionally, figure 2.10 shows composite profiles of diffusivity and heat flux for data partitioned by region alongside histograms of the pycnocline-averaged quantities. The small diffusivities that characterize the

permanent pycnocline operating on the background T profile yield vertical heat fluxes across the permanent pycnocline of < 1 W m^{-2} which is smaller than values reported by Howard et al. (2004), who used PP81. Diffusivities increase approximately log-linearly with depth to about 10^{-4} m^2 s^{-1} at 300 m (figure 2.10), which is as deep as the SADCP yields useable data.

As in figure 2.9, the central values are computed on log-transformed data, however now the spread is indicated by two standard deviations in order to indicate potential values instead of uncertainty in the mean. While the central values are small, the spread at any given depth is large and spans about two orders of magnitude, suggesting that the potential for strong mixing at any depth is high and that mixing is intermittent. Pycnocline diffusivities are significantly different between the Shelf and Slope, the Shelf and Coast, and between the Northern Shelf and Southern Shelf at an $\alpha = 10\%$ level. The variance seems to be larger in the Coast. The larger variance there is driven by larger variance in the shear. We also constructed two composites that should be more representative of the environment that most of the eddies are in. The first averages all profiles in the subregion of the Southern Shelf that is bounded by the 250 and 450 lines between stations 030 and 130 (the vicinity of Marguerite Trough) and the second averages only those profiles in that domain with a $T_{max} \geq 1.55$ ^{o}C. The heat fluxes in those regions are qualitatively different with a much greater heat flux divergence centered about the T_{max} but are statistically indistinguishable from the more comprehensive Southern Shelf in terms of cross-pycnocline metrics. However, compared to the Northern Shelf, the Southern Shelf and both Marguerite Trough composites have significantly lower pycnocline diffusivities, significantly lower shear variance ratios, and insignificantly larger pycnocline heat fluxes. The results suggest that any enhanced vertical heat flux within an eddy compared to its surroundings is due to the altered gradients of the temperature profiles and not the shear.

While the SADCP does not allow for estimates of diffusivity or heat flux below about 300 m, extrapolating the log-linear trend in K_z with depth and using observed temperature gradients suggests that below the T_{max}, the vertical temperature gradient is about one order of magnitude smaller than that in the permanent pycnocline, however the diffusivity should be about two orders of magnitude larger. This combines for a heat flux about 10 times greater below the eddy, and the spatial variability in the heat flux profiles is consistent with this scaling. The stratification on the Slope and Southern Shelf is dominated by pure UCDW and a mid-depth temperature maximum as in the eddies. The mid-depth maximum in temperature results in an upward heat flux above the T_{max} and a downward heat flux below, the former of which is apparent in the observed profiles and the latter of which is implied by the trend towards a ~ 0 W m^{-2} heat flux at 300 m (figure 2.10). Because the downward heat flux is about 10 times greater than the upward heat flux, the temperature maximum is mixed downwards in the water column as the UCDW is advected northward and shoreward. This is consistent with the positive vertical heat flux increasing with depth on the Northern Shelf and Coast stations (figure 2.10).

2.4.2) Thermohaline intrusions

Four of the five CTD casts taken along the Advective Path reveal that within and surrounding the eddies there is substantial along-isopycnal temperature and salinity variance associated with thermohaline intrusions (figure 2.6). Those data are plotted as profiles of temperature in figure 2.11 along with a background profile, which is constructed as a running median in density space with a window size of 0.015 kg m^{-3}. The UCDW eddies are essentially moving fronts. Joyce (1977) derived a model in which medium-scale advection of heat and salt across a density-compensated large-scale front is balanced by small-scale diffusion across thermohaline intrusions, attenuating their *T-S* characteristics. The medium-scale advection is

taken to be in the form of alternating interleaving structures, initiated by velocity perturbations with the energy source coming from thermoclinic energy of the cross-frontal property contrasts. His model makes no distinction as to what small-scale processes conduct the mixing.

The model balance leads to an effective cross-frontal diffusivity for T of

$$K_h = \overline{K_z^T \left(\frac{\partial T'}{\partial z} \right)^2} \Bigg/ \left(\frac{\partial \overline{T}}{\partial r} \right)^2 , \tag{2.9}$$

where primes indicate small-scale variance, overbars indicate large-scale averages (scales larger than intrusions), and the vertical eddy diffusivity is taken to encompass all mixing processes. To apply equation 2.9 we estimate the cross-frontal temperature gradient from the glider data along the Advective Path by averaging the lateral gradients of the 5 eddies encountered (A-E; 8.5 x 10^{-5} ^{o}C m^{-1}). The small-scale intrusion variance in the vertical is derived from the CTD profiles at approximately the same location: the background profile is subtracted and the variance of the derivative of the residual is calculated. We calculate K_h in two ways: once using a constant K_z typical of the midwater column (10^{-4} m^2 s^{-1}; Hebert et al. 1990; Pelland et al. 2013) and once using the diffusivities as parameterized from the modified G89 method. The results are 3.2 ± 1.4 and 7.9 ± 4.2 m^2 s^{-1}, respectively (two standard errors indicated). We now consider processes that may be responsible for generating the thermohaline intrusions.

2.4.2.1) Double-diffusive growth

Theories for the growth of thermohaline intrusions (e.g., McDougall 1985a,b) in a region of density-compensated thermohaline gradients depend on one of the components of density being unstably stratified in order for an infinitesimal disturbance to grow to finite length. Figure 2.11 shows that the WAP water column between the WW T_{min} and the UCDW T_{max} is diffusively unstable and that the layer immediately below the UCDW core can be salt finger unstable. One

way to quantify how much the unstably stratified component contributes to the stability of the water column is via the density ratio $R_\rho = \frac{\beta \partial S/\partial z}{\alpha \partial T/\partial z}$. A statically-stable column is diffusively unstable if $1 < R_\rho < \infty$, salt finger unstable if $0 < R_\rho < 1$, and doubly stable if $R_\rho < 0$. As the ratio approaches 1, double-diffusive fluxes increase because the effect of the gravitationally unstable gradient is increasingly canceled by that of the stably stratified component's gradient. Bormans (1992a) found that diffusively unstable fronts had lateral intrusion heat fluxes significantly exceeding those of doubly stable fronts only when R_ρ went below 1.54. Values in the lower pycnocline / eddy upper-hemisphere occasionally breach that threshold, and there is a correspondence between the locations of largest temperature variance and the locations of density ratio nearest to 1 (figure 2.11, lower panels).

2.4.2.2) Internal wave advection

Another possibility is that the intrusion-scale temperature variance is caused by advection due to internal waves. If we consider the simplest advection equation and the square of its Fourier transform,

$$\frac{\partial \tilde{T}}{\partial t}(z) = u_r(z)\frac{\partial \overline{T}}{\partial r} \quad \Leftrightarrow \quad \omega^2 \Phi_{\tilde{T}} = \Phi_{u_r}\left(\frac{\partial \overline{T}}{\partial r}\right)^2, \tag{2.10}$$

we can rearrange it to construct an inequality for the maximum contribution by internal waves to the intrusion-scale (tilde) temperature variance:

$$\Phi_{\tilde{T}_z} \le \frac{1}{f^2}\left(\frac{\partial \overline{T}}{\partial r}\right)^2 \Phi_{u_z}. \tag{2.11}$$

Here we have assumed that all waves are purely horizontal (inertial waves) and we have differentiated in depth by multiplying each side by β^2, the vertical wavenumber squared. Shear spectra are calculated over our defined pycnocline range and temperature spectra are calculated

over [180, 400] m, encompassing the eddy itself, the range of intrusions, and avoiding remnant diffusive staircases. The large-scale (overbar) temperature gradient is again the average across eddies A-E (table 2.1). Figure 2.12 shows the two sides of equation 2.11 and it implies that observed temperature variance is greater than the maximum contribution of internal waves acting on the cross-eddy temperature gradient. It is worth noting, however, that if we instead use the lateral temperature gradient of only the three upstream eddies (A-C; 1.2 x 10^{-4} ^{o}C m^{-1}) then the 90% error bars in figure 2.12 begin to overlap in the range of intrusion thicknesses.

2.4.2.3) Geostrophic turbulence

Under geostrophic turbulence, the steep roll-off of energy spectra in comparison to the more gradual roll-off of potential enstrophy and tracer variance spectra means that the density field is dominated by the large, low-mode energy containing eddies that stir along isopycnals (such as the first-mode baroclinic instability; section 2.3) whereas the *T*-*S* variance is dominated by small-scale filamentary features that must be density compensated (Smith and Ferrari 2009). The cascade of tracer variance is halted at high vertical wavenumbers by vertical mixing, which counters the variance production by mesoscale stirring. If the along-isopycnal passive tracer variance surrounding the eddies was generated by their own stirring, we would expect their sizes to match the eddy length scale associated with tracer variance generated by stirring across a mean gradient in accordance with mixing length theory (Tennekes and Lumley 1972):

$$L_{\text{mix}} = \frac{\left(\overline{C'C'}\right)^{1/2}}{\partial \overline{C} / \partial x} \tag{2.12}$$

where C is some passive tracer, x is the cross-slope coordinate, and overlines indicate an average in time or space.

To unite density-compensated variations into a single variable we consider spice (Flament 2002) which effectively serves as a quantification of distance in *T*-*S* space orthogonal to isopycnals. We compute spice profiles $C(z)$ from the glider data along the Advective Path in addition to high-passed spice profiles $C_{HP} = C - C_{LP}$, which are the total profiles minus a filtered profile (triangular filter with width 25 m), thus retaining only the interleaving layers. Inspection of composites of $\overline{C'_{HP} C'_{HP}}$ across eddies A-E, where the overline indicates averaging in the vertical between $[\sigma_{shal}, \sigma_{deep}]$, reveals that thermohaline variance is indeed largest at the eddy edges (figure 2.13). To visualize how spice variance is distributed more generally along the Advective Path, figure 2.14a shows a section of C on isopycnals and figure 2.14b collapses along-isopycnal variations into profiles of $\overline{C'C'}$ and $\overline{C'_{HP} C'_{HP}}$ where now primes are relative to the along-isopycnal mean and the products of anomalies are averaged on each isopycnal. Unsurprisingly, $\overline{C'C'}$ exhibits largest values in between $[\sigma_{shal}, \sigma_{deep}]$, being overwhelmed by the presence or absence of warm-core eddies. On the other hand, $\overline{C'_{HP} C'_{HP}}$ is less affected by the presence of eddies, making it much smaller within $[\sigma_{shal}, \sigma_{deep}]$ but of comparable magnitude above.

Estimation of the mixing length requires knowledge of the mean spice gradient that is presumably stirred. Figure 2.14c shows time-averaged spice $\overline{C}$ along the 300 line (location of Marguerite Trough) as computed from the historic Pal LTER CTD data. There is a very strong gradient at the continental slope (180 station; grey line in figure 2.14d), however, unlike other grid lines, on the 300 line there is also a secondary region of large cross-slope spice gradient within $[\sigma_{shal}, \sigma_{deep}]$ near the shoreward 130 station (blue line in figure 2.14d). We suspect that the gradient there is associated with the quasi-permanent diversion of the shelf-break current onto the shelf upon interacting with Marguerite Trough (figure 2.2).

Importantly, it is not known whether the interleaving layers are generated locally or remotely, so it is not obvious which is the relevant gradient to be stirred. Likewise, it is not immediately clear whether the relevant variance is $\overline{C'C'}$ or $\overline{C'_{\mathrm{HP}}C'_{\mathrm{HP}}}$ (i.e., should the high spice cores of the eddies be removed?). A conservative estimate is to assume that the variance is strictly that of the interleaving layers and that the gradient that is stirred is the local gradient within Marguerite Trough. That would suggest $L_{\mathrm{mix}} = \dfrac{\left(\overline{C'_{\mathrm{HP}}C'_{\mathrm{HP}}}\right)^{1/2}}{\partial\overline{C}/\partial x\Big|_{x=130}}$ = 5.6 km averaged between [σ_{shal}, σ_{deep}] (with range 3.4 - 7.5 km). An alternate perspective is to treat the warm eddy cores themselves as filamentary structures associated with stirring of the larger cross-slope gradient. In that case, $L_{\mathrm{mix}} = \dfrac{\left(\overline{C'C'}\right)^{1/2}}{\partial\overline{C}/\partial x\Big|_{x=180}}$ = 11.1 km (with range 3.4 - 17.2 km). Either way, the estimates are of the same order of magnitude as R and $\left|\mathbf{k}_{\max}\right|^{-1}$. This suggests that the observed eddies are of sufficient size to generate the observed spice variance by stirring the mean spice gradient.

2.4.2.4) Discussion

It is not obvious what causes the interleaving. Internal waves cannot provide enough temperature variance unless the lateral temperature gradient is on the larger end of those observed and the internal wave field is strongly biased towards inertial waves (which it somewhat is with $R_\omega = 9$). On the other hand, double-diffusion, while qualitatively consistent with the vertical structure of the observations, tends to have slow growth rates. A more likely candidate appears to be stirring by the eddies of the cross-shelf temperature gradient within Marguerite Trough. Spice variance is largest at the eddy edges and its magnitude is consistent

with the eddy sizes in accordance with mixing length theory. Thermohaline intrusions appear to be important for the decay of the eddies, particularly in their upper hemispheres, as cold neighboring water is brought inwards and warm slope water is ejected.

2.4.3) Frictional spindown

What appears to be cooling of the eddies may instead be redistribution of heat via a change in the buoyancy distribution of the eddy. Under the assumptions of a strictly vertical exchange of both mass and momentum, spindown of a geostrophically balanced along-front (or azimuthal) flow in the ocean interior leads to a secondary radial circulation that redistributes buoyancy so as to flatten isopycnals (Garrett 1982; Bormans 1992b). The potential vorticity equation takes the form of a diffusion equation in which the local time evolution of buoyancy B is balanced by a viscous spreading and a diapycnal diffusion of mass:

$$\frac{\partial B}{\partial t} = \frac{N^2}{f^2}\frac{\partial}{\partial r}\left(\nu \frac{\partial B}{\partial r}\right) + \frac{\partial}{\partial z}\left(K_z \frac{\partial B}{\partial z}\right). \tag{2.13}$$

Our data are incapable of being used to invert such a model, but we can make a few comments. The geostrophic shear we calculate is evaluated at approximately the depth of the eddy core and is relative to the bottom, a depth range where we have previously shown there is strong potential for diapycnal mixing. It is possible that the turbulent mixing itself flattens isopycnals without the need for friction to reduce the azimuthal geostrophic flow. We do not know the Prandtl number $\mathrm{Pr} = \nu / K_z$ within these eddies, but it is generally thought to be of order 1. Assuming that it is 7 (canonical seawater value), an upper bound for a mid-depth value of the effective viscous spreading coefficient is of order 1 $m^2\ s^{-1}$, which is comparable to the lateral diffusivity estimated in the previous section. There is insufficient evidence to confirm or refute any role of spindown in the eddies' decay.

2.5) Validation

Here we use a simple diffusion model informed by the results of the previous section to simulate the total heat loss of the eddy we tracked over crossings 1-5. We would like to emphasize that we do not expect to reproduce the small-scale structure of the eddy's cooling but instead aim to capture the bulk heat loss. The geometry of the first crossing gives us confidence that we passed directly through the eddy's center and through its entire diameter, therefore we set the initial condition as the hydrographic structure of the eddy as sampled on crossing 1. We identify the eddy's geographic center (x_1, y_1) and radius (R_1 = 3.4 km) as the mean and standard deviation, respectively, of a 2D Gaussian fit to the field of heat content per unit area integrated between σ_{shal} and σ_{deep}. We then assign each profile a radial distance from that center and grid the T and S on each isopycnal to construct a 3D field for the eddy. Outside of the eddy the domain is populated by the mCDW profile.

2.5.1) Diffusion model

We treat temperature and salinity as passive tracers and allow the eddy to diffuse in a domain x = [-10 km, +10 km], y = [-10 km, +10 km], and z = [0 m, 480 m] with 250-m grid spacing in the horizontal and 2.5 m grid spacing in the vertical. The equation for temperature is

$$\left.\begin{aligned} &\rho_0 c_p \frac{\partial T}{\partial t} = \rho_0 c_p K_h \left(\frac{\partial^2 T}{\partial x^2} + \frac{\partial^2 T}{\partial y^2} \right) + \rho_0 c_p \frac{\partial}{\partial z}\left(K_z(z) \frac{\partial T}{\partial z} \right) \\ &\frac{\partial T}{\partial z}(0) = \frac{\partial T}{\partial z}(-H) = 0 \\ &K_h = 3.2 \text{ m}^2\text{s}^{-1} \\ &K_z(z) = \begin{cases} K_{\text{top}} = 2.11\times10^{-5}\,\text{m}^2\text{s}^{-1} & z < 120 \text{ m} \\ \left[\text{log-linear increase bewteen } K_{\text{top}} \text{ and } K_{\text{bot}}\right] & 120 \le z \le 400 \text{ m} \\ K_{\text{bot}} = 2.44\times10^{-3}\,\text{m}^2\text{s}^{-1} & z > 400 \text{ m} \end{cases} \end{aligned}\right\}, \quad (2.14)$$

and it is integrated for 4.5 days with a time step of 150 s using a finite-difference control volume approach. The diffusivity values are constant in time and are based on those parameterized in the previous section. The Southern Shelf composite K_z profile (figure 2.10) increases log linearly with depth from a value of 4.23 x 10^{-6} m^2 s^{-1} at 120 m, however we found better results are achieved if we set K_{top} to be 5 times that value, which is within the reported 95% confidence interval.

2.5.2) Fit to data

We use a diffusion-only equation because the eddy's geographic coordinates $\left(x(t), y(t)\right)$ are additional unknowns. Therefore we assume that the eddy is advected by a depth-invariant current and seek an optimal $\left(x(\tau_i), y(\tau_i)\right)$ at each crossing *i*. We do this by performing a grid search by moving the modeled eddy to each location in a grid encompassing the glider track and then subsampling the modeled field along the glider track and calculating the depth-integrated heat content along the track. The position *k* that minimizes the root-mean-squared (RMS) error between $Q^{\text{obs}}(\tau_i)$ and $Q^{\text{model},\,k}(\tau_i)$ defines the eddy center's location at time τ_i. On each crossing, there are a few profiles where thermohaline intrusions significantly attenuate that profile's heat per unit area and the presumed symmetry of the eddy and therefore they are excluded in the RMS fit (but are included when evaluating total along-track heat content).

To place error bars on our modeled heat content, we perturb the best-fit eddy location by 1.2 km radially, again subsample the modeled field along the glider track, and then compute total along-track (*x*) and vertically (*z*) integrated heat content:

$$Q_{\text{along}}(\tau_i) = \int_{x_{\text{enter}}}^{x_{\text{exit}}} \int_{z_{\sigma_{\text{deep}}}}^{z_{\sigma_{\text{shal}}}} \rho_0 c_p T_{\text{anom}}(x, z, \tau_i)\, dz dx\,. \tag{2.15}$$

The spread in $Q_{\text{along}}(\tau_i)$ provides a measure of uncertainty in the heat content of the best-fit eddy.

2.5.3) Results and interpretation

The best-fit locations and modeled heat content are shown in figure 2.15. The predicted eddy track flows counterclockwise about the seamount east of Marguerite Trough (near 300.060), consistent with the mean flow, and the glider's excursion to the south confirms that this eddy did not go into Marguerite Bay. We are confident that the glider was indeed sampling the same eddy. Simulated particle trajectories (not shown) originating at $\left(x(\tau_1), y(\tau_1)\right)$ and using all possible 4-day sequences of the time-varying, depth-averaged current fields from Dinniman et al. (2011) confirm that parcels of water can follow the best-fit trajectory and can traverse the proposed distance traveled by the eddy over the total observation time.

In general, there is good agreement between the time series of observed and modeled along-track heat content (figure 2.15b). Particularly, the agreement is good near the edge of the eddy which contributes more to the integral of total heat content. There is a wide variety of intrusions, filamentation, and other submesoscale variability along the track. For example, the fourth crossing appears to skirt the eddy edge but contains a profile of water ejected from the eddy core. The second and third crossings appear to show the eddy core 'split' by the cool layer that began penetrating the eddy during the first crossing. Obviously the model does not simulate these processes though it does seem capable of parameterizing their consequences. The total integrated heat contents fall within the range of perturbed model fits (figure 2.15c).

The results can be used to estimate the rate of heat loss of the eddy between crossings 1 and 5. The total heat content of the eddy during crossing 1 is easily obtained by integrating the model initial condition (itself a fit to the data) vertically between σ_{shal} and σ_{deep} and then laterally out to R_1. At crossing 5, we obtain $Q_{\text{max, chord}}$ and R_{chord} by fitting equation 2.1 to the data but to

calculate the total heat content we need a cross section through the eddy center. Simple trigonometry shows that $R_{real}=\sqrt{R_{chord}^2+D^2}$ and $Q_{max,\,real} = Q_{max,\,chord}\exp\left(+\left(D/R_{real}\right)^2\right)$ where D is the distance between the true eddy center and the chord-length center. Using D = 2.5 km (figure 2.15a), the total heat content is then obtained from equation 2.2 by using $Q_{max,\,real}$ and R_{real} and integrating out to R_1. The initial and final heat contents are $Q_{tot}(\tau_1)$ = 7.9 x 10^{15} J and $Q_{tot}(\tau_5)$ = 5.5 x 10^{15} J, implying a cooling rate $\partial Q/\partial t$ = 7.0 x 10^9 J s^{-1}. It is worth noting that the modeled heat content on crossing 5 is 5.6 x 10^{15} J, only 2% greater than observed.

2.6) Discussions and conclusions

The first goal of this study was to understand the origin of UCDW eddies on the shelf. We conducted a linear stability analysis of the shelf-break current to show that its most unstable mode has a CDW-level amplitude maximum and an inverse wavenumber of 4.4 km. Glider observations confirmed that UCDW eddies on the shelf have diameters and crest-to-crest separation consistent with that metric and their anomalies are confined to the subpycnocline layer. The strong shear and weak stratification allow for sign changes in the interior potential vorticity gradient which causes instabilities smaller than the Rossby radius to persist even when Eady modes are suppressed by the bottom slope. This, in combination with the insensitivity to the planetary beta effect, suggests to us that similar UCDW eddies should be common around the Antarctic margins. However, we must be cautious with any broad extensions. While we have shown that either eastward or westward currents can support eddies, westward currents are often associated with the Antarctic Slope Front and very different stratification. The demonstrated sensitivity of eddy fluxes of CDW to other parameters that were not considered here, such as depth of the continental shelf or prominence of the Antarctic Slope Front (Stewart and

Thompson 2015), restricts any generalizations and suggests eddy fluxes are still likely highly localized (Stewart et al. 2018) with one region of importance being the WAP.

The second goal of this study was to identify the major mixing processes that disperse eddy heat into surrounding water. Shipboard CTD and SADCP measurements were used to show cross-pycnocline diffusive fluxes should on average be < 1 W m^{-2} while fluxes below the eddy T_{max} should be an order of magnitude larger. CTD and glider profiles reveal that interleaving layers and thermohaline intrusions are ubiquitous, particularly in the lower pycnocline / eddy upper-hemispheres where they link warm slope-type UCDW to the cooler waters within the adjacent water column's broad pycnocline. This water is most quickly eroded over the Advective Path while the deeper, core T_{max} at ~250 m persists longer. The erosion of the core heat content per unit area is more apparent than that of the temperature maximum, implying erosion at the eddy boundaries and/or a redistribution of heat within the eddy interior. Consistent with this, high-pass filtered spice variance is largest at the eddy edges.

The origin of the thermohaline intrusions is ambiguous. The magnitude of their thermal variance is larger than would be expected if due solely to internal wave shear, although this conclusion is highly dependent on the magnitude of the lateral temperature gradient across the eddy. In addition, thermal variance is largest above and just below the eddy core, both regions susceptible to double-diffusive instabilities. Instead, given the observed along-isopycnal spice variance, the mean spice gradient, and the size of the first-mode instability, a more plausible explanation for the origin of the interleaving layers may be stirring by the eddies themselves. A recent modeling study (Stewart et al. 2018) suggests that eddies may transfer heat across the Antarctic slope primarily by along-isopycnal stirring as opposed to advection by their

overturning streamfunction. This also supports stirring as an explanation for the thermohaline variance.

The flexibility afforded by Slocum gliders allows for real-time, data-adaptive sampling. One of the novel aspects of this study is the collection of cross sections through an eddy as it traversed the shelf, providing a first estimate of the eddies' rate of cooling, which is consistent with that of a 3D diffusion model applied to the initial crossing. A lower limit on the time required to eliminate all heat relative to the mCDW profile within one radius from the eddy center is given by $Q_{\mathrm{tot}}(\tau_1)/(\partial Q/\partial t)$ = 13.1 days which assumes that the gradients are constant in time. Because lateral mixing dominates, an alternate cooling time is given by the solution to the two-dimensional diffusion equation with homogeneous lateral boundary conditions at infinity and a Gaussian initial condition of radius *R*. That solution implies that the heat content per unit area at the eddy center decreases as $R^2/(R^2+4K_h t)$. For the tracked eddy a 50% decrease is achieved after 10.3 days. For a typical eddy $\left(R=|\mathbf{k}_{\max}|^{-1}\right)$, a 50% decrease takes 17.5 days.

We can synthesize these results with a heat budget integrated over a homogeneous eddy whose dimensions and gradients do not change in time:

$$\frac{1}{\rho_0 c_p}\frac{\partial Q_{\mathrm{total}}}{\partial t} = 2\pi RHK_h \left.\frac{\partial T}{\partial r}\right|_{r=R} + \pi R^2\left(K_z\left.\frac{\partial T}{\partial z}\right|_{z=\mathrm{top}} - K_z\left.\frac{\partial T}{\partial z}\right|_{z=\mathrm{bottom}}\right) + \varepsilon . \qquad (2.16)$$

In this formulation, ε collects mismatch between the left- and right-hand sides. It is meant to represent the effects of noise in the data but also captures the effects of processes that restructure the eddy. Because we only know $\partial Q/\partial t$ for the tracked eddy (7.0 x 10^9 J s^{-1}), we balance the budget with that eddy's gradients and geometry averaged across crossings 1 and 5. For the tracked eddy, *R* = 3.4 km, *H* = 188 m, $\langle \partial T/\partial z|_{\mathrm{top}} \rangle$ = 0.019 ºC m^{-1}, $\langle \partial T/\partial z|_{\mathrm{bot}} \rangle$ = -0.0014 ºC m^{-1},

$\left\langle \partial T/\partial r\big|_{r=R} \right\rangle$ = 1.1 x 10^{-4} ºC m^{-1}, and the diffusivities are those used in the model, evaluated at the average depths of σ_{shal} and σ_{deep}. The balance implies the following conceptual model of eddy cooling. About 2% of initial heat loss occurs diapycnally through the permanent pycnocline; about 3% occurs diapycnally through the bottom and 95% occurs laterally. The lateral heat loss, which occurs in part through thermohaline intrusions, directly warms the surrounding pycnocline base and mid-depth waters. The diapycnal mixing through the bottom also works to flatten isopycnals at and below the T_{max} which reduces the azimuthal geostrophic current. The mismatch $\varepsilon/\left(\partial Q/\partial t\right)$ = 10% is small, suggesting redistribution processes such as viscous spreading are of secondary importance compared to lateral mixing. To place this number in context, if the lateral diffusivity was increased from 3.2 to 3.6 m^2 s^{-1} (which is within one standard error) then ε goes to zero. The budget is shown schematically in figure 2.16 with fluxes estimated for a more typical eddy (gradients and geometry from table 2.1).

Importantly, a preference for the eddies to mix laterally and downwards suggests that the eddies are good at redistributing heat rather than immediately venting it to the atmosphere. This sheltering has implications for the ability of intra and subpycnocline heat to persist and make its way shoreward toward marine-terminating glaciers even as the eddies themselves cease to remain coherent structures.

Tables

Table 2.1: Fundamental statistics for eddies sampled by glider along Advective Path.

	R [km]	R_{TD} [km]	H [m]	Q_{max} [10^8 J m^{-2}]	Q_{tot} [10^{16} J]	gl_0 [km]	gs_0 [km]	V_g [m s^{-1}]	$\partial T/\partial z\|_{top}$ [10^{-2} ºC m^{-1}]	$\partial T/\partial z\|_{bot}$ [10^{-3} ºC m^{-1}]	$\partial T/\partial r\|_R$ [10^{-4} ºC m^{-1}]
A	3.3	5.7	195.7	3.08	0.67	293.6	109.3	0.07	1.66	-1.03	1.36
B	2.2	5.3	178.0	2.48	0.23	309.4	99.2	0.05	2.00	-1.09	0.69
C	2.8	5.5	222.5	5.46	0.88	328.0	92.6	0.09	3.38	-1.25	1.53
D	6.8	8.5	177.3	1.81	1.67	358.0	77.7	0.02	2.01	-1.60	0.32
E	7.1	10.4	188.8	2.25	2.25	372.3	67.9	0.02	1.90	-1.22	0.37

Figures

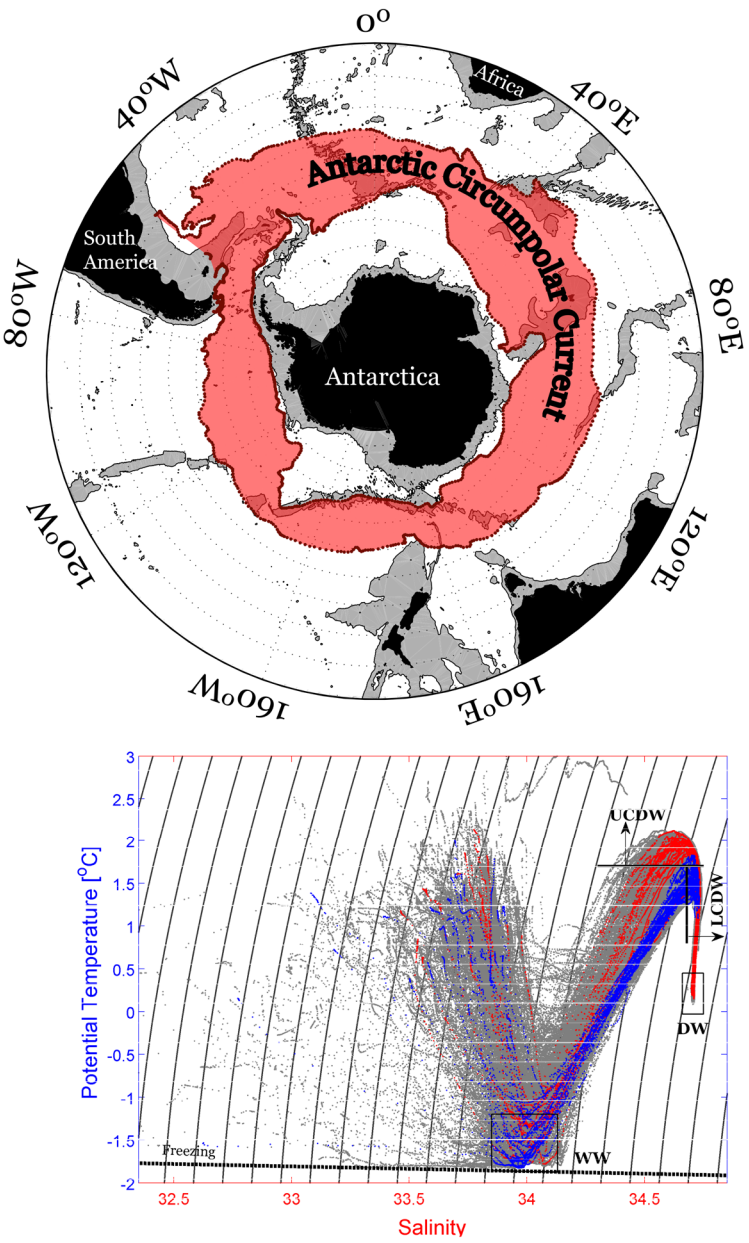

Figure 2.1: Top: Location of climatological ACC (Orsi et al. 1995), transporting warm UCDW. Bathymetry shallower than 3 km is shaded. **Bottom:** Potential temperature-salinity properties within the LTER sampling grid (grey) highlighting those from a shelf station (300.100, blue) and a slope station (200.160, red) to emphasize the difference in UCDW properties. UCDW is identified as a potential temperature greater than 1.7 ºC, LCDW is identified as a salinity greater than 34.68 (with potential temperature less than 1.7 ºC), and WW and Deep Water (DW) are defined as in Martinson et al. (2008). The DW is a definition used by Martinson et al. (2008) in order to define a local end-member for a water mass mixing analysis and is not an actual water mass of the Southern Ocean (and is not discussed here).

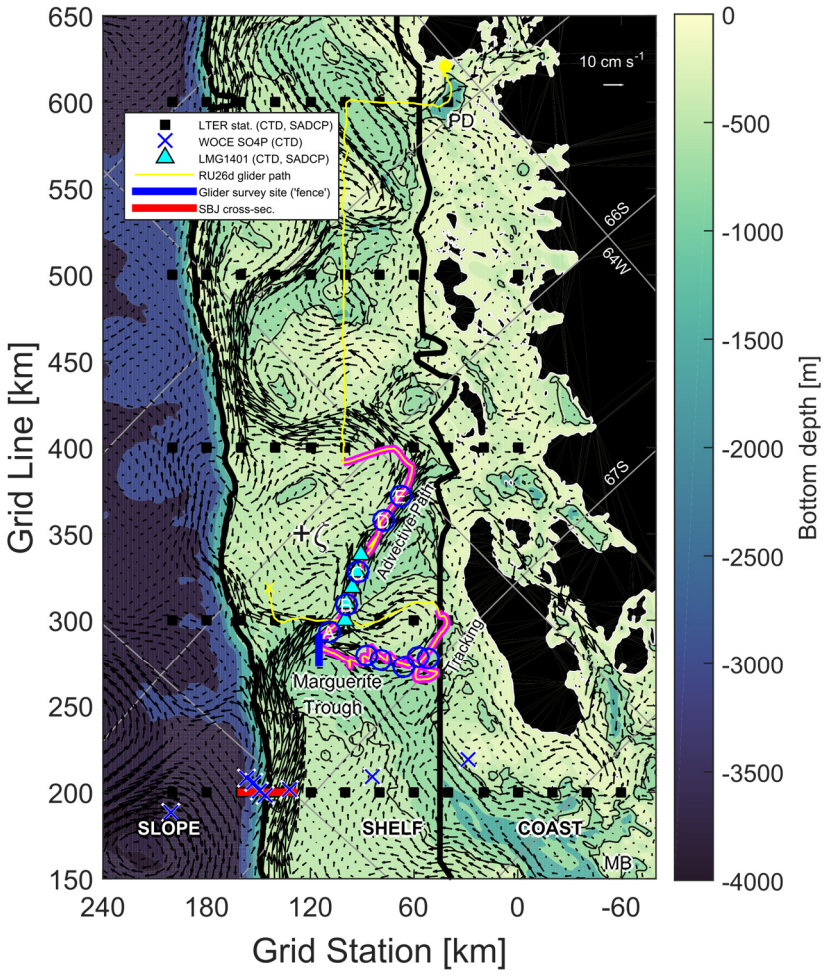

Figure 2.2: Map of study region and all data used. LTER sampling grid (shipboard CTD, ADCP) shown as black squares (100 grid line is not shown but is used). All locations in the paper use the LTER coordinate system and are given as GGG.SSS where GGG is the grid line (km) and SSS the grid station (km). Origin 000.000 is at ~69.0º S, ~73.6º W, near Alexander Island. WOCE S04P CTD locations are shown as 'x' symbols, and they are gridded onto the 200 line (red line, see text). Additional CTD casts taken in January 2014 are shown as triangles. The flight of glider RU26d is indicated by the yellow line (beginning at circle), and the survey fence is denoted by the blue line perpendicular to the eastern wall of Marguerite Trough. The two stages of the glider mission are described in section 2.2, are emphasized with a magenta outline, and are labeled; the eddies encountered are indicated by blue circles. Finally, for reference we present a snapshot of the depth-averaged currents during a CDW upwelling event from the model run of Dinniman et al. (2011) with reference vector in upper right corner. Marguerite Trough, which cuts across the center of the shelf into Marguerite Bay, is labeled along with Marguerite Bay (MB) and Palmer Deep (PD). The center of the anticyclonic cell extending out of Marguerite Trough is labeled +ζ. Grid bathymetry is shaded between contours at 0, 200, 350, 500, and 750 m and then at 750-m intervals until 3750 m. The 480-m isobath, which is continuous between Marguerite Trough and the Advective Path, is indicated in black. The bold black lines separate the Slope, Shelf, and Coast regimes.

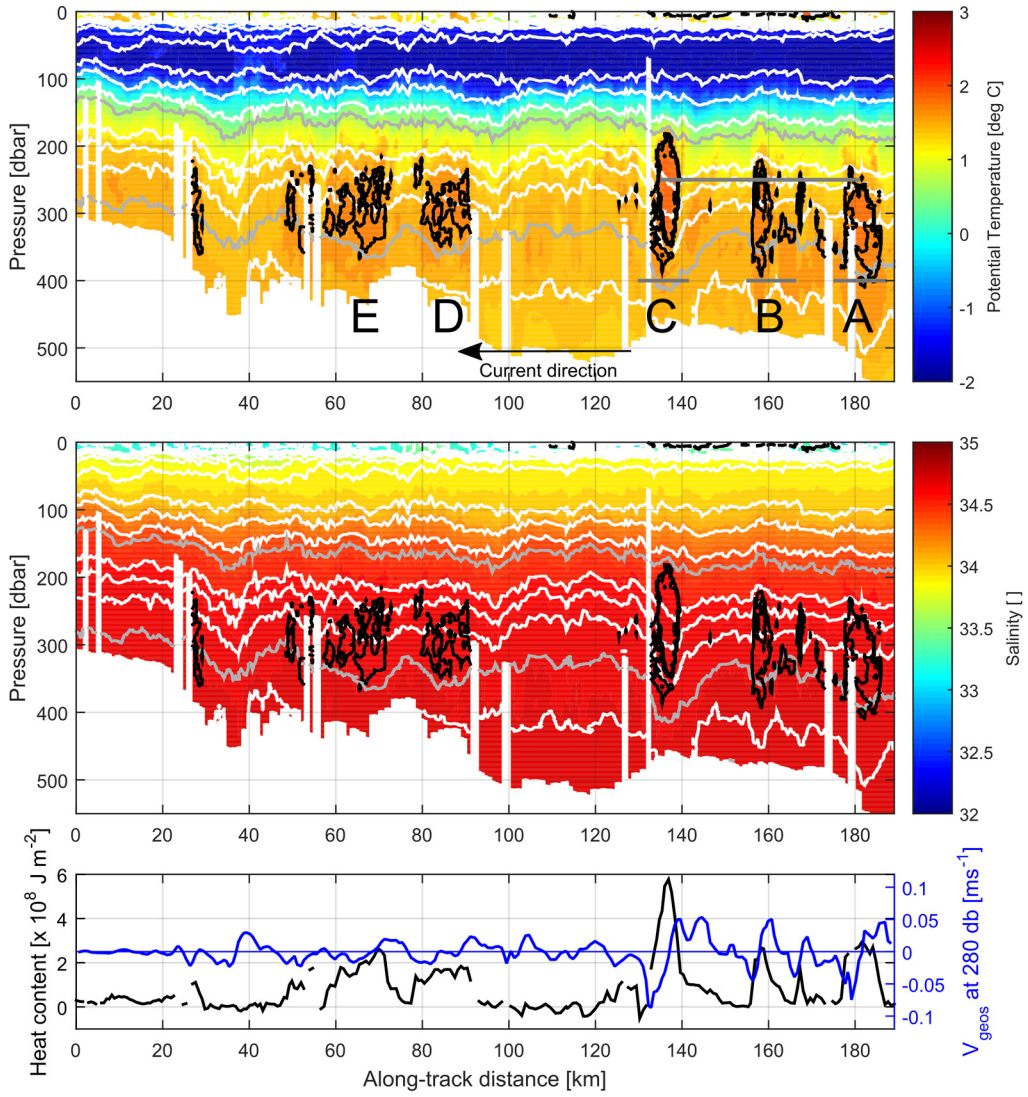

Figure 2.3: Summary of glider observations over the Advective Path. **Top:** Potential temperature (colors) with the 1.7 ºC and 1.8 ºC isotherms (black) and isopycnals (white; σ_{shal} and σ_{deep} in grey) indicated. Eddies are labeled A-E, alphabetically increasing with distance from shelf-break. Scales and separation distance of the upstream (at right) eddies are indicated with thick grey lines. **Middle:** As in the top panel, but for salinity. **Bottom:** Heat content relative to mCDW integrated between σ_{shal} and σ_{deep} (black) and geostrophic current at 280 dbar relative to seafloor (blue).

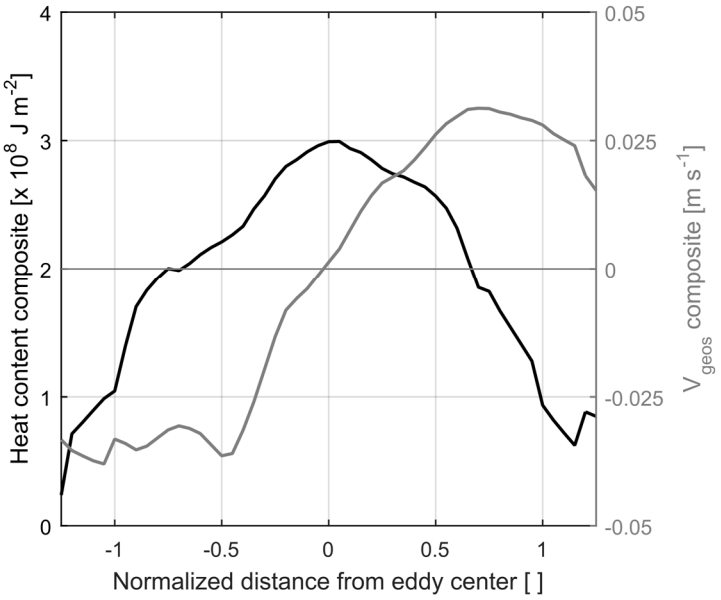

Figure 2.4: Composite heat content per unit area (black) and geostrophic current at 280 dbar relative to bottom (grey) for eddies A-E. To account for different eddy sizes, each is first stretched or squeezed by interpolating onto a dimensionless grid with values -1 and +1 at the downstream and upstream edges $\chi_0 - R$ and $\chi_0 + R$, respectively.

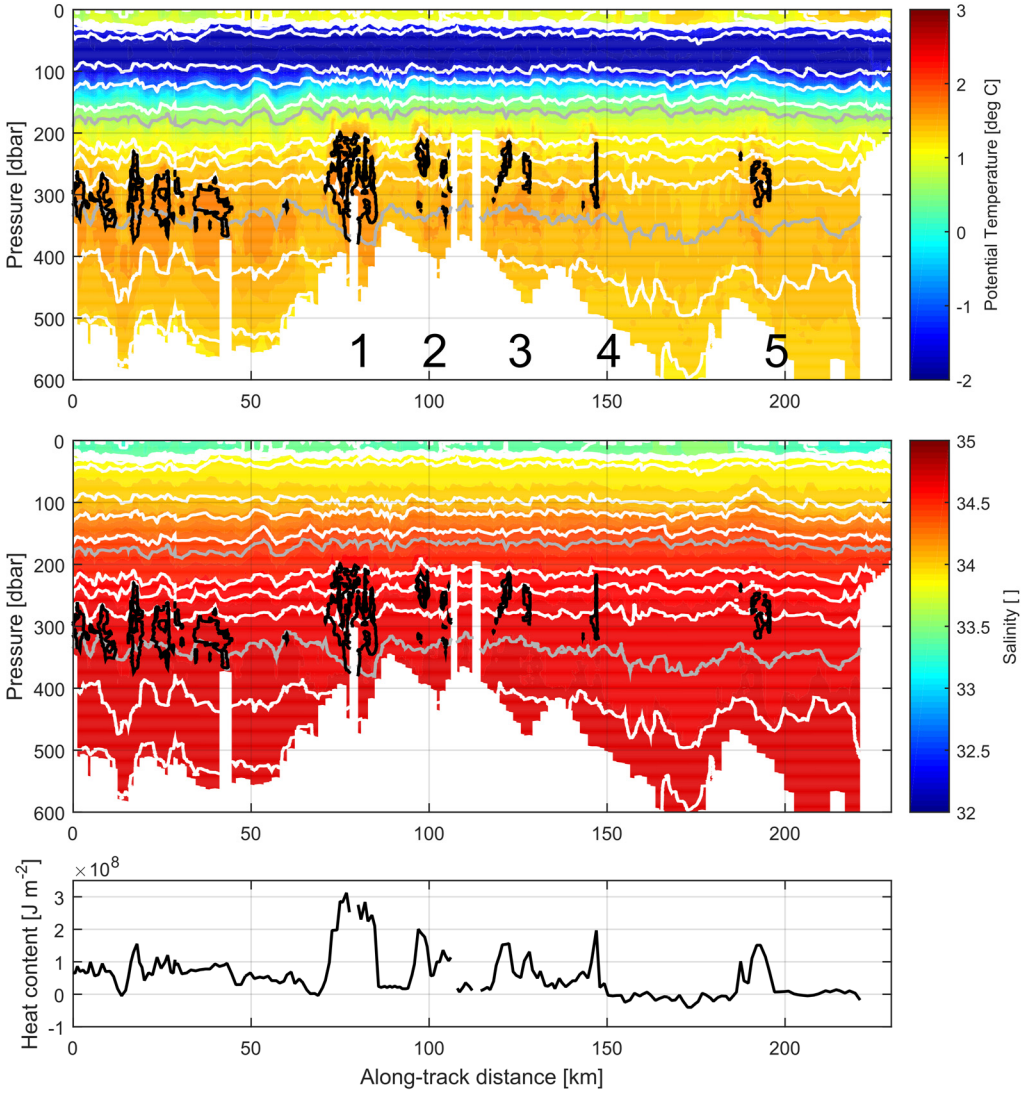

Figure 2.5: As in figure 2.3, but showing data for the Tracking Stage. The repeat glider crossings of the single tracked eddy are numbered 1-5. Since the glider path did not always cleanly intersect the eddy, geostrophic currents do not provide a meaningful measure of azimuthal velocity and they are not shown.

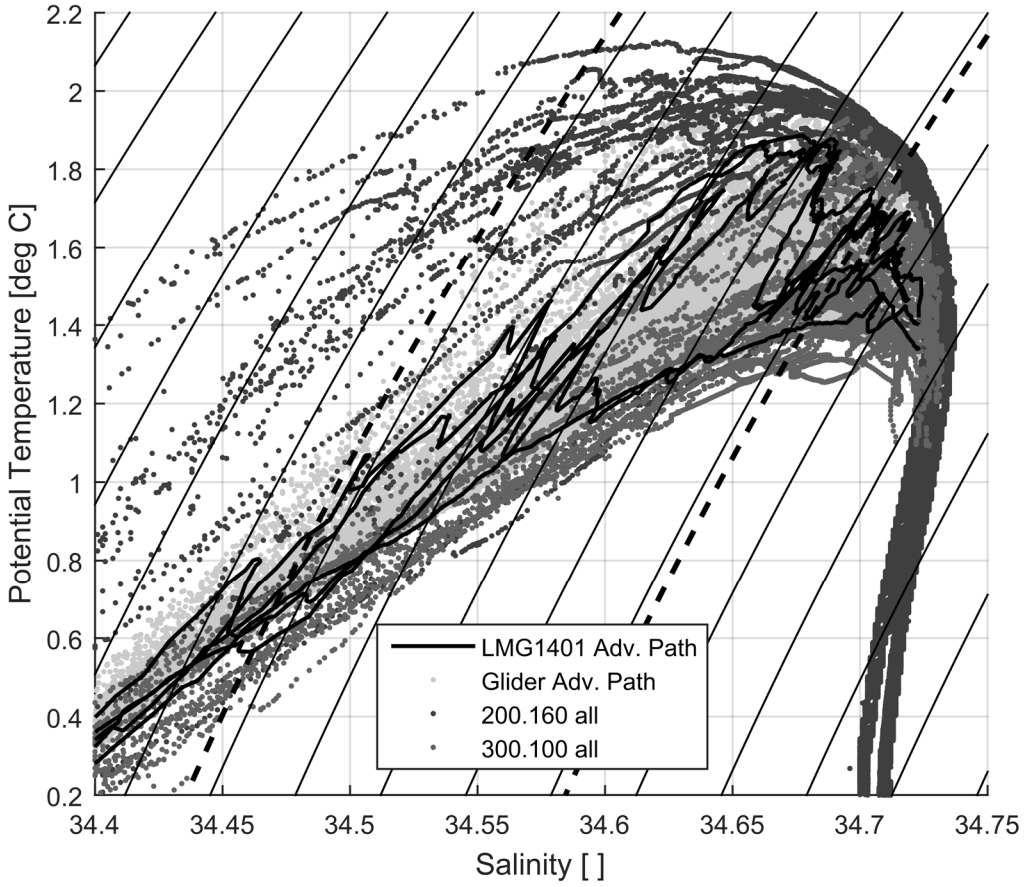

Figure 2.6: Potential temperature-salinity diagram zoomed in to the UCDW region showing the five CTD casts along the Advective Path (black lines) along with all historic casts from a slope station (200.160; dark grey) and a shelf station (300.100; medium grey). The interleaving layers join slope-type UCDW with cooler, shelf-type pycnocline waters. Isopycnals σ_{shal} and σ_{deep} used for integrations are indicated as black dashed lines, and the glider profiles in the same region are shown as light grey dots.

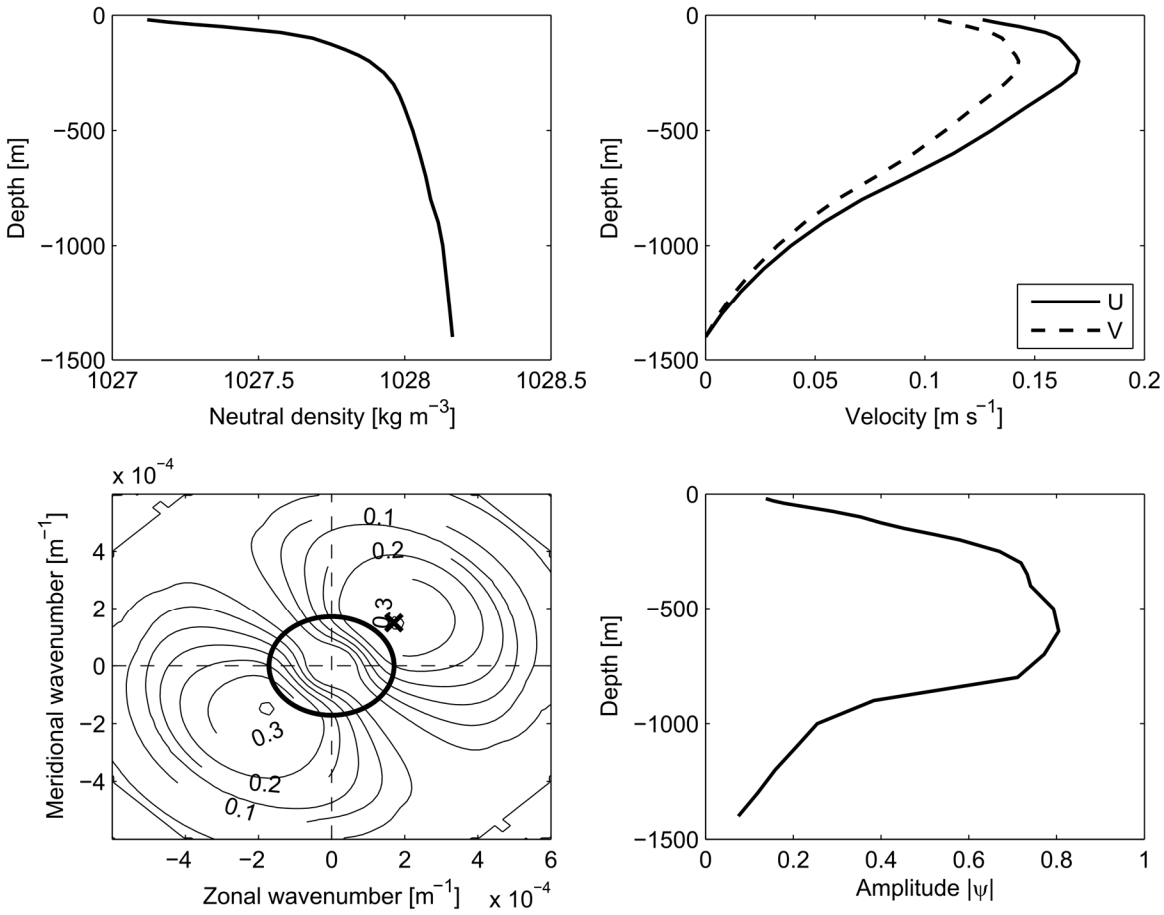

Figure 2.7: Profiles used for linear stability analysis and results. **Top:** Profiles of (left) neutral density and (right) geostrophic velocities used. **Bottom left:** Perturbation growth rates as a function of wavenumber. The overall most unstable mode is indicated with a black x. Locus of points $|\mathbf{k}| = L_R^{-1}$ is given by solid black circle. **Bottom right:** Amplitude structure of the most unstable mode.

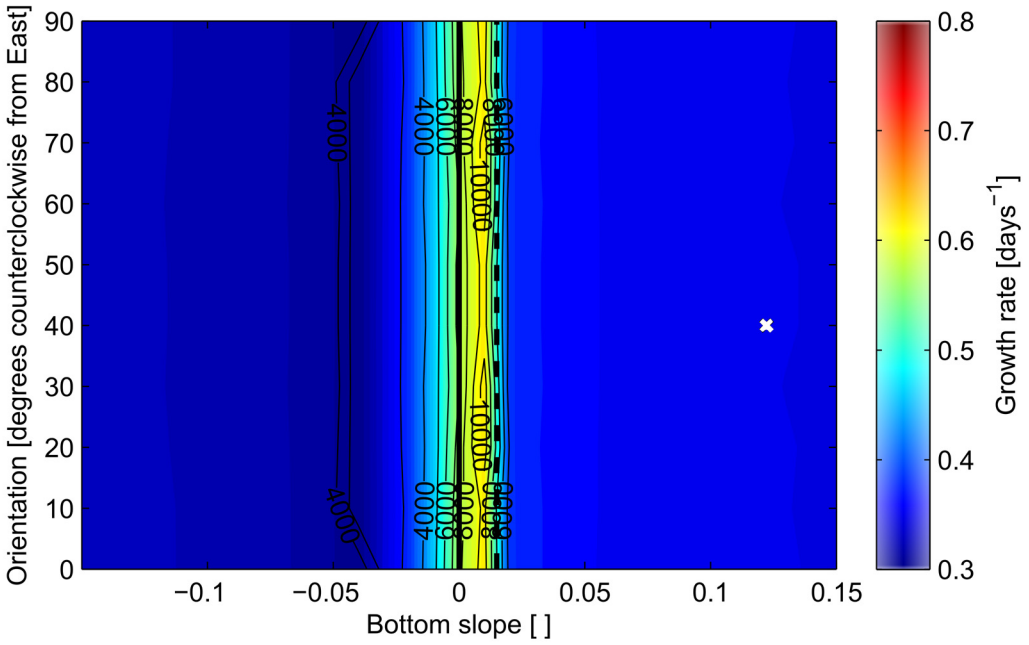

Figure 2.8: Growth rate (color) and inverse wavenumber (contours) of most unstable mode for various bottom slopes and current orientations. All cases use the same shear and stratification from figure 2.7 and assume that the current flows exactly parallel to the shelf-break. Slope of the 1028.0 kg m^{-3} neutral surface is indicated by a black dashed line. Actual bottom slope and current orientation indicated as white 'x'.

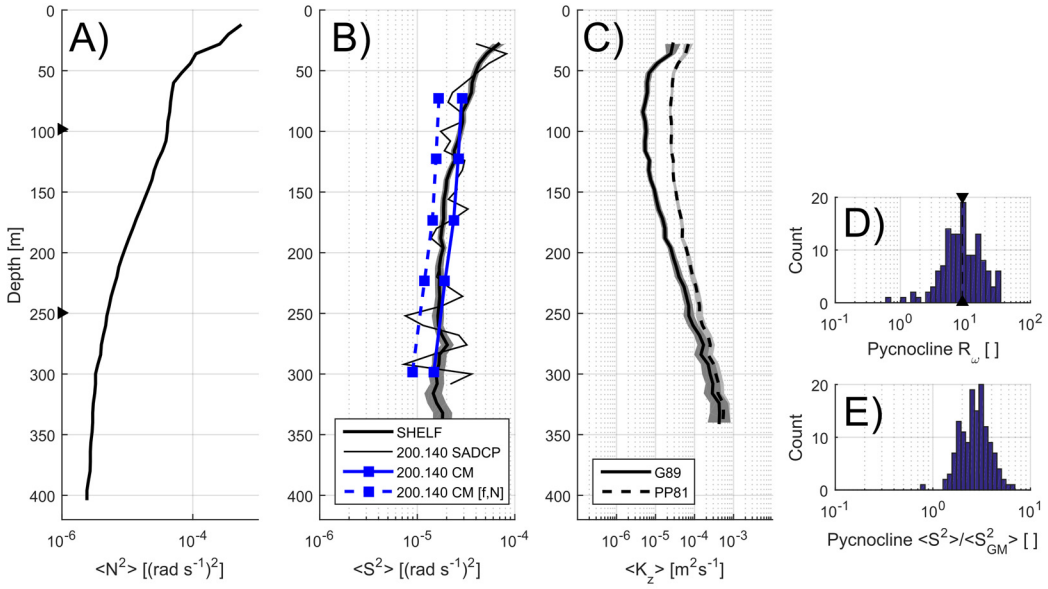

Figure 2.9: Summary of vertical mixing parameterizations for Shelf region. **(a)** The N^2 calculated on shelf-averaged density profile (see Appendix A). Range of the permanent pycnocline as defined in the text indicated with black wedges. **(b)** Composite S^2 profile from all SADCP profiles log-averaged on depth coordinates (bold black) with ± 2 log standard errors (grey shading); composite S^2 profile from all SADCP profiles at station 200.140 log-averaged on depth coordinates (thin black); log-averaged total (solid blue) and internal wave band (dashed blue) S^2 from moored current meters at station 200.140. **(c)** Composite K_z profiles log-averaged on depth coordinates (G89 solid; PP81 dashed) along with ± 2 log standard errors (grey shading). **(d)** Histogram of shear-to-strain variance ratios for all Shelf profiles with complete pycnocline coverage; $R_\omega = 9$ indicated with black dashed line. **(e)** Histogram of observed-to-GM pycnocline shear variance ratios for all Shelf profiles with complete pycnocline coverage.

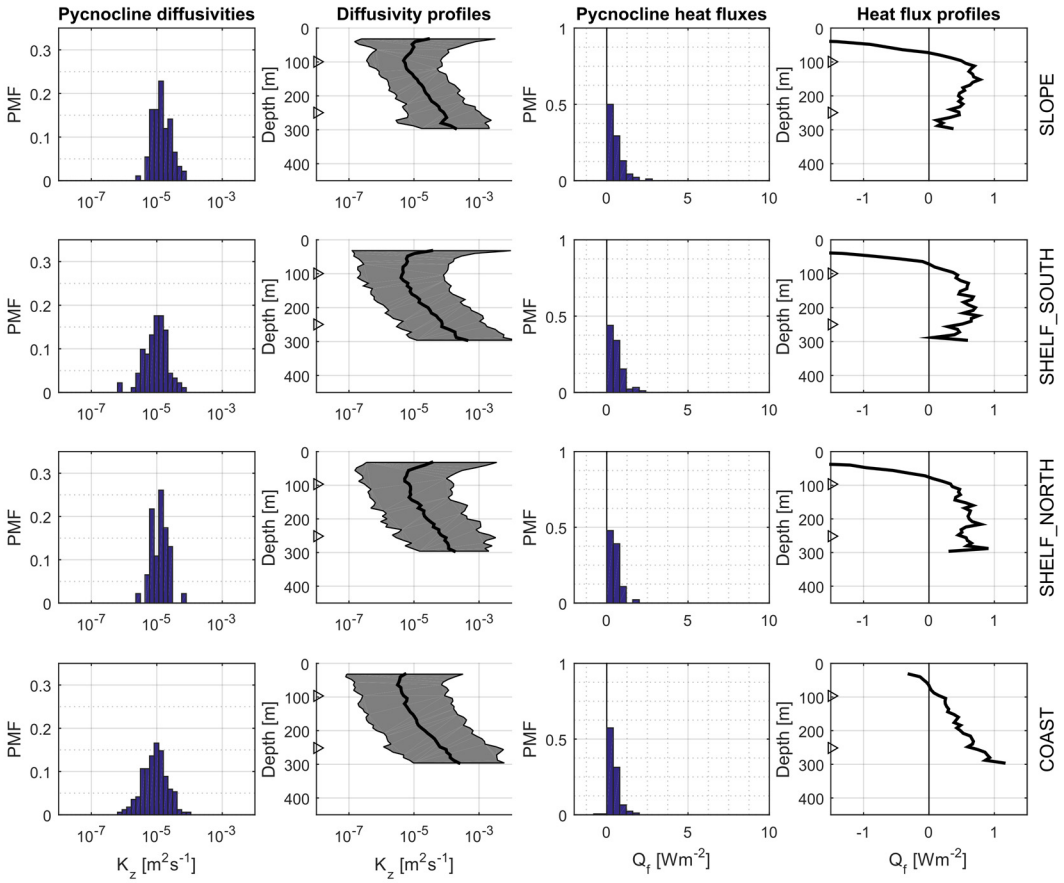

Figure 2.10: Summary of regional variability of vertical diffusivities and heat fluxes. Rows indicate different regions (Shelf, Slope, and Coast indicated in figure 2.2; North Shelf and South Shelf are separated by 450 grid line). **Column 1:** Histograms of G89 K_z, log-averaged over depth of pycnocline (blue bars). **Column 2:** Profile of G89 K_z, log-averaged across all profiles at each depth. Grey shading indicates 2 log standard deviations. **Column 3:** As in column 1, but for vertical heat fluxes, where depth-reduction is accomplished by using the median. **Column 4:** As in column 2, but for vertical heat fluxes, where space-reduction is accomplished by using the median. Because the heat fluxes do not follow a simple distribution, error bars are not shown. In total there are 1073 CTD casts north of the 000 grid line matched to an SADCP profile. Of those, 963 contain at least one good N^2 and S^2 value (used for composite profiles), 859 contain at least one good value within the pycnocline, and 398 contain good values throughout the pycnocline (used for depth-reduced histograms).

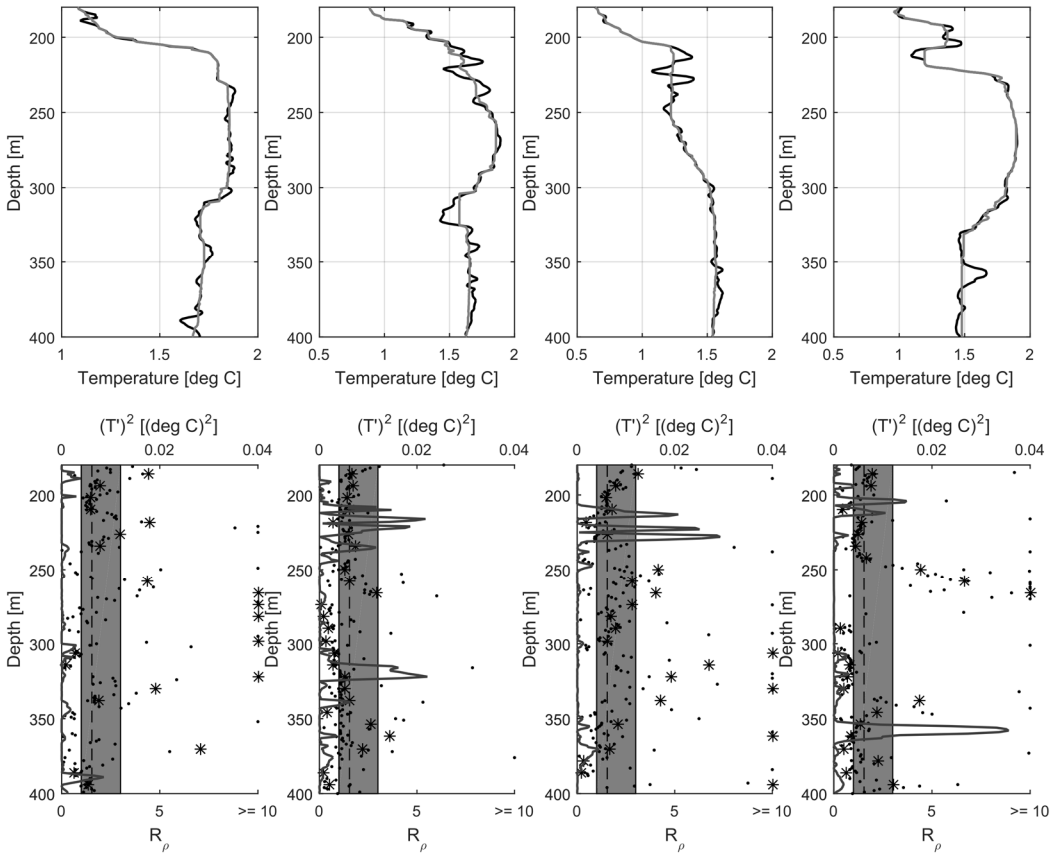

Figure 2.11: Summary of temperature variance in the four out of five Advective Path CTD casts that indicate substantial thermohaline intrusions (time and downstream-distance increase from left to right). **Top:** Full temperature profile (black) along with background temperature profile (grey; see text for definition). **Bottom:** Temperature anomaly squared (line) along with density ratio computed on 8-m profiles (stars) and on 1-m profiles (dots). Axes are saturated so that depths with $R_\rho > 10$ are shown at 10 and doubly-stable and statically-unstable values are not shown. The shaded region indicates highly diffusively unstable region [1, 3], and the dashed line indicates the critical threshold of Bormans (1992a) below which diffusive stratification contributes significantly to cross-frontal heat fluxes.

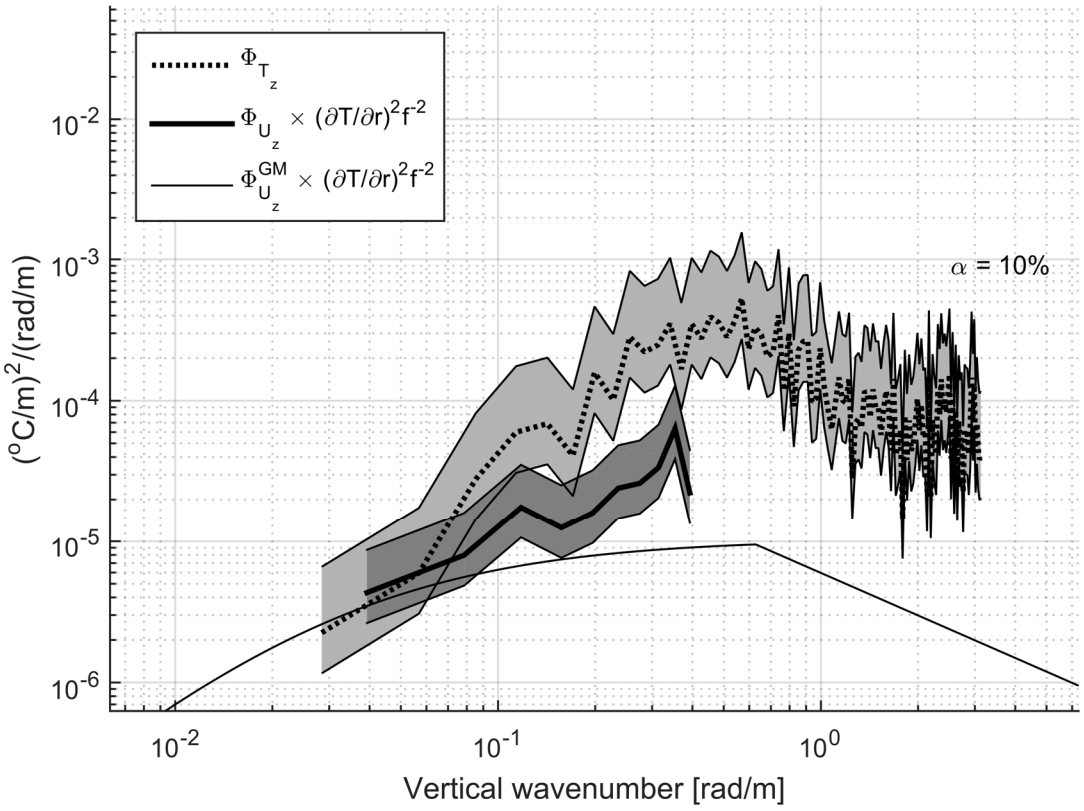

Figure 2.12: Spectra of vertical derivatives of medium-scale temperature anomalies (dashed) and shear times $\left(\partial\overline{T}/\partial r\right)^2 f^{-2}$ for observations (bold black) and local GM (thin black). Error bars at the α = 10% level are indicated by the shaded regions. If internal waves could account for all medium-scale temperature variance then the solid spectrum would exceed the dashed.

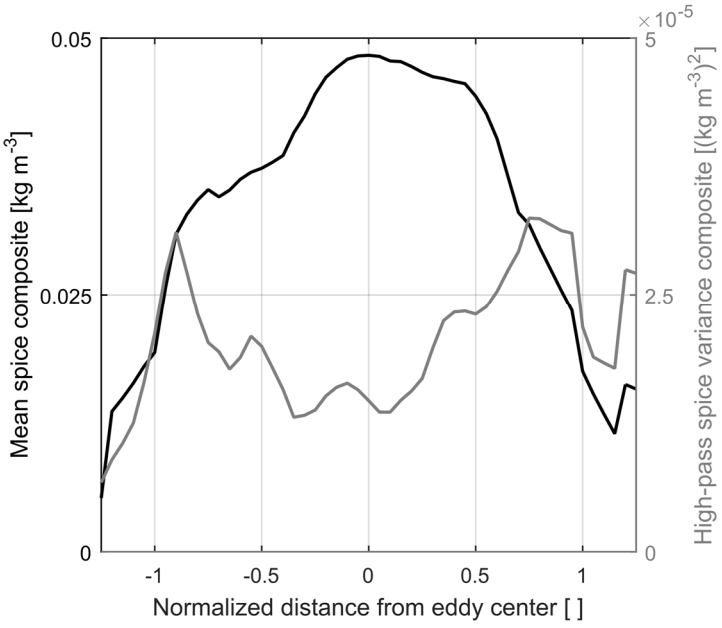

Figure 2.13: Composite depth-mean spice anomaly (black) and high-pass filtered spice variance (grey) between σ_{shal} and σ_{deep} for eddies A-E. Horizontal coordinate is stretched as in figure 2.4.

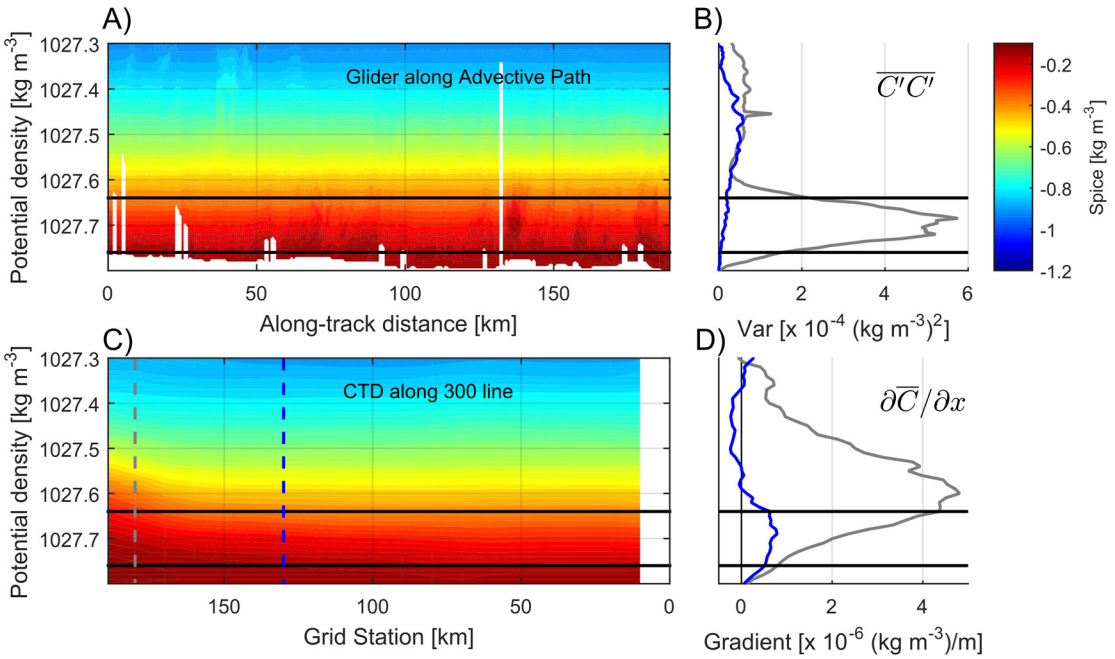

Figure 2.14: Observed spice variance and mean spice gradients used in mixing length calculations. **(a)** Spice C on isopycnals along Advective Path from glider. **(b)** Along-isopycnal variance of spice C (grey) and of high-pass filtered spice C_{HP} (blue) for section in (a). **(c)** Cross-slope section of mean spice from climatological CTD data across the continental shelf at the 300 line. **(d)** Magnitude of the cross-slope spice gradient on isopycnals at the locations of the dashed lines in (c). In all panels σ_{shal} and σ_{deep} are indicated with black lines.

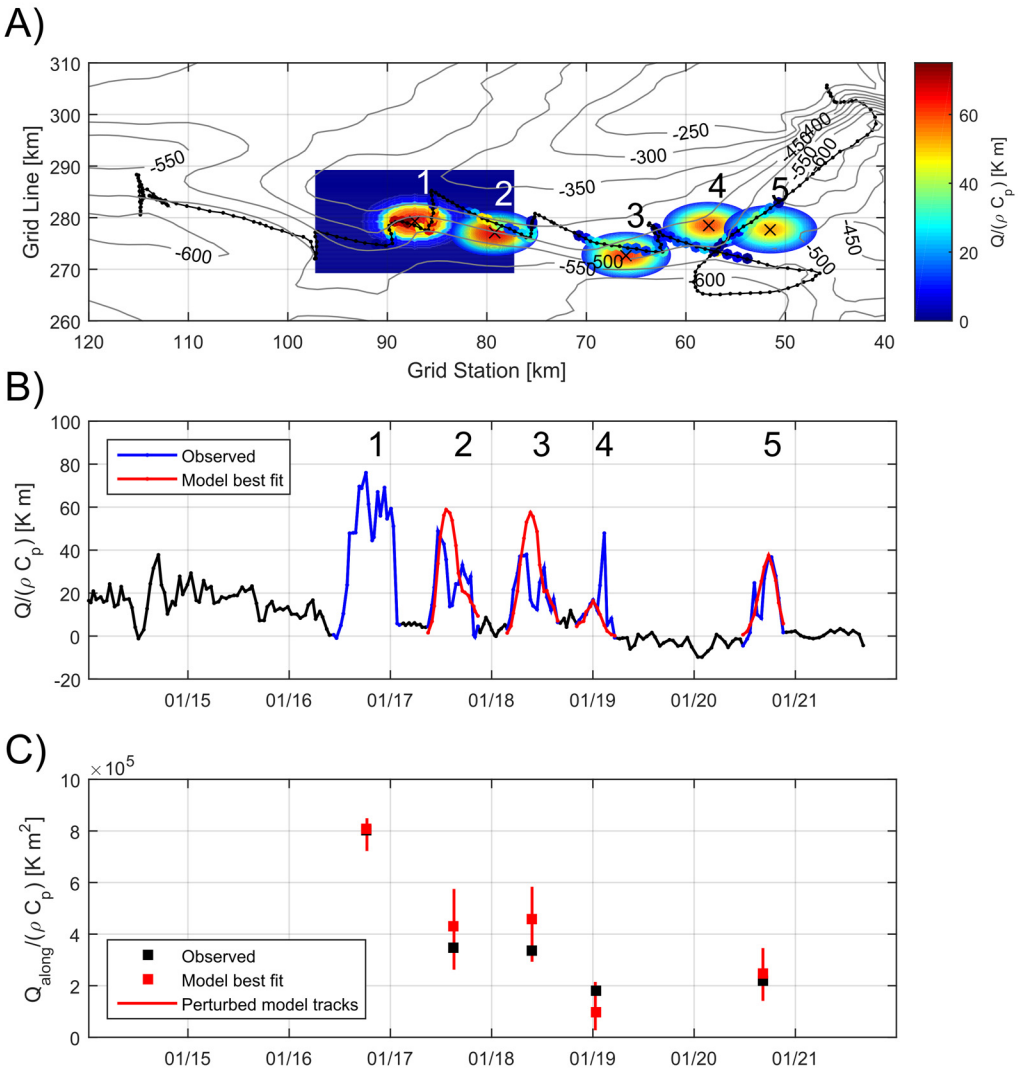

Figure 2.15: Forward model results in comparison with glider data. **(a)** Glider track during the Tracking Stage (black line) where profiles containing the eddy are color coded by the vertically-integrated heat content per unit area (dots). The contours are the diffusion model vertically-integrated heat content per unit area at the time step of the crossing, situated at the geographic location that minimizes RMS error between the observed along-track series and the model field subsampled along the glider track. The first crossing shows the full model domain for scale. **(b)** Time series of observed (blue) and modeled (red) along-track heat content per unit area for each crossing of the eddy. **(c)** Time series of vertically- and along-track-integrated heat content for each eddy. Observations are shown in black and the best fit model result is shown in red, along with error bars constructed by perturbing the model's best fit eddy location and then subsampling along the glider track and integrating.

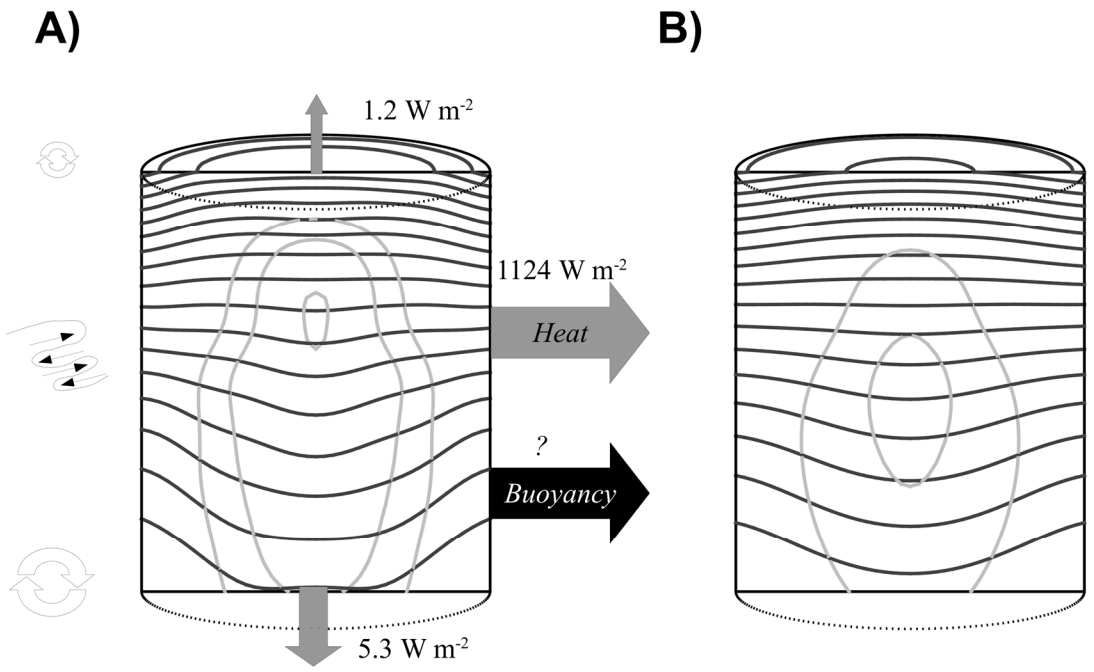

Figure 2.16: Schematic summary of eddy heat loss processes and typical values for their fluxes based on the values in Table 2.1. The eddy is presented as a cylinder as in the integrated, averaged heat budget in the text. Isopycnals are shown as black lines and three isotherms are shown as grey lines. **(a)** A schematic representation of the tracked eddy's initial condition and **(b)** schematic representation of the modeled eddy 4.5 days later. The same isolines are shown on each plot, suggesting that the temperature maximum is both eroded and mixed downward and that the geostrophic current is reduced. Lateral spreading of buoyancy by frictional spindown must occur, but its amount cannot be quantified with the glider data.

3) Spatially coherent subtidal velocity fluctuations

Abstract:

We analyze several year-long moored current meter records collected on the mid-shelf and shelf-break of the western Antarctic Peninsula in order to describe the major features of the subtidal circulation. An EOF analysis of all current meter records in any given year reveals that over 49% of the circulation variance follows a spatially coherent, nearly depth-invariant anticyclonic cell in the downstream vicinity of Marguerite Trough, qualitatively consistent with flow-topography interaction with the canyon. An analysis of kinetic energy spectra supports the interpretation that the shelf-break current is diverted shoreward at the location of the canyon and generates substantial counterclockwise energy at periods shorter than ~10 days as the flow is compressed by a downstream bank. Rotary coherency analysis of current meters separated by the permanent pycnocline suggests strong coherency and little veering with depth. The circulation is well correlated with the long-shore wind stress both local and remote. Composite velocity profiles under upwelling and downwelling winds show that the change in the barotropic current under different wind states is comparable to or larger than the shear of the mean profile in all years. The barotropic velocity fluctuations are generally not coherent with subpycnocline heat content.

3.1) Introduction

The western Antarctic Peninsula (WAP) is undergoing rapid climate change including strong wintertime atmospheric warming (Turner et al. 2013). The ocean is a primary heat source and presumably plays some role in the changing environment. For example, shelf waters along

the WAP have warmed and shoaled (Martinson et al. 2008; Schmidtko et al. 2014) and these warmed subpycnocline waters have been directly implicated in ice mass loss on the WAP as glaciers in contact with warm subpycnocline waters are in retreat while those in contact with colder waters of the Bransfield Strait are not (Cook et al. 2016). WAP hydrography is dominated by the influence of Upper Circumpolar Deep Water (UCDW), which is identified as a mid-water column temperature maximum (T_{max}) (Gordon 1971). The T_{max} on the WAP slope is several degrees above the *in-situ* freezing point and typically resides at depths of ~250 m as isopycnals shoal shoreward (Martinson et al. 2008). As the southern boundary of the Antarctic Circumpolar Current (ACC) flows adjacent to the WAP shelf (Orsi et al. 1995), UCDW is readily available at shelf depths.

The importance of water column heat content motivates an understanding of the circulation, which dictates its transport. The physical setting, major bathymetric features, and an overview of the circulation and major currents are indicated in figure 3.1. Recent reviews of the WAP circulation and of shelf-slope exchange along western Antarctica are given by Moffat and Meredith (2018) and Gille et al. (2016), respectively, but we provide a summary here. The mean circulation on the WAP is broadly characterized by a northeastward flow along the shelf-break associated with the southern boundary of the ACC (the Shelf-Break Jet; SBJ) and a southwestward flow along the coast (the Coastal Current; CC). Long-shore winds south of the Bransfield Strait are coastal-downwelling which act to drive the southward flow, although the baroclinic component of the coastal current is seasonally enhanced by a cross-shelf density gradient induced by near-surface melt water (Moffat et al. 2008). The prevailing cyclonic circulation induced by these two currents is generally captured in the geopotential height fields calculated from ship surveys, as in figure 3.1b. Eulerian-mean absolute currents from a database

of shipboard ADCP profiles corroborate many of the same features (Savidge and Amft 2009). On smaller scales (tens of kilometers), numerical models (Dinniman et al. 2011) and isolated moorings (Moffat et al. 2009; Martinson and McKee 2012) suggest the circulation is primarily barotropic with cyclonic flow over cross-cutting canyons and anticyclonic flow over shoals. In fact, drifter observations imply some imprint of these bathymetric features near the surface (Beardsley et al. 2004). Cross-cutting canyons also serve as conduits for UCDW to penetrate the shelf and be steered shoreward (Klinck 1998; Smith et al. 1999; Klinck et al. 2004). For example, the time-mean mooring currents in figure 3.1b indicate along-isobath flow and onflow along the downstream wall of the northeastward extension of Marguerite Trough. Regarding the time-varying circulation, UCDW has been shown to flow along isobaths in the form of mesoscale eddies along the downstream wall of Marguerite Trough and its northward extension (Couto et al. 2017; McKee et al. 2019) with temporal frequency of about 4 per month (Moffat et al. 2009; Martinson and McKee 2012). In general, either eddies or the mean flow may interact with a canyon to yield shelf-slope exchange (St-Laurent et al. 2013), however heat transport through Marguerite Trough is thought to be due primarily to the mean flow (Graham et al. 2016). Hence it is plausible to expect the speed of the long-shore flow to dictate any shelf-slope exchange and any trough-induced circulation on the WAP.

Numerical models point to the importance of the long-shore wind stress in accelerating the long-shore flow (Dinniman et al. 2011, 2012) and in driving shelf-slope exchange in Marguerite Trough canyon (Graham et al. 2016). As those studies used a regional model, they only considered the effects of local winds. However, the circumpolar waveguide of the Antarctic continent and the proximity of the ACC southern boundary invite the possibility for remote wind and sea surface height variability with low wavenumber to influence the long-shore flow,

particularly since circulation is thought to be barotropic. Coastal sea surface height is known to covary coherently around the continent on intraseasonal time scales (Aoki 2002) and to covary with ACC transport as measured in Drake Passage (Hughes et al. 2003). At shorter periods, finite-wavenumber variability propagates as coastal trapped waves (Kusahara and Ohshima 2009).

Observations thus far have often needed to make a trade-off between spatial and temporal coverage and no observational study has yet been able to reveal how the large-scale circulation of the WAP mid-shelf and shelf-break varies on intraseasonal time scales and how such circulation is related to the wind stress. In this study we present the first simultaneous measurements of intraseasonal subsurface current variability on the WAP shelf and shelf-break as sampled by an array of moored current meters that spans a spatial extent of ~427 km along shore and ~72 km across. These data were collected over several years (2008-2017) as part of the Palmer Long Term Ecological Research (Pal LTER) project (Smith et al. 1995). Our goal is to use these data to understand the major features of the circulation and shelf-slope exchange on intraseasonal time scales. Here we identify a spatially coherent circulation pattern via empirical orthogonal function (EOF) analysis and study the spatial variability of kinetic energy spectra to complement our understanding of the pattern. Time variability of the long-shore flow is compared to reanalysis wind stress. Finally, we discuss the circulation pattern in the context of flow-topography interaction and its implications for heat transport.

3.2) Data

3.2.1) Mooring data

3.2.1.1) Overview

The principal data set used in this study is a set of year-long moored current meter records collected on the WAP shelf and shelf-break. Oceanographic moorings containing thermistor arrays and one or more current meters have been deployed on the WAP shelf each year since 2007 as part of the Pal LTER project (Martinson and McKee 2012). Between one and four moorings are deployed on each annual January Pal LTER cruise (usually at the end) and recovered on the following January's cruise (usually at the beginning), making each record about 350 days in length. It is important to note that the array is not static and that different locations are occupied in different years. The most frequently occupied sites (300.100, 300.160, and 400.100; see figure 3.1 caption for grid convention) were originally chosen because CTD sampling revealed a large fraction of oceanic UCDW was consistently present at those sites (Martinson et al. 2008). Of those, 300.100, which is located above the downstream wall of Marguerite Trough, is occupied most regularly and has been indicated as a site of shelf-slope exchange (Martinson and McKee 2012). As it became increasingly apparent that canyons play an important role in steering the circulation, sites 347.088 and 500.120 (on the western flanks of two other submarine depressions) were sampled in 2014. Site 200.140 is located on the shelf-break in about 420 m of water and was deployed to sample the shelf-break jet (SBJ) upstream of where it impinges on Marguerite Trough canyon. Site 073.108 was added in 2017 to sample the SBJ even farther upstream. Since our focus in this study is on circulation in the mid-shelf, three coastal records near Palmer Deep and one coastal record at 460.046 are not included, and since

our focus is on spatially coherent circulation patterns, nor are years with only one non-coastal mooring (2007 and 2015-2016, with the exception of 2013).

Current meters are placed at discrete depths, nominally one at the temperature maximum (~250 dbar) and one at the temperature minimum (~80 dbar), though for individual process studies (e.g., 200.140 year 2013) or due to instrument failure there may be more or fewer in the vertical. We primarily use JFE Advantech Alec Infinity EM current meters though a few InterOcean S4 current meters were used in the early years. An overview of data coverage is given in table 3.1, the mooring locations and time-mean currents are shown in figure 3.1b, and velocity spectra of each record are shown in figures 3.2 and 3.3 (and are discussed in section 3.3.1).

3.2.1.2) Sampling and data processing

All current meters sample at least once per hour which is sufficient to avoid aliasing any major tidal constituent. Records that sampled faster than once per hour are subsampled at that interval. In addition, the record length of ~350 days satisfies the Rayleigh criterion for all major constituents, allowing independent resolution within each tidal group. Each Alec instrument was programmed to employ burst sampling, measuring and averaging either 25 (300.160 year 2010), 64 (all other sensors prior to 2012), or 81 (all sensors after 2012) samples at each increment. By invoking the Central Limit Theorem, this means nominal instrument uncertainties of ± 1 cm s^{-1} for speed and ± 2º for angle are reduced by a factor of 5, 8, or 9 at each time step. The few S4 sensors did not employ burst sampling and have an accuracy of ± 1 cm s^{-1}. Potential contamination of the current meter data by over-tilting during strong current events is considered in Appendix B.

Tidal variability in the current meter data was assessed with a harmonic analysis (Pawlowicz et al. 2002) and comparison with a barotropic tide model (Padman et al. 2002). Removal of short-period (diurnal and semidiurnal) tides by harmonic analysis is straightforward, simply removing any constituents that pass a signal to noise ratio (SNR) threshold of 1, where SNR is quantified as the square of the ratio of the fitted major axis amplitude to its uncertainty. The harmonic analysis and the tide model agree well on short-period tidal amplitudes. However, as our focus is on intraseasonal variability, it is mainly the long-period tides that we are concerned with removing. These potentially include the fortnightly (Mf, Msf), monthly (Mm, Msm), and longer (Ssa) harmonics. The tide model includes only (Mf, Mm), which are also the only two long constituents identified in coastal Antarctic tide gauges by Aoki (2002). Analysis of a multiyear time series at nearby Faraday tide gauge (described below) reveals that Ssa, Mm, and Mf have SNR greater than 1 on the WAP and Msm and Msf do not. Weather-band and mesoscale oceanic variability in the current meter series is very large at the fortnightly and monthly periods, yielding fits at Ssa, Mm, and Mf with much larger amplitude than predicted by the tide model and with low SNR. For example, of the 6 current meter records at 200.140 in 2013, none have a SNR > 1 for any of Ssa, Mm, or Mf, and of all current meter records at 300.100, between 0 and 2 records (out of 11) exhibit a SNR > 1 for any of those tides.

Thus, while we can conclude that Ssa, Mm, and Mf are likely present in our current meter time series, because we are interested in non-tidal variance at long periods, some of which may have similar intrinsic period (e.g., 15 day resonant period for wavenumber 1 first mode coastal trapped waves; Kusahara and Ohshima 2009), and because the amplitudes predicted by the tide model and the multiyear tide gauge analysis are so low, we determine that any attempt to remove the long-period tides by harmonic analysis with an uncertain fit would likely do more harm than

good. Therefore we decide to not make any attempt to remove long-period tides from the current meter records. All analyses in this chapter (and chapter 4) were repeated with forced removal of Ssa, Mm, and Mf and there is no systematic or significant difference in results.

After subsampling once per hour and de-tiding each record, the residual is then low-pass filtered to remove variability with periods shorter than 2 days. We use an ideal filter which zeroes out amplitude of the Fourier transformed signal below the cutoff frequency before inverse transforming back to the time domain. Unless otherwise specified, all time series in this study are filtered in such a manner, with the exception of 'intraseasonal variability' which is band-pass filtered with an ideal filter with passband 3-100 days.

3.2.1.3) Conventions

As mentioned earlier, locations are referred to by their Pal LTER grid coordinate, as described in figure 3.1. We define the long-shore dimension to be x, with velocity component u that increases to the northeast (increasing grid line) and we define the cross-shore dimension to be y, with velocity component v that increases towards the open ocean (increasing grid station). Current meters referred to as 'deep' are deeper than 225 dbar (containing the T_{max}), current meters referred to as 'pycnocline depth' are between 100 and 225 dbar, and current meters referred to as 'shallow' are shallower than 100 dbar (containing the T_{min}).

3.2.2) Other data sources

3.2.2.1) Reanalysis data

We use surface pressure, mean sea level pressure (SLP), and surface stress (wind stress) from the ECMWF ERA-Interim reanalysis project. The data are reported on a 0.75 x 0.75 degree grid at a temporal interval of 12 hours. Unlike other major reanalysis products, ERA-Interim uses a 4D-Var assimilation scheme which should incorporate observations in a more

dynamically consistent manner. Additionally, when compared explicitly to observations in the Pacific sector of the coastal Southern Ocean, ERA-Interim is found to yield a lower variance about the mean bias than other products, suggesting it is relatively more accurate at simulating specific weather events (Bracegirdle 2013). Note that the surface stress is technically a forecast variable, representing the downward turbulent stress at the surface accumulated over a 12 hour forecast. As such, we divide the surface stress by the time step and assign each value a new time stamp corresponding to the middle of the 12 hour forecast window.

3.2.2.2) Faraday tide gauge data

We acquire hourly, Research Quality tide gauge data from Faraday station from the University of Hawaii Sea Level Center to compare against the current meter data. Short-period tidal constituents are removed via harmonic analysis (Pawlowicz et al. 2002). To correct for the inverse barometer effect, the reanalysis surface pressure data are spatially interpolated onto the tide gauge site (with a bicubic spline) at each reanalysis time step and then interpolated in time (with a linear interpolant) onto the hourly tide gauge grid. Then, the interpolated surface pressure data are multiplied by the correction factor (1 cm sea level) / (1 mbar atmospheric pressure) and combined with the tide gauge signal. To enhance SNR for the long-period tides, we analyze the multiyear, inverse-barometer corrected record which reduces noise by distributing the non-tidal variance among more Fourier harmonics while preserving the line spectra of the tidal constituents. We find Ssa, Mm, and Mf to exhibit SNR > 1 and they are removed by harmonic analysis (Pawlowicz et al. 2002). Finally, small gaps are filled with linear interpolation and a low-pass filter with cutoff period of 2 days is applied.

3.2.2.3) Shipboard data

Shipboard data from the Pal LTER program are used to define the climatological physical environment in the vicinity of the current meter sites. CTD profiles are collected as part of the standard sampling on the annual cruises to the WAP each austral Summer since 1993, currently with a dual-pumped Sea-Bird 911+ CTD system (see details in Martinson et al. 2008). The standard grid locations are spaced every 20 km in the cross-shore dimension and every 100 km in the long-shore dimension. The entire grid was occupied until 2008 whereas now only a subset of stations is occupied (nominally three per grid line). The entire database is used to prepare the climatological map of geopotential heights in figure 3.1 and the section of geostrophic currents in figure 3.12. Data from the June 1999 cruise, which densely sampled across Marguerite Trough, are presented in figure 3.11. Cast locations for the two hydrographic sections presented in figures 3.11 and 3.12 are shown in figure 3.1c, alongside the relevant bathymetric features.

Processed, high-resolution (5 minute in time, 8 m in vertical) velocity profiles from the ARSV *L. M. Gould*'s hull-mounted RDI 150 kHz narrowband instrument were obtained from the Joint Archive for Shipboard ADCP (SADCP). The 150 kHz instrument provides velocity profiles good to about 300 m (depending on weather and sea state) when the vessel is on station. These data are used to quantify the mean circulation along the same CTD sections presented in figures 3.11 and 3.12. The data are not de-tided.

3.3) Results

3.3.1) Velocity spectra

The mooring locations and mean currents are shown in figure 3.1b while component and rotary velocity spectra are shown in figures 3.2 and 3.3, respectively. In order to give an

overview of the velocity variance, we describe the spectra here. Spectra are calculated using the multitaper method (Thomson 1982) with 7 DPSS functions for 14 degrees of freedom. These spectra compared favorably to spectra calculated by partitioning the time series into 7 non-overlapping segments (again yielding 14 degrees of freedom) and averaging the spectra of each segment, however the multitaper method does not suffer from decreased frequency resolution.

The long-shore power is substantially greater than the cross-shore power at 200.140, 300.100, and 347.088. At the former two sites, the long-shore power is greater at all frequencies (as much as 10 times the cross-shore power below 0.1 cpd) whereas at 347.088 this is only true for frequencies less than 0.2 cpd. The cross-shore power is similar at all sites, other than at 400.100, which has more cross-shore power at high frequencies compared to all other sites. Spectra are generally red to some degree, at least up to ~0.2-0.25 cpd, although 300.100 maintains a steep slope over all frequencies and 400.100 is unusually flat. Many sites have more power at depth for low frequencies (mainly so in the long-shore component) and either comparable or less power at depth for high frequencies. The slope stations (200.140 and 300.160) have an interesting divergence in long-shore versus cross-shore power at ~0.28 cpd. The slope stations also demonstrate an increase in power in both components at ~0.35 cpd, more so in the cross-shore component.

In regards to the rotary spectra, most records are approximately equipartitioned between positive (counterclockwise) and negative (clockwise) frequencies up until 0.15-0.25 cpd. Beyond that, 300.100, 347.088, and 500.120 have more power in the clockwise spectrum (they are in canyons), 400.100 and 073.108 have much more power in the counterclockwise spectrum (the former is on a bank), 300.160 is still approximately equipartitioned, and 200.140 has slightly more counterclockwise power. The colors of the spectra are similar to those of the component

spectra: generally red, with 300.100 being steeper and 400.100 being much flatter. Some of the spectra indicate a peak near ~0.12 cpd at either the positive (200.140) or negative (300.100, 300.160, 500.120) frequencies which may manifest at all depths or be primarily deep (200.140) or shallow (500.120). Some of the spectra also indicate a divergence in counterclockwise versus clockwise power at ~0.28 or ~0.35 cpd (300.100, 300.160, 347.088, 500.120) which may be related to the feature identified in the component spectra above. Frequencies of ~0.12 cpd, ~0.28 cpd, and ~0.46 cpd may correspond to the topographically trapped modes associated with the East Pacific Rise, the Mid-Atlantic Ridge, and the Kerguelen Plateau, respectively, that can be resonantly excited by the wind. Excitation of these modes may yield signal propagation around the Antarctic coastline as Kelvin waves (see discussion in Weijer and Gille 2005).

While both 200.140 and 300.160 are situated on the shelf-break at similar bottom depth, the spectrum at 200.140 resembles those at 300.100 and 347.088 more so than it does that at 300.160. Particularly so, all but 300.160 demonstrate a significant elevation in long-shore variance compared to cross-shore variance, primarily at frequencies lower than about 0.25 cpd. The similarity of the spectra suggests the possibility that the slope flow that passes 200.140 diverts onto the shelf prior to encountering 300.160 (it would be unusual for a slope current to not be dominated by long-shore variance, particularly at low frequencies). It would be natural, then, to ask why the spectrum at 400.100 is so different from those immediately upstream if an upwelled slope current is headed in that direction. To address this, recall that, while 400.100 is close to a cross-shelf depression, it is actually on a bank downstream of Marguerite Trough with bottom depth ~337 m, substantially shallower than the other mid-shelf sites. As the strong long-shore flows near the slope impinge on Marguerite Trough and then the shallow bank, after adjustment by radiation of topographic waves an anticyclonic (counterclockwise in southern

hemisphere) vortex forms over the bank due to compression of the water column (Fennel and Schmidt 1991; St-Laurent et al. 2013). As to why the divergence of clockwise versus counterclockwise power is greatest at high frequencies, we note that at periods longer than the spindown time the flow would be able to adjust to any perturbation before one cycle. The spindown time for barotropic motions (Pedlosky 1987) is $\tau = H/\sqrt{2A|f|}$, which at 65.9 ºS in 337 m depth, and assuming A = 5 x 10^{-4} m^2 s^{-1} is about 10.7 days, which is close to where the two spectra appear to diverge.

3.3.2) Spatial pattern of circulation

In order to identify a spatially coherent pattern in the WAP circulation we use empirical orthogonal function (EOF) analysis to decompose all current meter records in a given year into orthogonal patterns that maximize temporal covariance. For each year we construct the augmented data matrix **X** whose rows are all of the long-shore velocity time series followed by all of the cross-shore velocity time series, allowing us to diagonalize the covariance matrix $\mathbf{C} = \mathbf{X}\mathbf{X}^T$ that includes covariability across site, depth, and velocity component. To avoid contamination by the seasonal cycle, in this analysis we band-pass filter all signals into the intraseasonal band before decomposing.

Maps of the first EOF weights for every year of analysis are shown in figure 3.4. In each year with multiple sites, over half (49-81%) of the total variance can be explained by the first pattern. To the extent it is possible to determine (given different sampling each year), the pattern is qualitatively the same each year. This consistency is a testament to it truly being a spatially coherent pattern. More specifically, the orientation and magnitude of the weight vectors at each site are similar in each year, even if the decomposition involved covariances with different sets of locations.

In the positive state, the pattern consists of an upgrid flow along the shelf edge (073.108, 200.140), an anticyclonic cell in the downstream vicinity of Marguerite Trough (300.100, 347.088, 400.100), and an upgrid flow along the western wall of a second canyon downstream of Marguerite Trough (500.120). Importantly, the one location that consistently does not covary with the others is 300.160, which is located on the downstream wall of Marguerite Trough, but seaward of 300.100. As implied by the spectral analysis in 3.3.1, this argues for Marguerite Trough playing a role in the emergence of the pattern and essentially diverting the SBJ onto the shelf once it passes the 200 grid line, through the anticyclonic pathway, and bypassing site 300.160 on the shelf-break. Flow interaction with a canyon will be discussed in section 3.4.1.

Total EOF1 weights $\mathbf{E}_{\text{total}} = \sqrt{\mathbf{E}_{\text{long}}^2 + \mathbf{E}_{\text{cross}}^2}$ are shown as histograms in figure 3.5. The vectors (figure 3.4) and the total EOF1 weights (figure 3.5) suggest that the pattern is quasi-barotropic, perhaps somewhat bottom-intensified (e.g., see weights in 2014). Consistent with this, the vectors at each site are aligned along-isobath. There is also little veering with depth. The weights for 300.100 are largest each year, but that is partially compensating for the larger total variance at 300.100 as compared to 400.100. To get a better sense of the spatial coherency than can be provided by the EOF weights alone, we correlate the time variability of the pattern with each velocity component (table 3.2). Correlations between the pattern and each current meter record are all strong along the component(s) most aligned with major variability, except at site 300.160, where correlations are always low for both components ($|r| < 0.23$). Significance of correlation coefficients is evaluated using a bootstrapping approach (see Appendix C). For sites other than 300.160, in the majority of cases no simulated time series had a correlation coefficient greater than that observed. Note that the correlations tend to decrease with increasing distance

from Marguerite Trough, suggesting that the whole pattern may be forced by flow interaction with that bathymetric feature and communicated upgrid by continuity.

3.3.3) Baroclinicity and veering

While the EOF analysis suggests that the dominant pattern isolates covariance that is quasi-barotropic, we would like to know to what extent the entire circulation at each site is vertically coherent. To gauge this, for every mooring that had at least two current meters spanning the permanent pycnocline (approximately the depths of the T_{max} and the T_{min}), we computed the complex coherency and phase lag between the shallowest and deepest velocity signals (figure 3.6). Each velocity series is partitioned into 7 non-overlapping segments and the squared coherency is then calculated in the standard manner.

At each site, where the squared coherency is significant at a 95% level the cross-phase spectrum indicates little veering with depth with values generally close to 0^o and almost always less than $|45^o|$ (figure 3.6, right panels). In general, motions are significantly coherent across the pycnocline for periods longer than about 3 days, with the coherency increasing for longer periods. Of all sites, motions at 300.100 are most clearly barotropic. Based on the results of the EOF analysis, if the current at 300.100 is a diversion of the SBJ onto the shelf we might expect the vertical structure at 200.140 to have a similar frequency relationship. The coherence spectrum at 200.140 is similar to that at 300.100 although with lower values. This might be because the shallowest current meter there is nominally at 44 dbar which is shallow enough to feel the influence of the seasonal mixed layer in summer. It may also be because the Burger number is larger over the slope than on the shelf. At both sites, for periods longer than about 3 days, the counterclockwise coherency drops off faster than the clockwise coherency. The coherency spectrum at 400.100 is substantially different from the other sites. There,

counterclockwise motions are generally coherent across all frequencies while clockwise motions are generally incoherent. The polarization of the current at 400.100 was considered in section 3.3.1.

3.3.4) Relation to the wind

Regional models of the WAP point to the importance of the local long-shore wind stress in driving shelf-slope exchange and onshore flux of CDW (Dinniman et al. 2011, 2012) with a potential role for the wind stress curl as well (Graham et al. 2016). As a first test of the influence of long-shore wind stress in forcing our circulation pattern we construct composites of the velocity records under positive long-shore wind stress (northeastward) and negative long-shore wind stress (southwestward). At this stage we make no assumptions about the spatial scale of the wind and only assume that the influence occurs via barotropic dynamics: Northeastward (southwestward) wind stress induces an Ekman transport away from (towards) the coast which induces a coastal sea surface height drop (rise) and a stronger (weaker) northeastward flow along the slope and shelf. We isolate the reanalysis surface stress signal nearest to mooring site 300.100, extract the component parallel to the coast, and identify all time steps where it is greater than 1 standard deviation above the 2007-2016 mean and less than 1 standard deviation below that mean. After determining an appropriate lag time (the lag that yields maximum correlation between 300.100 depth-average U and the long-shore wind stress series; 20 hours), the ocean velocity vectors are averaged at corresponding time steps to create positive and negative composites, respectively. The wind and velocity series are band-pass filtered in the intraseasonal band beforehand.

The results are shown in figure 3.7 and mirror the first EOF pattern: positive long-shore winds yield a strong shelf-break flow and strong anticyclonic cell while negative long-shore

winds the opposite. Again the pattern is approximately depth-invariant and again 300.160 does not respond in a consistent manner (and the composite anomalies there are relatively smaller). In addition to maps, composite profiles are shown in figure 3.8, but they are constructed by averaging the total velocity profiles instead of the band-pass filtered profiles. Variance at 200.140 and 300.100 is stronger in the long-shore component and the total shear between the shallowest and deepest current meter at each site is less than the barotropic offset between the two wind states. Variance at 400.100 is stronger in the cross-shore component and the barotropic offset between the two wind states is less than, but of the same order of magnitude as, the shear.

The agreement between the wind-state composites and the first EOF suggests that the dominant circulation variability on the WAP is wind-driven. Further, the spatial coherence suggests that the scale of the wind forcing is at least as large as the array length (427 km). To evaluate what atmospheric forcing is relevant for the WAP circulation we compute heterogeneous correlation maps between the depth-averaged long-shore current at 300.100 and the reanalysis SLP, zonal surface stress, and meridional surface stress at zero lag (figure 3.9). The spatial pattern of the correlations with the SLP is approximately like the spatial pattern of the Southern Annular Mode (SAM; Thompson and Wallace 2000) with negative values near the Antarctic continent and positive values towards the mid-latitudes, which, broadly speaking, means that more southern westerlies and/or stronger westerlies lead to a stronger WAP circulation. Correlations with SLP are statistically significant at a 95% level around the entire continent, particularly near the coast and the continent itself. However, an important deviation from the SAM-like pattern is the center of alternating positive and negative correlation on opposite sides of the Antarctic peninsula. The western center of correlation, which is the largest

positive correlation in the domain, is distinct from the non-annular component of the SAM that projects onto the Amundsen Sea Low (Lefebvre et al. 2004) and appears to be spatially coincident with the ridge associated with the Pacific-South America wave train that operates on intraseasonal time scales (Mo and Higgins 1998). The spatial pattern of the correlations with the wind stress follows that of the correlations with the SLP under geostrophic balance: The strongest correlations are along-slope over the WAP itself (r = +0.60, 63.50 ^{o}S, 63.00 ^{o}W) and there (as around most of the continent) they follow a sign convention consistent with barotropic Ekman dynamics at the Antarctic coast. Note that the location of maximum correlation with the long-shore stress is actually several hundred kilometers northeast of the mooring site as opposed to directly over it (grey triangle versus square in figure 3.9).

3.4) Discussion

3.4.1) Role of Marguerite Trough

We identified a pattern in our current meter records on the WAP shelf that explains over 49% of the total variance. The pattern suggests that an acceleration of the along-slope flow upstream of and over Marguerite Trough is accompanied by the strengthening of an anticyclonic circulation pattern downstream of Marguerite Trough canyon and of the flow on the western flank of another canyon ~200 km downstream. The pattern does not covary with the current on the shelf-break immediately downstream of Marguerite Trough canyon, suggesting that the pattern emerges as an upwelling of the shelf-break current upon interacting with the canyon. The velocity spectrum from a current meter on a bank downstream of the canyon shows enhanced anticyclonic rotation consistent with vortex compression of an incident flow. Composites of the velocity records under positive and negative long-shore wind states suggest that on intraseasonal

time scales the pattern is strongest under positive winds (which accelerate the long-shore flow via barotropic dynamics) and is weaker or even reversed under negative winds. An idealized schematic of the circulation is given in figure 3.10. As suggested in that figure, the upwelling current effectively 'pinches' the shelf-scale cyclone (formed by the SBJ and the CC) by inducing onflow of oceanic water near Marguerite Trough and outflow on the 400 line. We hereby refer to the pattern as the 'pinch pattern'.

Theories for flow interaction with a canyon suggest that when a right-bounded flow in the southern hemisphere (as is the SBJ against the WAP) impinges upon a submarine canyon, cyclonic vorticity is induced into the water flowing over the canyon, steering flow up-canyon along the downstream wall (Allen et al. 2001; Kämpf 2006, 2007; Allen and Hickey 2010). The initial interaction (inertial overshoot of the impinging slope flow) sets up a cross-canyon pressure gradient which is balanced by the Coriolis and inertial terms (the latter being smaller but significant), yielding a nearly geostrophic flow up the canyon (Kämpf 2006). Because it is the cross-canyon pressure gradient that initiates the upwelling and not an along-canyon pressure gradient, the upwelling flux is not very sensitive to the canyon width (Kämpf 2007) and wide canyons (canyon width is wider than the Rossby radius) such as Marguerite Trough are able to support upwelling. The Canyon Rossby number (taking into account curvature of isobaths) reflects the notion that canyons decrease the relevant length scale and that metric may be large even if the Rossby number is not, allowing up-canyon flow to cross isobaths and upwell onto the shelf-proper at a location shoreward of the impinging flow. Once on the shelf, vortex compression will steer the flow again seaward in the downstream direction, generating an anticyclonic counterpart to the canyon cyclone.

Stratification tends to diminish the response in the upper ocean which is consistent with our observed pattern being somewhat bottom-intensified (figure 3.5). The upwelling-favorable current orientation must hold down to shelf-break depth which it certainly does along the WAP under positive long-shore winds since the barotropic variance in the current is strong and larger than the mean shear (figure 3.8). Additionally, the incident flow speed is important for the process. When the flow is slow (or reversed), the cyclonic vortex generated at the canyon mouth remains in place and the SBJ passes by largely unaffected (Waterhouse et al. 2009). However, if the flow is sufficiently strong, the cyclonic vortex is swept shoreward to occupy the entire canyon and cross-isobath flow out of the canyon is enhanced by nonlinear effects. St-Laurent et al. (2013) show that the proximity (or width) of the incident SBJ has a strong bearing on the flow interaction with topography. If the jet is wide and straddles the slope, the mean flow itself interacts with the submarine canyon and yields a cyclone over the canyon and an anticyclone on the shelf-proper that is advected within the mean flow. On the other hand, if the jet is narrow (or held offshore), eddy-topography interaction ensues. The latter point might partially explain why Marguerite Trough is such an important site for shelf-slope exchange. Regional modeling suggests that the SBJ near Marguerite Trough is wider than it is farther south (Graham et al. 2016) and it clearly straddles the slope since it is sampled by our mooring at 200.140 which is in ~420 m depth and about 10 km inshore of the shelf-break. The SBJ farther south is either held over the slope or is nonexistent as velocity spectra at 073.108 are different from those at 200.140 (figures 3.2-3.3) and fields of geopotential height have little gradient there (figure 3.1b).

The dynamics of the flow-topography interaction at Marguerite Trough are not well understood and should be investigated further. Scaling laws to predict upwelling flux depend on canyon geometry, buoyancy frequency N, perhaps Coriolis frequency f, and incident flow speed

with sometimes conflicting results. For example, upwelling flux may depend on incident flow speed squared (Kämpf 2007), to the 8/3 power (Mirshak and Allen 2005), or cubed (Allen and Hickey 2010). Owing to nonlinearity it is also possible that an oscillatory flow (e.g. induced by coastal trapped waves) may induce a net transport onto the shelf. In 2017 we sampled the shelf-break flow at 073.108 (though probably not the SBJ-proper) and the inner shelf at 300.100 simultaneously. The along-isobath currents at each site in the intraseasonal band are well correlated with an exponent of 1 ($r = 0.68$, $p \approx 0$).

In contrast to the theories on canyon-induced dynamics, a more general explanation for flow-topography interaction was considered by Dinniman and Klinck (2004) who found a significant spatial correlation between isobath curvature (defined as $\frac{\partial}{\partial \chi}\left(\frac{\nabla H}{|\nabla H|}\right)$ for along-shore element χ) and the time-averaged cross-shore volume transport with shoreward flux strongest ~10 km downstream of curvature. In analyzing the time-mean momentum budget, the nonlinear momentum advection term was found to have strong bearing on the cross-shelf-break transport. Thus, in their model, much of the cross-isobath advection is just due to curvature of isobaths. There is a large seaward bend in the continental slope between the 000 and 200 grid lines which would act to bring the SBJ onto the shelf edge (as sampled by mooring 200.140), but this alone is not enough to cause the flow to penetrate far onto the continental shelf and yield the spatially coherent pattern. Instead, to yield transport farther shoreward on the shelf, the circulation on the inner shelf must act to pull the SBJ onshore. This would require simultaneous acceleration of the long-shore flow at both the shelf-break and inner shelf downstream of the canyon, which is consistent with the pinch pattern and its scale, but not possible to diagnose without a proper momentum and vorticity budget analysis, which our data do not permit.

At this point it is useful to introduce representations of the climatological circulation in the cross-shore direction (through the 100 station, figure 3.11) and in the long-shore direction (through the 300 line, figure 3.12). These sections were prepared from the database of Pal LTER SADCP and CTD data as described in the figure captions. The general case of the pinch circulation, with onflow along the downstream wall of Marguerite Trough and outflow north of the bank at the 400 line is apparent from figure 3.11. There is also clearly cyclonic vorticity introduced over Marguerite Trough. Assuming the impinging current has no relative vorticity, the amount of barotropic stretching vorticity expected to be introduced as a current descends from an upstream shelf depth of $H_1 \sim 400$ m to a mean canyon depth of $H_2 \sim 550$ m is

$$\zeta_{\text{stretch}} = \left(\frac{H_2}{H_1} - 1 \right) f \,, \tag{3.1}$$

which is ~0.38*f*. The actual cyclonic vorticity over the canyon as implied by figure 3.11a, though, is about an order of magnitude less. The anticyclone over the downstream Bank is also well pronounced in the mean. The climatological section along the 300 line was sampled multiple times, allowing a robust estimate of the geostrophic shear for comparison with the absolute SADCP currents. There is clearly anticyclonic vorticity generated over the MT Fork which manifests in both the geostrophic shear (referenced to the seafloor) and the SADCP currents with equivalent magnitude (figures 3.12b and 3.12c). The long-shore flow over the continental slope is also well represented in the geostrophic currents, but it appears distinct from the SBJ upstream of Marguerite Trough on the 200 line as it no longer straddles the shelf (labeled 'Slope Current' instead of SBJ). Instead, the diversion of the SBJ onto the 300 line associated with the pinch pattern is apparent, and it is clearly barotropic (and/or ageostrophic) as it exists only in the SADCP data. Its depth-averaged magnitude is larger than the flow along the shelf-break (figure 3.12a).

If the long-shore flow is everywhere (on the scale of the pinch pattern) accelerated by barotropic dynamics then the flow originating on the shelf out of Marguerite Trough on the northward limb of the MT Fork (figure 3.1c) would 'pull' the SBJ shoreward at the mouth of Marguerite Trough by continuity. The SBJ there is already shoreward due to curved isobaths and momentum advection and has already gained cyclonic vorticity (figure 3.11). With the pinch pattern existing in the mean in both the mooring and SADCP data, and with some degree of nonlinearity required for the diverted SBJ to exit Marguerite Trough at the MT Fork towards its northern limb, it is useful to regard EOF1 as an enhancement or suppression of the pinch pattern. When the long-shore flow is accelerated to drive the spatially coherent pattern, the geostrophic flow around the MT Fork persists but a strongly barotropic component emerges, associated with the pinch circulation pattern and a diversion of the SBJ towards the northern limb at the MT Fork as opposed to following barotropic f/H contours towards Marguerite Bay (figure 3.12). This long-shore flow follows the bathymetry to the north, is compressed by the bank, and is funneled along the 400 line by the narrow gap between two adjacent banks (figure 3.11).

While we noted that the velocity at 400.100 is generally highly rotary, that is time dependent. Under strong long-shore flow and upwelling (positive circulation pattern) conditions, the strong flow funneled seaward along the 400 line tends to force rectilinear variations and suppress the free anticyclonic, potential vorticity conserving motions. This is illustrated through time variability of the rotary coefficient evaluated in 75% overlapping 15-day windows,

$$r(\omega,t)=\frac{P_{+}(\omega)-P_{-}(\omega)}{P_{+}(\omega)+P_{-}(\omega)}, \tag{3.2}$$

where P_+ and P_- are the counterclockwise and clockwise power spectra, respectively. The frequency-time series of the rotary coefficient can be collapsed into a single time series by averaging over the most rotary band of 2-5 days (figure 3.13),

$$r_c(t) = \frac{1}{N_\omega} \int_{\omega_1}^{\omega_2} r(\omega, t) d\omega. \tag{3.3}$$

This metric, which is +1 (-1) for purely anticyclonic (cyclonic) motions and 0 for rectilinear motions, reveals that motions at 400.100 are almost always anticyclonic to some degree but become more rectilinear when the long-shore flow at 300.100 (and hence the circulation pattern) is more positive. The two time series are weakly anti-correlated (r = -0.34, p = 0.02 in 2010; r = -0.45, $p \approx 0$ in 2011).

Thus, an interpretation of the pinch circulation is as follows. The basic state time-mean circulation mimics that of EOF1 (compare figure 3.4 to figures 3.1b, 3.11, and 3.12). When the EOF is in its negative state, the circulation relaxes, flow at 300.100 falls to f/H contours, a cyclonic circulation remains in Marguerite Trough, and flow at 400.100 falls to free potential vorticity conserving anticyclonic motions. When the EOF is in its positive state, the long-shore flow is accelerated, the SBJ is pulled shoreward (through some combination of continuity at the northern limb out of Marguerite Trough and through canyon-induced cyclonicity and momentum advection over the Trough), the mid-shelf anticyclone is enhanced, and flow at 400.100 is rectilinear and seaward.

Proper exploration of these ideas would require evaluation of momentum and vorticity budgets in a numerical model. We emphasize that the role of the wind in driving the circulation on the WAP appears to be related to modulating the incident flow speed at the shelf-break and inner shelf. This is in contrast to the role of the wind observed elsewhere in West Antarctica, for

example in the Amundsen Sea where up-trough flow was related to the long-shore wind stress in an Ekman upwelling sense (Wåhlin et al. 2013). This suggests that the close proximity of the ACC southern boundary and/or the width of the SBJ along the WAP near the trough may make the circulation there more 'ACC-like' than that on other shelves around the continent.

3.4.2) Scale of the pattern

If the pinch circulation pattern is induced by continuity of the impinging SBJ with an accelerated long-shore, inner-shelf flow, a necessary assumption is that variations in the long-shore flow are of large enough spatial extent to accelerate both flows simultaneously. The analyses conducted thus far reveal that (1) the scale is at least as large as the array length of several hundred kilometers, (2) the fluctuations are nearly barotropic, and (3) the long-shore wind stress that is significantly correlated to the fluctuations has influence both locally and remotely along the coastline. Inspection of inverse-barometer corrected subsurface pressure at nearby Faraday tide gauge (~577.012) reveals very good agreement with the barotropic long-shore current at 300.100 in the time and frequency domains (figure 3.14). The two are significantly correlated at zero lag (r = -0.75, $p \approx 0$), significantly coherent at a 95% level over most frequencies, and are approximately anti-phased in accordance with geostrophic balance. Interestingly, the correlation improves to r = -0.82 when the Faraday SSH signal leads by 18 hours, which requires a phase propagation of ~ -4.2 m s^{-1} in the coastal trapped wave direction.

Weather-band variability in Antarctic tide gauges (including Faraday) is known to be dominated by wind-driven fluctuations in coastal sea surface height in accordance with a wavenumber zero mode (Aoki 2002) and low-wavenumber coastal trapped waves (Kusahara and Ohshima 2009). Curiously, there are energetic, geostrophically balanced barotropic fluctuations with ~40 day period apparent in both time series. Variability at that period has been shown to

affect ACC transport in Drake Passage by projecting tropically forced variability onto the SAM with wavenumber zero signature (Matthews and Meredith 2004). Variability at that period is also associated with the PSA wave train (Iijima et al. 2009) that may carry the teleconnection to high latitudes. The latter should have a pronounced influence in the southeast Pacific and the high correlation with SLP in the vicinity of the WAP could reflect wind-driven barotropic shelf waves with a finite damping scale. An analysis of wind-driven velocity fluctuations and coastal trapped wave dynamics is considered in detail in chapter 4 but at this point a plausible connection to large-scale, wind-forced sea surface height variability is clear.

3.4.3) Heat transport

While the focus of this paper is on the circulation, we briefly comment on the heat transport since its variability sheds some light on the former. Owing to the density of the thermistor arrays in the vertical, heat content from the winter mixed layer depth (WMLD) down to 350 dbar can be calculated as

$$Q(t) = \rho_0 c_p \int_{350\ \mathrm{db}}^{\mathrm{WMLD}} \left(T(z,t) - T_{\mathrm{freeze}}\right) dz \tag{3.4}$$

with an average bias of under 0.1% (Martinson and McKee 2012). Thermistor data are interpolated onto 1-dbar profiles as described in Martinson and McKee (2012) before integrating. From those interpolated profiles we also obtain the temperature maximum $T_{\max}$. These are used to define heat transports in the long-shore (similar in the cross-shore) dimension as $UQ = \left(U_0 + u\right)\left(Q_0 + q\right)$ and $T_{\max}$-weighted velocities $UT = \left(U_0 + u\right)\left(T_0 + t\right)$, where subscript 0 indicates the time-mean and lower case letters represent fluctuations about that mean. Mean total transports are defined as the time mean of the transports over a mooring-year (e.g. $\overline{UQ} = U_0 Q_0 + \overline{uq}$). Figure 3.15 shows time series of Q, $T_{\max}$, U, V, and their associated transports

for one year at 300.100 and table 3.3 shows the time-mean transports for all years at that site. The heat content and the T_{max} tend to be well correlated (Martinson and McKee 2012), suggesting the subpycnocline heat content is driven by the CDW-level T_{max}, although the former contains additional vertically driven signals, including sea ice production, the WMLD (which sets integration depth), pycnocline strength, and air-sea fluxes.

Overall, mean total transports $\overline{UQ}$ and $\overline{VQ}$ and mean total temperature-weighted velocities $\overline{UT}$ and $\overline{VT}$ are large and shoreward in a manner consistent with the circulation pattern (shoreward and out of Marguerite Trough), however closer inspection reveals that this quantity is driven almost entirely by the mean terms. The mean term is large because the circulation pattern exists in the mean. The time-mean eddy term, on the other hand, is < 2% of the total mean magnitude and is always offshore (or near zero) for $\overline{ut}$ but of varying sign for $\overline{uq}$ (table 3.3). Hence, in a surprising result, velocity fluctuations are generally uncorrelated to temperature (and vertically-integrated heat content) fluctuations. This is also true in a spectral sense: evaluating $\overline{U(\omega)Q(\omega)}$ or $\overline{U(\omega)T(\omega)}$ via a coherency analysis reveals no frequencies significant at any reasonable α level. As the fluctuations are intermittent, some additional detail is gained via a cross-wavelet coherency analysis (Grinsted et al. 2004) of $U(s)T(s)$ for wavelet scale s, shown for example for the same year in figure 3.16. There are fluctuations with periods 2-16 days that are variously in and out of phase, but these are intermittent and the squared wavelet coherency averaged over the entire year is less than 50%. On the other hand, at scales s of ~40-60 days, there is generally significant coherency for the months May-July that shows up in $U(s)T(s)$ (but less consistently in $U(s)Q(s)$), is generally anti-phased, and is only prominent in certain years.

In general, though, fluctuations in the two variables are incoherent. As discussed by Martinson and McKee (2012), the Q series is dominated by sharp, episodic warming events also seen in the T_{max} record that are consistent with eddies with weak azimuthal velocity signal. Slightly farther south, Moffat et al. (2009) found similar eddy-like signatures with weak rotation. The importance of mesoscale eddies in dominating the thermal variance on the WAP has been corroborated by recent glider surveys (Couto et al. 2017; McKee et al. 2019), however the studies cited thus far point to a weak or nonapparent velocity signature. All of this is consistent with the findings of Graham et al. (2016) who ran a model of the WAP under 1.5 km (eddy resolving) and 4 km (non-eddy resolving) resolution and found that the upstream temperature and onshore heat transport were significantly correlated only when eddies were not resolved. That being said, the large velocity variance associated with intraseasonal fluctuations can yield a substantial heat transport at any given moment when operating on the total heat content, as indicated in figure 3.15. The transport fluctuations UQ and VQ (and UT and VT) are significantly correlated with U and V, respectively, and not with Q (or T). This is also consistent with Graham et al. (2016) who identified the incident SBJ flow speed as being the major determinant of onshore heat transport in the vicinity of Marguerite Trough. Thus, mesoscale eddies may dominate the thermal variance while intraseasonal velocity fluctuations dominate the velocity variance and heat transport.

It is worth noting that the pinch pattern is in close proximity to the location of strong wintertime atmospheric warming identified by Turner et al. (2013), downstream of the major onflow at Marguerite Trough. Those authors identified a region on the WAP shelf near Faraday station that demonstrated a strong delayed sea ice advance and a strong wintertime warming over 1979-2007 associated primarily with a loss of very cold days (days with surface air temperature

< -15 ^{o}C). While the intraseasonal variance is incoherent, the mean heat transports at the Marguerite Trough Fork are shoreward and upgrid, towards the Faraday area. As observed mixed layer warming (Meredith and King 2005) is likely not enough to explain the entire trend in delayed sea ice advance in the WAP area (Stammerjohn et al. 2012), an additional deep ocean heat source may be necessary to precondition the upper ocean and that heat may be sourced by the pinch circulation pattern.

3.5) Conclusions

We present the first observational view of intraseasonal variability in the circulation on the WAP mid-shelf as measured by an array of current meters that spans the two layers of the water column in the vertical, ~427 km in the long-shore dimension, and samples continuously for up to a year in length. Through EOF analysis of those records we identify a pattern in the circulation variance that explains over 49% of total variance and that remains the same across years regardless of which current meters were sampling. The pattern is related to the long-shore wind stress in accordance with barotropic dynamics and is qualitatively consistent with flow-topography interaction near Marguerite Trough for the following reasons: (1) Under positive long-shore wind stress, the SBJ upstream of Marguerite Trough is accelerated and emerges on the shelf shoreward of the shelf-break after encountering the canyon, bypassing another mooring along the slope downstream of the canyon, and continuing along an anticyclonic pathway before returning seaward; (2) The pattern is quasi-barotropic, but somewhat bottom-intensified; (3) Velocity spectra on a bank downstream of the canyon are anticyclonically polarized, indicating vortex compression downstream of the canyon; (4) Correlation coefficients between the circulation EOF's principal component and individual velocity records decrease with increasing

distance from the canyon. The circulation pattern essentially enhances or shuts down the mean flow pattern, with momentum advection carrying flow out of Marguerite Trough towards its northward extension at the MT Fork and suppressing potential vorticity conserving anticyclonic rotation over a downstream bank when the pattern is in its positive state.

With the prevailing circulation on the WAP shelf being cyclonic, comprised of the northward SBJ and the broad southward CC, the circulation pattern identified here effectively 'pinches' the WAP mid-shelf into a northern and a southern half. Palmer Deep canyon to the north and Marguerite Bay to the south each host highly productive seasonal blooms. It would be interesting to see if the strength of blooms at each site and/or continuity of tracer variance along the shelf vary in response to the magnitude of the circulation pattern.

The pattern is driven by the speed of the flow along the shelf-break and over Marguerite Trough and the current there is related to the wind. Heterogeneous correlation maps suggest that the wind influence is SAM-like but also point to major influence from the PSA wave train in the Southeast Pacific. The relation to the long-shore wind stress in accordance with barotropic dynamics and the spatially coherent nature of the pattern over hundreds of kilometers points to large-scale variability in the atmosphere. In a companion study (chapter 4) we investigate in detail the dynamics by which the long-shore wind stress drives low-wavenumber variability in the long-shore flow via a wavenumber zero mode and barotropic shelf waves that thus drive the WAP circulation variance presented here.

Tables

Table 3.1: List of current meters used in this study along with their nominal pressures in dbar.

'S' indicates InterOcean S4 whereas all other instruments are Alec EM current meters.

	2008	2010	2011	2012	2013	2014	2017
073.108	--	--	--	--	--	--	289
200.140	--	--	--	--	44, 95, 145, 196, 246, 348	--	--
300.100	279 (S)	189, 288	91, 193	95, 180, 279	--	74, 263	236
300.160	323 (S)	188	94, 280	287	--	--	--
347.088	--	--	--	--	--	69, 247	--
400.100	299 (S)	89, 233	265	--	--	--	--
500.120	--	--	--	--	--	72, 275	--

Table 3.2: Correlation coefficient of EOF1's principal component against each current meter record. The correlation for long-shore component is followed by correlation for cross-shore component in parentheses. Those significant with $p \leq 0.05$ are emphasized in bold.

	2008	2010	2011	2012	2013	2014	2017
073.108, Deep	--	--	--	--	--	--	**0.72 (0.79)**
200.140, 44 dbar	--	--	--	--	**0.91 (0.44)**	--	--
200.140, 95 dbar	--	--	--	--	**0.95 (0.39)**	--	--
200.140, 145 dbar	--	--	--	--	**0.98 (0.59)**	--	--
200.140, 196 dbar	--	--	--	--	**0.99 (0.55)**	--	--
200.140, 246 dbar	--	--	--	--	**0.98 (0.48)**	--	--
200.140, 348 dbar	--	--	--	--	**0.94 (0.74)**	--	--
300.100, Shal.	--	--	**0.97 (-0.15)**	**0.98 (-0.23)**	--	**0.89** (0.03)	--
300.100, Pyc.	--	**0.98 (-0.44)**	**0.98 (-0.43)**	**0.99 (-0.41)**	--	--	--
300.100, Deep	**0.99** (-0.15)	**0.98 (-0.55)**	--	**0.99 (-0.63)**	--	**0.94 (-0.34)**	**0.98 (-0.46)**
300.160, Shal.	--	--	**0.23** (0.07)	--	--	--	--
300.160, Pyc.	--	0.05 **(0.21)**	--	--	--	--	--
300.160, Deep	0.06 (0.02)	--	0.11 (0.17)	0.19 (0.16)	--	--	--
347.088, Shal.	--	--	--	--	--	**0.73 (-0.31)**	--
347.088, Deep	--	--	--	--	--	**0.82 (-0.68)**	--
400.100, Shal.	--	**-0.61 (0.63)**	--	--	--	--	--
400.100, Deep	**-0.50 (0.62)**	**-0.53 (0.49)**	**-0.40 (0.55)**	--	--	--	--
500.120, Shal.	--	--	--	--	--	**0.36 (-0.57)**	--
500.120, Deep	--	--	--	--	--	**0.57 (-0.68)**	--

Table 3.3: Subpycnocline (WMLD to 350 dbar) heat transports and T_{max}-weighted velocities at site 300.100. Note that heat content cannot be calculated in 2014 because several thermistors were lost during recovery.

	2008	2010	2011	2012	2017
$\overline{UQ}$ (x 10^8 J m^{-1} s^{-1})	+2.30	+2.99	+2.07	+1.63	+2.10
$\overline{VQ}$ (x 10^8 J m^{-1} s^{-1})	-1.17	-1.26	-0.99	-0.74	-0.85
$\overline{UT}$ (x 10^{-2} ºC m s^{-1})	+7.06	+9.83	+7.18	+5.67	+6.93
$\overline{VT}$ (x 10^{-2} ºC m s^{-1})	-3.59	-4.14	-3.45	-2.53	-2.80
$\overline{uq}$ (x 10^6 J m^{-1} s^{-1})	+2.58	+1.71	-0.07	-0.58	-1.22
$\overline{vq}$ (x 10^6 J m^{-1} s^{-1})	-2.27	-1.70	+0.81	-0.93	+0.22
$\overline{ut}$ (x 10^{-4} ºC m s^{-1})	-6.30	-15.30	+0.21	-5.15	-9.25
$\overline{vt}$ (x 10^{-4} ºC m s^{-1})	+0.29	+4.02	+2.27	+3.28	+2.33

Figures

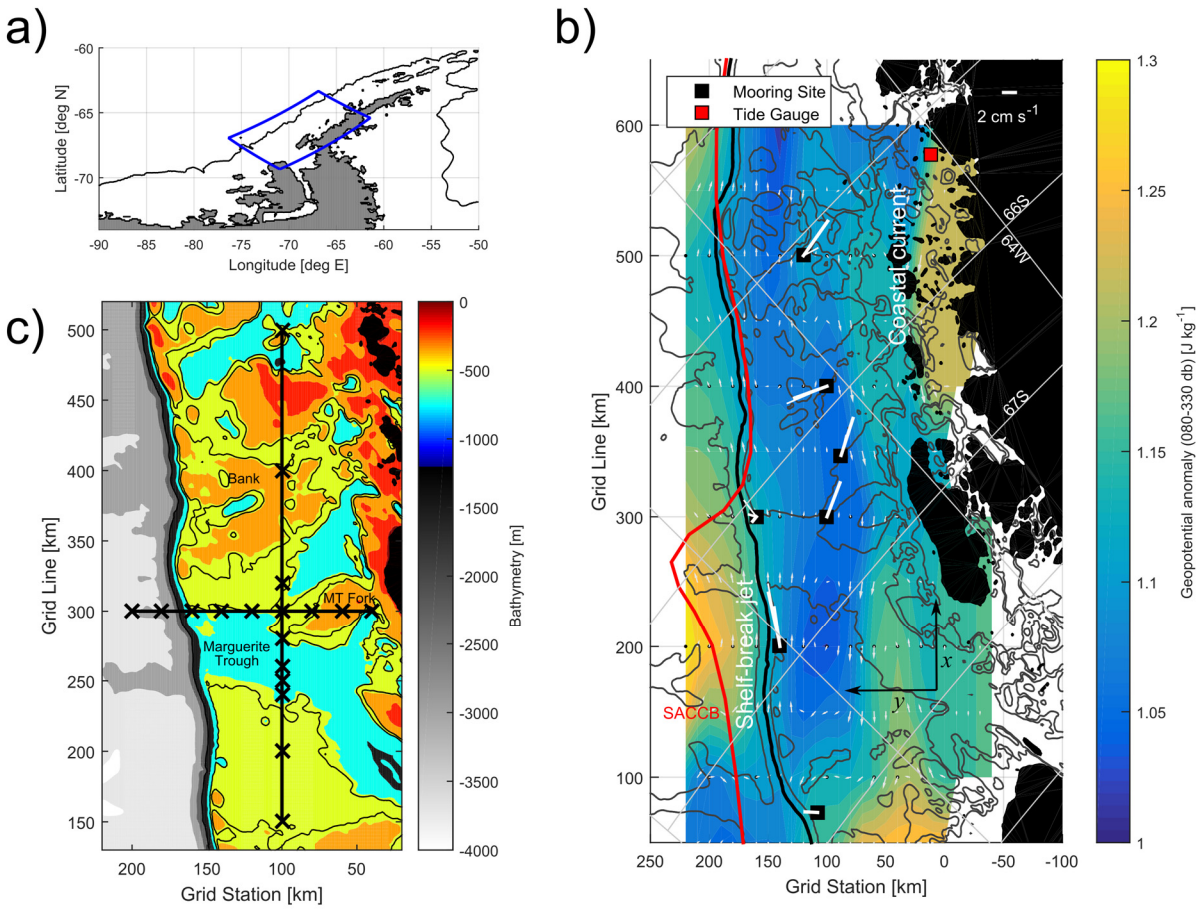

Figure 3.1: Overview of physical setting, mean circulation, and data sources used. **(a)** Regional map showing the study grid, outlined in blue, and the 1500 m isobath. **(b)** Inset showing the Pal LTER grid corresponding to the blue rectangle in (a). All locations in the paper use the LTER coordinate system and are given as GGG.SSS where GGG is the grid line (units of kilometers) and SSS the grid station (units of kilometers). The seven mooring sites analyzed in this paper are indicated with black squares and the time-mean currents over all years are shown with white lines where the thickest lines are currents below the pycnocline, medium within, and thinnest above. Color contours indicate the time-mean geopotential height anomalies at 80 dbar relative to 330 dbar from Pal LTER annual January CTD sampling (stations at black dots) and the white vectors are the associated geostrophic currents with arbitrary scale. The location of the Southern ACC Boundary (SACCB; the 0.35 dyn m contour from Orsi et al. (1995)) is indicated. The 3500, 1500, 480, and 300 m isobaths are shown as grey contours with the 1500 m contour outlined in bold black. **(c)** Inset showing the regional bathymetry in greater detail, emphasizing the major bathymetric features referred to in this study. The 375 and 480 m isobaths are outlined. The x's indicate ship stations where CTD and shipboard ADCP profiles were taken. The section along the 100 station was occupied in June 1999 and the section along the 300 line was occupied completely in January 1993-2008 and incompletely since then.

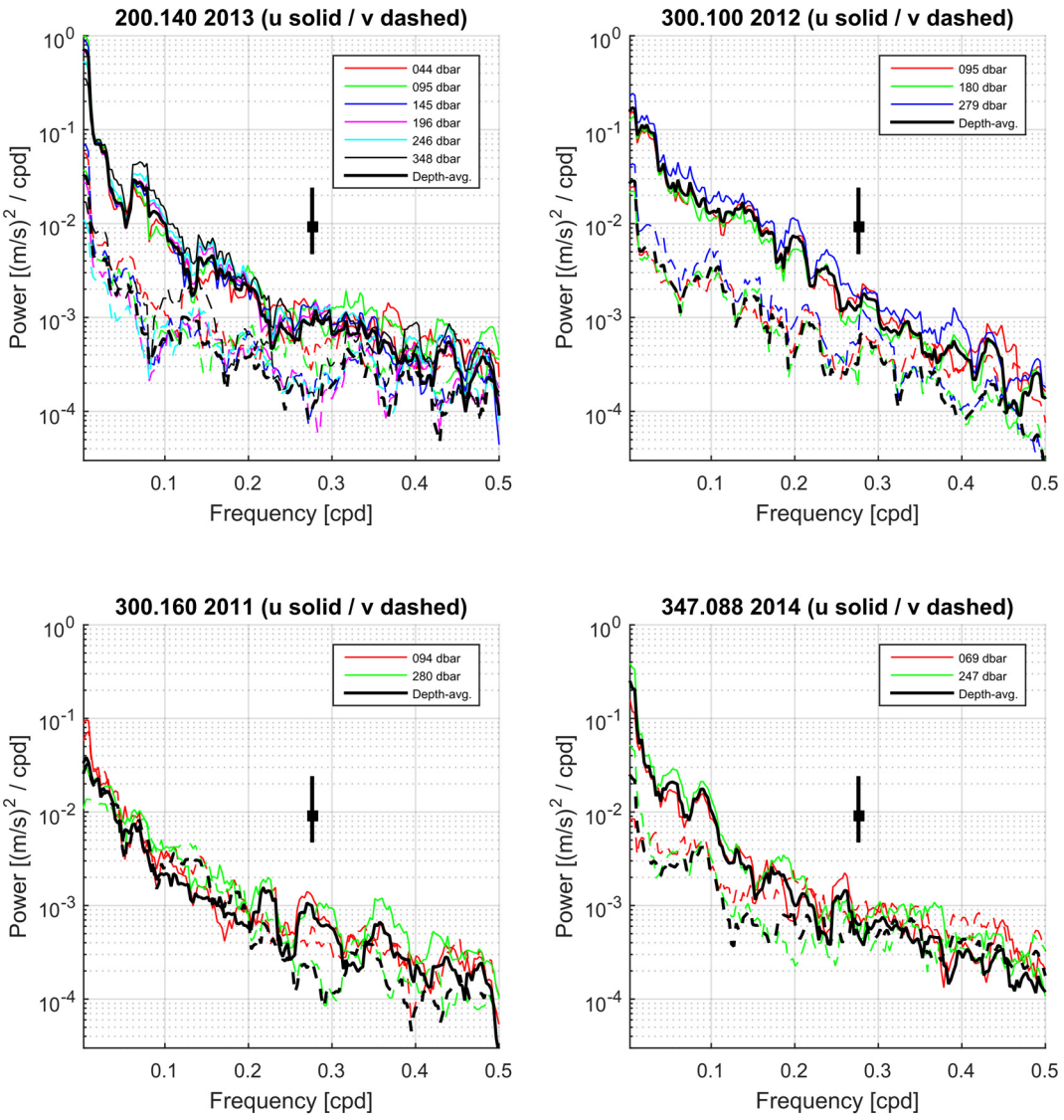

Figure 3.2: Component kinetic energy spectra for each current meter at each mooring site for one year of sampling (continued on next page). The year with the vertically densest current meter array is shown. Spectra are colored by depth and the bold black spectrum corresponds to the depth-averaged current. The long-shore spectra are solid and the cross-shore spectra are dashed. An error bar at the $\alpha = 5\%$ level is indicated.

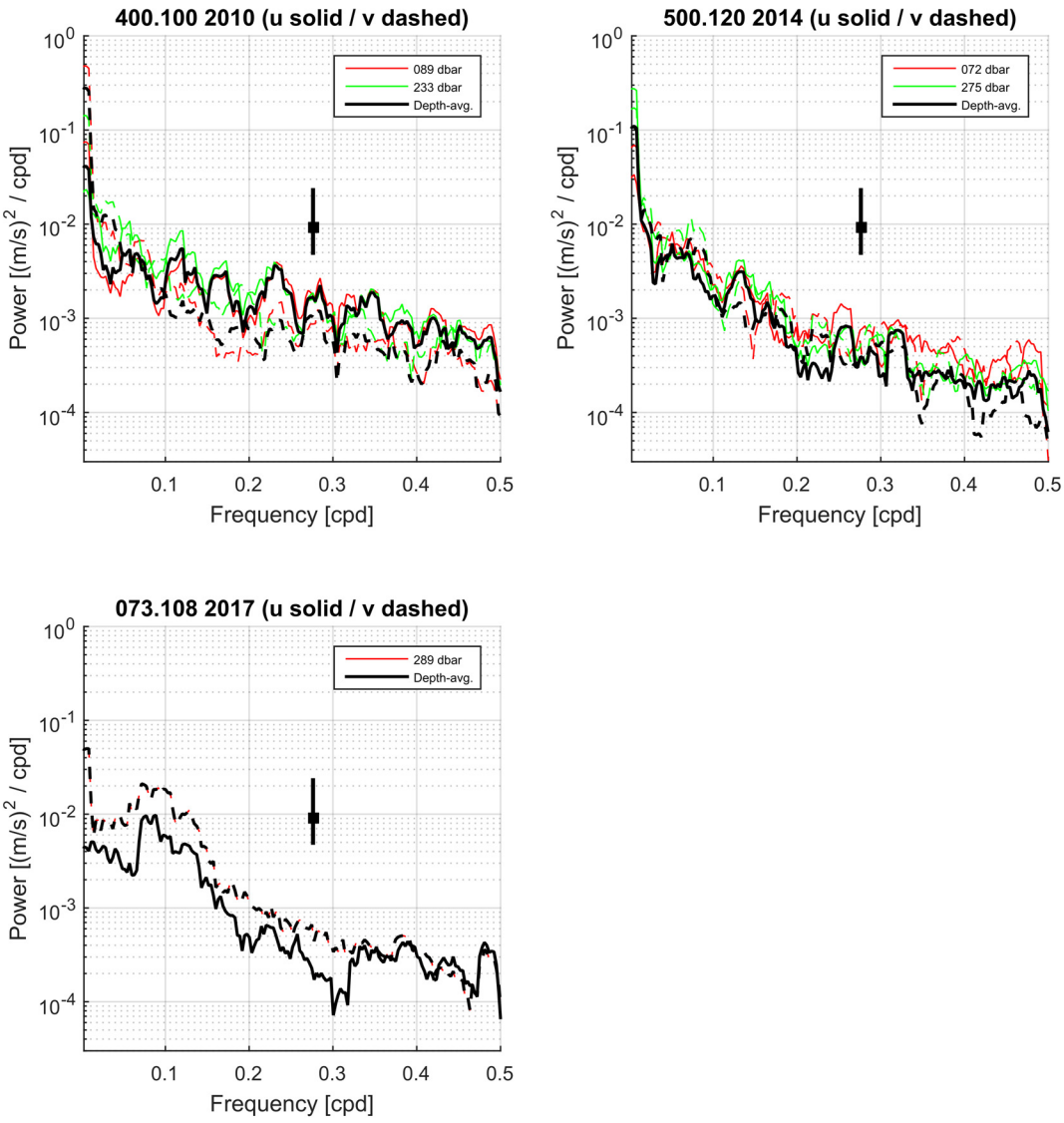

Figure 3.2 (continued from previous page).

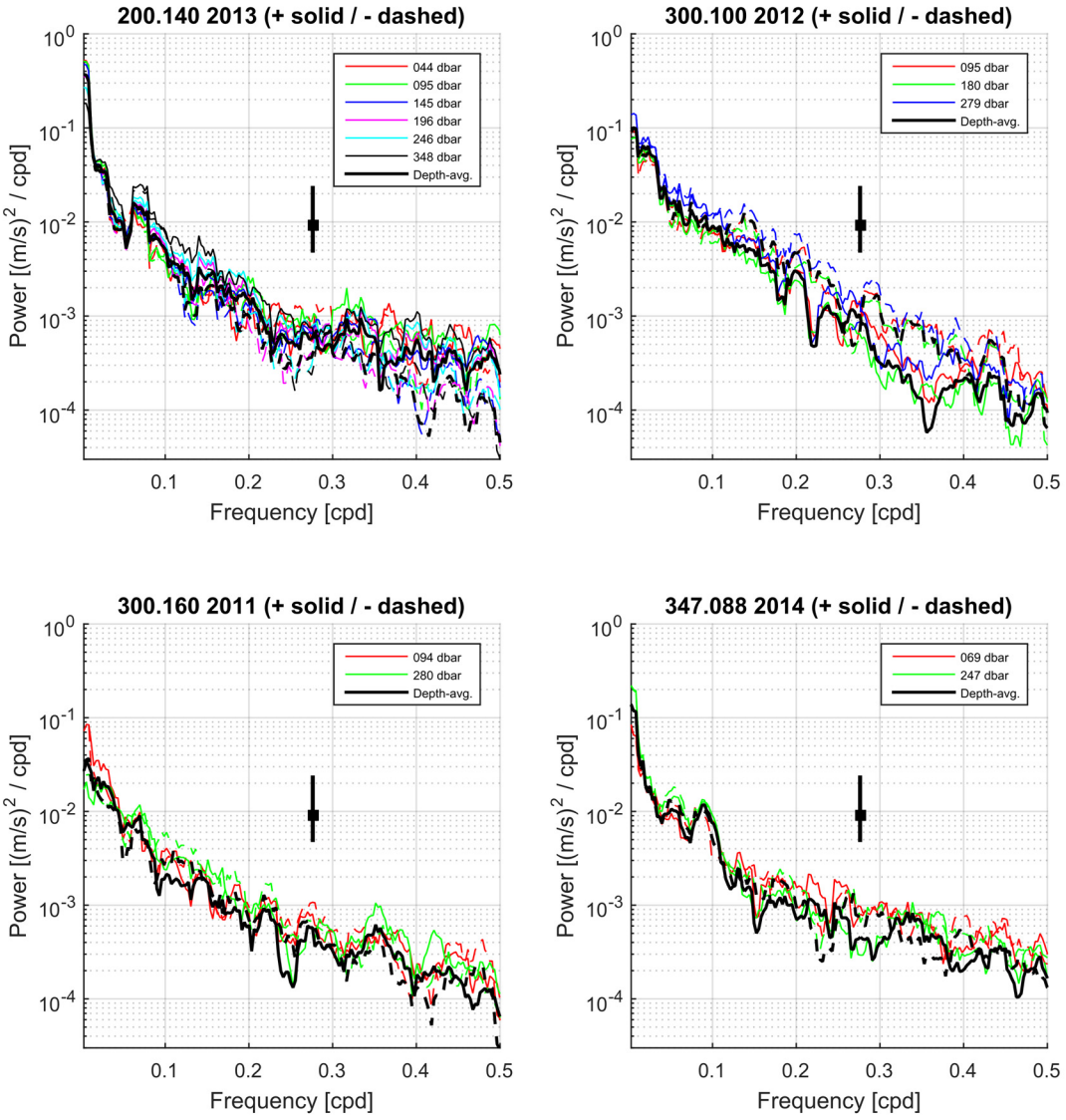

Figure 3.3: As in figure 3.2 but for rotary kinetic energy spectra (continued on next page). The counterclockwise spectra are solid and the clockwise spectra are dashed.

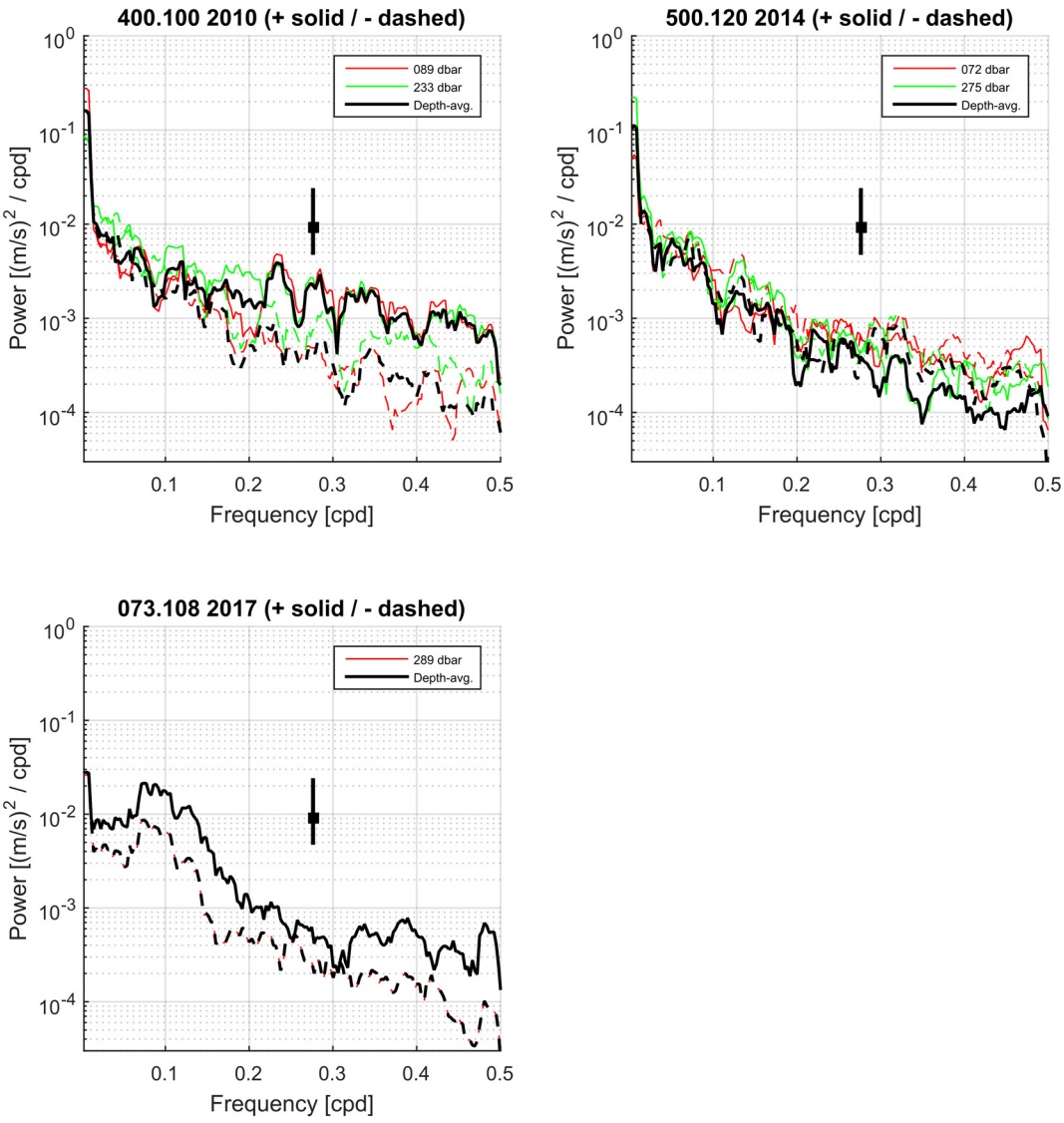

Figure 3.3 (continued from previous page).

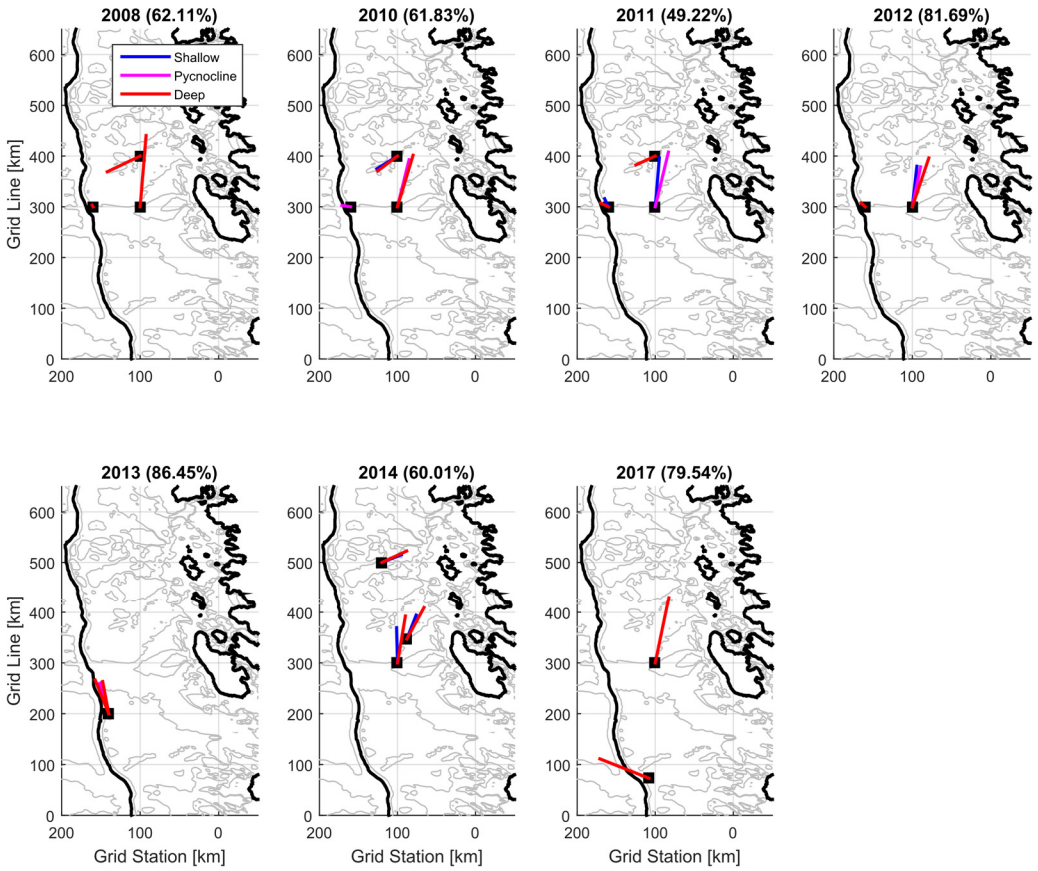

Figure 3.4: Maps of the first circulation EOF vector weights for each current meter for each year of sampling. Vectors are color coded by depth as indicated in the legend and the percentage of the total variance explained by the pattern is given in the title.

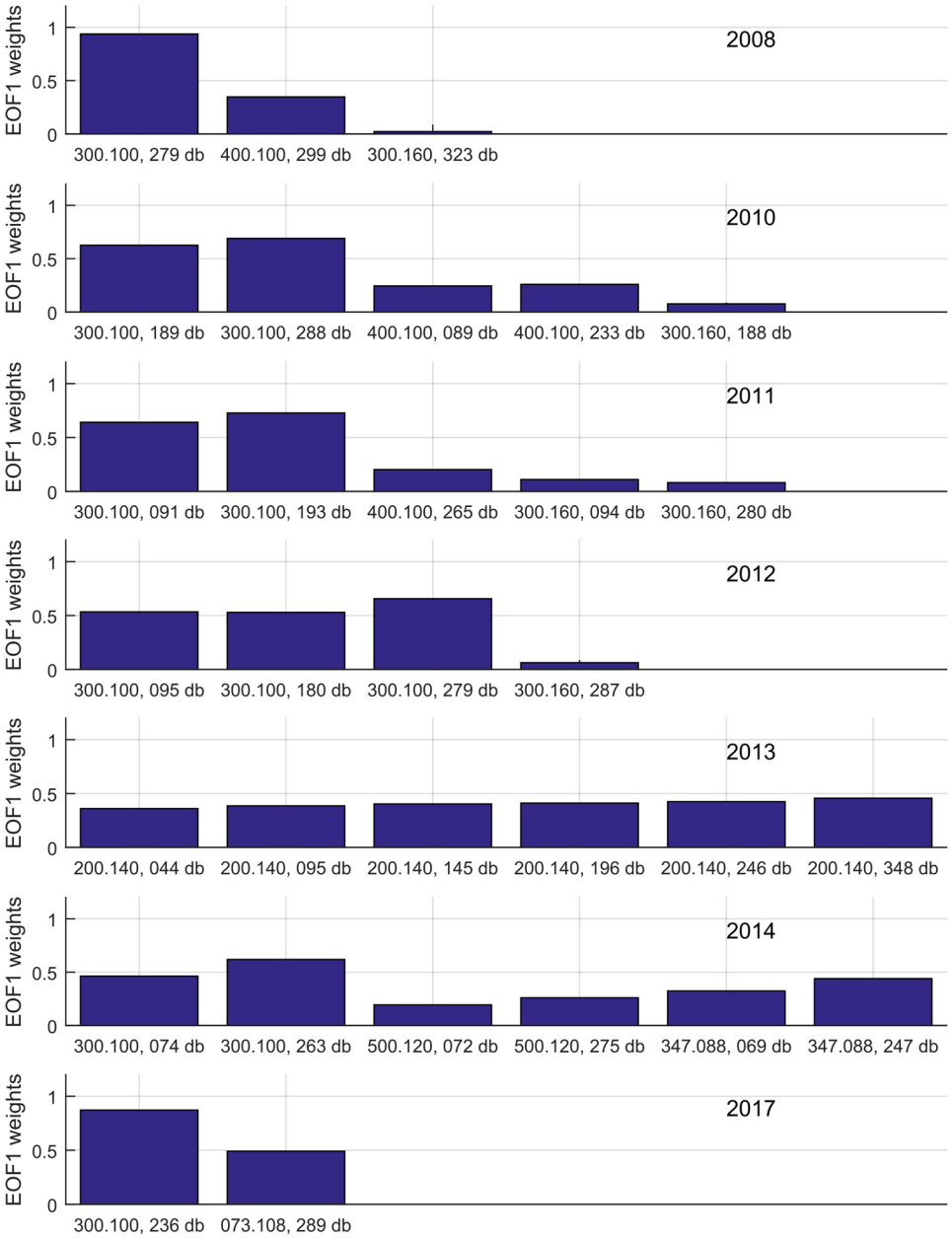

Figure 3.5: Histograms indicating the total EOF1 weight $\sqrt{\mathbf{E}_{\text{long}}^2 + \mathbf{E}_{\text{cross}}^2}$ for each current vector for each year of analysis.

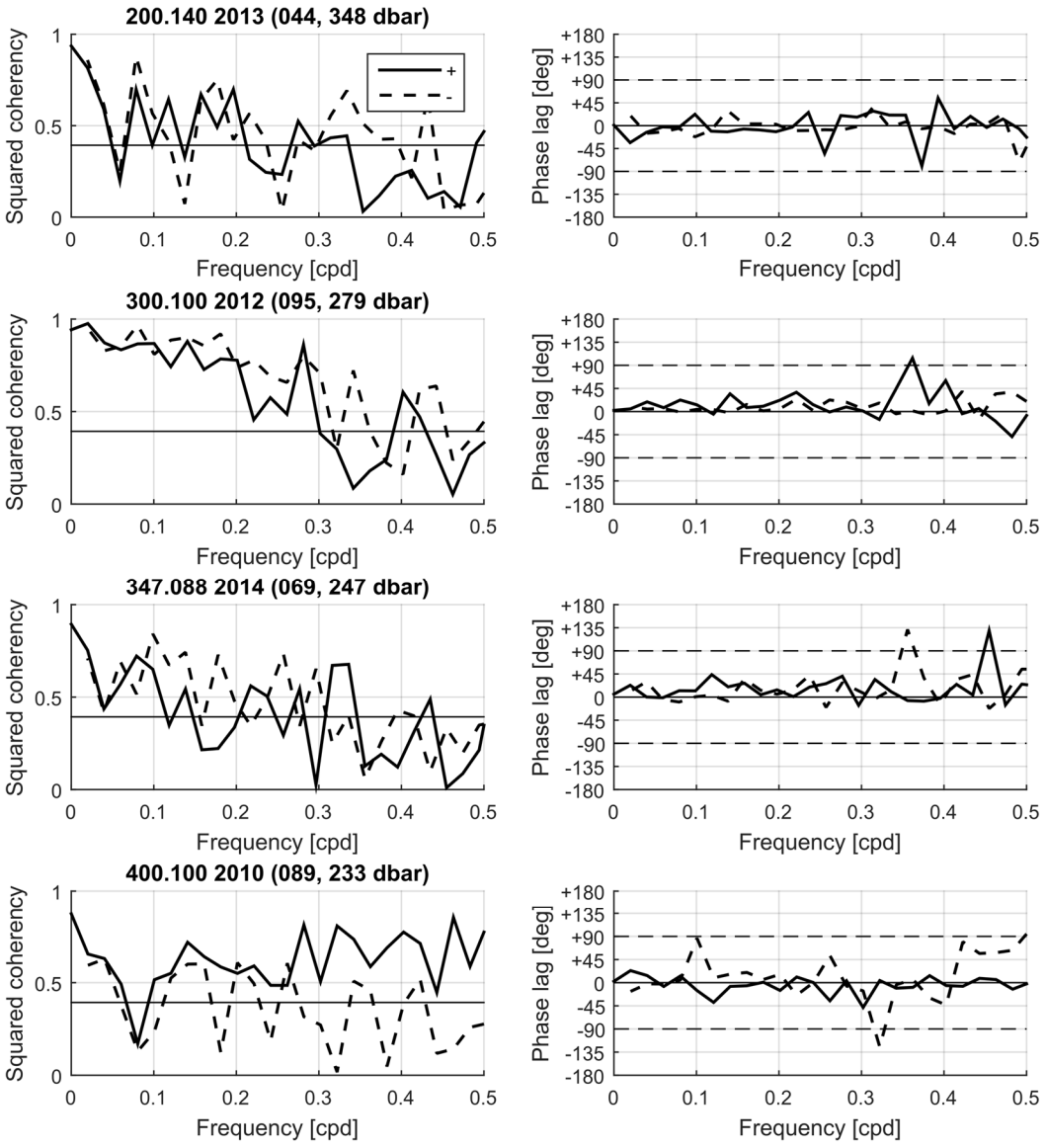

Figure 3.6: Complex squared coherency and cross-phase spectrum between the shallowest and deepest current meter record at each site for one year. Only locations with current meters spanning the permanent pycnocline are displayed. The counterclockwise spectra are solid and the clockwise spectra are dashed. The black horizontal line indicates the threshold for significant coherence compared against a white-noise null hypothesis of zero coherence at an $\alpha = 5\%$ level.

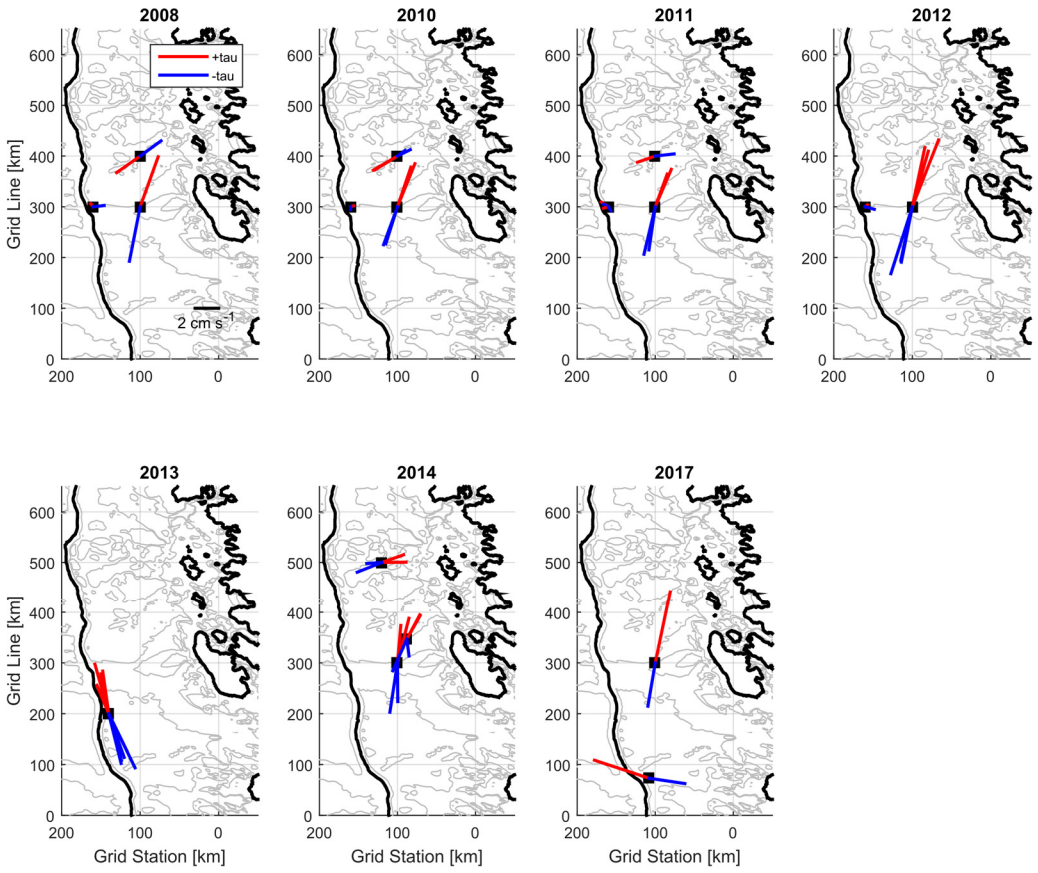

Figure 3.7: Composite intraseasonal velocity vectors under positive (red) and negative (blue) long-shore wind stress for each year of analysis.

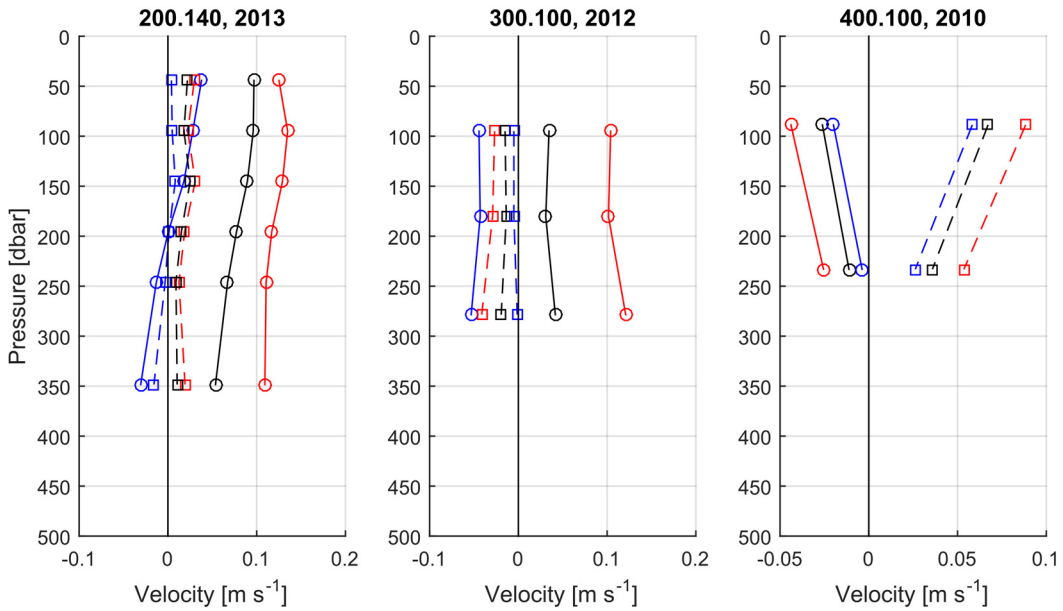

Figure 3.8: Selected total velocity profile composites under the same wind states. Long-shore currents are solid with circles at nominal depths and cross-shore currents are dashed with squares. Red profiles are under positive wind state, blue profiles are under negative wind state, and black profiles are averages over all time.

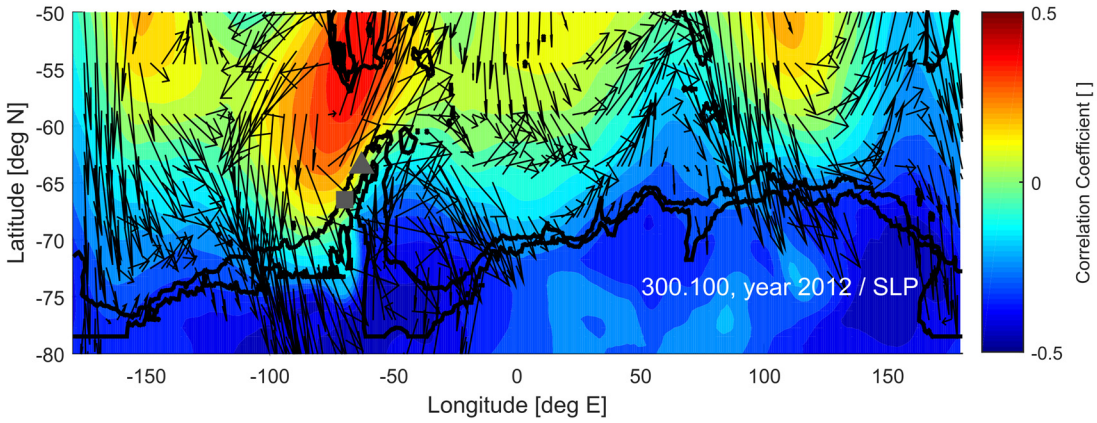

Figure 3.9: Heterogeneous correlation maps at zero lag for the long-shore barotropic velocity at 300.100 (year 2012; grey square) against the reanalysis sea level pressure (contours) and zonal and meridional surface stresses (vectors). The location of maximum correlation with the long-shore stress is indicated with a grey triangle. For orientation, the 1500 and 0 m isobaths are plotted.

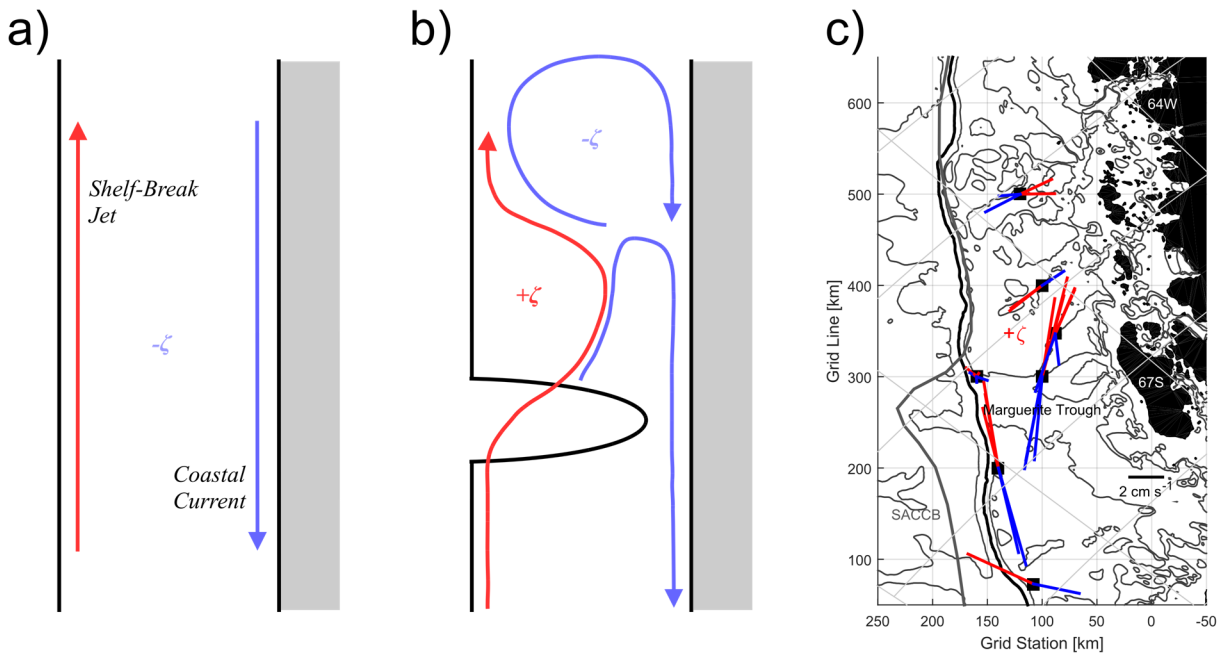

Figure 3.10: Schematic summary of WAP 'pinch' circulation pattern. **(a)** Schematic circulation induced by regional winds on WAP without Marguerite Trough. The SBJ and the Coastal Current form a large cyclone. **(b)** Schematic circulation induced by regional winds on WAP with Marguerite Trough. An anticyclonic cell is generated downstream of the canyon which pinches off the large wind-generated cyclone. **(c)** Actual WAP circulation as inferred from intraseasonal up and downwelling composites as in figure 3.7 but for all years. The anticyclonic cell is indicated by +ζ.

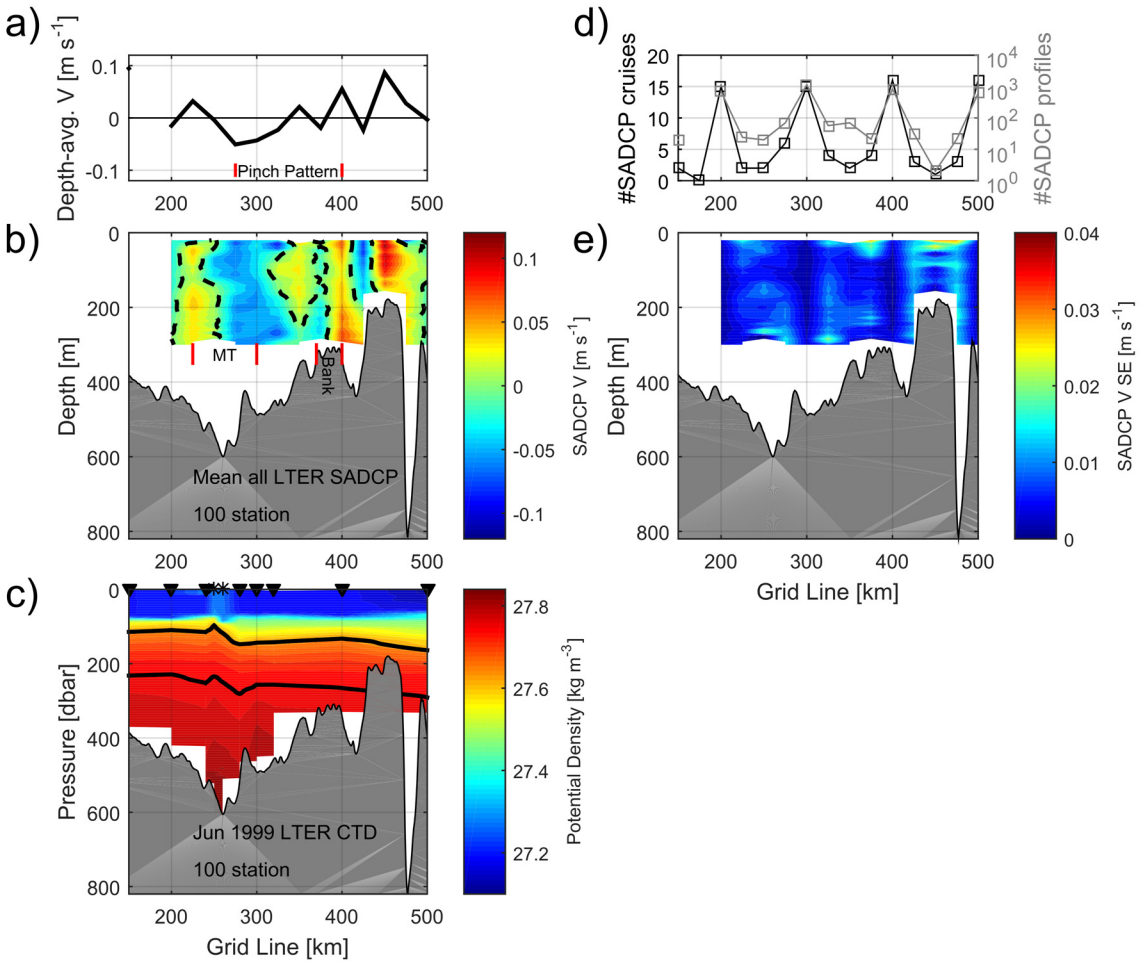

Figure 3.11: Overview of circulation as sampled by SADCP on the 100 station. **(a)** Depth-average (0-300 m) cross-shore current from all SADCP profiles on Pal LTER cruises (2000-2015), bin-averaged into 8 m depth and 25 km long-shore bins before integrating. The anticyclonic pinch circulation pattern, with onflow in Marguerite Trough and outflow on the 400 line, is indicated. **(b)** The bin-averaged cross-shore profiles (contours) along with labels for major bathymetric and circulation features. **(c)** Potential density sampled in June 1999. Profile locations indicated with black triangles are synoptic while the two profiles indicated by stars were sampled a few weeks later. The 27.64 and 27.76 kg m^{-3} surfaces, which carry UCDW (see chapter 2) are indicated. **(d)** Counts of SADCP profiles and cruises represented in each long-shore bin. Note that the standard LTER stations are much better sampled than the intermediate bins. **(e)** Standard error in each SADCP velocity bin.

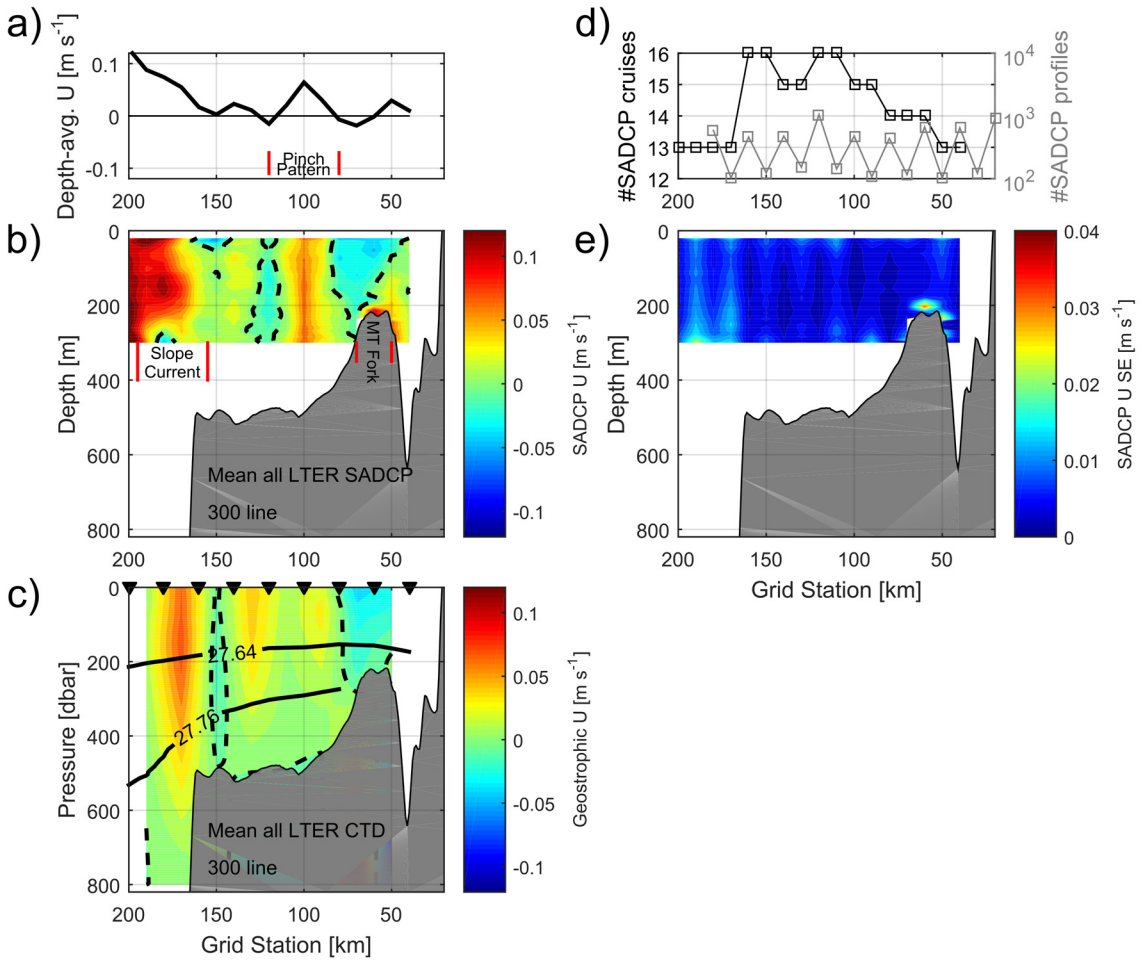

Figure 3.12: Overview of circulation as sampled by SADCP on the 300 line. **(a)** Depth-average (0-300 m) long-shore current from all SADCP profiles on Pal LTER cruises (2000-2015), bin-averaged into 8 m depth and 10 km cross-shore bins before integrating. **(b)** The bin-averaged long-shore profiles (contours) along with labels for major bathymetric features and currents. **(c)** Geostrophic currents calculated from first-differencing the station-average of all historic Pal LTER CTD data (stations at black triangles). The same isopycnals from figure 3.11 are labeled. **(d)** Counts of SADCP profiles and cruises represented in each cross-shore bin. **(e)** Standard error in each SADCP velocity bin.

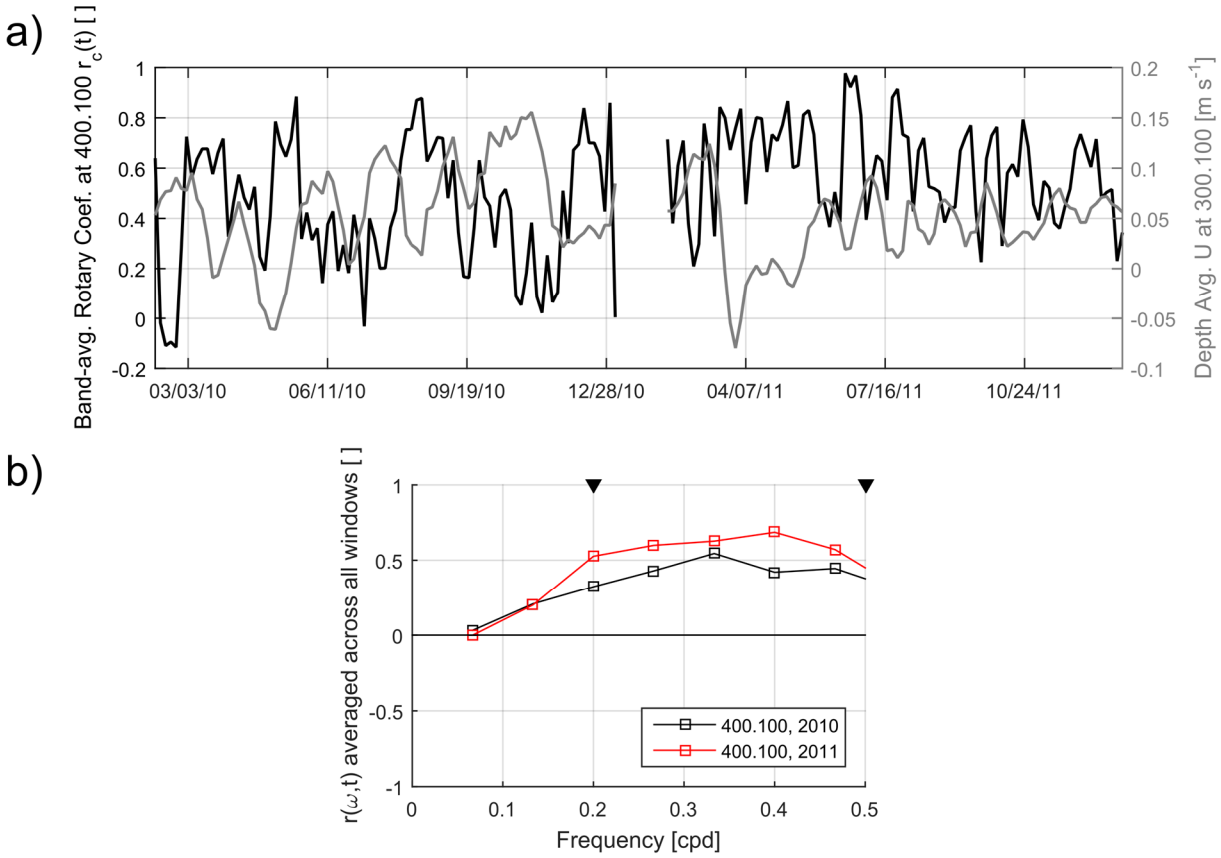

Figure 3.13: Rotary coefficient time series for barotropic current at 400.100. **(a)** Time series of band-averaged rotary coefficient $r_c(t)$ at 400.100 for both years of sampling (black) along with the depth-averaged long-shore current at 300.100 (grey), where each sample of the latter is the time average within each window used to compute the moving spectra. **(b)** Time average of all of the 15-day rotary coefficient spectral windows. The band used in the integration to compute $r_c(t)$ is indicated with black triangles.

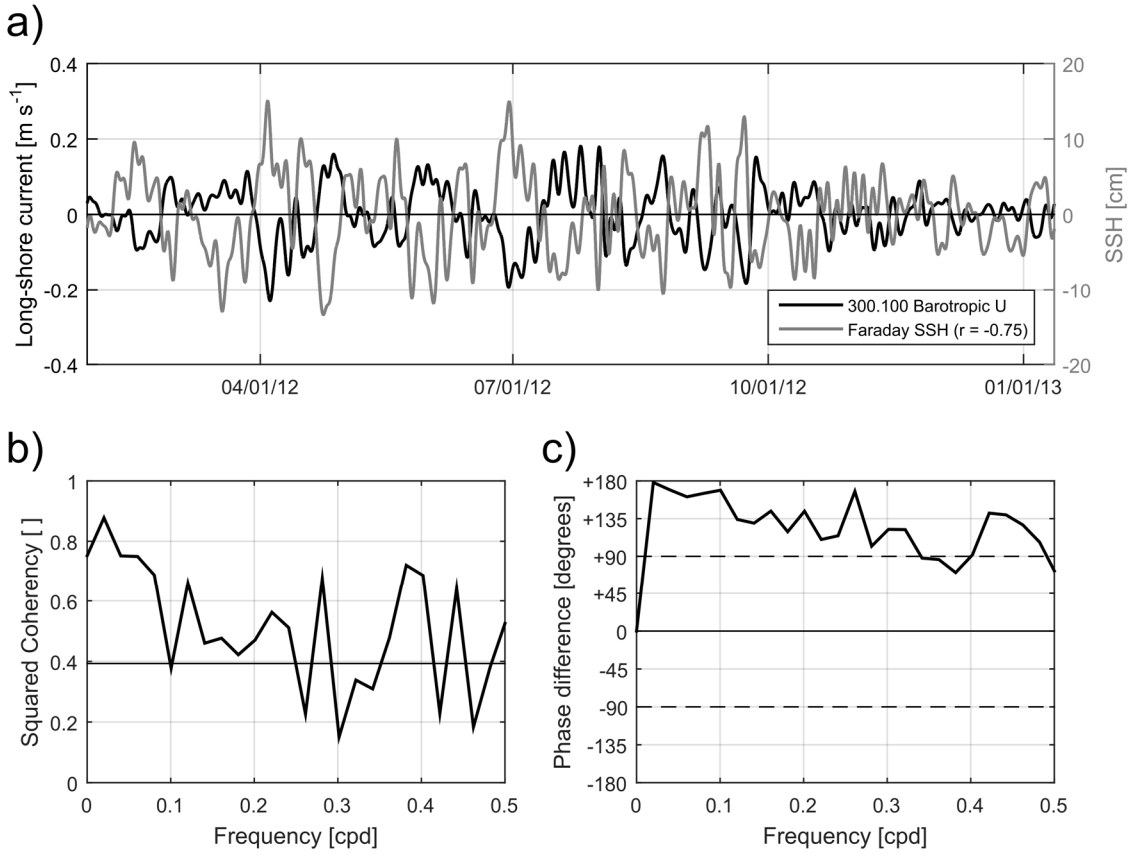

Figure 3.14: Comparison of barotropic current at 300.100 to SSH at Faraday tide gauge. **(a)** Long-shore barotropic current at 300.100 (black) with the SSH at Faraday tide gauge (grey). Both records have been filtered to retain intraseasonal variance. **(b)** Squared coherency between those two time series (without intraseasonal filtering). Threshold for significance at an $\alpha = 5\%$ level is indicated with a horizontal line. **(c)** As in (b) but for the cross-phase spectrum.

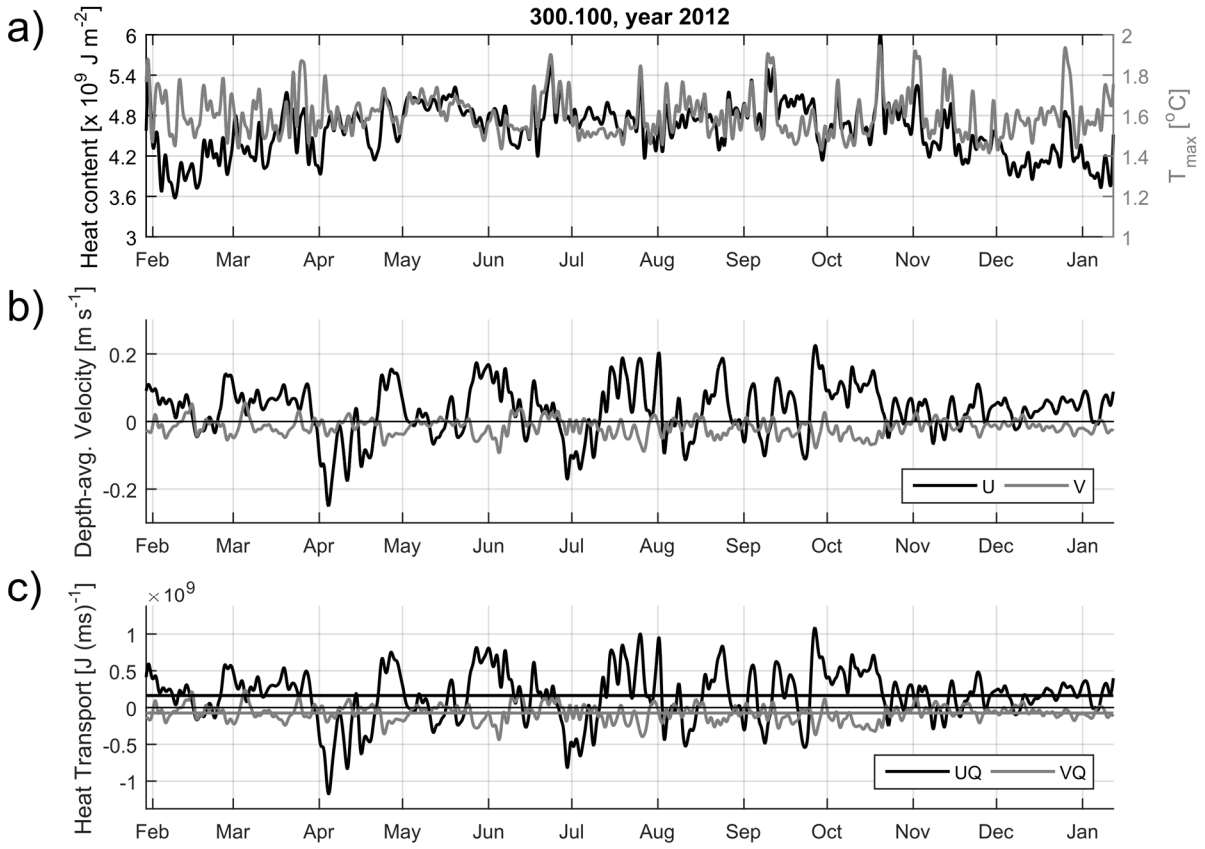

Figure 3.15: Heat transport time series for one year at 300.100. **(a)** Heat content Q (black) and T_{max} (grey) for one year at 300.100. **(b)** Long-shore U (black) and cross-shore V (grey) barotropic current at same site. **(c)** Heat transport components UQ (black) and VQ (grey) with time-mean of each component presented as thin horizontal lines, colored in the same manner.

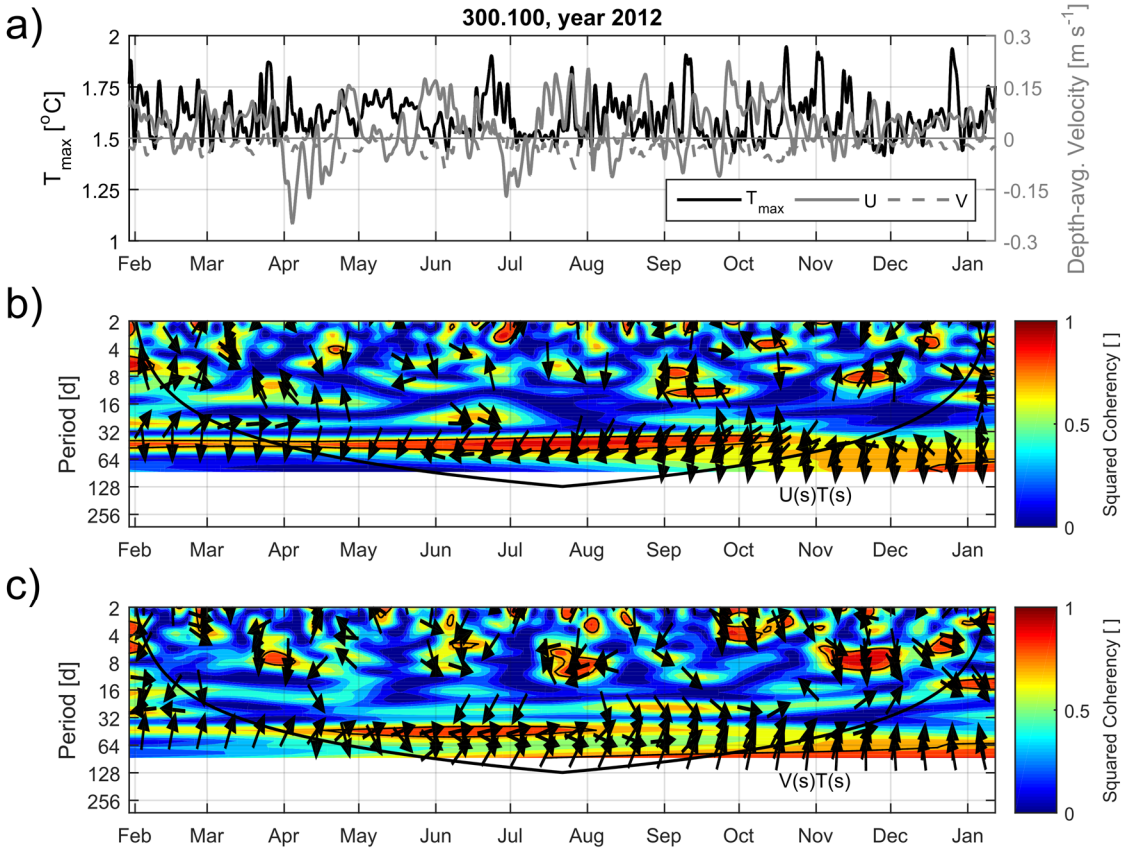

Figure 3.16: Cross-wavelet coherency analysis of T_{max} against U and V. **(a)** Temperature maximum T_{max} (black) and long-shore U (solid grey) and cross-shore V (dashed grey) barotropic currents as presented in figure 3.15. **(b)** Cross-wavelet coherency time-period spectrum between U and T_{max}. The threshold for significance at a 95% level based on generation of 500 bootstrapped time series is indicated with a thin black line and the cone of influence is indicated with a thick black line. The arrows indicate the relative phasing, with arrows to the right (left) meaning in-phase (anti-phased) and arrows upward (downward) meaning T_{max} leads (lags) U. The wavelet calculations use a Morlet mother wavelet, 0.125 octaves per scale, 80 total scales, and a minimum scale of 2 hours (analogous to a Nyquist period for our sampling). **(c)** As in (b) but for V against T_{max}.

4) Wind-driven barotropic velocity dynamics

Abstract:

We expand upon earlier studies that investigated the wind-driven sea surface height (SSH) dynamics along the Antarctic coastline in order to quantify to what degree long-shore velocity fluctuations are driven by cross-shore SSH fluctuations. We do this by analyzing an array of moored current meter records collected on the western Antarctic peninsula shelf. We use reanalysis surface stress integrated along wave characteristics around the continent to predict the cross-shelf SSH gradient from the shallow water equations in the long-wave limit and compare the result to the observed barotropic current. Similar to the dynamics of SSH, we find that the velocity fluctuations largely consist of a circumpolar-coherent wavenumber zero mode and of propagating barotropic shelf waves, however an important distinction from previous studies is the importance of mode $n = 2$ waves in the velocity signal. Velocity fluctuations with period 40-60 days are particularly energetic. This is partly due to strong fluctuations in the coherent mode of variability at this period, as previously demonstrated in Drake Passage transport, but also due to excitement of the second mode wave. After diagnosing the wind-driven dynamics we discuss some of their implications for shelf-slope exchange. Firstly, we show that wintertime upwelling of warm water at a coastal canyon head is associated with a coastal SSH drop and pressure gradient up the canyon. Secondly, we hypothesize a mechanism by which the baroclinicity over the steep continental slope associated with the second mode wave can cut off warm isopycnals from the shelf but potentially increase eddy fluxes of heat by steepening isopycnal slopes.

4.1) Introduction

Mid-depth and bottom waters on the Antarctic Peninsula shelf are warming (Martinson et al. 2008; Schmidtko et al. 2014) and marine-terminating glaciers in contact with warm subpycnocline waters are retreating (Cook et al. 2016). These results may be due to a change in the boundary condition at the continental shelf-break (e.g., warmer and/or shoaled subpycnocline waters), an increased transport of mass across the continental slope, or a combination of the two. The magnitude and direction of the long-shore current is important in driving exchange across the continental slope with stronger eastward flows leading to increased flow-topography interaction with bathymetric irregularities such as submarine canyons (chapter 3; Dinniman and Klinck 2004; St-Laurent et al. 2013) or to the development of arrested bottom Ekman layers (Wåhlin et al. 2012; Spence et al. 2017). Each of these processes is asymmetric (different response for eastward versus westward flow) and potentially nonlinear, suggesting the need to understand variance in the long-shore flow in addition to the mean.

There is a major gap in our understanding of the dynamics of shelf currents around the Antarctic margins at intraseasonal time scales. At time scales of less than one to a few days, several studies point to the importance of near-resonant, short coastal trapped waves that may be forced by short-duration wind events (Wåhlin et al. 2016), dense water overflows (Jensen et al. 2013), or tides (Middleton et al. 1987). However, on longer time scales, while robust statistical links between the long-shore wind stress and long-shore currents have been established in regional numerical models (Thoma et al. 2008; Dinniman et al. 2011, 2012) and observations (e.g., chapter 3; Assmann et al. 2013; Wåhlin et al. 2013), there is not yet any dynamical framework to quantitatively explain current fluctuations.

In chapter 3 we demonstrated the existence of a large-scale (hundreds of kilometers), spatially coherent circulation pattern on the western Antarctic Peninsula (WAP) shelf that is associated with an increase in the long-shore flow speed, is strongly barotropic, and is well correlated to the long-shore wind stress. These observations motivate us to consider the possibility that the major fluctuations in the long-shore flow around the Antarctic continent are driven by low-wavenumber fluctuations in the coastal sea surface height (SSH). The dynamics of low-frequency, low-wavenumber SSH variations around Antarctica are now relatively well understood. Kusahara and Ohshima (2009) used a barotropic model and coastal tide gauge data to show that sea level fluctuations at periods longer than about 10 days are dominated by a circumpolar-coherent wavenumber zero response whereas fluctuations at periods of 15, 7.5, and 5 days are dominated by barotropic shelf waves (BSW) that resonate with westward propagating variability in the atmosphere at integer wavenumbers. However, it is not known to what extent these fluctuations translate into long-shore velocity fluctuations. The only known test of correspondence between coastal SSH and velocity fluctuations comes from measurements of Antarctic Circumpolar Current (ACC) transport through Drake Passage. Measurements of bottom pressure in Drake Passage are shown to correlate with coastal SSH variability on intraseasonal time scales at short time lag (Hughes et al. 2003) and these fluctuations are attributed to wavenumber zero forcing (Matthews and Meredith 2004), however the open-ocean dynamics of the ACC associated with the wavenumber zero variability (Hughes et al. 1999; Weijer and Gille 2005) are not necessarily of primary importance along the shelf-break where other coastal-trapped phenomena may be relevant.

In this study we test the hypothesis that the long-shore velocity fluctuations along the Antarctic shelf are in geostrophic balance with a wavenumber zero SSH variation and the sum of

multiple BSW modes by making use of an array of moored current meter time series collected on the WAP continental shelf as part of the Palmer Long Term Ecological Research project (Pal LTER; Smith et al. 1995). We first inversely seek the signature of wavenumber zero variability through empirical orthogonal function (EOF) analysis of an array of moored current meters and subsurface pressure sensors around the continent and seek the signature of BSW through quantitative analysis of cross-characteristic variance in a hovmöller matrix of those same time series. After showing that the unstratified, nondispersive long-wave limit of BSW is a good approximation for the more general coastal trapped waves (CTW) along the Antarctic margin on intraseasonal time scales (3-100 days) and showing that their phase speeds are consistent with the results of the inversion, we utilize a representative bathymetric profile and reanalysis surface stress to predict time series of long-shore current at the mooring sites using the analytical framework of Gill and Schumann (1974, hereafter GS74), explaining on average about half of the signal variance. These predictions form the major contribution of this study and reveal a previously unreported importance of the second mode shelf wave and the importance of a 40-60 day period in the total velocity variance.

The paper is organized as follows. In section 4.2 we review the theory of wavenumber zero variability and of BSW, re-deriving the GS74 model. Then in sections 4.3 and 4.4 we describe the data and methodology, respectively. In section 4.5 we present the results, beginning with the wave modal analysis for regional bathymetry and stratification, then presenting the inverse detection results, and finally presenting the predictions and their evaluation in the time and frequency domains. In section 4.6 we discuss why the $n = 2$ shelf wave is so important and why variability with 40-60 day period dominates the observed signals. We also consider some implications of the findings for shelf-slope exchange. Finally, we conclude in section 4.7.

4.2) Theory

4.2.1) Wavenumber zero variability

The circumpolar waveguide of the Antarctic coast and the existence of a nearly annular atmospheric forcing allow for the possibility of a wavenumber zero variability in coastal SSH. Studies of tide gauge records collected around the continent with approximately circumpolar coverage demonstrate a coherent response in SSH at time scales longer than 10 days (Aoki 2002; Hughes et al. 2003; Matthews and Meredith 2004; Kusahara and Ohshima 2009) which is shown to correlate significantly to barotropic ACC transport as measured in Southern Drake Passage (Hughes et al. 2003; Matthews and Meredith 2004) and to indices of the SAM (Aoki 2002; Hughes et al. 2003), but more precisely to winds in the southern portion of the ACC (below the latitudes of Drake Passage) and close to the Antarctic continent (Hughes et al. 1999; Kusahara and Ohshima 2009). While the nature of the relationship between wind stress, coastal SSH, and along-isobath transport is consistent with anomalies induced by a circumpolar-coherent Ekman transport normal to the coast, Hughes et al. (1999) show that the dynamics are somewhat subtler. Essentially, along closed f/H contours, an acceleration can be generated by an along-f/H wind stress and, as the ACC accelerates, it generates a cross-f/H pressure gradient. Most of the f/H contours that are closed around the continent are in the southern portion of the ACC, hence the major effect on ACC transport comes from SSH changes (and winds) south of the ACC and along the coast. The coherent SSH response is therefore a free mode (or a "nearly free mode"; Hughes et al. 1999) that can be excited by winds at any frequency, and the negligible time lag between wind forcing and ocean response suggests it is strongly damped (Weijer and Gille 2005).

Kusahara and Ohshima (2009) considered the inviscid, nondivergent shallow water equations in a re-entrant channel (long-shore in the *x*-direction) in order to model wavenumber zero variability around the continent. Uniform variability requires terms with $\partial/\partial x$ go to zero and requires the offshore mass flux be constant in the long-shore dimension. Further, the boundary condition at the coast requires no mass flux there. These requirements reduce the set of shallow water equations to

$$\left(\frac{\partial}{\partial t}+r_t\right)\frac{d\eta}{dy}=-\frac{f}{g}\frac{\tau^x}{\rho_0 H} \tag{4.1}$$

which when subject to sinusoidal forcing $\tau^x=\tau_0(\omega)\sin(\omega t+\theta)$ has solution

$$\eta(y,t)=\eta(L,t)+\frac{f\tau_0}{g\rho_0\sqrt{r_t^2+\omega^2}}\int_L^y\frac{1}{H}\cos\left(\omega t+\theta+\operatorname{atan}\left(r_t/\omega\right)\right)dy\,. \tag{4.2}$$

Given knowledge of a representative cross-slope bathymetry profile *H*(*y*) and a choice of damping parameter r_t, this equation can be used to predict the SSH response to wavenumber zero wind stress (and associated geostrophically balanced long-shore current by taking the *y* derivative). In their study, those authors also explain why the wavenumber zero response is greatest at low frequencies: The amplitude term in (4.2) suggests that when $\omega \gg r_t$ the response amplitude is inversely proportional to frequency whereas when $\omega \ll r_t$ the amplitude approaches a maximal asymptotic value $f\left(gr_t\right)^{-1}$.

4.2.2) Barotropic shelf waves in the long-wave limit

The long-shore current on continental shelves is often correlated to the long-shore wind stress (Gill 1982) and BSW are the natural response to wind forcing in an unstratified ocean: as the long-shore wind induces an Ekman transport across the sloping shelf, the associated vorticity anomaly causes the disturbance to propagate with the coast to its left in the southern hemisphere.

The dispersion relation for BSW varies with shelf profile and background flow but always consists of two distinct regimes. For long waves the dispersion relation is linear with the phase and group velocities oriented in the same direction. At a certain wavenumber there is a maximal frequency with zero group velocity, beyond which the frequency decreases with increasing wavenumber. Observations and theoretical arguments suggest that the shelf wave response to the wind consists of a highly rotary, resonant short-wave response to impulsive short-duration wind events and a long-wave response to lower frequency wind stress across a continuous range of frequencies with small phase lag (Gordon and Huthnance 1987). It is the latter that we seek in this study.

We employ the analytical model of GS74. Owing to its central importance to this work, we redevelop their model here. GS74 seek to explain low-frequency, low-wavenumber, wind-driven SSH variability on the continental shelf. The model considers the shallow water equations forced by the long-shore (x) wind stress in the long-wave limit and assumes a continental slope that varies only in the cross-shore (y) dimension. The presumed scale of the wind systems conducting the forcing is large compared to the width of the shelf (so $\tau^x(x,y,t) \equiv \tau^x(x,t)$) and the long-wave limit results in only the long-shore component of the wind mattering. The long-wave approximation provides the practical leap that enables easy solution, rendering the waves nondispersive and allowing for a separation of variables.

The underlying equations are

$$\frac{\partial u}{\partial t} - fv = -g\frac{\partial \eta}{\partial x} + \frac{\tau^x}{\rho_0 H} \tag{4.3a}$$

$$fu = -g\frac{\partial \eta}{\partial y} \tag{4.3b}$$

$$\frac{\partial \eta'}{\partial t} + \frac{\partial}{\partial x}\left(Hu\right) + \frac{\partial}{\partial y}\left(Hv\right) = 0 \,. \tag{4.3c}$$

The velocity variables are depth-averaged components and the sea surface height $\eta(x,y,t) = \eta'(x,y,t) + \eta_a(x,t)$ is the sum of the SSH anomaly η' and that due to the local atmospheric pressure η_a. Omission of the *v* tendency term and the cross-shore forcing term are justified by the low-frequency $\left(\omega \ll f\right)$ and long-wave ($L_{\text{shelf}} k \ll 1$, equivalently $\partial/\partial x \ll \partial/\partial y$) assumptions. In consequence, note that the cross-shore momentum equation is simply the geostrophic balance, which is consistent with the good agreement between the barotropic long-shore current at mooring site 300.100 and the coastal SSH at Faraday tide gauge (chapter 3).

Going further, in the event that the divergence parameter $D^2 = \dfrac{\left(fL\right)^2}{gH} \ll 1$, which is the case around the margins of Antarctica, the surface divergence can be neglected. This sets the SSH anomaly tendency in the continuity equation to zero and allows for construction of a streamfunction:

$$Hu = -\partial\psi/\partial y \,, \qquad Hv = +\partial\psi/\partial x \,. \tag{4.4}$$

With a streamfunction defined, we can manipulate the shallow water equations (4.3) into the single vorticity equation

$$\frac{\partial^2}{\partial y \partial t}\left(\frac{1}{H}\frac{\partial \psi}{\partial y}\right) - \frac{f}{H^2}\frac{dH}{dy}\frac{\partial \psi}{\partial x} = \frac{1}{H^2}\frac{dH}{dy}\frac{\tau^x}{\rho_0} \,. \tag{4.5}$$

The goal at this point is to solve (4.5) subject to the boundary conditions $\psi\left(y=0\right)=0$ (no normal flow at the coast) and $\partial\psi\left(y=L\right)/\partial y = 0$ (no long-shore flow at the oceanic edge).

To proceed, the first step is to consider free solutions to (4.5) by setting the right-hand side to zero. Defining a separation of variables

$$\psi(x,y,t) = \Phi(x,t)F(y) \tag{4.6}$$

and substituting into (4.5) with zero forcing, we obtain

$$\frac{\partial}{\partial y}\left(\frac{1}{H}\frac{dF}{dy}\right)\frac{\partial \Phi}{\partial t} - \frac{f}{H^2}\frac{dH}{dy}\frac{\partial \Phi}{\partial x}F = 0 \tag{4.7}$$

which requires

$$\frac{d}{dy}\left(\frac{1}{H}\frac{dF}{dy}\right) + \frac{1}{c}\frac{f}{H^2}\frac{dH}{dy}F = 0 \tag{4.8}$$

and

$$\frac{1}{c}\frac{\partial \Phi}{\partial t} + \frac{\partial \Phi}{\partial x} = 0\,. \tag{4.9}$$

The latter is a first-order wave equation for the free waves while the former is a Sturm-Liouville eigenvalue problem whose eigenvalues are one over the phase speed c_n and whose eigenvectors $F_n(y)$ define the wave modal structures, subject to the boundary conditions $F(0) = 0$ and $dF(L)/dy = 0$. The spectrum of wave modal structures and phase speeds is easily solved for numerically given a cross-shelf bathymetry profile $H(y)$ (see Appendix D).

With knowledge of the free wave modal structures, the solution to the full, forced vorticity equation (4.5) is obtained by expanding the streamfunction and the Ekman flux in terms of the free wave modes $F_n(y)$. For the streamfunction, we write

$$\psi(x,y,t) = \sum_n \varphi_n(x,t)F_n(y) \tag{4.10}$$

with yet unknown wave amplitudes $\varphi_n(x,t)$. For the Ekman flux, we write

$$1 = \sum_n b_n F_n(y) \tag{4.11}$$

where

$$b_n = \int_0^L \frac{1}{H^2} \frac{dH}{dy} F_n(y)\, dy \tag{4.12}$$

are defined as the wind-coupling coefficients. Finally, substitution of these expansions into the forced vorticity equation yields the spectrum of first-order wave equations

$$\frac{1}{c_n}\frac{\partial \varphi_n}{\partial t} + \frac{\partial \varphi_n}{\partial x} = -\frac{b_n}{f\rho_0}\tau^x(x,t), \tag{4.13a}$$

to which we can add a linear damping term,

$$\frac{1}{c_n}\frac{\partial \varphi_n}{\partial t} + \frac{\partial \varphi_n}{\partial x} + \underbrace{r_n \varphi_n}_{\text{damping}} = -\frac{b_n}{f\rho_0}\tau^x(x,t) \tag{4.13b}$$

and simplify by evaluating along a characteristic

$$\frac{\partial \varphi_n}{\partial x} + r_n \varphi_n = -\frac{b_n}{f\rho_0}\tau^x\left(x, t + \frac{x}{c_n}\right). \tag{4.13c}$$

The solution of these damped wave equations for the wave amplitude at the location $x = 0$ and time t is obtained via an integrating factor as

$$\varphi_n(0,t) = -\frac{b_n}{f\rho_0}\int_{x_{\text{inf}}}^{0} \exp(-r_n x')\,\tau^x\left(x', t + \frac{x'}{c_n}\right) dx' \tag{4.14}$$

where integration is carried out along the wave characteristic, in the direction of wave propagation, to the observation site $x' = 0$ from some point x_{inf} where wave amplitude is negligible. Qualitatively, the wind stress at locations upstream (in a wave propagation sense) of the observation site is lagged by x'/c_n, where x' is the distance from the observation site and c_n is the phase speed (negative in the Southern Hemisphere). The mode-dependent damping is such that sites farther from the observation site contribute less to the integral as they are damped en-route.

Armed with solutions to the cross-shelf modal problem and the spectrum of time-dependent wave equations, all that remains is to obtain final dimensional sums for SSH and long-shore velocity. From the definition of the streamfunction (equation 4.4) and its expansion into free wave modes (equation 4.10), we have

$$u(x,y,t) = -\frac{1}{H}\frac{\partial \psi}{\partial y}(x,y,t) = \sum_n \varphi_n(x,t)\left(-\frac{1}{H}\frac{dF_n(y)}{dy}\right) = \sum_n \varphi_n(x,t)u_n(y) \tag{4.15}$$

where

$$u_n(y) = -\frac{1}{H}\frac{dF_n(y)}{dy}. \tag{4.16}$$

To determine the SSH $\eta(y)$ we just integrate the geostrophic balance

$$\frac{f}{H}\frac{\partial \psi}{\partial y} = g\frac{\partial \eta}{\partial y} \tag{4.17}$$

between each point *y* and the oceanic edge *L* and assume that $\eta(L) = 0$. This reveals

$$G_n(y) = \int_L^y \frac{f}{g}\frac{1}{H}\frac{dF_n}{dy'}dy' \tag{4.18}$$

so that

$$\eta(x,y,t) = \sum_n \varphi_n(x,t)G_n(y). \tag{4.19}$$

To recap, the prediction proceeds as follows. For a bathymetry profile *H*(*y*) representative of the Antarctic margins, we solve the Sturm-Liouville equation (4.8) to obtain the modal structures F_n and phase speeds c_n of the free waves. From those free wave solutions we compute the wind-coupling coefficients b_n from (4.12) and the cross-shelf structures for long-shore current and SSH anomaly from (4.16) and (4.18), respectively. Then, to obtain the wave amplitudes $\varphi_n(x,t)$ at some location *x* along the coast we integrate the long-shore wind stress

along the coast on a wave characteristic via (4.14). Finally, we use the wave amplitudes and the dimensional cross-shelf structures to compute time series of u and η across the slope at x via (4.15) and (4.19). On many shelves sufficient signal can be explained with a first mode wave only (GS74; Brink 1982a; Gordon and Huthnance 1987; Schulz et al. 2012; Rivas 2017), however for reasons discussed later we consider up to three modes.

4.2.3) General coastal trapped waves

The more general class of CTW are dispersive and their modal structures and properties are influenced by stratification. These waves can be modeled with the Boussinesq, hydrostatic, linearized equations of motion (e.g., Brink 2006) as:

$$\frac{\partial u}{\partial t} - fv = -\frac{1}{\rho_0}\frac{\partial p}{\partial x} + \frac{1}{\rho_0}\frac{\partial \tau^x}{\partial z} \tag{4.20a}$$

$$\frac{\partial v}{\partial t} + fu = -\frac{1}{\rho_0}\frac{\partial p}{\partial y} + \frac{1}{\rho_0}\frac{\partial \tau^y}{\partial z} \tag{4.20b}$$

$$\frac{\partial p}{\partial z} = -g\rho_2 \tag{4.20c}$$

$$\frac{\partial u}{\partial x} + \frac{\partial v}{\partial y} + \frac{\partial w}{\partial z} = 0 \tag{4.20d}$$

$$\frac{\partial \rho_2}{\partial t} + w\frac{\partial \rho_1}{\partial z} = 0 \tag{4.20e}$$

where $\rho = \rho_0 + \underbrace{\rho_1(z)}_{\text{background}} + \underbrace{\rho_2(x,y,z,t)}_{\text{wave perturbation}}$ and $\rho_0 \gg \rho_1 \gg |\rho_2|$. These equations can be manipulated into a single equation for pressure, which serves as the analog to the vorticity equation (4.5) for BSW with zero forcing:

$$\frac{\partial}{\partial t}\left(\frac{\partial^2 p}{\partial x^2} + \frac{\partial^2 p}{\partial y^2}\right) + \left(f^2 + \frac{\partial^2}{\partial t^2}\right)\frac{\partial}{\partial z}\left(\frac{1}{N^2}\frac{\partial^2 p}{\partial z \partial t}\right) = 0\,. \tag{4.21}$$

Solution proceeds by assuming plane-wave solutions for perturbation variables and then seeking the corresponding frequency for a given wavenumber through resonance iteration and software packages (Brink 2006) exist for doing so. Qualitatively, the modes are hybrids of internal Kelvin waves and BSW and become increasingly bottom-trapped as stratification increases. It can be shown that BSW are CTW in the limit of vanishing stratification (Huthnance 1978).

In general, an analytical prediction scheme for dimensional, dispersive CTW from wind forcing is not possible. For the Antarctic environment where stratification is weak and, yet more restrictively, for the spectral region we are interested in $(\omega \ll f,\ k < 4)$, the added complexities of a stratified, dispersive model are not necessary. In this study we will obtain the CTW modes for the Antarctic bathymetry and stratification only to test the aptness of the BSW model that we employ for prediction.

4.3) Data

4.3.1) Moored current meters

Predicted velocity signals are compared to measurements of the barotropic current on the WAP shelf. We use a set of moored current meter records collected on the WAP shelf and shelf-break as part of the Pal LTER program (chapter 3; Martinson and McKee 2012). This is the same data set used in chapter 3 and we refer the reader to that source for details on the array motivation, sampling strategy, instrument uncertainty, and tidal analysis. All instruments sample at least once per hour (and are subsampled at that interval if they sampled faster) and are low-pass filtered with an ideal filter with cutoff period 2 days. Because the moorings are deployed and recovered on annual January cruises, all predictions and comparisons with data in this study will be conducted for one 'mooring-year', which is approximately 350 days long. Most

deployments contain two or more current meters sampling in the vertical (nominally one at the Winter Water T_{min} above the permanent pycnocline and one at the Circumpolar Deep Water T_{max} below the permanent pycnocline) and for each mooring all data are reduced to a single measure of 'long-shore current' which is taken as the depth average of the long-shore component of each current meter time series. Data coverage of individual current meters is given in table 3.1 of chapter 3 while data coverage of depth-average current estimates is given here in table 4.1.

We focus on two principal sites in this study: Grid station 300.100, which is on the mid-shelf in the vicinity of Marguerite Trough canyon, and grid station 200.140 which is at the shelf-break and samples the shelf-break jet before it impinges upon the canyon (figure 4.1b). These sites are chosen as they demonstrate strong long-shore variance and because they have good coverage in the vertical (six current meters at 200.140 in year 2013; three current meters at 300.100 in year 2012, two in years 2010-2011, 2014).

4.3.2) Thermistor mooring at Palmer Station E

Year-long time series from a thermistor mooring deployed at Palmer Station E (Pal E) in 2014 are used to assess implications of the barotropic variance for coastal upwelling at a submarine canyon head. The site is located at the head of Palmer Deep canyon in 158 m water (figure 4.1b). The mooring had seven SBE39 thermistors that nominally spanned 34-146 dbar in the water column, each of which were subsampled once per hour and used to construct 1-dbar temperature profiles at each time step by interpolation with a piecewise cubic Hermite interpolating polynomial. The deepest record has periodic gaps due to an EEPROM failure but this does not affect the quality of the interpolant nor our interpretation of the data.

4.3.3) Reanalysis data

We use surface stress and surface pressure from the ECMWF ERA-Interim reanalysis project. The former is used to force our velocity and SSH predictions and the latter is used to correct tide gauge records for the inverse barometer effect. Both data sets are reported on a 0.75 x 0.75 degree grid at a temporal interval of 12 hours. Unlike other major reanalysis products, ERA-Interim uses a 4D-Var assimilation scheme which should incorporate observations in a more dynamically consistent manner. Additionally, when compared explicitly to observations in the Pacific sector of the coastal Southern Ocean, ERA-Interim is found to yield a lower variance about the mean bias than other products, suggesting it is relatively more accurate at simulating specific weather events (Bracegirdle 2013). While the surface pressure is a true reanalysis variable, the surface stress is technically a forecast variable, representing the downward turbulent stress at the surface accumulated over a 12 hour forecast. As such, we divide the surface stress by the time step and assign each value a new time stamp corresponding to the middle of the 12 hour forecast window.

Ocean reanalysis data from the World Ocean Atlas 2018 (WOA18; Locarnini et al. 2018; Zweng et al. 2018) are used to construct a relevant circumpolar, coastal stratification profile for use when calculating CTW modal structures. We use the product that objectively analyzes all seasons and decades on a 0.25 x 0.25 degree grid and compute potential density from the fields of analyzed temperature and salinity.

4.3.4) Oceanic subsurface pressure measurements

In order to relate barotropic velocity fluctuations on the WAP to barotropic signals elsewhere around the circumpolar waveguide we compare them to various oceanic subsurface pressure signals described below. Most analyses in this regard will focus on year 2012 since (1)

in that year we can best estimate the barotropic current at mooring site 300.100 (3 current meters in the vertical as opposed to 2) and (2) that year provides the most complete coverage of circum-Antarctic sea level data over our sampling period. Data coverage is given in table 4.1.

We acquire tide gauge data from Faraday, Syowa, and Scott Base stations (figure 4.1a) from the University of Hawaii Sea Level Center. These are Research Quality records distributed on an hourly time step. Short-period (semidiurnal and diurnal) tidal constituents identified with a signal to noise ratio greater than 1 are removed from each record via harmonic analysis (Pawlowicz et al. 2002). To correct for the inverse barometer effect, the reanalysis surface pressure data are spatially interpolated onto the tide gauge site (with a bicubic spline) at each reanalysis time step and then interpolated in time (with a linear interpolant) onto the hourly tide gauge grid. Then, the interpolated surface pressure data are multiplied by the correction factor (1 cm sea level) / (1 mbar atmospheric pressure) and combined with the tide gauge signal. Because long-period tides (fortnightly and longer) often have low amplitude compared to weather-band variability, robust identification in year-long records is difficult and signal to noise ratios are generally low. To enhance signal to noise ratios, we examine the multiyear inverse-barometer corrected records at each site which reduces noise by distributing the non-tidal variance among more Fourier harmonics while preserving the line spectra of the tidal constituents. We find Ssa, Mm, and Mf to exhibit signal to noise ratios greater than 1 and they are removed from the multiyear time series by harmonic analysis (Pawlowicz et al. 2002). Finally, small gaps are filled with linear interpolation and a low-pass filter with cutoff period of 2 days is applied.

Tide gauge data are complemented by bottom pressure data in southern Drake Passage (Drake Passage South Deep; 1980 m depth in 2009-11, 1920 m in 2011-13; figure 4.1a) acquired from the Permanent Service for Mean Sea Level. Bottom pressure in southern Drake Passage

has been shown to correlate with ACC transport and near-coastal Southern Ocean winds south of Drake Passage (Hughes et al. 2003; Matthews and Meredith 2004) for theoretical reasons argued by Hughes et al. (1999). These data are already de-tided for short-period tides so we remove only Ssa, Mm, and Mf via harmonic analysis as described above. They are interpolated where appropriate and low-pass filtered as above.

4.3.5) Bathymetry

Bathymetry is derived from the ETOPO5 product (National Geophysical Data Center 1988) which reports surface depth and elevation values on a 5 minute by 5 minute global grid. We use the coarser ETOPO5 product in place of the newer ETOPO1 since we ultimately need a smoothed representation of the topographic slope and coastal pathway and the details of small-scale bathymetric features are not important for long waves with wavelengths on the order of thousands of kilometers.

To locate the continental shelf-break, the ETOPO5 bathymetry data are further smoothed in a two step procedure. Firstly, the 5-minute data are bin-averaged into [2º longitude, 1º latitude] bins and then those binned data are smoothed again by averaging each cell with its neighboring 8 cells. On the resulting grid, cells with bottom depth shallower than -100 m are set to 0 m and treated as land. From this smoothed database we extract the location of the -1500 m isobath to define the Continental Shelf-Break Contour.

To locate the coast, the smoothing procedure is repeated as above except the bottom depth values are gridded onto [1º longitude, 0.5º latitude] bins before averaging with their 8 neighboring values and this finer database is used to extract the location of the -100 m isobath, which defines the Coast Contour. Both contours are shown in figure 4.1a.

4.4) Methods

4.4.1) Characterizing the wave propagation environment

The wave propagation environment defines the wave modal properties (cross-shelf structure and phase speeds) and the pathway upon which the waves are forced and propagate. The environment is defined by the cross-shelf bathymetry profile $H(y)$, the curvature of the coastline (and the surface stress parallel to the coastline), and the background stratification $N(z)$. We describe here how those quantities were estimated.

4.4.1.1) Defining the cross-shelf bathymetry profile

The procedure used to construct a bathymetric profile $H(y)$ is shown schematically in figure 4.2. Since the continental shelf-break is generally smoother than the coast, we use the Continental Shelf-Break Contour to define the direction of the large-scale coastal tangential and normal vectors. For every location x on the contour we approximate a local Cartesian, planar coordinate system and apply orthogonal least squares to the geographic coordinates of x and its two neighboring values, yielding a local tangential angle β. We then discretize the Continental Shelf-Break Contour into 100 evenly spaced segments x_i and linearly interpolate the latitudes, longitudes, and tangential angles β onto those segments. The tangential angle β_i defines the local tangential $\left(\hat{\mathbf{t}}_\mathbf{i}\right)$ and normal $\left(\hat{\mathbf{n}}_\mathbf{i}\right)$ vectors. We then grid the raw ETOPO5 bathymetry onto a path r_i^b normal to the Shelf-Break Contour 800 km in each direction (seaward and shoreward) spaced at 5 km (which is approximately the average of 5 minutes in the meridional and zonal directions for the relevant latitudes). After constructing 100 such bathymetric profiles around the continent $H_i\left(r_i^b\right)$, we find where each one intersects the smoothed Coast Contour. This is used to adjust

the cross-shelf coordinate so that for each profile, the location $y = 0$ is the position of the coast $\left(H_i\left(r_i^b\right) \to H_i\left(y\right)\right)$.

At this point, the 100 bathymetric profiles can be averaged in the long-shore dimension to construct a single representative bathymetric profile $H(y)$ felt by the waves. For very long waves (wavelengths of thousands of kilometers) and for wavenumber zero variability, the relevant bathymetric profile should span the entire continent. We therefore define our Circumpolar bathymetry profile as the average of all profiles $H_i\left(y\right)$ with x_i found in the ranges 0 - 150 ^{o}E and 200 - 300 ^{o}E where we have excluded only the Weddell and Ross Seas. We exclude those seas since the bathymetry and coastline under their associated ice shelves are relatively unknown and, because the shelves are so broad, they would bear a strong (and uncertain) influence on the long-shore average. This is the same averaging domain used by Kusahara and Ohshima (2009).

We also consider a local WAP bathymetry profile to diagnose how modal properties differ in the local environment compared to the circumpolar average. This is constructed by averaging the bathymetric profiles for segments x_i found in the range 280 - 300 ^{o}E.

4.4.1.2) Defining the path of wave propagation

The integral along wave characteristics to determine wave amplitude (eqn. 4.14) requires a path upon which to integrate the lagged long-shore wind stress. The wave propagation pathway is taken to be the Continental Shelf-Break Contour. The contour is discretized as in section 4.4.1.1 with the additional detail that the location $x_0 = 0$ is always defined to be the location on the contour linearly interpolated so as to be closest to the mooring or tide gauge site where we are predicting the velocity (or subsurface pressure) signal.

To obtain the wind stress series that forces the waves along their axis of propagation, we do the following. The eastward and northward ECMWF surface stress components are bilinearly interpolated onto a section r_i^w normal to the discretized Continental Shelf-Break Contour (figure 4.2) with cross-slope spacing 50 km (which is approximately the average of 0.75 degrees in the meridional and zonal directions at the relevant latitudes) at each time step. Then, the interpolated surface stresses on r_i^w are each dotted into $\hat{\mathbf{t}}_\mathbf{i}$ to yield long-shore wind stress profiles across the slope. Finally, the single long-shore wind stress at x_i is defined as the long-shore wind stress averaged on r_i^w between the Continental Shelf-Break and Coast Contours.

Note that since the 100 evenly spaced positions are chosen such that $x_0 = 0$ is the location of prediction, a consequence is that the actual locations of the wind stress that go into the integral (4.14) are different for the different mooring and tide gauge sites.

4.4.1.3) Defining the background stratification

While the BSW modal properties can be determined from a bathymetry profile alone, the CTW modal properties also need a stratification profile. Stratification associated with the Circumpolar bathymetry profile is computed from the WOA18 by isolating all temperature and salinity profiles in the same longitudinal domain used to define the averaged bathymetry profile (with bottom depth shallower than 3000 m), computing potential density on those profiles, averaging them all on their native depth levels, and finite differencing the composite potential density profile to compute buoyancy frequency $N(z)$.

To compute a relevant stratification profile for the WAP environment, we follow the procedure in Appendix A (used in chapter 2) which isolates all historic summertime Pal LTER CTD profiles, finds the average depth of a set of standard isopycnals, and finite differences the resulting average density profile. Because overturns become apparent shallower than 24 m, the

value of the $N(z)$ profile at all depths shallower than 24 m is set to the value at 24 m. This ensures that when the CTW modal analysis software discretizes the vertical grid it reads in one value in each of the seasonal and permanent pycnoclines.

4.4.2) Wave properties and modal analyses

BSW modal properties are obtained in order to predict SSH and long-shore current from reanalysis wind stress and then compare the predictions to observations. CTW modal properties are obtained strictly to assess the validity of the barotropic and long-wave assumptions used in the BSW model. All modal analyses evaluate f at 67 ºS. We consider four bathymetric profiles in each analysis: (1) Circumpolar profile; (2) Circumpolar profile with bottom depth capped at 4000 m; (3) WAP profile; (4) WAP profile with bottom depth capped at 4000 m. The reasons for capping the bottom depth will be discussed in the results section.

4.4.2.1) Barotropic shelf waves

The BSW modal properties are obtained from the eigenvalue problem (4.8) and are solved for numerically as outlined in Appendix D. After solving the eigen-system, long-shore current is obtained from equation (4.16) and SSH from (4.18). Finally, equation (4.12) yields the wind-coupling coefficients. All calculations assume a uniform density $\rho_0 = 1027$ kg m^{-3}.

4.4.2.2) General coastal trapped waves

The CTW modal properties are obtained numerically with the inviscid bigr*.m software package (Brink 2006). The model grid is discretized into 80 cross-shore points and between 40 and 44 vertical points (depending on maximum bottom profile depth) which ensures accurate representation of the cross-slope bathymetry and of the major features of the water column stratification, respectively. The model is run with a rigid lid, a closed boundary condition at the coastal $y = 0$ boundary and an open boundary condition at the seaward boundary, and wave

solutions are obtained for wavenumbers 1-10. Although the model framework allows for it, we do not consider the effect of a background long-shore flow.

4.4.3) Detection and prediction of wavenumber zero variability

4.4.3.1) Detection

Circumpolar-coherent, wavenumber zero variability is identified in the data via empirical orthogonal function (EOF) decomposition of the lag-zero covariance within the array of circumpolar tide gauge series in years 2011 and 2012, which afford the greatest coverage around the continent. The time series at each site are reconstructed using EOF1 alone and then averaged to obtain a single index of dimensional, coastal wavenumber zero variability that is compared to an analytical prediction.

4.4.3.2) Prediction

A time series of wavenumber zero variability is calculated from equation (4.2). To implement this, the long-shore wind stress is calculated as in section 4.4.1.2 and the wavenumber zero amplitude and phase at each frequency are extracted via a two-dimensional Fourier Transform. In the integral, we assume that L_{coh} = 450 km as this is where the bathymetric profile becomes substantially flatter. This parameter affects only the amplitude of the prediction and not its phasing. As for the frictional parameter, we use a value r_t^{-1} = 5 days as this yields good agreement between the phasing of the prediction and the observations, and also because this value yields good results for the prediction of the BSW signal. Kusahara and Ohshima (2009) conducted a similar analysis and recommended a value of r_t^{-1} = 5 or 10 days. The parameter r_t is discussed more in the next section.

4.4.4) Detection and prediction of barotropic shelf waves

4.4.4.1) Detection

We seek out wave signatures in the data in order to obtain optimal phase speeds and compare them to the theoretical ones. The incredibly sparse sampling around the continent makes this difficult. Firstly, the sparseness in space renders most wave modes severely aliased in space (though not in time) thus eliminating the usefulness of most spectral approaches. Even if the data coverage were sufficiently dense, the uneven spacing of time series along the coast makes most quantitative analyses of hovmöller-type matrices inapplicable (e.g., the Radon Transform; Lecointre et al. 2008).

Our approach is to find the phase speeds that maximize the cross-characteristic variance for the hovmöller matrix $\mathbf{d}^{\text{waves}}_{\text{circumpolar}} = d(x,t)$ whose columns are the five time series from the various moored current meters and subsurface pressure sensors available around the continent in 2012 (or the four time series in 2013; table 4.1) after an estimate of the coherent mode has been removed (first EOF of the data band-pass filtered to retain variance with periods 10-200 days; $\mathbf{d}^{\text{waves}}_{\text{circumpolar}} = \mathbf{d}_{\text{circumpolar}} - \mathbf{d}^{\text{BPF, EOF1}}_{\text{circumpolar}}$). This cross-characteristic variance is quantified in the parameter

$$R_j = \text{Var}\left[\sum_{i=1}^{5} d\left(x_i, t + \frac{x_i - x_1}{c_j}\right)\right] \tag{4.22}$$

where the sum is carried out along a wave characteristic for each trial phase speed -30.0 m $s^{-1} \leq c_j \leq$ -0.5 m s^{-1} and the variance is taken over all time. Qualitatively, this iterative procedure rotates the hovmöller matrix into coordinates along and perpendicular to trial wave characteristics. If the corresponding phase speed c_j is present within the data, the temporal variance of the along-characteristic sum will be maximal. This method is similar in spirit to the Radon Transform but is feasible with unevenly spaced data. We compute R_j for $\mathbf{d}^{\text{waves}}_{\text{circumpolar}}$ and

for $\mathbf{d}_{\mathrm{WAP}}^{\mathrm{waves}}$, which is the same matrix except only the three time series collected on the WAP are retained. This allows us to see if local wave propagation on the WAP differs from that around the entire continent.

In addition to determining whether or not propagating signals exist in the data, this analysis serves to help us determine which bathymetry profile yields the most appropriate modal properties to use in our predictions.

4.4.4.2) Prediction

The major calculation prepared in this study is the prediction of dimensional long-shore current and SSH on the WAP within the framework of barotropic dynamics forced by long-shore surface stress. This is computed as the sum of wavenumber zero variability (calculated from equation 4.2 as described in section 4.4.3) and of barotropic shelf waves (calculated from equations 4.15 and 4.19 as described here). The predictions are then compared to observations measured by moored current meters and coastal tide gauges on the WAP in the time domain (by correlation analysis) and in the frequency domain (by coherency analysis).

The BSW signal for long-shore current is summed cumulatively over three modes. To compute the amplitude in equation 4.14, the long-shore wind stress along the wave path is that described in section 4.4.1.2 where the contribution from the segment at x_i is lagged by the mode-dependent time lag $T_n(x_i) = \left(x_i - x_0\right)/c_n$ which represents the time it takes for an Ekman flux perturbation generated at x_i to reach the observation site $x_0 = 0$ if it propagates at the phase speed c_n. Wind stress over each segment at the appropriate time lag is calculated from the gridded data by interpolation in time with a cubic Hermite interpolating polynomial. To acknowledge the periodic domain, the wind-wave pathway is effectively unwrapped and duplicated twice around the continent. The wave properties and cross-shelf structures are calculated following the

procedure in section 4.4.2.1 and predictions of long-shore velocity are evaluated at the shoreward-most location of the 450 m isobath (which represents a typical mooring depth) and predictions of SSH are evaluated at the coast ($y = 0$).

Predictions are computed on the 12-h grid of the reanalysis data. Wavenumber zero variability is removed from the wind stress space-time series via a 2D Fourier Transform (since wavenumber zero variability manifests via the coherent mode dynamics, not BSW) and additional temporal filtering is applied through a 2D ideal filter. A high-frequency cutoff period of 3 days is imposed so that the mode 1 wave is approximately nondispersive and a low-frequency cutoff period of 100 days is used to represent the full spectrum of intraseasonal variability. To compare the data to the predictions, they are linearly interpolated (effectively subsampled) onto the reanalysis grid prior. Predictions are made and evaluated at grid sites 300.100 (mid-shelf, near Marguerite Trough), 200.140 (near the shelf-break, upstream of Marguerite Trough), and at Faraday tide gauge, where we have data with which to evaluate them.

In equation (4.14), the linear damping coefficient is $r_n = r_t / c_n$ and therefore varies for each mode: higher order (slower) modes are damped more than lower order (faster) modes. As this parameter serves as the exponential weight for the lagged wind stress, it indicates that higher order modes are increasingly dependent on local wind stress as opposed to remote wind stress. Note, however, that even if the spatial damping scale is small this does not mean that the wavelengths of the waves are short. Instead it means that the information content of the wind systems that force the waves exists in the wave memory for only a relatively short distance.

The parameter r_t has dimensions time^{-1} and can be regarded as a resistivity coefficient r (with units of velocity) divided by the column depth H. A canonical resistivity coefficient used in the literature is $r = 0.05$ cm s^{-1} (Brink 2006). Empirically, it can be calculated from $r = C_D u_{\text{rms}}$

where $C_D = 0.003$ is a drag coefficient and u_{rms} is the rms deviation of near-bottom long-shore velocities (Brink 1982b). We do not have measurements of near-bottom velocities but rms mid-depth long-shore currents are about 8 cm s^{-1}. For a typical shelf depth of 450 m, the above suggests $r_t^{-1} \sim 10.4$ or 21.7 days. We find setting $r_t^{-1} = 5$ days yields good results for prediction of BSW amplitude and phase and hereby use that value throughout (note that while the damping parameter does not affect the amplitude of the coherent mode, it does affect the amplitude of the BSW by permitting a larger or smaller contribution of the wave history).

Importantly, note that we have followed GS74 by simply adding a linear damping term to the wave equations as opposed to formally including attenuation in the original model. More sophisticated treatments model damping with a bottom Ekman layer friction (e.g., Brink and Allen 1978; Brink 1982b). In such cases, because the bottom stress depends on the variable bottom depth, friction causes wave energy to be scattered among modes, coupling them together in a manner that is not considered here (or by GS74). Brink and Allen (1978) use perturbation methods in the limit of small Ekman number to show that the wave amplitude is approximately governed by a zeroth order wave equation identical to equation (4.13b) with damping parameter $r_n = \left[A_v \left(2fH_{\text{coast}}^2 \right)^{-1} \right]^{1/2} a_{nn}$ and a first order wave equation that introduces the coupling. The a_{nn} for the circumpolar-capped profile yield $r_t^{-1} \approx 5$ days for both mode 1 and 2, which is the number we suggested empirically. Treatment of damping in the GS74 model is empirical and its function is not limited to bottom friction. Their $r_n = r_t c_n^{-1}$ represents attenuation by any process which may include friction, effects of scattering, and other attenuation processes related to dissipation or morphological changes in the continental slope. Waves may be scattered, for example, by rapidly turning coastlines or other topographical irregularities (Griffin and

Middleton 1986). The sharply turning coastline at Drake Passage and obstruction by the South Shetland Islands near Bransfield Strait may significantly impact wave propagation in ways that could be comparable to the effects of friction causing us to prefer the more general approach of GS74. In short, our treatment of damping can be regarded as an empirical term encompassing multiple attenuation processes or as a zeroth order treatment of Ekman layer friction.

4.5) Results

4.5.1) Modal structures and validity of the barotropic and long-wave assumptions

The BSW and CTW dispersion relations for each bathymetry profile are shown in figure 4.3 and the bathymetry profiles and the BSW and CTW modal structures are shown in figures 4.4-4.7. The circumpolar-averaged bathymetry profile (figure 4.4) does not exhibit a very prominent continental shelf because it is constructed by averaging regions with broad shelves (e.g., Amundsen Sea) along with regions with narrow shelves (e.g., Eastern Weddell Sea). The major continental slope is within about 450 km from the coast, though the bathymetry continues falling to ~4500 m at 800 km from the coast. The dispersion relation suggests that BSW and CTW properties agree well in the long-wave limit, certainly for wavenumbers $k \leq 3$ (figure 4.3). Out as far as wavenumber $k = 10$, the curves' maximum frequencies are not reached and waves are not short. The stratification has almost no effect on the wavenumber-frequency relationship because the circumpolar composite stratification profile from WOA18 is very weak. While there is not a clear shelf-break for this profile, the mode $n = 1$ BSW structure for SSH is largest near the coast and the corresponding velocity structure is of uniform sign. Mode $n = 2$ SSH has a maximum over the steepest part of the continental slope and thus the velocity structure changes sign there. The CTW modal structures are essentially unstratified over the entire domain and

have the same inflection points as the BSW modes. There is a hint of baroclinicity and bottom trapping over the slope, but this isn't very pronounced. Note that unlike the CTW, the BSW structures go to zero at the seaward boundary because equations (4.18-4.19) really give the SSH anomaly relative to that at the seaward boundary, which we have assumed is zero.

The WAP profile (figure 4.5) has a well-defined continental shelf of ~150 km width adjacent to a steep continental slope, followed by a more gradual roll-off. The profile reaches 4000 m depth at about 500 km from the coast and continues falling to ~4400 m at 800 km from the coast. The phase speeds for the WAP bathymetry are faster (figure 4.3). This is consistent with the continental shelf being more pronounced and, thus, wider with steeper slope (Huthnance 1978). Again, the BSW and CTW agree well in the long-wave limit, at least for wavenumbers $k \leq 3$. In general, maximal frequency for each mode is not reached and the waves are not short, with the possible exception of the $n = 2$ wave in the case where the WAP bathymetry is set to a constant value when it reaches 4000 m. The mode $n = 1$ BSW structure for SSH has amplitude confined to the continental shelf, out to just past the edge of the shelf-break (figure 4.5). Consequently, the $n = 1$ velocity structure has ~uniform amplitude over the shelf. The $n = 2$ SSH structure has largest amplitude over the steepest part of the slope meaning that the $n = 2$ velocity changes sign there. Much like the case of the circumpolar profile, the CTW modes are essentially unstratified and their inflection points mirror those of the BSW, with the exception that baroclinicity over the continental slope is more pronounced than it is for the circumpolar profile. For the WAP, both stratification and bottom slope α at the continental slope are larger than the Circumpolar average. Baroclinicity of CTW depends on both the bottom slope and stratification through their combined influence via the Burger number (Huthnance 1978, 1981),

$$\mathrm{Bu} = \left(\frac{NH}{fL} \right)^2 = \left(\frac{N\alpha}{f} \right)^2, \tag{4.23}$$

which is larger over the slope for the WAP. We emphasize, however, that for both bathymetry profiles, the modal structures at the mooring prediction sites are essentially barotropic and that the dispersion relations are almost identical to those when setting $N(z) = 0$. Consequences of the baroclinicity over the slope for shelf-slope exchange will be considered in the Discussions section.

For both bathymetry profiles discussed thus far, modal structures and phase speeds vary slightly when allowing the bathymetry to fall to its natural bottom depth at the edge of the domain (800 km) versus when capping the bathymetry at a fixed depth of 4000 m. In general, not capping the bottom depth has the effect of increasing the phase speeds (figure 4.3 panels a and c versus panels b and d) and 'dragging' the modal structures seaward (figures 4.4 and 4.5 versus figures 4.6 and 4.7). These effects are more pronounced for higher mode waves ($n > 1$) and for the Circumpolar profile, likely because that profile does not have a well-defined continental shelf-break and associated vorticity gradient to 'anchor' the modes. This behavior tends to 'stretch' the SSH modal amplitude without affecting its amplitude, however that means the velocity modal amplitude will be much weaker since the SSH gradient is reduced. The reason why modal amplitude persists far from the coast is because the seaward boundary condition is for no long-shore flow at the seaward edge of the domain. So as long as there is a bathymetry gradient (and hence vorticity gradient), however far from the coast, there will be modal amplitude. It is not clear how physically correct this behavior is. In any circumstance, a choice must be made when preparing a bathymetry profile, and any choice is subjective and somewhat artificial.

We will use the bottom-capped circumpolar profile in all wind-driven predictions (BSW and wavenumber zero variability) as we will show that its associated phase speeds are close to

those that emerge in our search for BSW within the data and it yields a coherent mode with comparable amplitude to that observed. We will consider the range of phase speeds (all four profiles) and the possible effects of dispersion when analyzing our predictions. Overall these results indicate that the waves can be treated as BSW on the continental shelf in the low-frequency range of predictive interest.

4.5.2) Inverse detection

4.5.2.1) Coherent mode

The depth-averaged long-shore current at site 300.100 is plotted in figure 4.8a along with the pressure-corrected Faraday, Syowa, and Scott Base tide gauge signals and a Drake Passage bottom pressure signal. As indicated in figure 4.1a, the three tide gauge records available in year 2012 provide a reasonably complete spatial coverage around the continent. On these time scales, the series are well correlated to the barotropic velocity signal at 300.100 (correlation coefficients indicated in figure). The correlation is strongest with the nearby Faraday SSH signal (~277 km downstream), but the correlations are statistically significant (at the 1% level) with the other series. The zero-lag correlation is clearly dominated by large swings with period 40-60 days, which will be discussed later. A similar plot is made for the depth-averaged long-shore current at site 200.140 (figure 4.8b). For that site, correlations with available circum-Antarctic subsurface pressure series are all weaker, suggesting that coherent-mode variability may be less important than other processes at the shelf edge.

Significant zero-lag correlation around the continent requires that some amount of the velocity variance consists of a coherent mode, and that amount is quantified here. While the time series are visually similar and well correlated to each other, we quantitatively identify a coherent mode via an EOF decomposition of the covariance matrix between the different time

series at zero lag. We consider a dimensional estimate of the coherent mode by decomposing coastal SSH signals only ('T.g.') and we consider a second estimate that takes advantage of all available time series, additionally including the Drake Passage Bottom pressure and the depth-average current meter series ('T.g., DPS, U'). When decomposing series of different variables we must standardize them before computing covariances. In each case, the first EOF is clearly 'a coherent mode' in the sense that EOF weights for each constituent time series are of same sign. EOF1 explains either 67% ('T.g.') or 63% ('T.g., DPS, U') of the total intraseasonal variance. The correlation coefficients of the two estimates against each other and against the 300.100 velocity signal are given in table 4.2.

To verify that the detected coherent variability is wind-driven, we compare the detected coherent mode with a wind-driven prediction using equation 4.2 and the circumpolar-average bathymetry capped at 4000 m. The dimensional estimate is recomputed via EOF analysis using the 2012 tide gauge data band-pass filtered to retain periods of 10-200 days. Then, we reconstruct the SSH at each site from EOF1 only and average all of them, yielding an average amplitude of SSH that is spatially coherent around the continent. The detected and predicted series are plotted together in figure 4.9. The two are reasonably well correlated ($r = 0.69$, $p \approx 0$) and have similar amplitude (though the prediction tends to be somewhat larger). Further, in the frequency domain, the phase lag is negligible where the coherence is significant at the $\alpha = 0.05$ level, suggesting a good choice of damping parameter (figure 4.9c). Analysis of year 2011 (same spatial coverage as 2012) yields similar results ($r = 0.65$, $p \approx 0$).

We have shown that a coherent mode can be detected from tide gauges only and/or tide gauges along with bottom pressure and current meter series and that the two estimates are similar (table 4.2). The detected coherent mode explains over 50% of the intraseasonal long-shore

velocity variance at 300.100 in 2012. The detected coherent mode is consistent with the analytical model, having similar amplitude (figure 4.9a) and small phase lag over the periods predicted (figure 4.9c).

4.5.2.2) BSW

Propagating signals are detected through analysis of hovmöller matrices with the coherent mode removed. The parameter R_j (equation 4.22) is presented in figure 4.10 for matrices $\mathbf{d}^{\text{waves}}_{\text{circumpolar}}$ and $\mathbf{d}^{\text{waves}}_{\text{WAP}}$ for years 2012 and 2013. Importantly, we found that our results are strongly dependent on the Drake Passage South bottom pressure series. We determined that that series should be multiplied by -1. This is because that site is located at 1920 m depth, midway across the continental slope where the $n = 2$ wave has large, oppositely signed amplitude compared to its value at the coast (figures 4.4, 4.6) and where the $n = 1$ wave is less important.

When flipping the sign of the Drake Passage bottom pressure series, R_j for the 2012 data yields two peaks, one each near the $n = 1$ and $n = 2$ BSW phase speeds for circumpolar bathymetry capped at 4000 m (figure 4.10a). This is apparent when decomposing $\mathbf{d}^{\text{waves}}_{\text{circumpolar}}$ (solid lines). When decomposing $\mathbf{d}^{\text{waves}}_{\text{WAP}}$ (dashed lines), R_j has a single peak at the $n = 2$ speed, suggesting that the $n = 1$ wave may be locally less important on the WAP. If we do not flip the sign of the Drake Passage bottom pressure series then the $n = 2$ wave is not detected and instead there is a broad maximum between phase speeds -22 m s^{-1} and -6 m s^{-1} which includes the theoretical $n = 1$ speeds for all bathymetry profiles (figure 4.10c). This makes sense because the $n = 2$ signal is rendered incoherent if the sign is not flipped.

Results for 2013 data (with 200.140 current instead of 300.100 current and with no signal at Scott Base) are similar, although less convincing. When the sign of the Drake Passage bottom pressure series is flipped, there is a peak in R_j at the $n = 2$ phase speed as expected, but no peak

at the $n = 1$ speed (figure 4.10b). Recall that there are no data from Scott Base in 2013, leaving over half of the continent unrepresented in $\mathbf{d}^{\text{waves}}_{\text{circumpolar}}$. Additionally, recall that the $n = 1$ wave is less important than the $n = 2$ wave on the WAP (figure 4.10a and discussion above), which hosts 75% of the time series included in the matrix in 2013. Hence, it is possible that data around the entire continent are required to robustly detect the $n = 1$ wave. If we do not flip the sign of the Drake Passage bottom pressure series then the peak at the $n = 2$ phase speed goes away (as it did in the 2012 data) and a peak near to, but slightly slower than, the $n = 1$ phase speed emerges (figure 4.10d). An additional very large peak in R_j exists near the $n = 3$ speed. This is not investigated further.

Overall this analysis suggests that signals with propagation speeds near the theoretical $n = 1$ and $n = 2$ (and maybe $n = 3$) BSW speeds for circumpolar bathymetry capped at 4000 m can be detected in our current meter data in conjunction with circum-Antarctic subsurface pressure series. It also suggests that the $n = 2$ wave is unusually important on the WAP.

4.5.3) Prediction of total signal and comparison to data

The combined results of sections 4.5.2 suggest that a coherent mode and propagating signals can be detected in time series collected on the WAP. In this section we show that much of the variance in those series can be predicted from the same long-wave barotropic theory forced by surface stress data. We carry out dimensional predictions of the long-shore velocity at the long-shore location (x) of each mooring site and cross-shelf distance (y) corresponding to the approximate isobath of mooring depth (450 m), for every time step (t) of each mooring-year that we can compare to the observed barotropic current (the years in table 4.1). Predictions include the wavenumber zero mode summed cumulatively with the $n = 1$, 2, and 3 waves and are carried out with the surface stress filtered to retain periods 3-100 days beforehand.

4.5.3.1) Long-shore current at 300.100

Correlation coefficients for all predictions are shown in table 4.3, time series of a representative prediction (year 2012) are shown in figure 4.11, and coherency and cross-phase spectra for the same prediction against observations are shown in figure 4.12. Overall, the quality of the predictions is quite good, being able to explain on average about 50% of the velocity variance at site 300.100. The table suggests that the total variance explained tends to be similar for each year, but sometimes it comes from different sources. Notably, the importance of the coherent mode varies year by year. Inspection of the time series (figure 4.11) reveals that, in addition to the phasing between the signals agreeing, thus yielding the positive correlation coefficients, the amplitude of the prediction is remarkably close to the observed. The similarity of the amplitudes lends credence to the physical model representing the appropriate transferal of any covarying wind signal to the ocean. The table and time series reveal that there is generally substantial improvement in the correlation when introducing the $n = 2$ wave.

The coherency spectra (figure 4.12) suggest that the wavenumber zero mode contributes most at periods longer than 20 days. The first mode wave is most coherent at periods 5-15 days while the second mode is most coherent at periods longer than ~7 days, and the coherency in general seems to increase with decreasing frequency. Phase lags are small where coherency is significant at the 5% level (figure 4.12), and by the time the wavenumber zero mode is summed with the two BSW, coherency is generally significant over the full spectrum with small phase lag, suggesting most of the essential physics have been captured.

The predictions utilize a fixed set of modal structures and phase speeds corresponding to a representative bathymetry profile. To evaluate the quality of the chosen phase speeds we conduct a bootstrapping procedure that assesses the quality of prediction for arbitrary phase

speeds. Specifically, after removing the predicted wavenumber zero mode from the observed time series, we consider pairs of all phase speeds $c_{n,j}$ in the range -30.0 m s^{-1} $\leq c_{1,j} < c_{2,j} <$ 0.0 m s^{-1} at 0.5 m s^{-1} increments and for each pair we fit the function

$$U_{\text{obs}}(0,t) = \sum_{n=1}^{2}\left[A_{n,j} \int_{x_{\text{inf}}}^{0} \exp\left(-x' r_t / \left|c_{n,j}\right|\right) \tau^{x}\left(x', t + \frac{x'}{c_{n,j}} \right) dx' \right] + \varepsilon \tag{4.24}$$

to the observed time series via linear regression, solving for arbitrary amplitudes $A_{1,j}$ and $A_{2,j}$. For each fit we compute the correlation coefficient between the observations and the test prediction (eqn. 4.24 with the best fit amplitudes). The function is also fit at each trial phase speed to our actual wind-driven prediction and we compute the correlation coefficient between the actual prediction and the test predictions. The latter evaluates how much spread we should expect to see in the correlation coefficients if the data truly constitute the sum of two BSW. This is done for every mooring-year and symmetric matrices of correlation coefficient squared as a function of trial phase speeds are computed and averaged together over all mooring-years.

Figure 4.13 shows the averaged correlation coefficients for the trial predictions against the actual prediction (left) and the data (right). The phase speeds used in the actual prediction are shown as a black square along with grey 'axes' indicating possible dispersion from the CTW modal curves for each bathymetry profile (see figure caption). Also shown are the best fit trial phase speeds for each year of data (blue circles). Overall, the plots agree remarkably well. The contours on each plot have the same sense, with two very fast or two very slow waves fitting poorly and similar overall shapes for the contours. The trial fits to observations do not separate into two ridges as do the trial fits to the actual prediction, though this may be because in reality the phase speeds vary along the axis of propagation. There is a bit of scatter in the best fit phase speeds for each year although their average over all years is close to the phase speeds of the

chosen bathymetry (compare the center of mass of the blue dots to the black square). The contour of high correlation continues towards the upper right of the matrix, suggesting decreasing phase speeds, consistent with increasing dispersion at increasing frequency. There is some evidence that the phase speeds corresponding to WAP bathymetry (left-most two grey axes) fall on the ridge of high correlation coefficient, but they are not as close to the optimal pairs of trial phase speeds as are the circum-Antarctic phase speeds (right-most grey axes and black square and axes).

We note that comparisons of prediction to data (via all methods described above) improve slightly upon introduction of a small lead time to the wind stress (less than a day) and/or upon projecting the wind stress vector onto a tangential (figure 4.2) determined from latitude / longitude coordinates as opposed to one determined from absolute geographical coordinates. However, as these choices are not easily justifiable, they are not considered further.

4.5.3.2) Long-shore current at 200.140

For mooring site 200.140, an analogous set of plots (figures 4.14-4.16) and correlations (table 4.3) were constructed. With the inclusion of the coherent mode and the first three BSW, 47% of the total velocity variance can be explained. The results are similar to those at site 300.100 except overall point to the $n = 2$ wave contributing far more at this site (compare the increase in variance explained with its addition to each site's signal; table 4.3). For example, inspection of the time series (figure 4.14) indicates that the mode is strongly dominated by very sharp variations with period 40-50 days. However, although at low frequency, these fluctuations do not actually come from the coherent mode (figure 4.14, top). Instead, the greatest increase in amplitude comes from the inclusion of the $n = 2$ BSW (figure 4.14, third panel), with a large increase in correlation coefficient and alignment of extrema.

Although less apparent in the time domain, analysis in the frequency domain (figure 4.15) suggests that the $n = 1$ wave does contribute at periods of ~5 and ~15 days and suggests that the second mode is important at periods longer than about 5 days, which would span the full range of wavenumbers evaluated for the dispersive CTW. Again, when summing the coherent mode with the first two BSW, coherency is significant over almost the entire spectrum with small phase lag (but larger than for 300.100).

Inspection of the matrix of correlation coefficients corresponding to the trial phase speed bootstrapping analysis (figure 4.16) also suggests that there is a ridge of high correlation at a phase speed near the circum-Antarctic $n = 2$ phase speed with little concern for what the other wave's phase speed is, although there is a slight increase in correlation for an optimal $n = 1$ speed that is slower than the theoretical.

4.5.3.3) SSH at Faraday tide gauge

For Faraday tide gauge, a corresponding set of figures is constructed (figures 4.17-4.19) and correlation coefficients calculated (table 4.3). Correlation coefficients in the time domain are not as good as those for velocity, seemingly because, while the phasing of the signal seems to be predicted well, the amplitudes of the higher-period fluctuations (periods of a few days) are overestimated (figure 4.17). An overestimate of the coastal amplitude is likely due to our assumption that the SSH anomaly at the domain edge is zero, which changes the nodal points of each mode. On average, only 35% of the SSH variance can be explained.

In the frequency domain (figure 4.18), coherence with the wavenumber zero coherent mode is strong at periods longer than ~20 days with small lag, as was seen for the velocity at site 300.100. The $n = 1$ wave is significantly coherent (at a 5% level) with the data at small phase lag for periods between about 5 and 15 days. Strangely, there is strong coherency at periods longer

than ~20 days that is in quadrature with the observations. The $n = 2$ wave is significantly coherent (but not necessarily of large amplitude) with small phase lag for most periods longer than about 7 days. Finally, when the two modes are summed with the coherent mode, the prediction and data are significantly coherent over most of the spectrum with small phase lag, as was the case for the velocity predictions.

Consistent with the unimportance of the $n = 2$ wave near the coast, correlation coefficients do not improve with its inclusion (table 4.3; figure 4.17). In addition, the bootstrapped trial phase speed predictions are sensitive to primarily one wave mode, which is near the circum-Antarctic $n = 1$ speed, but slower (figure 4.19). The spread in the best fit trial phase speeds is larger than it was for site 300.100 (compare figures 4.13 and 4.19) though we suspect this is because the residual signal is contaminated by subtracting an overestimate of the coherent mode (compare data to observations in figure 4.17) before fitting. Note that for this location we sought optimal phase speeds with absolute value greater than 1 m s^{-1} as there is an unexplained band of high correlation for very slow phase speed, inconsistent with the BSW.

4.5.4) Properties of the predictions

Here we assess the frequency content of the predictions. This sheds some light on their underlying properties, including any resonances, and provides necessary information to understand temporal variability of the barotropic dynamics and links to climate forcing. To do so, we estimate the power spectral density of the $n = 1$, $n = 2$, and coherent mode long-shore current signals over the entire range of prediction (2008-2017) for all time and for winters only, where winter is defined to span May through October. The spectra over all time use 50% overlapping 180-day Hanning windows (figure 4.20, top row) while the winter-only spectra average all of the 183-day unwindowed May-October spectra (10 spectra). Because the surface

stress was filtered to retain periods between 3-100 days prior to prediction, all spectra are presented within those bounds.

The $n = 1$ spectrum has largest amplitude at the middle of the frequency range. Superimposed atop that background spectrum are three peaks, one each at periods near ~15.5, ~7.8, and ~5.2 days (black wedges in panel a), the former two of which are significant at the $\alpha =$ 10% level (see figure caption for details about null spectrum estimation). Assuming a circumpolar wavelength corresponding to the circumference of the Earth at 67 ^{o}S (15641 km), these periods correspond to integer wavenumbers of 1, 2, and 3. The $n = 2$ wave spectrum is shifted towards lower frequency. In the all-time spectrum (figure 4.20b) there are no apparent peaks however in the winter-only spectrum (figure 4.20e) there are peaks at periods near ~43.4, ~21.7, and ~14.5 days, the first and last of which are barely significant at an $\alpha = 10\%$ level. Assuming the same circumpolar wavelength these correspond approximately to integer wavenumbers of 1, 2, and 3. The spectrum for the coherent mode is much redder and seems to peak at a period slightly longer than 40 days (figure 4.20c, white wedge). This peak becomes statistically significant at the same level in the winter-only spectrum (figure 4.20f).

The integral (4.14) for wave amplitude is analytical if the wind stress takes the form of a progressive wave, $\tau^x = \tau_0(k,\omega)\cos(kx - \omega t)$. It can be shown that, when subject to linear damping, there is a response at both the forcing frequency and at the free wave frequency (GS74). In the case that the wind system moves at the free wave speed ($\omega \to kc_n$), resonance with the wind occurs. This is because the wave amplitude of each Fourier component is proportional to

$$\varphi(x,t) \sim \frac{b_n \tau_0}{f(k - \omega/c_n)}. \tag{4.25}$$

The peaked nature of the BSW spectra can be interpreted as resonances with atmospheric variability. This is similar to the results of Kusahara and Ohshima (2009) who showed that BSW with $k \leq 3$ were most pronounced at their resonant period and were otherwise swamped by wavenumber zero variability. We have, however, additionally shown that resonances are observed for the $n = 2$ wave, albeit only in wintertime. Resonances for the $n = 2$ wave are overall less pronounced because the mode's resonant frequencies (at k = 1-3) are comparable to the inverse damping time scale ($r_t \sim c_2 k$) whereas the resonant frequencies for the $n = 1$ wave are much greater than the inverse damping time scale ($r_t < c_1 k$). In general, the resonant peaks are not always statistically significant because the wind forcing does not strictly include westward propagating variability (in fact, it is dominated by standing and eastward propagating variability) and the wave signals additionally include a response at the various forcing frequencies (the smooth underlying portion of the spectra). The importance of a ~40 day period, and why a response there should be stronger in wintertime, will be considered in the following Discussions section.

4.6) Discussions

We have shown that the barotropic long-shore current and the SSH on the WAP shelf as measured by moored current meters and a tide gauge, respectively, consist of a wavenumber zero coherent mode (figure 4.9; table 4.2) and at least two BSW modes (figure 4.10). Further, we have shown that these dynamical modes are forced by the long-shore wind stress, being able to predict on average about half of the total velocity variance at intraseasonal time scales (3-100 days) with nothing more than surface stress data (figures 4.11-4.19, table 4.3). Importantly, the predictions do a good job capturing both the phasing and the dimensional amplitude of the

observed variability. The coherent mode is most energetic at increasingly low frequencies, as expected from its transfer function (equation 4.2), while the BSW tend to be slightly more apparent at periods where they may resonate with westward propagating atmospheric structures at integer wavenumber (figure 4.20). Both of these phenomena are consistent with the analysis of circum-Antarctic SSH dynamics by Kusahara and Ohshima (2009) but we now show that they comprise a large portion of the velocity variance as well and can be predicted from the wind in the time domain. Two additional unexpected findings are the importance of higher modal variability and the dominance of variability at 40-60 day periods. We consider each of these findings in more detail below and then discuss a few practical applications of the results for shelf-slope exchange.

4.6.1) Why is the $n = 2$ wave so important?

On most continental shelves, the first mode BSW is most prominent and explains most of the observed variance. A crucial result of this study is the apparent importance of the mode $n = 2$ BSW in shelf signals, particularly velocity signals. This is evident from the results of figure 4.10, which shows that a hovmöller matrix of coastal signals (with the wavenumber zero mode removed) consists of two waves of comparable importance, one each at the $n = 1$ and 2 phase speeds. It is also apparent in the quality of the wind-driven velocity predictions, which tends to increase substantially upon introduction of the $n = 2$ wave to the sum of the wavenumber zero mode and the $n = 1$ wave. The importance of the $n = 2$ wave may have been missed in earlier studies that focused on coastal SSH only as its modal SSH amplitude is relatively small at the coast. On the other hand, it may have been missed because it is most energetic at periods that tend to overlap with where the coherent mode is very strong (40-60 days) or where the $n = 1$ wave is also resonant (e.g., ~15 days; figure 4.20).

Part of the importance of the $n = 2$ wave is determined directly from the bathymetry: its wind-coupling coefficient is comparable to that of the $n = 1$ wave (figure 4.3) and its amplitude at the mooring isobath is slightly larger than that of the $n = 1$ wave (figure 4.6), combining to give a very similar amplitude factor ($b_1 u_1 \approx b_2 u_2$). Going further, note that higher mode waves ($n = 2, 3, \ldots$) exist at a lower frequency for a given wavenumber than does the $n = 1$ wave. Intraseasonal wind forcing with low wavenumber and low frequency is very energetic around the Antarctic margins (Matthews and Meredith 2004; Pohl et al. 2010) and in the southeastern Pacific (Iijima et al. 2009; Mo and Higgins 1998). Resonance of the $n = 2$ wave occurs at a period of ~43 days, which, as will be discussed in the next section, is a major period of atmospheric forcing. Thus, the $n = 2$ wave may be particularly prominent on the WAP because it contains more power at lower frequencies than does the $n = 1$ wave (figure 4.20) and its resonances for a given wavenumber occur at a lower frequency (figures 4.3, 4.20).

Another possibility hinted at by figure 4.10 is that the apparent importance of the $n = 2$ wave on the WAP may be more appropriately phrased as the apparent unimportance of the $n = 1$ wave on the WAP. The $n = 1$ wave may be preferentially scattered by the South Shetland Islands or the rapidly turning coastline at Drake Passage, a possibility that warrants further study.

4.6.2) Why does variability with period 40-60 days dominate?

The coherency spectra between the predicted coherent mode (and $n = 2$ wave) and observations and the power spectra of the coherent mode and the $n = 2$ wave all have peaks at periods close to 40 days. The strength of spectral power varies interannually and is strongest in the winter season, both of which are consistent with tropical teleconnection: efficacy of atmospheric Rossby wave propagation depends on the phase of the Southern Annular Mode (SAM) (Fogt et al. 2011), which varies interannually, and tropical Rossby wave propagation

tends to occur primarily into the winter hemisphere (Kiladis and Mo 1998). A period of ~40 days is consistent with intraseasonal tropical teleconnection via the Madden-Julian Oscillation (MJO). Variability in Drake Passage transport in the 30-70 day range has been attributed to the MJO (Matthews and Meredith 2004). While those authors attributed the increase in ACC transport at ~40 day period to a modulation of SAM-like, zonally symmetric forcing by the MJO, there is some debate as to whether or not the MJO and SAM interact at all. Pohl et al. (2010) suggest that the MJO anomalies manifest with more of a dipolar ($k = 1$) structure and suggest that the variance with 40 day period might be due to variability intrinsic to the SAM.

At higher wavenumbers, the leading EOFs decomposing intraseasonal atmospheric variability within various variables tend to exist in quadrature, spatially representing the Pacific-South American (PSA) pattern propagating eastward with a period near 40 days (e.g., scatterometer surface winds (Iijima et al. 2009) or 200-hPa eddy streamfunction (Mo and Higgins 1998)). The PSA pattern consists of an approximately $k = 3$ sequence of alternating cyclones and anticyclones that carry the teleconnection to the Antarctic and its amplitude is largest in the southern Pacific / South America region (Mo and Higgins 1998). While the PSA pattern can originate from the MJO in austral winter (Kiladis and Mo 1998), it may have different origin and only episodically interact with tropical convection (Mo and Higgins 1998). The large center of action in the southeastern Pacific suggests the potential for a strong imprint on WAP SSH and currents. The heterogeneous correlation maps between long-shore velocity and SLP in chapter 3 indicate strongest correlations in this vicinity (figure 3.9). This may be because the damping associated with the $n = 2$ wave is such that the length scale for memory of atmospheric forcing is only $c_2/r_t \sim 1800$ km, which is about the size of the alternating high and low pressure centers of the PSA. That is, the spatial memory of the $n = 2$ wave is the same size

as regular, coherent atmospheric variability. Thus, variability in the southeastern Pacific may leave an unusually large imprint on WAP currents.

In short, in the 40-60 day range, atmospheric variability potentially associated with the MJO may project onto the wavenumber zero mode whose transfer function permits response at arbitrary frequency, may resonate with the second mode BSW at $k = 1$, or may project onto the second mode BSW with disproportionate influence on the WAP due to the PSA's large center of action there and the second mode's short frictional damping scale.

4.6.3) Implication: Upwelling at a coastal canyon head

Palmer Station is a shallow coastal environment situated at the head of Palmer Deep canyon on the WAP shelf. At the head of Palmer Deep canyon, the food web consists of one or more seasonal phytoplankton blooms (Kim et al. 2016) which is grazed by Antarctic krill, who serve as the major prey source for penguins and other top predators. Canyon heads on the WAP such as that of Palmer Deep tend to be ecological hotspots as identified, in part, by locations of permanent Adelie penguin breeding sites and increased phytoplankton biomass (Fraser and Trivelpiece 1996; Ducklow et al. 2007; Schofield et al. 2013). Several hypotheses attempt to explain why canyon heads are so ecologically significant. The fact that macronutrients are generally not limiting at the onset of the annual bloom (Carvalho et al. 2016; Kim et al. 2016) suggests that it is not the macronutrient enrichment of the Circumpolar Deep Water (CDW), which is advected to the canyon head, that matters. Instead, mixed layer depth seems to place a major control on bloom onset (Carvalho et al. 2016).

In general, compared to the shallower adjacent shelf, coastal submarine canyons have reduced sea ice, elevated sea surface temperature, elevated chlorophyll, and an elevated abundance of diatoms (Kavanaugh et al. 2015). The coincidence of canyon heads with reduced

sea ice and elevated sea surface temperature seems to suggest that some type of mechanical upwelling of warm water places a physical, bottom-up control on the environment. Recent results from an ocean observing system suggest that residence times associated with advection by surface currents are about 1-2 days, which is shorter than phytoplankton doubling time growth rates (Kohut et al. 2018). We therefore test the possibility that lateral advection towards the canyon head, driven by large-scale barotropic dynamics, dynamically replenishes water in the Palmer environment.

Palmer Station E (Pal E; 158 m) is regularly sampled as part of the quasi-semiweekly oceanic sampling conducted at Palmer Station. It is situated at the outermost reaches of the Palmer coastal environment, just adjacent to the slope leading into the much deeper Palmer Deep canyon (1400 m), thus rendering it an ideal location to test communication between the deeper canyon and the coastal environment. A year-long thermistor mooring was deployed in 2014 which sufficiently resolves water column structure (figure 4.21a). The summertime water column features a warm seasonal mixed layer but by the onset of winter the entire water column is mixed to near the freezing point. Significantly, the homogenous freezing water in winter is punctuated by episodic, bottom-driven warming events. These events become more apparent when band-pass filtering the temperature signal at each depth to retain periods 3-100 days (figure 4.21b). The pulses have a period of about 40 days. Because the warming is bottom-intensified and the surface remains near the freezing point, the signal must originate from deeper in the canyon. The *T*-*S* relationships between sampling at Pal E and sampling in Palmer Deep during the two straddling field seasons confirm that the warm water comes from the permanent pycnocline of Palmer Deep and that the warm water then mixes with overlaying surface water (figure 4.22).

The time series of band-pass filtered near-bottom (120 dbar) temperature at Pal E is significantly correlated ($p \approx 0$) to the predicted SSH signal (coherent mode plus n = 1, 2 BSW) at the latitude of Palmer canyon (r = -0.38, lag = 4.5 days). The relationship is displayed in figure 4.21c. Correlations improve if we consider the coherent mode only (r = -0.43, lag = 5.5 days) and if we isolate the ~40-day pulses by band-pass filtering to retain periods of 30-70 days beforehand (r = -0.59, lag = 9 days). We thus hypothesize that the shoreward pressure gradient force steers flow through the network of canyons towards the coast, and/or upwelling at the slope happens via flow-topography interactions with a canyon (e.g., Kämpf 2006; Allen and Hickey 2010; see discussion in chapter 3) and forces upwelling at the canyon head. The lag allows time for the signal to reach the coast. The process mechanically shoals the pycnocline which may reduce the mixed layer depth assuming no change to surface fluxes. A major novel result is the idea that small-scale bathymetric features can link very disparate length scales: O(1000 km) BSW and/or coherent mode SSH variability is funneled down to O(10 km) local canyon-scale response.

4.6.4) Implication: Isopycnal displacement at the shelf edge

In chapter 3 we considered the coherence between barotropic velocity fluctuations and subpycnocline heat content (and T_{max}) on the WAP. To our surprise, the two variables are generally incoherent. This seemed unusual because the major velocity fluctuations identified in that study are clearly consistent with a spatially coherent circulation that encompasses upwelling of the slope current onto the continental shelf. The current on the slope should presumably advect warm CDW onto the shelf and yield a positive correlation between the two variables. The apparent incoherence was explained by noting that, while velocity variance is dominated by wind-driven, large-scale, quasi-barotropic fluctuations, the thermal variance is dominated by

small-scale mesoscale features with weak azimuthal rotation (chapter 2; Martinson and McKee 2012; Graham et al. 2016; McKee et al. 2019).

The one exception to this incoherence occurs at periods in the 40-50 day range, for which the long-shore current and the T_{max} are weakly anti-correlated, the opposite of what the above reasoning would suggest. This study shows that the wavenumber zero mode and the second mode wave are energetic in that range. While the former is strictly barotropic, the latter – although well approximated by a BSW – is technically a stratified CTW. In fact, the modal structure is most baroclinic and bottom-trapped over the steep continental slope of the WAP, which is to be expected as this is the only region where the Burger number is large (Huthnance 1978, 1981).

The modal structure for $n = 2$ density anomaly for WAP bathymetry at $k = 1$ is shown in figure 4.23a, zoomed in to the shelf edge. It is bottom-trapped and confined to the steepest portion of the slope. To obtain an estimate of the magnitude of isopycnal displacement, we need to scale this pattern because the modal structures provided by the bigr*.m code have arbitrary amplitude. To scale the pattern, we take all of the Pal LTER CTD casts on the 300 line (1993-2017), bin the potential density into vertical bins whose size is the same as the grid used to solve for the modal solutions, and compute the standard deviation in each bin. We take the largest standard deviation that is clearly below the winter mixed layer and set the largest value of the modal density field to have that value. The modal density pattern is then 'gridded' onto the Pal LTER 300 line by lining the two fields up at the cross-shelf position of the 650 m isobath, which corresponds approximately to largest modal amplitude.

Figure 4.23b shows the climatological potential density field from all CTD casts along the 300 line. In panels c and d, respectively, we subtract and add the scaled, gridded $n = 2$ modal

density anomaly to the mean potential density field. In each panel, a reference isopycnal (one near T_{max} in the climatological state) is plotted. Clearly the waves are able to displace that isopycnal. This is similar to the phenomenon observed by Griffin and Middleton (1986) who observed $n = 2$ CTW to yield thermocline excursions of ~30 m over the slope. It would appear that an additional consequence of the $n = 2$ wave is the ability to enhance or suppress warm water access to the continental shelf.

While that is certainly a possibility, the weak correlation observed between long-shore current and T_{max} at site 300.100 is actually of opposite sign: a stronger long-shore flow (positive wave state) yields a cooler T_{max} at long period. While we have no means of testing it, we outline the following hypothetical scenario that would yield a warmer T_{max} in a negative wave state. As cited above, the thermal variance on the WAP is dominated by mesoscale features. In the mean, the T_{max}-containing isopycnal shoals approximately monotonically towards the coast (figure 4.23b), which is generally the case for regions without a strong Antarctic Slope Front. In addition to enhancing or suppressing deep isopycnal access to the shelf, the wave also moves the location of steepest isopycnal slope shoreward (negative state; figure 4.23c) or seaward (positive state; figure 4.23d). As most of the CDW on the WAP shelf is contained in small mesoscale features, we can postulate that they originate through stirring on the T_{max} isopycnal across the slope by mesoscale eddies generated through baroclinic instability. Although eddies can form on the steep continental slope (see chapter 2), growth rates of baroclinic instability are generally suppressed when the bottom slope is steep relative to the isopycnal slope (Blumsack and Gierasch 1972). Thus, it is plausible that growth rates of baroclinic instability (and magnitude of cross-slope stirring of heat) are enhanced in the wave's negative state when the eddies are generated over the flat shelf as opposed to the steeper slope. The growth time scales for

baroclinic instability in this environment are of order 1 day (see chapter 2) which is much shorter than the wave period of ~43 days, so it can be imagined that an $n = 2$ wave continually propagating into the WAP environment maintains steep isopycnals at the shelf edge while the eddies continually try to flatten them until the wave changes phase.

Although the details cannot be tested with present data, we have outlined two possible means by which the baroclinicity of the $n = 2$ wave over the WAP slope may modulate heat transport onto the WAP shelf. Firstly, the modulation of isopycnal depth at the shelf edge can reduce warm isopycnal access to the shelf in the wave's negative state. Alternatively, the wave's alteration of the background density field may move the location of steepest isopycnal slope onshore in the negative state which may periodically enhance cross-slope heat transport by modulating growth rates of baroclinic instability.

4.7) Conclusions

We have shown that about half of the intraseasonal (3-100 days) variance in the barotropic long-shore current on the WAP shelf can be predicted by a wavenumber zero coherent mode and at least two BSW modes forced by nothing more than surface stress data. The coherent mode is most energetic at increasingly low frequencies with a peak at periods between 40-50 days in wintertime. The first mode BSW is most energetic at periods 5-15 days with spectral peaks where it may resonate with westward propagating atmospheric structures at integer wavenumbers while the second mode wave is more energetic at lower frequencies with significant resonant peaks only in wintertime. The phase speeds detected from a cross-characteristic analysis of a hovmöller matrix of circum-Antarctic time series agree well with the phase speeds of the first two BSW for a representative bathymetry profile. Calculation of

dispersive, stratified CTW modes suggests that the long-wave, barotropic assumptions are good on intraseasonal time scales, although dispersion may account for some of the scatter in the predictions (figure 4.13). Importantly, the second mode BSW is found to be present in velocity signals, particularly at low frequencies. Prominence of the second mode wave may simply be because atmospheric variability is more energetic at low frequencies, perhaps due in part to MJO teleconnection or PSA-type patterns, or may be due to a coincidence between the wave's frictional damping length scale and the size of the PSA pressure centers.

The wind-driven velocity fluctuations have major impacts on shelf-slope exchange. Firstly, acceleration of the long-shore flow drives flow-topography interaction and the emergence of a spatially coherent circulation pattern hundreds of kilometers in scale as reported in chapter 3. Secondly, the shoreward pressure gradient force leads to episodic upwelling of warm water at an ecologically productive canyon head that may keep sea ice thin in winter, may aggregate phytoplankton biomass, and may mechanically shoal the pycnocline. Thirdly, the subtle baroclinicity of the second mode wave over the continental slope yields isopycnal migrations near the depth of the temperature maximum. These excursions may cut off shelf access for deep isopycnals or they may enhance eddy heat fluxes by shifting the location of steepest isopycnal slope onto the flatter continental shelf. This latter effect is likely to be most pronounced in environments with steep slopes like the WAP where the Burger number, and hence wave baroclinicity, are large.

Eastward undercurrents are observed in regions with an Antarctic Slope Front such as the western Amundsen Sea (Walker et al. 2013) or the eastern Weddell Sea (Chavanne et al. 2010). Chavanne et al. (2010) show that these currents exhibit synoptic variability associated with isotherm excursions at the shelf edge. Counter-flowing undercurrents are a characteristic feature

of coastal upwelling (Suginohara 1982) and downwelling (Middleton and Cirano 1999) regions and their establishment can be explained by CTW dynamics. In particular, for coastal wind forcing with finite spatial extent, arrival of the first mode wave establishes the long-shore jet in the direction of wind forcing while arrival of the second mode wave induces the undercurrent (Suginohara 1982). As an additional implication of the results of this study, we postulate that the second mode CTW may play an important role in undercurrents around the Antarctic continent.

The prediction scheme is overall successful but there is room for improvement. Firstly, our treatment of damping was somewhat arbitrary by merely adding a linear term to the spectrum of wave equations (as done by GS74) and by assuming a spatial damping parameter $r_n = r_t / c_n$ with a single value of r_t. A more sophisticated prediction that includes frictional coupling between modes (Brink and Allen 1978; Brink 1982b) may improve results. Further, the assumption of a spatially uniform phase speed compounds errors when integrals are conducted in the time domain. A prediction that allows for slow variations in phase speed to account for varying coastal profiles (e.g., Brink 1982a) may yield more accurate results. Nevertheless, the fact that we can explain as much variance as we can is encouraging and the three major results, namely (1) the importance of the $n = 2$ mode, (2) the prominence of variability with period 40-60 days, and (3) the implications of the wind-driven dynamics for shelf-slope exchange are unequivocal and not subject to change with an improved prediction scheme.

Tables

Table 4.1: Data coverage for each mooring-year, which spans 405 days from 1 January. In each analysis, series are truncated to the actual length of the current meter mooring time series which is generally ~350 days long. Only years with current meter data at one of 300.100 or 200.140 are considered. Tide gauge series with large gaps are not used. DPS indicates Drake Passage South Deep bottom pressure.

	300.100	200.140	Faraday	Syowa	Scott Base	DPS
2008	**x**		**x**	**x**		
2010	**x**		**x**			**x**
2011	**x**		**x**	**x**	**x**	**x**
2012	**x**		**x**	**x**	**x**	**x**
2013		**x**	**x**	**x**		**x**
2014	**x**			**x**		
2017	**x**					

Table 4.2: Comparison of the different estimates of the coherent mode to each other and to 300.100 depth-averaged long-shore current for year 2012. All correlations are significant with $p \approx 0$.

	T.g.	T.g., DPS, U	300.100 U
T.g.	1	0.97	0.71
T.g., DPS, U	0.97	1	0.77
300.100 U	0.71	0.77	1

Table 4.3: Correlation coefficients for predictions against observations, filtered to retain variance with periods 3-100 days. Predictions in parentheses involve the wave modes only. Records marked with * did not sample below the permanent pycnocline and records marked with † are derived from only one current meter. All correlations are significant at the $\alpha = 0.01$ level.

	Coh. mode	Coh. + n=1	Coh. + n=1,2	Coh. + n=1,2,3
300.100 / 2008†	0.36	(0.48) 0.59	(0.61) 0.69	(0.63) 0.71
300.100 / 2010	0.40	(0.37) 0.56	(0.51) 0.66	(0.53) 0.68
300.100 / 2011*	0.28	(0.34) 0.47	(0.50) 0.60	(0.53) 0.63
300.100 / 2012	0.65	(0.36) 0.71	(0.55) 0.78	(0.57) 0.79
300.100 / 2014	0.41	(0.48) 0.63	(0.60) 0.74	(0.61) 0.75
300.100 / 2017†	0.39	(0.45) 0.57	(0.63) 0.72	(0.65) 0.74
200.140 / 2013	0.41	(0.30) 0.47	(0.55) 0.66	(0.58) 0.69
Faraday / 2008	0.36	(0.24) 0.42	(0.27) 0.43	(0.34) 0.48
Faraday / 2010	0.54	(0.26) 0.59	(0.28) 0.60	(0.33) 0.62
Faraday / 2011	0.48	(0.26) 0.56	(0.28) 0.57	(0.32) 0.60
Faraday / 2012	0.55	(0.31) 0.64	(0.34) 0.65	(0.40) 0.67
Faraday / 2013	0.45	(0.36) 0.55	(0.38) 0.57	(0.43) 0.61

Figures

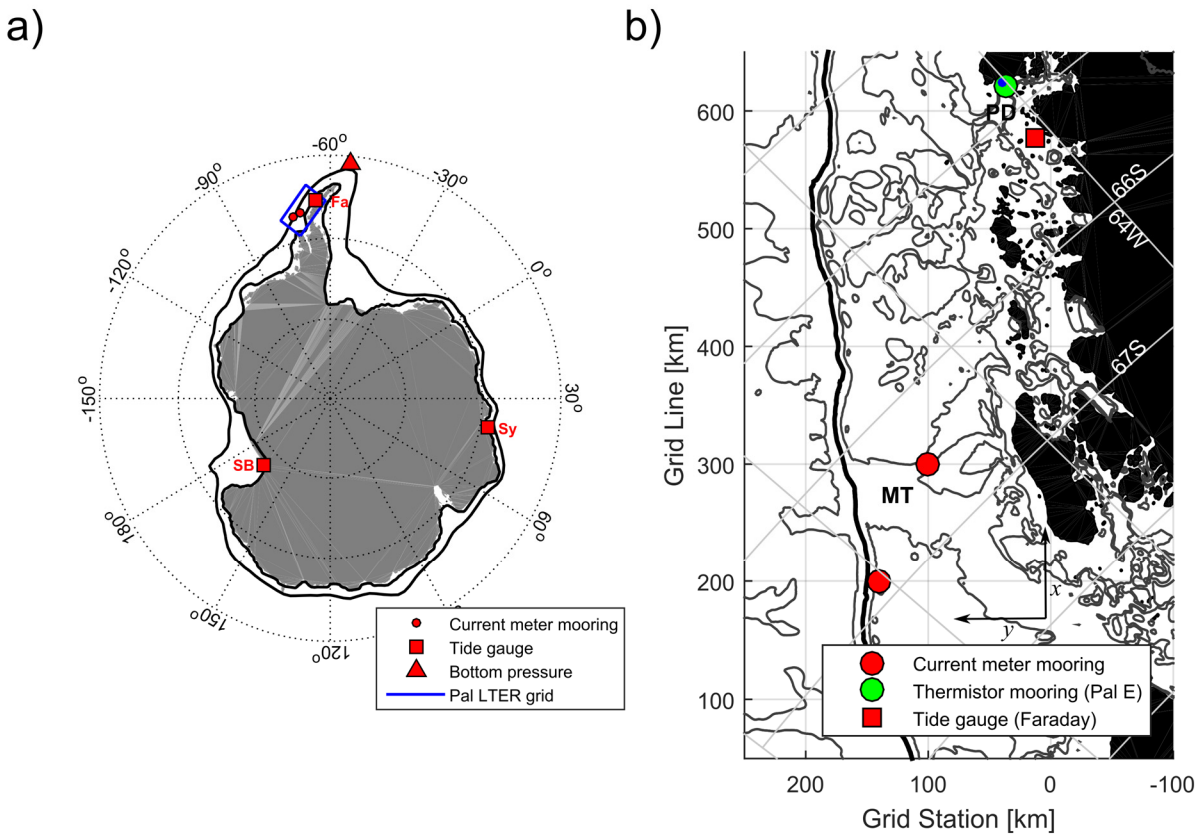

Figure 4.1: Overview of the physical setting and data sources used. **(a)** Polar projection map showing the Antarctic continent as defined by the 0 m isobath in ETOPO5 (grey shading) along with the Continental Shelf-Break and Coast Contours (see text) as bold black lines. Lines of latitude are indicated every 10º. The two current meter moorings (red circles), the single Drake Passage South bottom pressure sensor (red triangle), and the three tide gauges (red squares; Fa = Faraday, Sy = Syowa, SB = Scott Base) are indicated. The Pal LTER sampling grid is enclosed by a blue rectangle. **(b)** Inset showing the Pal LTER sampling grid and the data sampled therein. Locations are generally referred to with the LTER coordinate system and are given as GGG.SSS where GGG is the grid line (units of kilometers) and SSS the grid station (units of kilometers). The two current meter moorings (red circles) and the single thermistor mooring (green circle) are indicated, as is the location of Faraday Tide gauge (red square). Locations of Marguerite Trough (MT), Palmer Deep canyon (PD), and Palmer Station (small blue dot near the thermistor mooring) are indicated.

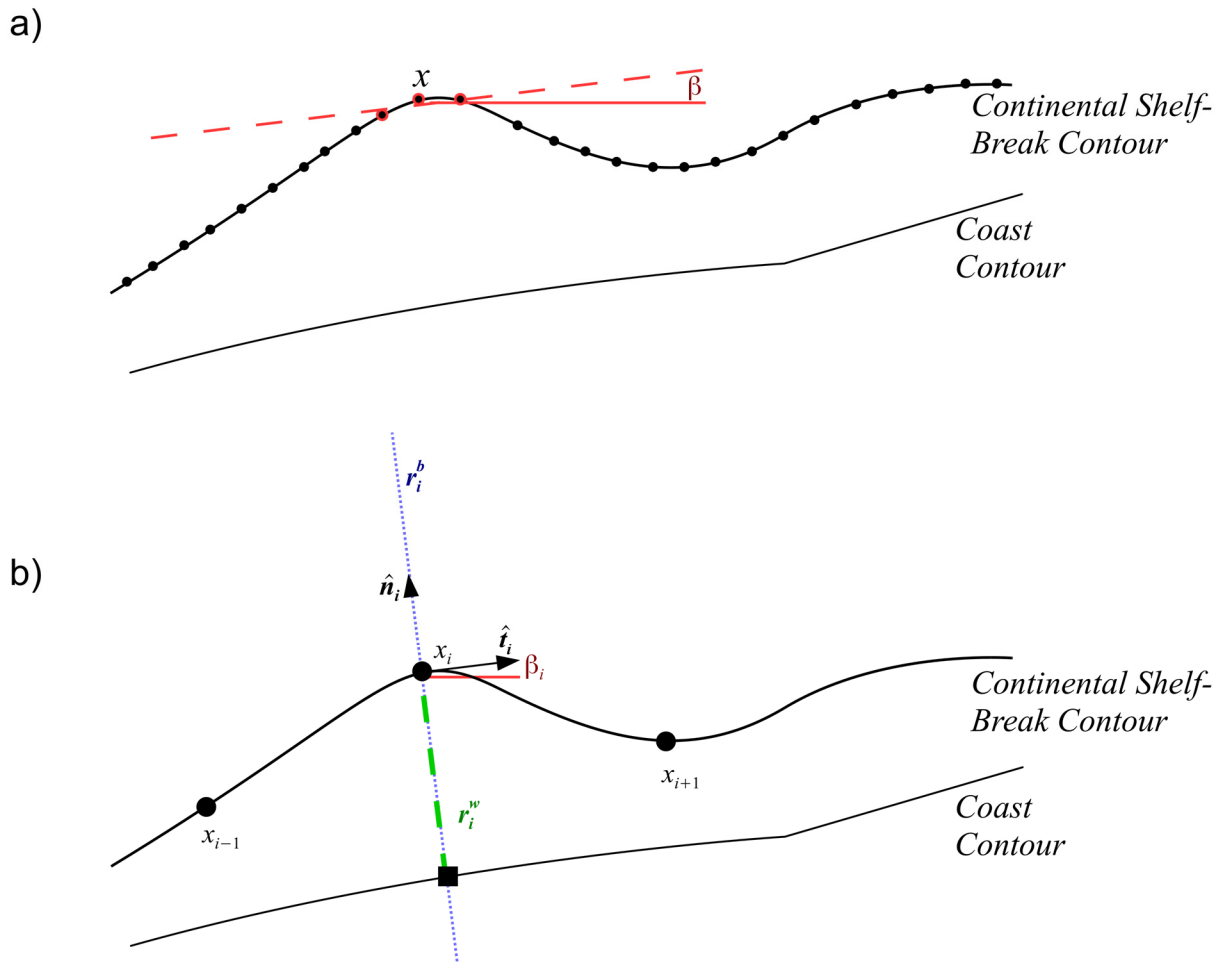

Figure 4.2: Schematic of the procedure for obtaining both bathymetry and long-shore surface stress across the continental slope. **(a)** The orthogonal least squares procedure used to define tangential angles β on the full contour. The three locations outlined in red are included in the regression. **(b)** The discretized, evenly spaced Continental Shelf-Break Contour upon which data are gridded. For the segment at x_i, angle β_i (linearly interpolated from above) defines the tangential $\left(\hat{\mathbf{t}}_\mathbf{i}\right)$ and normal $\left(\hat{\mathbf{n}}_\mathbf{i}\right)$ vectors. Bathymetry is gridded onto section r_i^b (dotted blue line). Surface stress is gridded onto section r_i^w (dashed green line), dotted into tangential vector $\hat{\mathbf{t}}_\mathbf{i}$, and averaged between the Continental Shelf-Break and Coast contours.

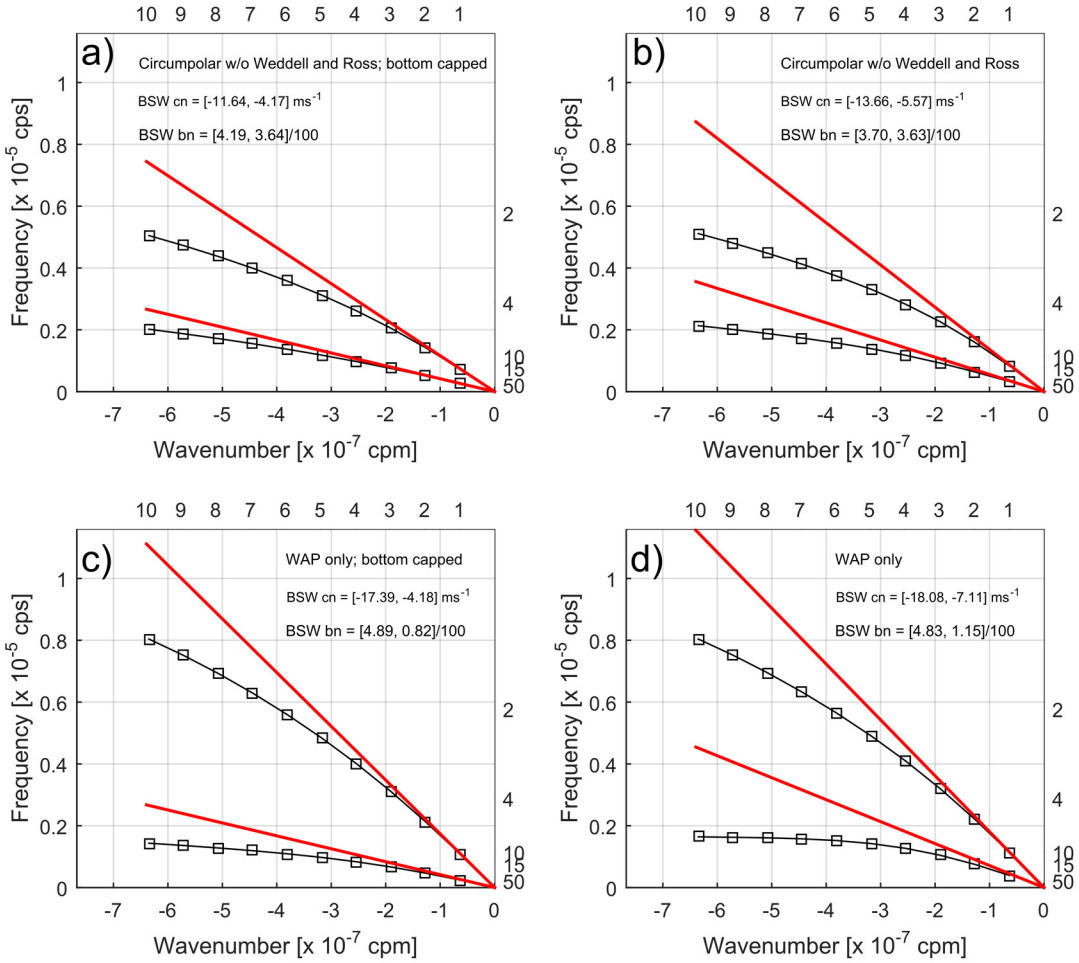

Figure 4.3: Dispersion relations for BSW (red lines) and CTW (black squares) for the first two wave modes for a variety of shelf profiles. The additional horizontal axis indicates wavenumber as a fraction of the circumpolar distance and the additional vertical axis indicates period in days. **(a)** Circumpolar profile with bottom depth capped at 4000 m; **(b)** Circumpolar profile; **(c)** WAP profile with bottom depth capped at 4000 m; **(d)** WAP profile.

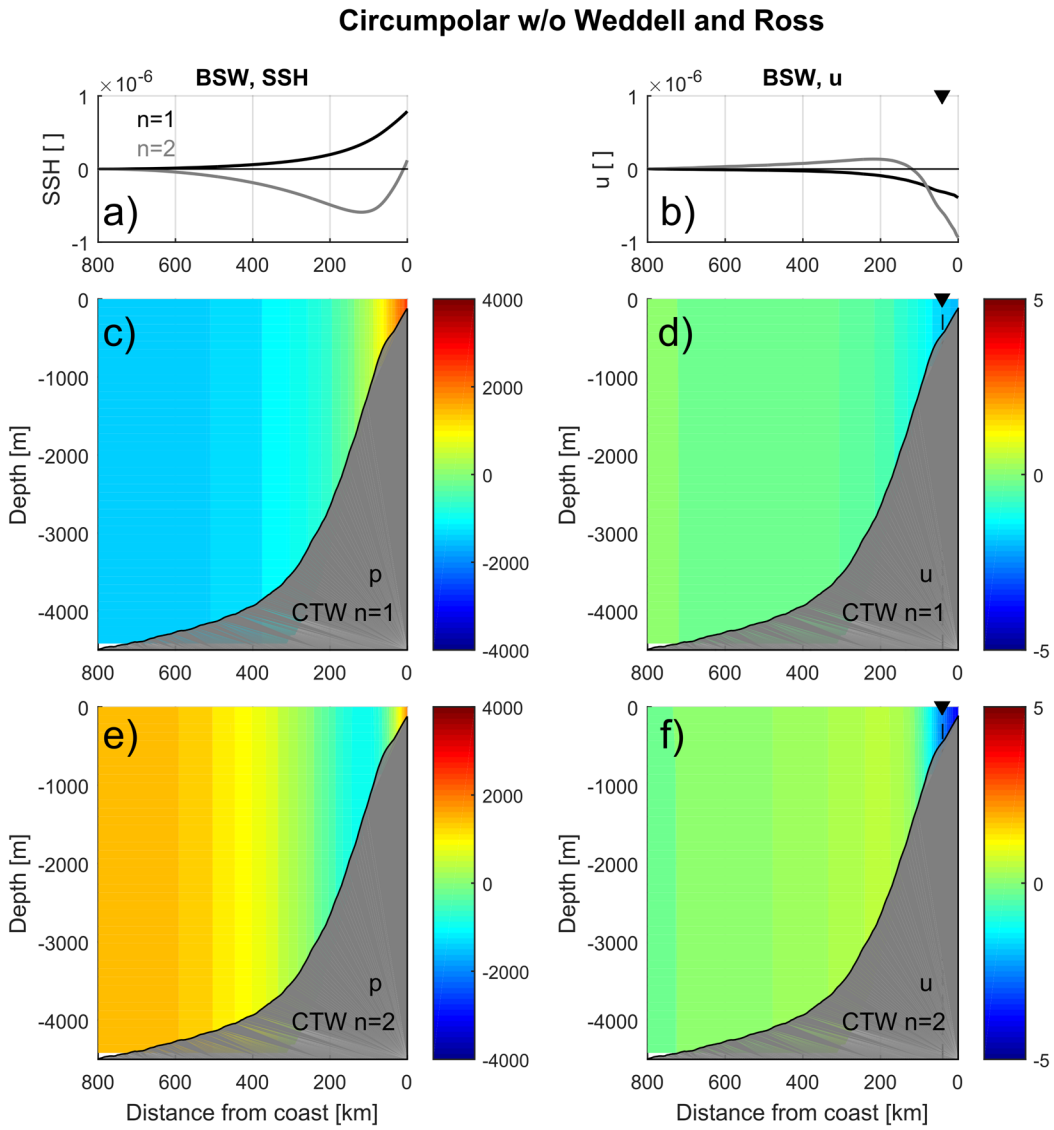

Figure 4.4: BSW and CTW modal structures for the circumpolar, uncapped depth profile. All amplitudes are arbitrary. **(a)** Modal SSH for the first two BSW. **(b)** Modal long-shore current for the first two BSW. **(c)** Modal pressure for the first CTW. **(d)** Modal long-shore current for the first CTW. **(e)** Modal pressure for the second CTW. **(f)** Modal long-shore current for the second CTW.

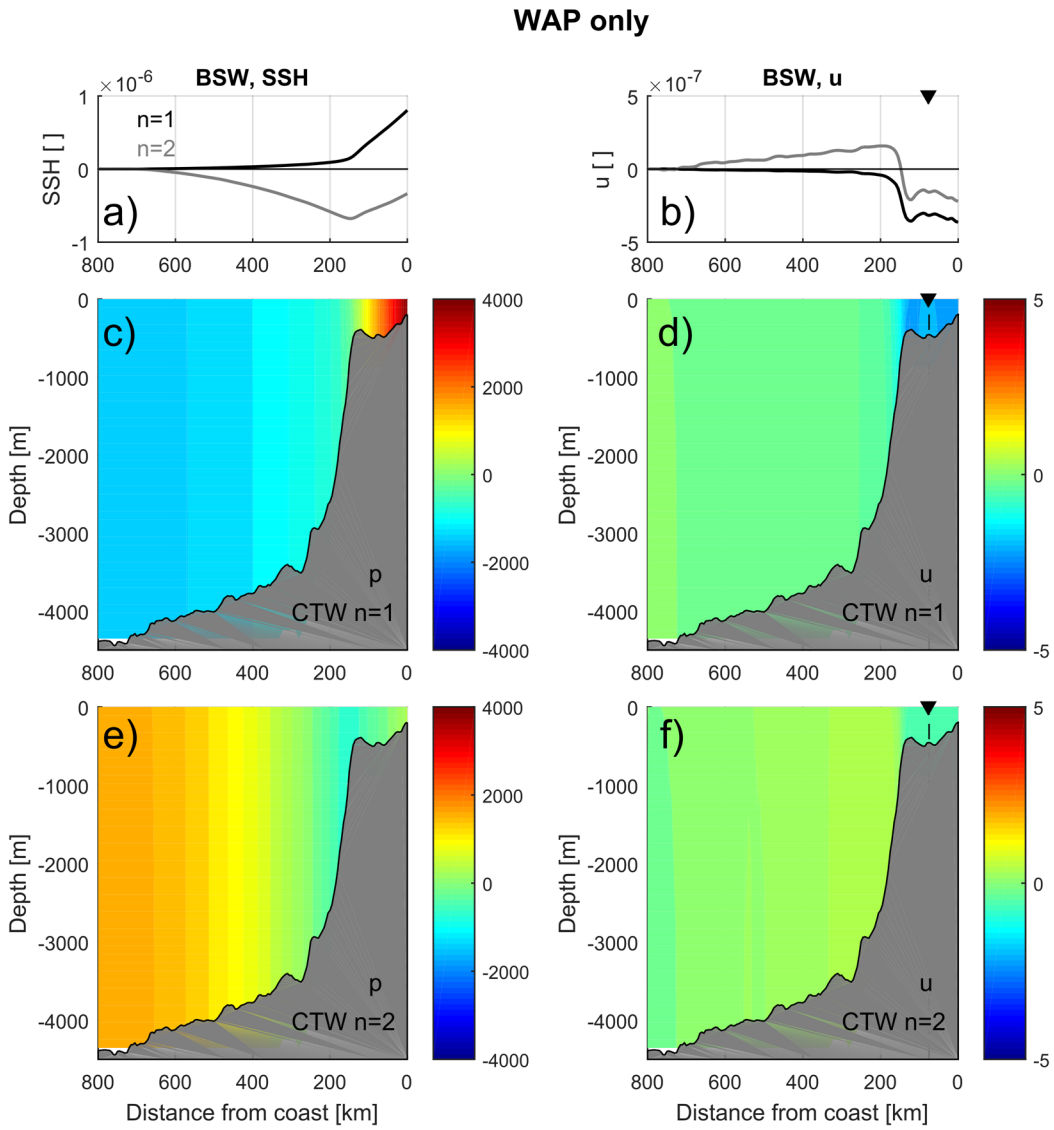

Figure 4.5: Exactly as in figure 4.4 but for the WAP, uncapped depth profile.

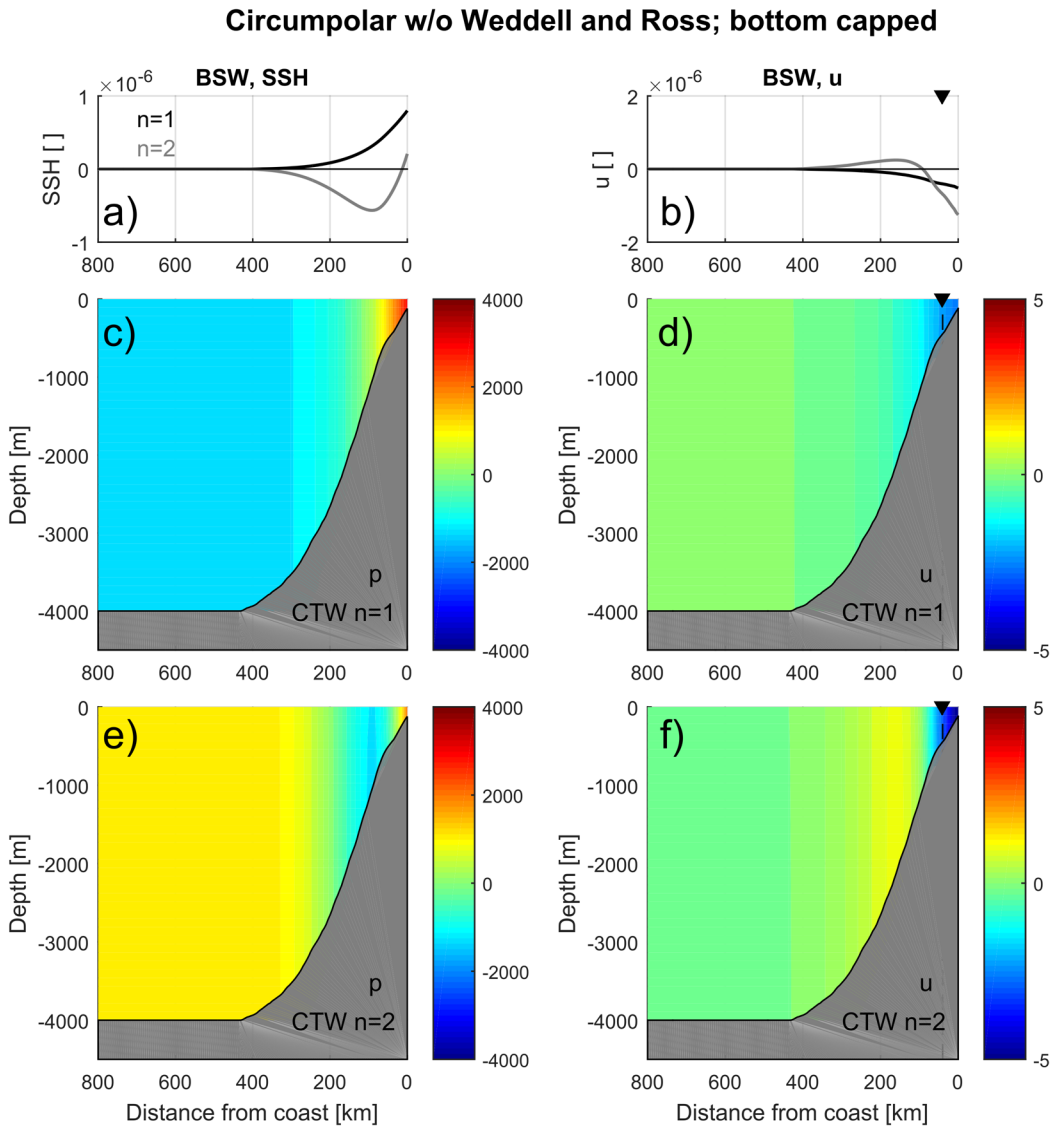

Figure 4.6: Exactly as in figure 4.4 but for the circumpolar, bottom-capped depth profile.

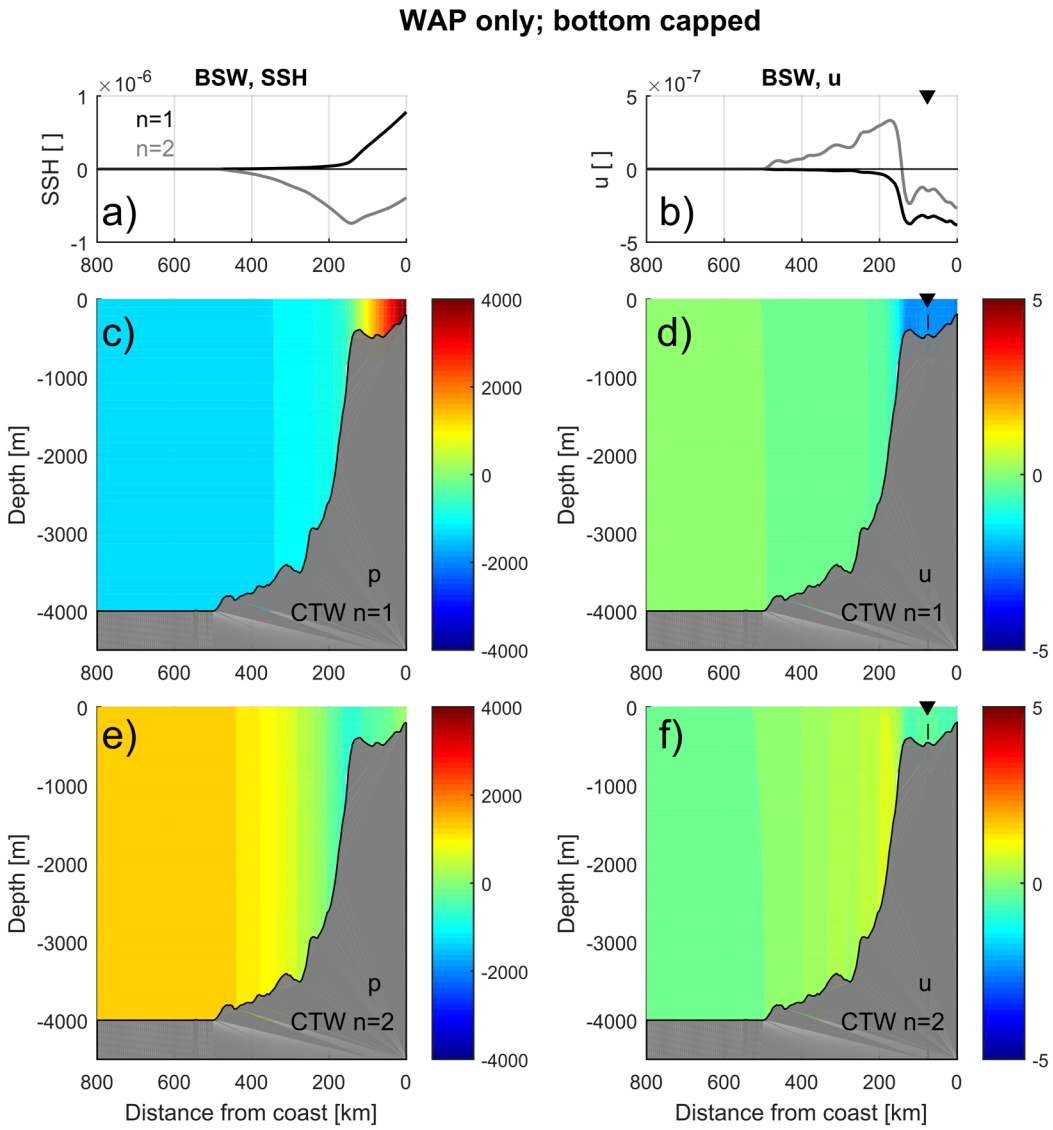

Figure 4.7: Exactly as in figure 4.4 but for the WAP, bottom-capped depth profile.

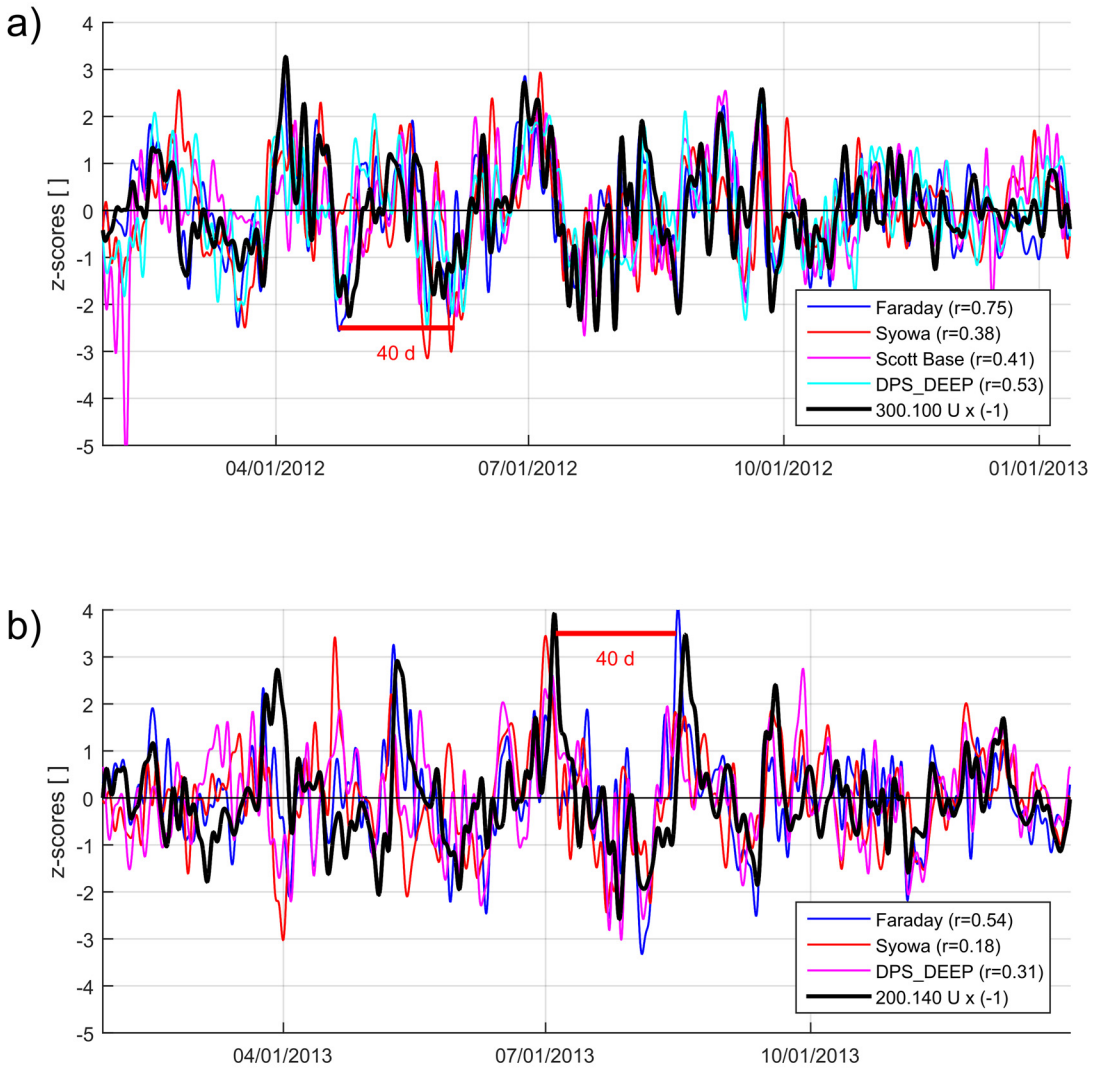

Figure 4.8: Time series of long-shore current (bold black) at **(a)** 300.100 year 2012 and at **(b)** 200.140 year 2013 along with the various subsurface pressure series around the continent (thin colors). All time series have been standardized owing to the different units and have been band pass filtered to retain periods 3-100 days. The velocity series has been multiplied by -1. Correlation coefficients at zero lag are indicated in the legend.

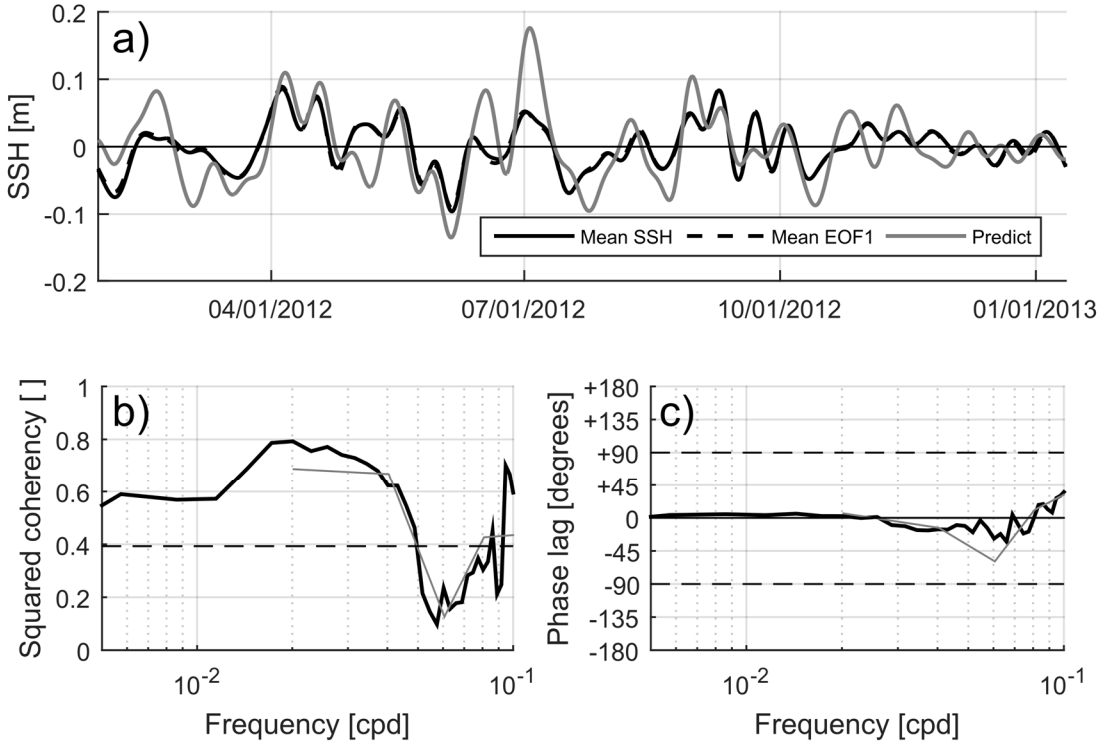

Figure 4.9: Comparison of dimensional predicted coherent mode against inversely detected coherent mode. **(a)** Plot of the prediction (grey line) against two estimates (mean of 20-100 day filtered tide gauge signal, black solid; mean of reconstructed EOF1 tide gauge signal, black dashed) in the time domain. **(b)** Squared coherency and **(c)** cross-phase spectra between the prediction and the first estimate (mean of the filtered tide gauge signals). The bold black spectra utilize multitaper smoothing (7 DPSS) functions and the thin grey spectra utilize 7 non-overlapping windows for smoothing, each yielding 14 EDOF. The horizontal black dashed line in (b) indicates the threshold for significant coherence compared against a white-noise null hypothesis of zero coherence at an $\alpha = 0.05$ level.

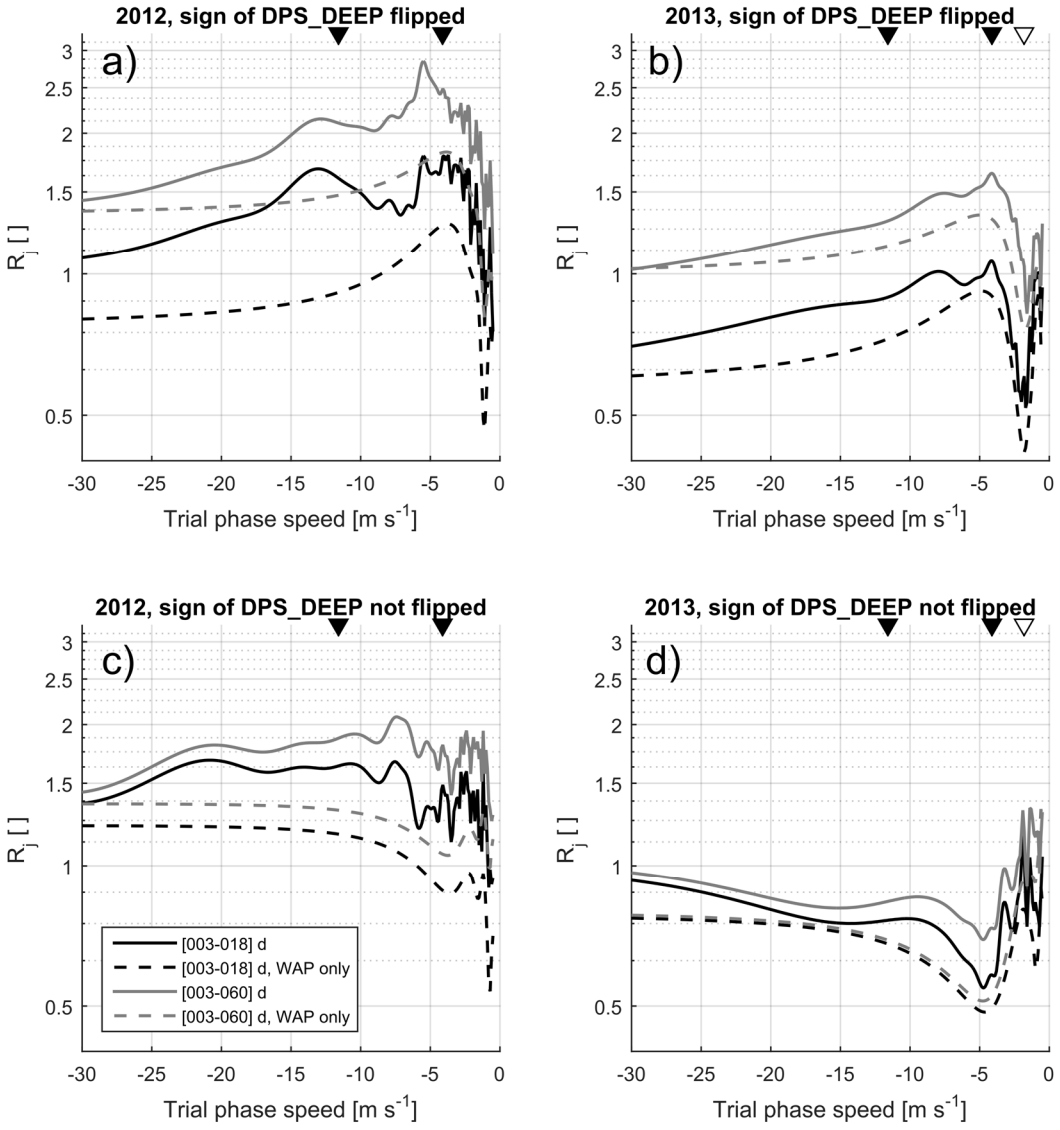

Figure 4.10: Parameter R_j as a function of trial phase speed for years with sufficient spatial coverage of signals around the continent and with sufficient current meter coverage in the vertical to define a depth-averaged current. In each panel, decompositions of $\mathbf{d}^{\text{waves}}_{\text{circumpolar}}$ are solid and decompositions of $\mathbf{d}^{\text{waves}}_{\text{WAP}}$ are dashed; decompositions filtered to retain periods 3-18 days are black and decompositions filtered to retain periods 3-60 days are grey. The solid wedges indicate theoretical n = 1, 2, BSW phase speeds and the hollow wedge indicates theoretical n = 3 BSW phase speed. **(a)** Results for year 2012 with the sign of the DPS bottom pressure signal flipped. **(b)** Results for year 2013 with the sign of the DPS bottom pressure signal flipped. **(c)** and **(d)** are as in (a) and (b), respectively, but with the sign of the DPS bottom pressure signal left alone.

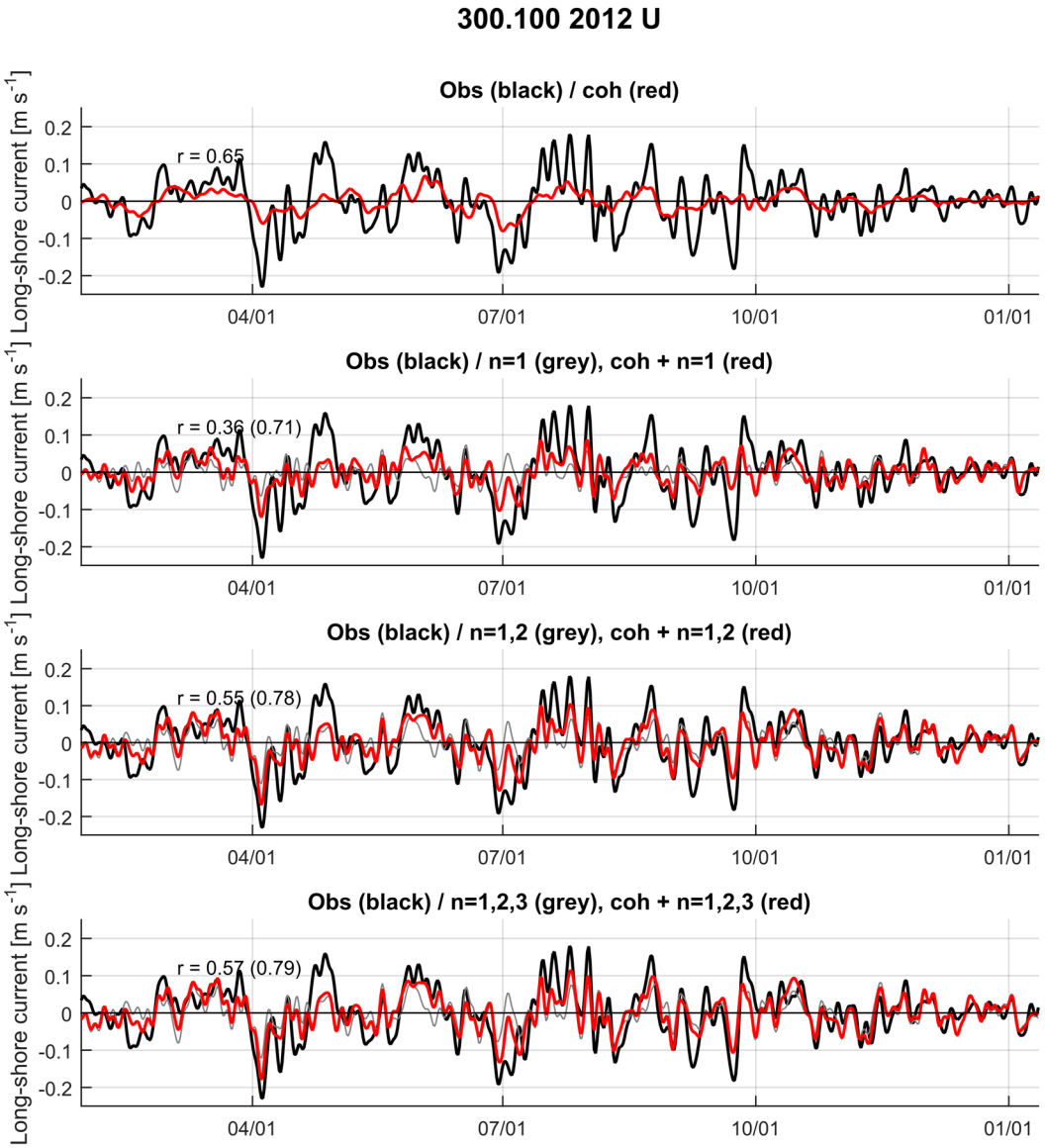

Figure 4.11: Time domain results of the prediction compared to the depth-averaged long-shore current at site 300.100 for the year with the best sensor coverage in the vertical (2012). In each panel, the observations are indicated with a thick black line and the prediction using the coherent mode plus some number of waves (using just the waves) is given as a thick red line (thin grey line). From top to bottom, the predictions cumulatively add the coherent mode, the $n = 1$ mode, the $n = 2$ mode, and the $n = 3$ mode.

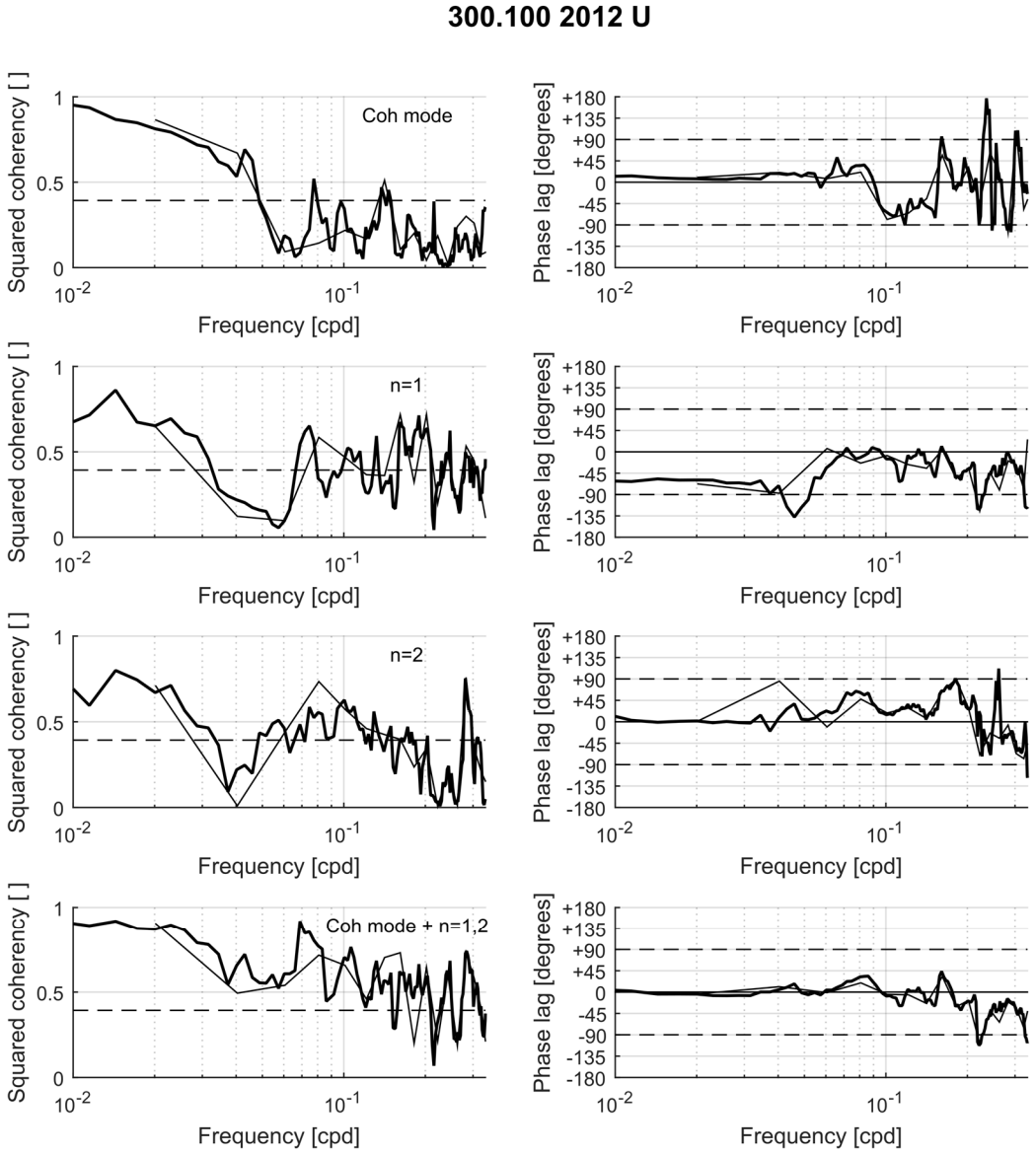

Figure 4.12: Frequency domain results of the prediction compared to the depth-averaged long-shore current at site 300.100 for the year with the best sensor coverage in the vertical (2012). Panels at left show the squared coherency spectra and panels at right the cross-phase spectra. The signals retained are labeled in the upper right of the coherency plots. Thick black spectra use the multitaper method and thin spectra average non-overlapping windows, each with 14 EDOF. The horizontal dashed line indicates coherence significant at an $\alpha = 0.05$ level.

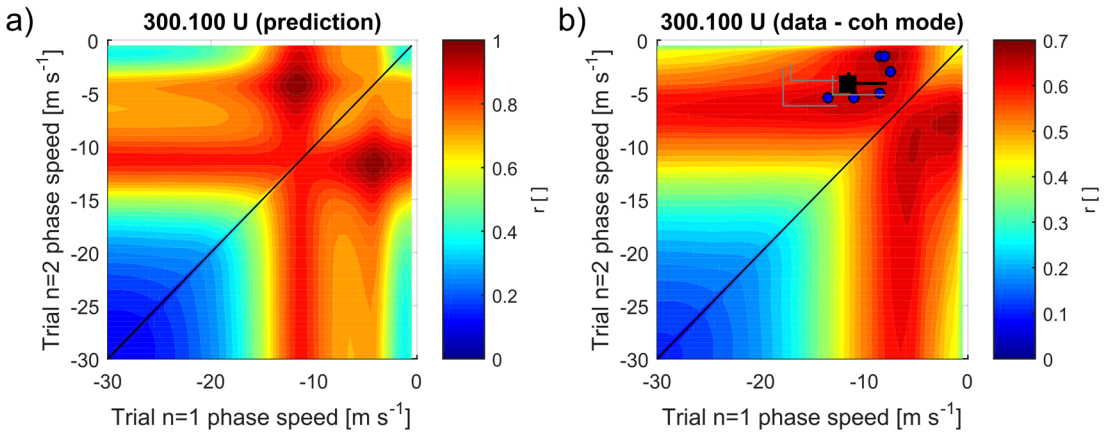

Figure 4.13: Contour plots of correlation coefficients for the trial predictions (optimal results from equation 4.24) averaged across all mooring-years that have current meter data at site 300.100 (years predicted given in table 4.3). Panel **(a)** shows the correlation coefficients for the optimal fits against the actual wind-driven prediction (as a test) while panel **(b)** shows the correlation coefficients for the optimal fits against the data minus the predicted coherent mode (the residual being the waves). In panel **(b)**, the blue circles indicate the optimal phase speed pairs for each year of prediction, the black square indicates the actual BSW $n = 1, 2$ phase speed pair for the circumpolar bottom-capped bathymetry, and the L-shaped axes indicate the range of dispersive CTW $n = 1$ and 2 phase speeds for wavenumbers 1 - 10 for each of the four bathymetry profiles (see figure 4.3; the axes for the circumpolar bottom-capped bathymetry are black while the other three are grey).

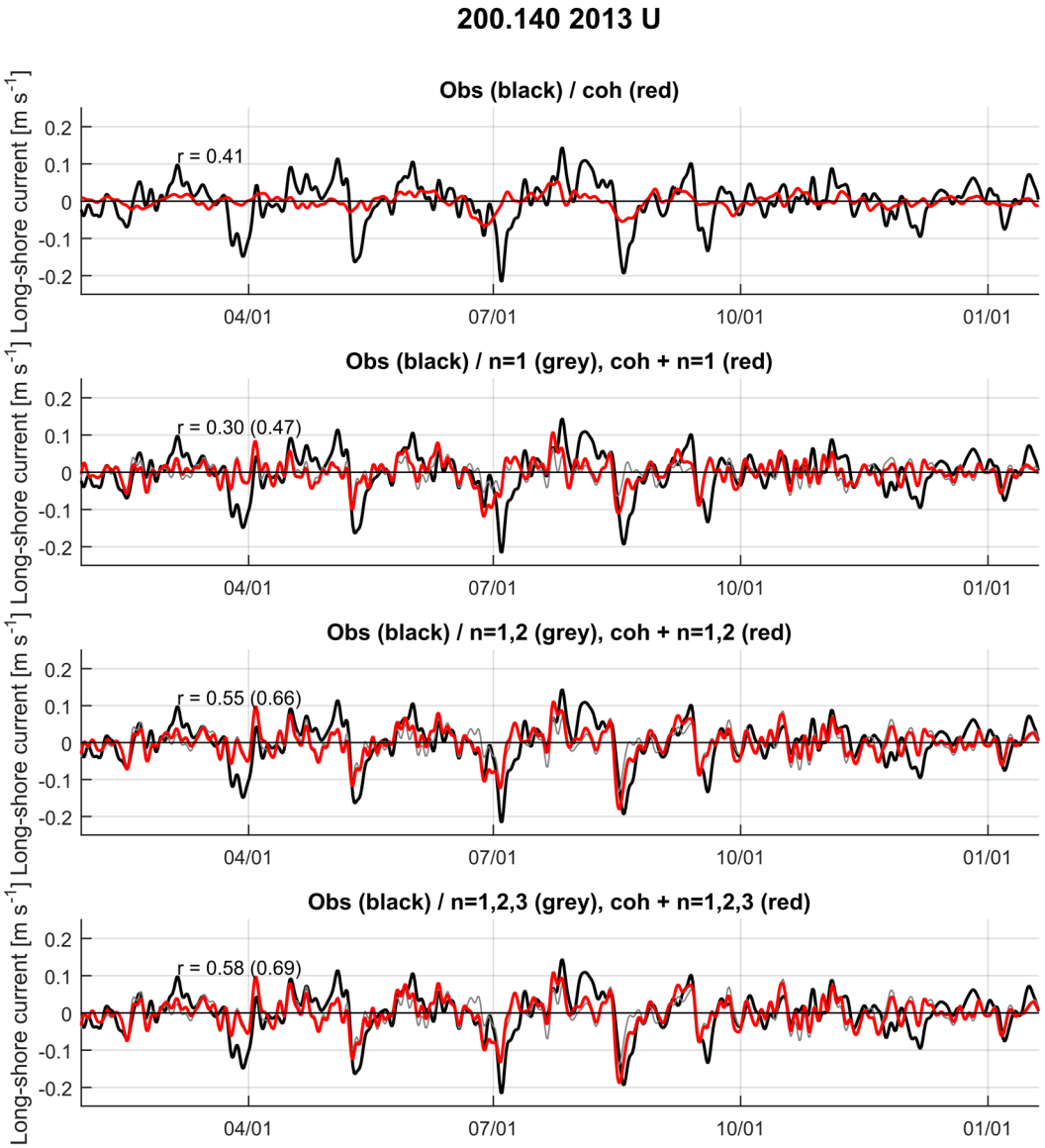

Figure 4.14: Exactly as in figure 4.11 except displaying the prediction compared to the depth-averaged long-shore current at site 200.140 for the only year of sampling (2013).

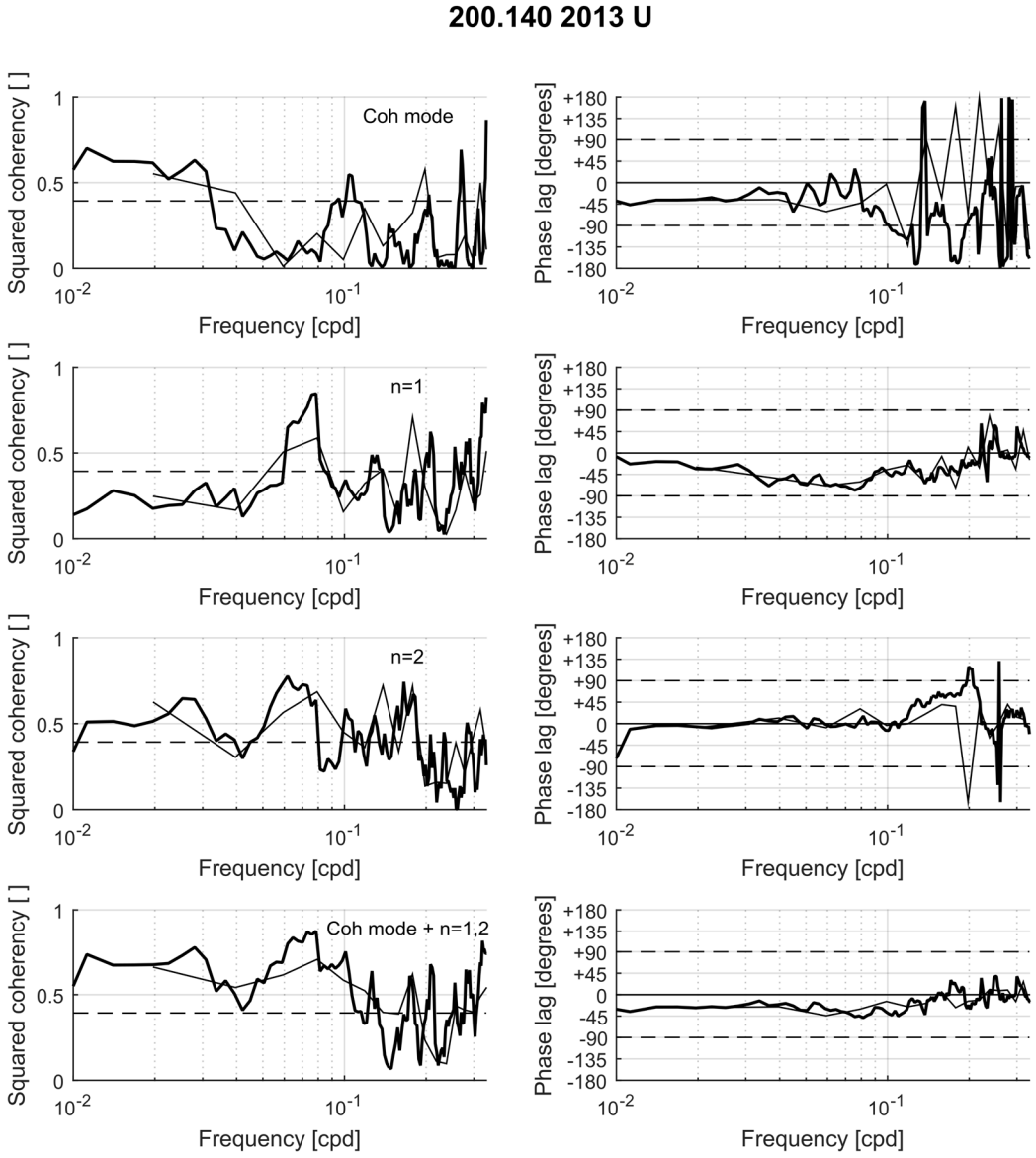

Figure 4.15: Exactly as in figure 4.12 except displaying results of the prediction compared to the depth-averaged long-shore current at site 200.140 for the only year of sampling (2013).

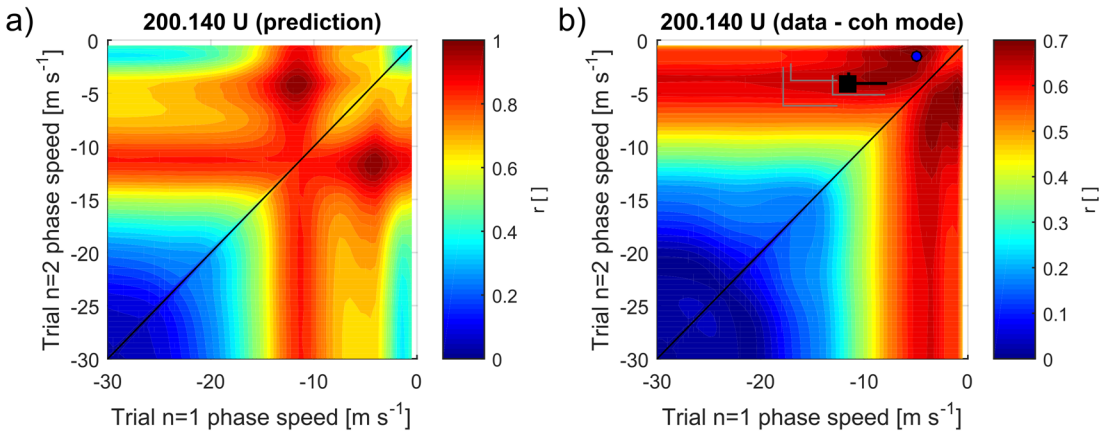

Figure 4.16: Exactly as in figure 4.13 except for the single prediction at site 200.140.

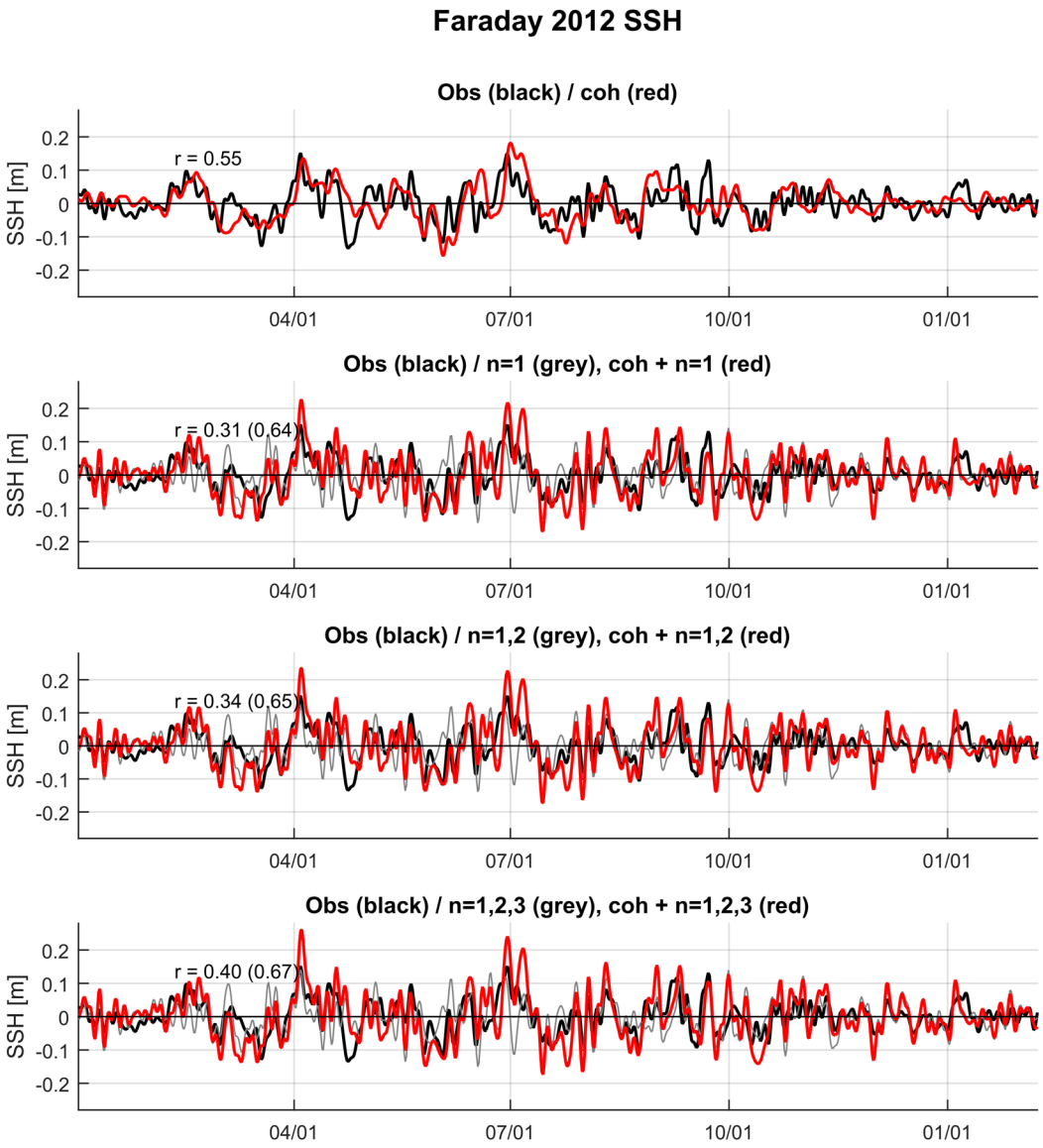

Figure 4.17: Exactly as in figure 4.11 except displaying the prediction compared to the SSH signal at Faraday tide gauge for a representative year of sampling (2012).

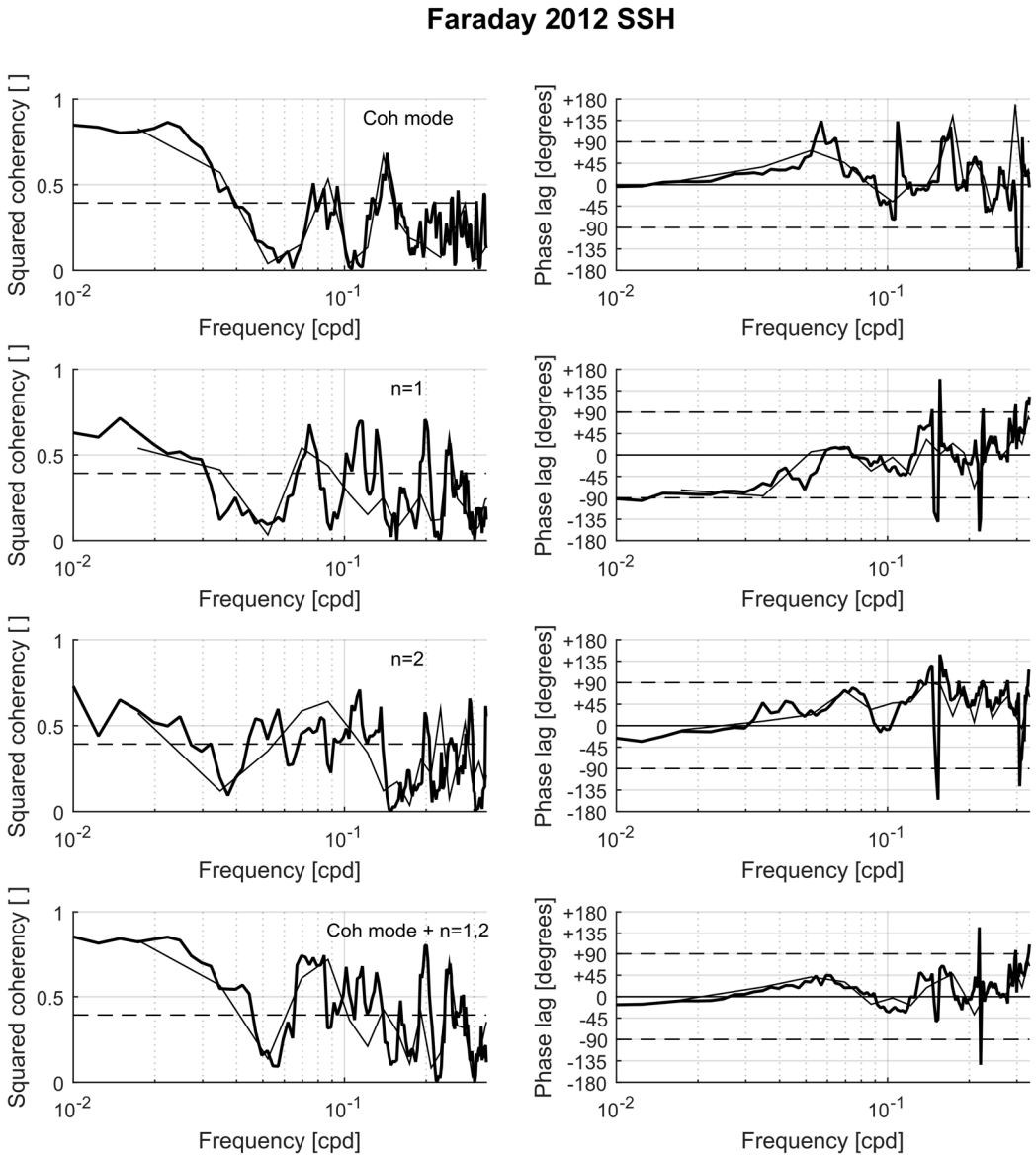

Figure 4.18: Exactly as in figure 4.12 except displaying results of the prediction compared to the SSH signal at Faraday tide gauge for a representative year of sampling (2012).

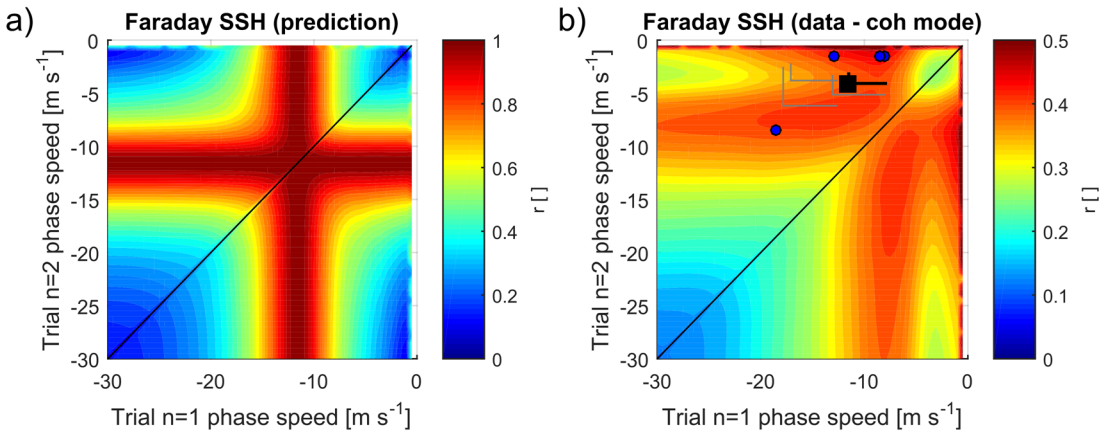

Figure 4.19: Exactly as in figure 4.13 except for all predictions at Faraday tide gauge (years predicted shown in table 4.3).

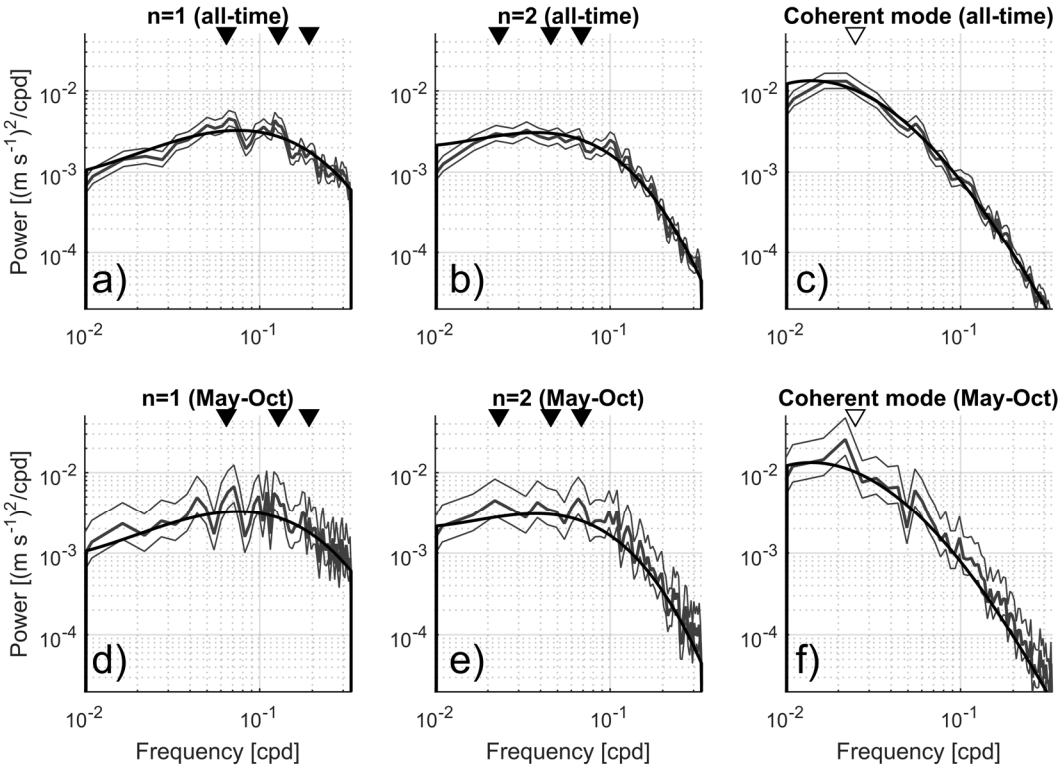

Figure 4.20: Power spectral estimates of the predicted velocity signals evaluated over the entire length of reanalysis stress (2008-2017). **(a)** Power spectrum for the $n = 1$ velocity signal computed with 50% overlapping 180-day Hanning windows (bold grey). Error bars at an $\alpha = 0.10$ level are indicated about that spectrum (thin grey). For assessment of statistical significance, a null spectrum is estimated by fitting a cubic polynomial to the log-transformed spectrum (bold black). For reference, expected resonances at wavenumbers 1-3 are indicated with black wedges. **(b)** Exactly as in (a) but for the $n = 2$ signal. **(c)** Exactly as in (a) but for the coherent mode, where an empirical peak is indicated with a hollow wedge. **(d)** Power spectrum for winter-only $n = 1$ velocity signal computed by averaging the 183-day unwindowed spectra (May-October) for every winter of reanalysis stress. Error bars at an $\alpha = 0.10$ level are indicated (thin grey) and the same null spectrum based on the all-time spectral estimate in (a) is shown (bold black). **(e)** Exactly as in (d) but for the $n = 2$ signal and with the null spectrum from (b). **(f)** Exactly as in (d) but for the coherent mode and with the null spectrum from (c).

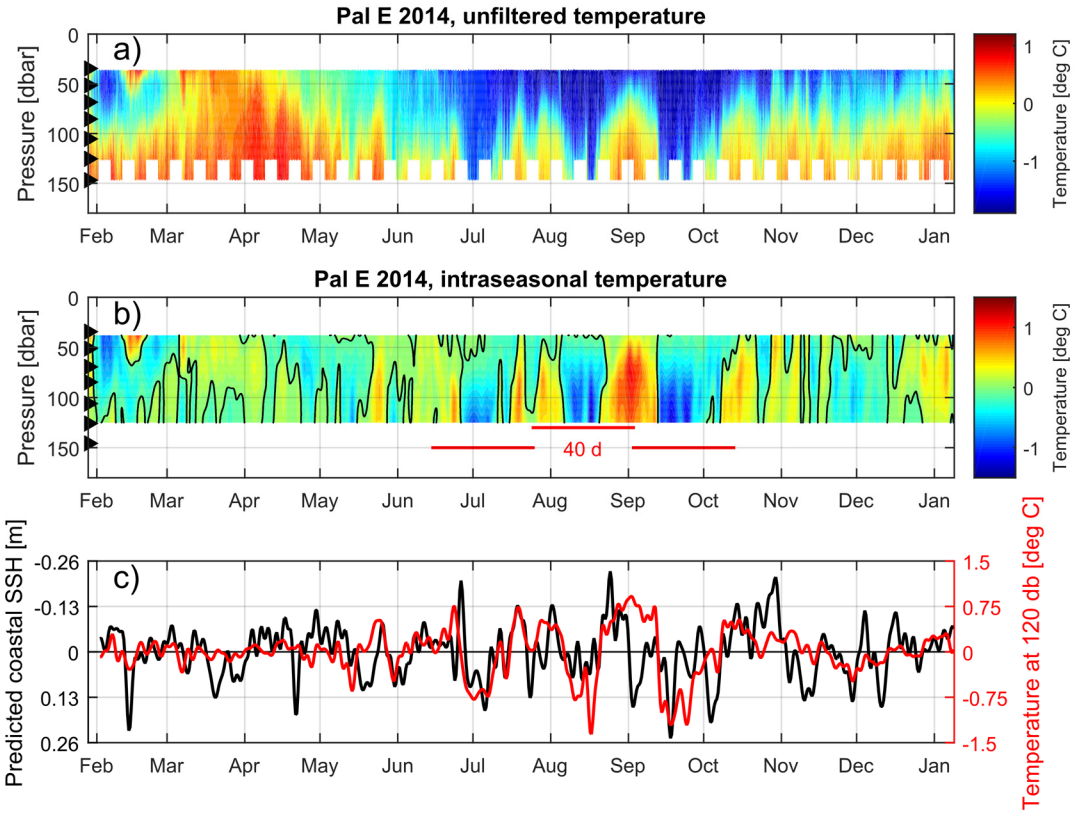

Figure 4.21: Upwelling signal at coastal site Pal E compared to predicted SSH. **(a)** Presentation of temperature profiles as measured by thermistor mooring at Pal E in mooring-year 2014. The nominal thermistor depths are indicated with black wedges at left. **(b)** The depth-interpolated temperature profiles from (a) band pass filtered in time to retain periods 3-100 days. The 0 ºC temperature anomaly contour is indicated in black. The three red lines are each 40 days long, cumulatively increasing from 15 June 2014. **(c)** The filtered temperature signal at 120 dbar from panel (b) (red) plotted along with the predicted coastal SSH anomaly at the 600 grid line due to the coherent mode plus the first two BSW (black). The axis for the SSH anomaly is flipped in order to enhance presentation of the expected relationship.

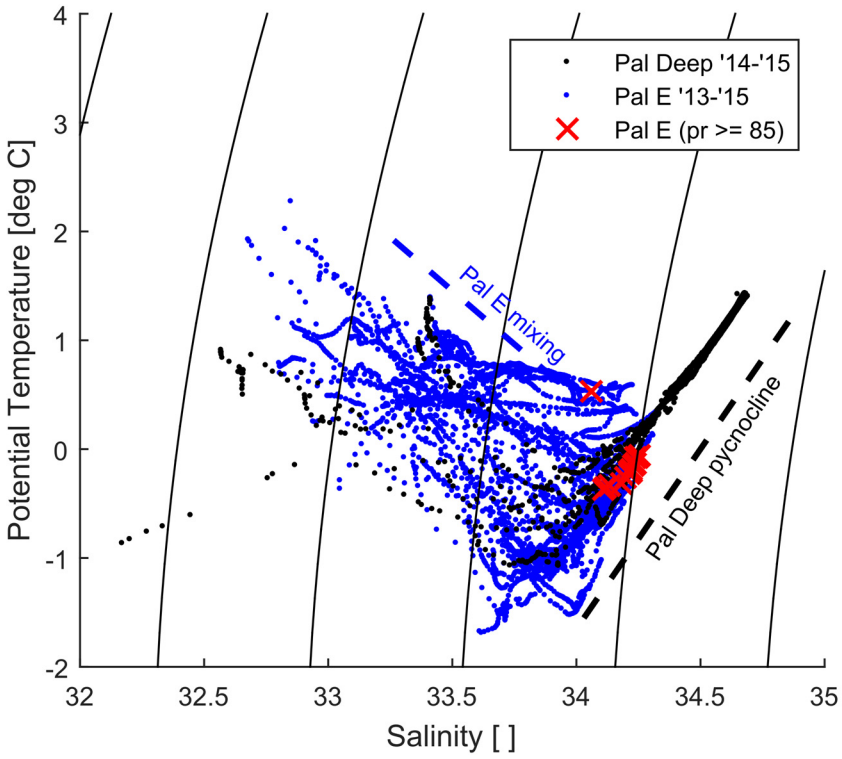

Figure 4.22: *T-S* diagram of the Palmer area emphasizing source water to the Palmer environment. Data from CTD casts at Palmer Deep on cruises straddling the Pal E thermistor mooring deployment (January 2014 and 2015) are shown as black dots while data from CTD casts at Pal E from field seasons straddling the deployment (2013-14 and 2014-15 summer seasons) are shown as blue dots. Samples from Pal E CTD casts deeper than 85 dbar are indicated with red x's, are coincident in *T-S* space with samples from the Palmer Deep permanent pycnocline (schematically as dashed black line), and are made more buoyant through mixing with overlaying water (schematically as dashed blue line). Note that the median depth of deepest sample for all Pal E CTD casts is 82 dbar even though the actual bottom depth of the site is 158 dbar.

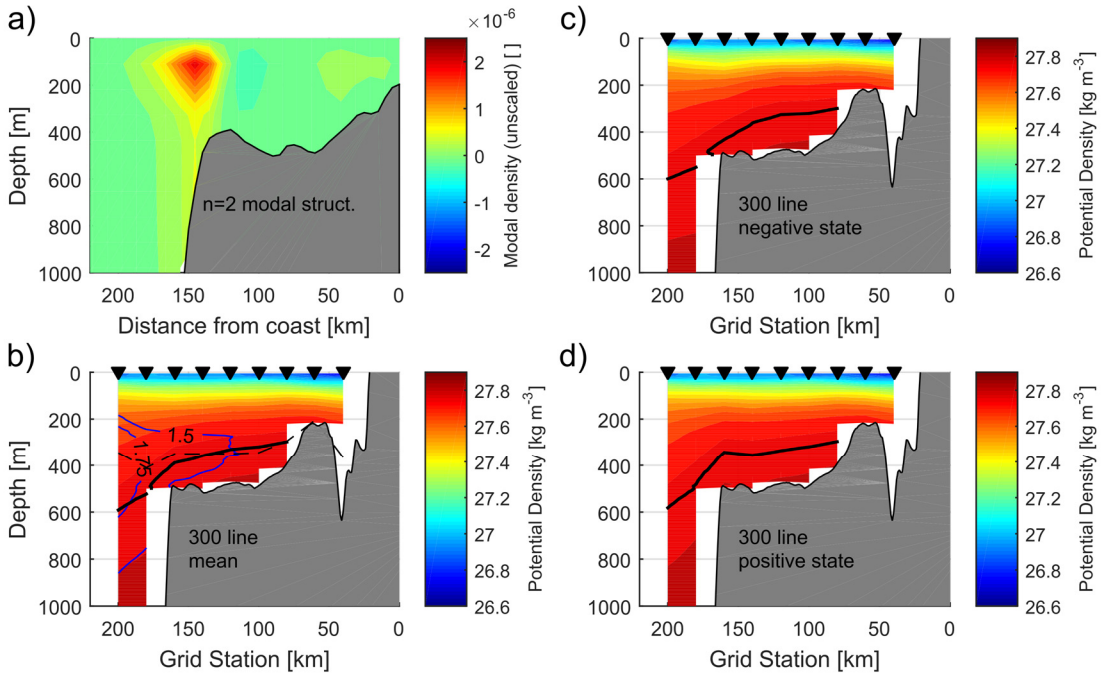

Figure 4.23: Demonstration of the potential consequences of the baroclinicity of the $n = 2$ wave over the steep WAP continental slope. **(a)** The CTW $n = 2$ modal structure for density anomaly for the WAP bathymetry profile at wavenumber 1. Units are arbitrary. **(b)** Color contours showing climatological cross-shelf field of potential density on the 300 line calculated from the full database of shipboard Pal LTER CTD sampling (stations shown as black wedges). The depth of the climatological T_{max} is shown as a black dashed line and an isopycnal that approximately overlaps with the T_{max} on the shelf is shown as a solid black line. Two isotherms (1.5 ºC and 1.75 ºC) are shown as blue contours. **(c)** The climatological potential density from (b) minus the modal density anomaly from (a) gridded onto the Pal LTER coordinates and scaled by the temporal variance of the CTD potential density (see text). The same isopycnal plotted in (b) is plotted here. **(d)** As in (c) but the scaled, gridded modal density anomaly is added to the climatological potential density.

5) Conclusions and suggestions for future work

5.1) Synthesis

This work used a rare and novel observational data set collected on the WAP shelf to enhance our understanding of the circulation and shelf-slope exchange on weather band through intraseasonal time scales. Our focus was on elucidating underlying physical processes, particularly those relevant for the Pal LTER project. We also set out to understand how the processes identified might respond to local and remote wind stress, capitalizing on the efficacy of the circumpolar waveguide. The major findings of this dissertation are synthesized in a conceptual diagram (figure 5.1) and summarized below.

In chapter 2 we found that thermal variance below the pycnocline is dominated by small, anticyclonic mesoscale features that contain UCDW as found on the continental slope. Their size and separation are consistent with a linear instability along the continental slope. In seeking out how the eddies mix with surrounding water, we parameterized vertical diffusivities and heat fluxes and found that vertical heat fluxes are generally small (< 1 W m^{-2}) and associated with shear slightly above a local Garrett-Munk spectrum. On the other hand, substantial thermohaline intrusions – probably associated with stirring by the eddies themselves – imply that lateral mixing is quite large. To verify these findings, we compared the cooling of an eddy repeatedly sampled by a glider with a forward diffusion model. Their agreement suggests that almost all of the initial eddy heat loss is by lateral mixing. We deduce that the mesoscale eddies transport pure UCDW onto the shelf and cause lateral mixing which defines the properties of the subpycnocline layer, and that the layer is further modified by weaker mixing with overlying WW, defining the structure of the permanent pycnocline.

In chapter 3 we found that over 50% of the total circulation variance on the WAP shelf as measured by moored current meters can be described by a spatially coherent pattern associated with flow-topography interaction in the vicinity of Marguerite Trough. An analysis of rotary and component kinetic energy spectra in combination with EOF analysis and upwelling/downwelling velocity composites suggests that wind-driven northeastward fluctuations in the long-shore flow of scale larger than the array length lead to a diversion of the SBJ upon encountering the trough, steering the flow through the northern limb at the fork of the canyon, diverting it onto the shelf-proper, and compressing it to generate an anticyclonic upwelling pattern. On the other hand, when subject to downwelling wind stress, the pattern is weakened and the flow falls to potential vorticity conserving motions (along-isobath flow within Marguerite Trough and free anticyclonic motions on a bank). Other than in the mean, the circulation is generally incoherent with subpycnocline temperature. While surprising, this is consistent with the findings of chapter 2 which revealed that the thermal variance is dominated by small eddies with weak azimuthal rotation.

Struck by the scale of the circulation pattern and its correlation to wind stress both local and remote, in chapter 4 we tested the hypothesis that long-shore barotropic currents along the Antarctic shelf are in geostrophic balance with low-wavenumber, wind-driven SSH fluctuations. We found that on average about half of the intraseasonal (3-100 days) variance in the barotropic current as measured by moored current meters can be predicted by a wavenumber zero coherent mode and at least two BSW modes forced by reanalysis surface stress. The coherent mode variability has a reddish spectrum while the BSW tend to be slightly more apparent at periods where they can resonate with westward propagating atmospheric patterns. The phase speeds detected from an analysis of a hovmöller matrix of circum-Antarctic time series agree reasonably

well with the phase speeds of the first two BSW, and nondispersive BSW are shown to be a good approximation to CTW. Importantly, we found the second mode BSW to be very important in velocity signals, particularly at low frequencies. We also found most signals to be dominated by periods of ~40 days which can be linked to the MJO by multiple hypothesized physical pathways. We also considered two explicit applications for the wind-driven phenomena relevant for shelf-slope exchange. We found that the shoreward pressure gradient associated with the wind-driven fluctuations correlates significantly with upwelling of warm water at an ecologically productive canyon head. We also found that the subtle baroclinicity of the second mode wave can plausibly depress the pycnocline at the shelf-break.

We have shown that large-scale wind forcing can be funneled into near-shore environments owing in large part to the highly barotropic nature of the flow which gets 'enhanced' when subject to a shelf-scale sea surface height drop. At least at Palmer canyon, low-frequency temperature oscillations correlate to the large-scale wind-driven SSH signal. It is likely that there is a correspondence at shorter periods as well, although the complicated link between forcing and response means only the slowest and largest fluctuations stand out in the data. Regarding the canyon hypothesis of the Pal LTER, this suggests the possibility that canyons are highly productive because they are choke points for strong lateral advection. The warm water that episodically replenishes the near-bottom of the Palmer Station area may be able to place a bottom-up control on mixed layer depth – an ecologically critical parameter – by shoaling the pycnocline or inducing sea ice melt.

5.2) Concluding remarks

This study would not have been possible without novel observing platforms (Slocum gliders) or the resources to deploy and maintain a long-term sampling array of moored current meters (the Pal LTER project). Such observations in the harsh Antarctic conditions (particularly long-term sampling arrays) are rare. We hope that we have demonstrated their value. Remote surface observations are limited by sea ice and cloudiness and subsurface floats are limited by their spatial coverage (which is improving). We suggest that the best observational approach moving forward may be to leverage the strengths of complementary platforms and to focus efforts on sampling topographic choke points and bathymetric irregularities that we (and others) have shown tend to enhance signal to noise ratios and couple length scales. One example of an observing system is that of the Converge project (Kohut et al. 2018) which samples the head of Palmer Deep canyon with HF radar, gliders, and ADCP moorings in concert with biological sampling, acoustics, and animal tagging. While sparser and covering a larger spatial scale, the Pal LTER also leverages moored current meters, gliders, and ship sampling to their strengths.

Observations should be conducted in coordination with numerical modeling. Regional models of the WAP (e.g., Graham et al. 2016), Amundsen Sea (e.g., St-Laurent et al. 2017), and Ross Sea (e.g., Mack et al. 2017) shelves, for example, have become increasingly high resolution (1.5. km), comprehensive (inclusion of ecological models, ice shelves, and/or tides), and impressively accurate in terms of comparison with data. Still, we think there is more to be mined from these models in terms of testing more fundamental dynamical questions such as those considered in this study. Idealized process studies have been very useful in that regard (e.g., St-Laurent et al. 2013; Stern et al. 2015; Stewart and Thompson 2015). Analysis of very high-

resolution global models that now simulate eddies and internal tides is beginning and is already yielding exciting results (Stewart et al. 2018).

As is true with any study of this scope, more questions were raised throughout than were actually answered. We conclude by posing a few of them.

- *Do the processes identified herein scale up in time?*

We identified processes that operate with periods shorter than about 100 days. There are two questions we would like to ask: (1) Do the intraseasonal fluctuations matter for the net shoreward heat transport when integrated over longer periods of time? (2) Do the processes operating on intraeasonal time scales also operate on longer time scales? When we refer to longer periods of time, let us refer to periods of several years or decades. Beginning with the advective processes of chapters 3 and 4, the long-shore intraseasonal velocity fluctuations associated with the spatially coherent pinch pattern likely do not matter when integrated over a period of time. The time mean of the eddy heat transport term evaluated over each year of mooring deployments is less than about 2% of the mean term and its sign is not the same year by year. On the other hand, the heat transport by the mean term is large and positive. Thus, while the fluctuations do not seem to yield a significant mean transport, on average, if there were a change to the mean state (say, the long-shore wind stress and/or coastal SSH gradient on time scales longer than ~100 days), then perhaps there would be an increased shoreward heat transport. Such a change may be associated with a more positive phase of the SAM. Reduced polar easterlies would drop the coastal sea surface height by maintaining an enhanced wavenumber zero state and/or 'switching on' a steadily forced barotropic shelf wave. This is

similar to the idea proposed by Spence et al. (2017), although they posited Kelvin waves to propagate the SSH signal. Such a change to the long-shore flow would accelerate the pinch pattern and its mean onshore heat transport (chapter 3), could generate a bottom Ekman layer onflow (Spence et al. 2017), and/or could raise isopycnals through the wave's cross-shelf structure and baroclinicity over the slope (chapter 4). Note that this discussion considered changes resulting from the wind-driven barotropic sea surface height fluctuations associated with a more +SAM. On the other hand, in a doubled CO_2 experiment, there is the suggestion that the cross-shelf dynamic height gradient associated with a coastal halosteric sea level rise would generate stratified disturbances that affect long-shore flow in the opposite sense (Goddard et al. 2017).

For the mesoscale eddies, the answer is not clear. For regions such as the WAP without a significant ASF, a trend towards a more positive phase of the SAM reduces the effects of the polar easterlies and reduces coastal downwelling, potentially giving more UCDW-containing isopycnals access to the shelf (Spence et al. 2014). In regions with a prominent ASF, weaker easterlies reduce the front strength and yield more continuous isopycnals for a greater eddy heat flux (Stewart and Thompson 2015). There is also some suggestion that a trend towards fresher shelf waters under doubled CO_2 (due to more CDW onflow, more melt water, and reduced vertical mixing) would enhance lateral density gradients at the shelf edge, sharpen the ASF, and thereby reduce eddy heat fluxes (Goddard et al. 2017), though those results should be considered cautiously as their model resolution near the slope was 4-6 km and other authors have shown a grid spacing < 1.5 km is essential to properly simulate the mesoscale eddy field there (St-Laurent et al. 2013; Stewart and Thompson 2015). While the arguments for isopycnal access are somewhat clear, changes in baroclinicity associated with altered isopycnal slopes and lateral

density gradients are less clear. As eddy heat fluxes are highly regionally localized (Stewart et al. 2018) since they depend on a great number of regional parameters (Stewart and Thompson 2015), the answer likely varies by sector around the continent.

- *Are these processes relevant elsewhere around Antarctica?*

The major parameters we identified earlier as favorable for a shoreward flux of CDW are an eastward current (which promotes flow-canyon interaction and bottom Ekman layer onflow), an adjacent Southern ACC Boundary (which yields source of CDW), and a weak or absent ASF (which reduces the barrier for the CDW). These three conditions are essentially one in the same, corresponding to the portion of the Antarctic slope where the ACC flows adjacent, un-buffered by the Weddell or Ross Gyres. These conditions are met, for example, in much of west Antarctica, and similar shoreward fluxes of CDW have been observed in submarine troughs (e.g., Assmann et al. 2013; Wåhlin et al. 2013; Walker et al. 2013). While the role of the wind and origin of the velocity fluctuations in those studies was not necessarily conclusive, it is plausibly the same as that considered here. Owing to their low wavenumber, we suspect that the wind dynamics identified here are very general.

The sensitivity tests performed in chapter 2 suggest that mesoscale eddies should also be quite general. They should certainly be common where the ASF is absent or where it is raised by descending plumes of Antarctic Bottom Water and where the bottom slope mirrors the isopycnal slope (yielding maximal Eady growth rate). Their small size means observations are limited, particularly to the heavily sampled WAP (Moffat et al. 2009; Martinson and McKee 2012; Couto et al. 2017; McKee et al. 2019) although eddies have been simulated in the Amundsen (St-

Laurent et al. 2017) and Ross (Mack et al. 2017) Seas. Stewart et al. (2018) suggest that cross-isobath eddy heat flux is highly localized in space but is generally strongest over the deeper part of the continental slope. They also find that the eddy heat flux is not well approximated by combining an eddy overturning streamfunction with along-isobath eddy potential temperature, suggesting that much of the cross-isobath eddy heat flux is accomplished by stirring of heat. An important caveat is that what those authors term eddy variability encompasses all variability at subtidal time scales, so it is not confined to mesoscale eddies-proper and also includes other weather-band and intraseasonal variability.

A parameter that may make shelf-slope exchange on the WAP unique is its bottom slope, which is comparatively steep. The steep bottom slope should enhance baroclinicity relative to more gradual slopes. It also strongly modifies the CTW cross-shelf structure compared to those calculated with a circumpolar bathymetry, to the point that oceanic isopycnals can be made discontinuous with the shelf as shown in chapter 4. The steep bottom slope is also implicated in the relatively large modeled bottom Ekman layer onflow on the WAP compared to other environments (Spence et al. 2017).

- *Do the processes affect each other?*

The CTW affect the flow-topography interaction pattern as identified in chapters 3 and 4. But do the CTW and the mesoscale eddies interact at all? While we approximate the eddy origin via a linear baroclinic instability analysis and we approximate the CTW as BSW, in reality the eddies are drawing from both available potential energy and mean kinetic energy and in reality the weakly baroclinic CTW are modulating both of those pools. As discussed in chapter 4, the

second mode CTW modulates pycnocline depth over the continental slope and also alters the lateral position of the shoreward isopycnal slope. Additionally, its major periods are much longer than the linear growth times of the eddies. Interaction between these phenomena should be considered.

- *Is the wind forcing related to regular intraseasonal patterns in the Antarctic winds?*

In this study we chose to focus on mechanistic links between the long-shore wind stress and velocity fluctuations. Although along the way analyses in the frequency domain and heterogeneous correlation maps revealed some information about important frequencies and spatial scales of the forcing, we did not consider explicitly how certain patterns of atmospheric circulation might be responsible for driving the observed variability.

The omnipresence of 40-day fluctuations (e.g. in total velocity signals, in coherent mode and second mode BSW variability, and in coastal bottom temperature variability) led us to preliminarily speculate on the role of the Madden-Julian Oscillation (MJO). The MJO has been shown to yield an atmospheric wave response to tropical convection that projects onto wavenumber zero atmospheric (SAM-like) variability about a week after tropical forcing which then affects wavenumber zero fluctuations in SSH and Drake Passage Transport about three days later (Matthews and Meredith 2004). Additionally, the PSA patterns represent an atmospheric wave train propagating towards the Antarctic continent with period of ~40 days (Mo and Higgins 1998) and have a center of action in the southeast Pacific that may impact the WAP more locally. However, as we discussed in the text, there is some debate as to whether the MJO projects on to the SAM at all (Pohl et al. 2010) and the PSA wave train may only episodically interact with

tropical convection, having different physical origin at other times (Mo and Higgins 1998). Thus, the wind forcing that drives the observed velocity fluctuations may not be externally forced.

A candidate for internal atmospheric variability on intraseasonal time scales is the SAM. The SAM has a natural time scale of about 10 days (Gerber et al. 2008) and Pohl et al. (2010) claim that variability with periods 30-60 days previously attributed to the MJO could be due to internal variability of the SAM. Although primarily annular by definition and thus most likely to contribute to the coherent mode of variability (as has been demonstrated; Aoki 2002), the zonal structure of the SAM varies seasonally in response to large-scale temperature gradients, being more zonal in the summer and taking on more of a wavenumber 2 or 3 structure in winter. The SAM also has a distinctly non-annular component in the southeastern Pacific (e.g., Lefebvre et al. 2004) that may project onto the Amundsen Sea Low. The Amundsen Sea Low is a climatological low pressure center that makes up one of a stationary set of alternating high and low pressure centers around the continent at zonal wavenumber 3 (ZW3). While most atmospheric variability at $k = 3$ in the Antarctic is eastward propagating, the standing component is energetic predominantly with period 20-40 days (Dell'Aquila et al. 2007).

The quasi-regularity of the velocity fluctuations and their occurrence largely at periods longer than the weather band (which is dominated by individual synoptic disturbances) suggests that they are likely associated with regular patterns of variability in the atmosphere. Any relevant wind pattern must have a strong imprint on the coastal winds. In addition, for an ocean wave response, any pattern would more likely generate a large response if it is westward propagating (as it may resonate with the ocean) or standing. Attribution of relevant atmospheric phenomena warrants further investigation.

Figures

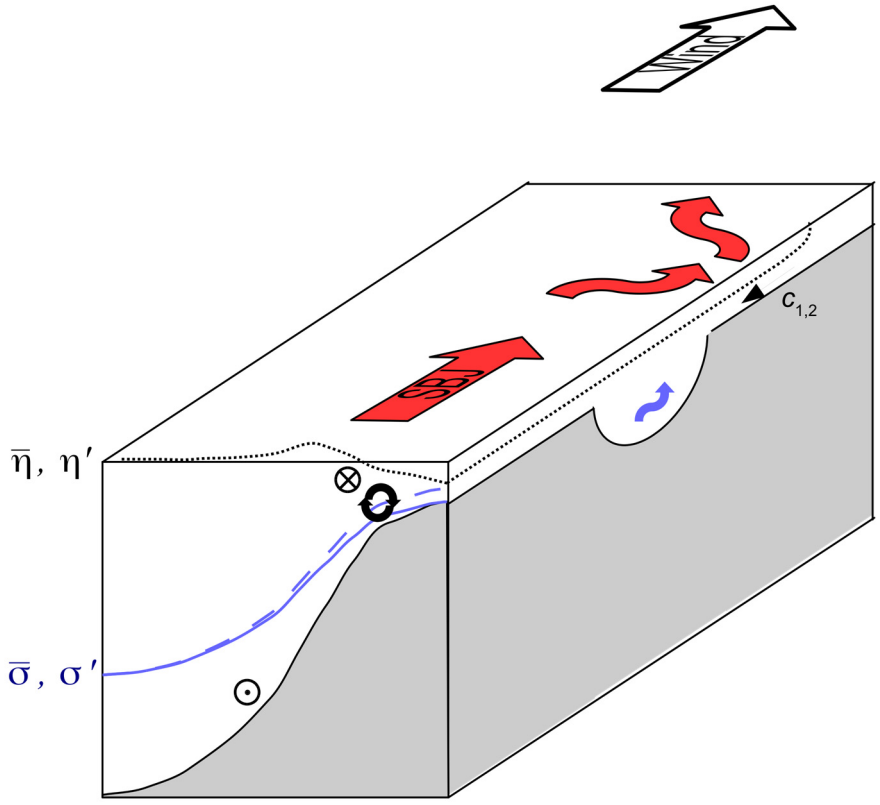

Figure 5.1: Conceptual diagram of intraseasonal circulation processes developed in this dissertation. Mean (solid) and perturbation (dashed) SSH (black) and T_{max} isopycnal (blue) are indicated. A long-shore wind stress perturbation (either local or remote) generates a SSH perturbation that propagates westward as waves with phase speeds c_1 and c_2. Upon arrival in the LTER grid, the SSH drop increases the long-shore shelf-break jet (SBJ; red) in geostrophic balance. The consequences are (1) a diversion of the SBJ onto the shelf downstream of Marguerite Trough (wavy red arrows) with an enhancement of the barotropic circulation and (2) a lateral advection towards the canyon head with upwelling of warm water, even in wintertime (blue curved arrow). Because eddy growth rates are faster than the major periods of wind variability, warm-core eddy generation proceeds at the shelf edge in the background (black curved arrows).

Bibliography

Allen, S. E., and B. M. Hickey, 2010: Dynamics of advection-driven upwelling over a shelf break submarine canyon. *J. Geophys. Res.*, **115** (**C8**), C08018, doi:10.1029/2009JC005731.

——, C. Vindeirinho, R. E. Thomson, M. G. Foreman, and D. L. Mackas, 2001: Physical and biological processes over a submarine canyon during an upwelling event. *Can. J. Fish. Aquat. Sci.*, **58** (**4**), 671–684, doi:10.1139/f01-008.

Amante, C., and B. W. Eakins, 2009: ETOPO1 1 Arc-Minute Global Relief Model: Procedures, Data Sources and Analysis. NOAA Technical Memorandum NESDIS NGDC-24, NOAA, National Geophysical Data Center.

Annett, A. L., J. N. Fitzsimmons, M. J. M. Séguret, M. Lagerström, M. P. Meredith, O. Schofield, and R. M. Sherrell, 2017: Controls on dissolved and particulate iron distributions in surface waters of the Western Antarctic Peninsula shelf. *Mar. Chem.*, **196**, 81–97, doi:10.1016/j.marchem.2017.06.004.

Aoki, S., 2002: Coherent sea level response to the Antarctic Oscillation. *Geophys. Res. Lett.*, **29** (**20**), 11.1-11.4, doi:10.1029/2002GL015733.

Assmann, K. M., A. Jenkins, D. R. Shoosmith, D. P. Walker, S. S. Jacobs, and K. W. Nicholls, 2013: Variability of Circumpolar Deep Water transport onto the Amundsen Sea Continental shelf through a shelf break trough. *J. Geophys. Res. - Oceans*, **118** (**12**), 6603–6620, doi:10.1002/2013JC008871.

Beardsley, R. C., R. Limeburner, and W. Brechner Owens, 2004: Drifter measurements of surface currents near Marguerite Bay on the western Antarctic Peninsula shelf during austral summer and fall, 2001 and 2002. *Deep-Sea Res. Pt II*, **51** (**17**), 1947–1964, doi:10.1016/j.dsr2.2004.07.031.

Bernard, K. S., and D. K. Steinberg, 2013: Krill biomass and aggregation structure in relation to tidal cycle in a penguin foraging region off the Western Antarctic Peninsula. *ICES J. Mar. Sci.*, **70** (**4**), 834–849, doi:10.1093/icesjms/fst088.

Blumsack, S. L., and P. J. Gierasch, 1972: Mars: The Effects of Topography on Baroclinic Instability. *J. Atmos. Sci.*, **29** (**6**), 1081–1089, doi:10.1175/1520-0469(1972)029<1081:MTEOTO>2.0.CO;2.

Bormans, M., 1992a: Effect of R_ρ on double diffusive interleaving. *Deep-Sea Res.*, **39** (**5**), 871–884, doi:10.1016/0198-0149(92)90126-E.

——, 1992b: An experimental study on the formation and survival of stratified subsurface eddies. *J. Geophys. Res. - Oceans*, **97** (**C12**), 20155–20167, doi:10.1029/92JC01973.

Bracegirdle, T. J., 2013: Climatology and recent increase of westerly winds over the Amundsen Sea derived from six reanalyses. *Int. J. Climatol.*, **33** (**4**), 843–851, doi:10.1002/joc.3473.

Brink, K. H., 1982a: A Comparison of Long Coastal Trapped Wave Theory with Observations off Peru. *J. Phys. Oceanogr.*, **12** (**8**), 897–913, doi:10.1175/1520-0485(1982)012<0897:ACOLCT>2.0.CO;2.

——, 1982b: The Effect of Bottom Friction on Low-Frequency Coastal Trapped Waves. *J. Phys. Oceanogr.*, **12** (**2**), 127–133, doi:10.1175/1520-0485(1982)012<0127:TEOBFO>2.0.CO;2.

——, 2006: Coastal-trapped waves with finite bottom friction. *Dynam. Atmos. Oceans*, **41** (**3**), 172–190, doi:10.1016/j.dynatmoce.2006.05.001.

——, and J. S. Allen, 1978: On the Effect of Bottom Friction on Barotropic Motion Over the Continental Shelf. *J. Phys. Oceanogr.*, **8** (**5**), 919–922, doi:10.1175/1520-0485(1978)008<0919:OTEOBF>2.0.CO;2.

Carvajal, G. K., A. K. Wåhlin, L. E. B. Eriksson, and L. M. H. Ulander, 2013: Correlation between Synthetic Aperture Radar Surface Winds and Deep Water Velocity in the Amundsen Sea, Antarctica. *Remote Sens.*, **5** (**8**), 4088–4106, doi:10.3390/rs5084088.

Carvalho, F., J. Kohut, M. J. Oliver, R. M. Sherrell, and O. Schofield, 2016: Mixing and phytoplankton dynamics in a submarine canyon in the West Antarctic Peninsula. *J. Geophys. Res. - Oceans*, **121** (**7**), 5069–5083, doi:10.1002/2016JC011650.

Chavanne, C. P., K. J. Heywood, K. W. Nicholls, and I. Fer, 2010: Observations of the Antarctic Slope Undercurrent in the southeastern Weddell Sea. *Geophys. Res. Lett.*, **37** (**13**), L13601, doi:10.1029/2010GL043603.

Cook, A. J., P. R. Holland, M. P. Meredith, T. Murray, A. Luckman, and D. G. Vaughan, 2016: Ocean forcing of glacier retreat in the western Antarctic Peninsula. *Science*, **353** (**6296**), 283–286, doi:10.1126/science.aae0017.

Couto, N., D. G. Martinson, J. Kohut, and O. Schofield, 2017: Distribution of Upper Circumpolar Deep Water on the warming continental shelf of the West Antarctic Peninsula. *J. Geophys. Res. - Oceans*, **122** (**7**), 5306–5315, doi:10.1002/2017JC012840.

Dell'Aquila, A., P. M. Ruti, S. Calmanti, and V. Lucarini, 2007: Southern Hemisphere midlatitude atmospheric variability of the NCEP-NCAR and ECMWF reanalyses. *J. Geophys. Res. - Atmos.*, **112** (**D8**), D08106, doi:10.1029/2006JD007376.

Dewey, R., R. Muench, and J. Gunn, 1999: Mixing and vertical heat flux estimates in the Arctic Eurasian Basin. *J. Marine Syst.*, **21** (**1**), 199–205, doi:10.1016/S0924-7963(99)00014-7.

Dinniman, M. S., and J. M. Klinck, 2004: A model study of circulation and cross-shelf exchange on the west Antarctic Peninsula continental shelf. *Deep-Sea Res. Pt II*, **51** (**17**), 2003–2022, doi:10.1016/j.dsr2.2004.07.030.

——, ——, and W. O. Smith, 2011: A model study of Circumpolar Deep Water on the West Antarctic Peninsula and Ross Sea continental shelves. *Deep-Sea Res. Pt II*, **58** (**13**), 1508–1523, doi:10.1016/j.dsr2.2010.11.013.

——, ——, and E. E. Hofmann, 2012: Sensitivity of Circumpolar Deep Water Transport and Ice Shelf Basal Melt along the West Antarctic Peninsula to Changes in the Winds. *J. Climate*, **25** (**14**), 4799–4816, doi:10.1175/JCLI-D-11-00307.1.

Ducklow, H. W., K. Baker, D. G. Martinson, L. B. Quetin, R. M. Ross, R. C. Smith, S. E. Stammerjohn, M. Vernet, and W. Fraser, 2007: Marine pelagic ecosystems: the west Antarctic Peninsula. *Phil. Trans. R. Soc. B*, **362** (**1477**), 67–94, doi:10.1098/rstb.2006.1955.

Eveleth, R., N. Cassar, S. C. Doney, D. R. Munro, and C. Sweeney, 2017: Biological and physical controls on O2/Ar, Ar and pCO2 variability at the Western Antarctic Peninsula and in the Drake Passage. *Deep-Sea Res. Pt II*, **139**, 77–88, doi:10.1016/j.dsr2.2016.05.002.

Fennel, W., and M. Schmidt, 1991: Responses to topographical forcing. *J. Fluid Mech.*, **223**, 209–240, doi:10.1017/S0022112091001404.

Flament, P., 2002: A state variable for characterizing water masses and their diffusive stability: spiciness. *Prog. Oceanogr.*, **54** (**1**), 493–501, doi:10.1016/S0079-6611(02)00065-4.

Fogt, R. L., D. H. Bromwich, and K. M. Hines, 2011: Understanding the SAM influence on the South Pacific ENSO teleconnection. *Clim. Dynam.*, **36** (**7**), 1555–1576, doi:10.1007/s00382-010-0905-0.

Fraser, W. R., and W. Z. Trivelpiece, 1996: Factors Controlling the Distribution of Seabirds: Winter-Summer Heterogeneity in the Distribution of Adélie Penguin Populations. *Foundations for Ecological Research West of the Antarctic Peninsula*, R.M. Ross, E.E. Hofmann, and L.B. Quetin, Eds., Vol. 70 of *Antarctic Research Series*, American Geophysical Union (AGU), 257–272.

Garau, B., S. Ruiz, W. G. Zhang, A. Pascual, E. Heslop, J. Kerfoot, and J. Tintoré, 2011: Thermal Lag Correction on Slocum CTD Glider Data. *J. Atmos. Oceanic Technol.*, **28** (**9**), 1065–1071, doi:10.1175/JTECH-D-10-05030.1.

Garrett, C., 1982: On Spindown in the Ocean Interior. *J. Phys. Oceanogr.*, **12** (**9**), 989–993, doi:10.1175/1520-0485(1982)012<0989:OSITOI>2.0.CO;2.

——, and W. Munk, 1975: Space-time scales of internal waves: A progress report. *J. Geophys. Res.*, **80** (**3**), 291–297, doi:10.1029/JC080i003p00291.

Gerber, E. P., L. M. Polvani, and D. Ancukiewicz, 2008: Annular mode time scales in the Intergovernmental Panel on Climate Change Fourth Assessment Report models. *Geophys. Res. Lett.*, **35** (**22**), L22707, doi:10.1029/2008GL035712.

Gill, A. E., 1973: Circulation and bottom water production in the Weddell Sea. *Deep-Sea Res. Oceanogr. Abstr.*, **20** (**2**), 111–140, doi:10.1016/0011-7471(73)90048-X.

——, 1982: *Atmosphere-Ocean Dynamics*. 1st ed. Academic Press, 662 pp.

——, and E. H. Schumann, 1974: The Generation of Long Shelf Waves by the Wind. *J. Phys. Oceanogr.*, **4** (**1**), 83–90, doi:10.1175/1520-0485(1974)004<0083:TGOLSW>2.0.CO;2.

Gille, S. T., D. C. McKee, and D. G. Martinson, 2016: Temporal changes in the Antarctic Circumpolar Current: Implications for the Antarctic continental shelves. *Oceanography*, **29** (**4**), 96–105, doi:https://doi.org/10.5670/oceanog.2016.102.

Goddard, P. B., C. O. Dufour, J. Yin, S. M. Griffies, and M. Winton, 2017: CO2-Induced Ocean Warming of the Antarctic Continental Shelf in an Eddying Global Climate Model. *J. Geophys. Res. - Oceans*, **122** (**10**), 8079–8101, doi:10.1002/2017JC012849.

Gordon, A. L., 1971: Oceanography of Antarctic Waters. *Antarctic Oceanology I*, Vol. 15 of *Antarctic Research Series*, American Geophysical Union (AGU), 169–203.

——, and W. D. Nowlin, 1978: The Basin Waters of the Bransfield Strait. *J. Phys. Oceanogr.*, **8** (**2**), 258–264, doi:10.1175/1520-0485(1978)008<0258:TBWOTB>2.0.CO;2.

Gordon, R. L., and N. F. Marshall, 1976: Submarine canyons: Internal wave traps? *Geophys. Res. Lett.*, **3** (**10**), 622–624, doi:10.1029/GL003i010p00622.

——, and J. M. Huthnance, 1987: Storm-driven continental shelf waves over the Scottish continental shelf. *Cont. Shelf Res.*, **7** (**9**), 1015–1048, doi:10.1016/0278-4343(87)90097-5.

Gouretski, V. V., and K. P. Koltermann, 2004: WOCE Global Hydrographic Climatology, A Technical Report. Berichte des Bundesamtes für Seeschifffahrt und Hydrographie 35, 52 pp.

Graham, J. A., M. S. Dinniman, and J. M. Klinck, 2016: Impact of model resolution for on-shelf heat transport along the West Antarctic Peninsula. *J. Geophys. Res. - Oceans*, **121** (**10**), 7880–7897, doi:10.1002/2016JC011875.

Gregg, M. C., 1989: Scaling turbulent dissipation in the thermocline. *J. Geophys. Res. - Oceans*, **94** (**C7**), 9686–9698, doi:10.1029/JC094iC07p09686.

——, and T. B. Sanford, 1988: The dependence of turbulent dissipation on stratification in a diffusively stable thermocline. *J. Geophys. Res. - Oceans*, **93** (**C10**), 12381–12392, doi:10.1029/JC093iC10p12381.

——, T. B. Sanford, and D. P. Winkel, 2003: Reduced mixing from the breaking of internal waves in equatorial waters. *Nature*, **422** (**6931**), 513–515, doi:10.1038/nature01507.

Griffin, D. A., and J. H. Middleton, 1986: Coastal-Trapped Waves behind a Large Continental Shelf Island, Southern Great Barrier Reef. *J. Phys. Oceanogr.*, **16** (**10**), 1651–1664, doi:10.1175/1520-0485(1986)016<1651:CTWBAL>2.0.CO;2.

Grinsted, A., J. C. Moore, and S. Jevrejeva, 2004: Application of the cross wavelet transform and wavelet coherence to geophysical time series. *Nonlinear Proc. Geoph.*, **11** (**5/6**), 561–566, doi:https://doi.org/10.5194/npg-11-561-2004.

Haberman, R., 2003: *Applied Partial Differential Equations with Fourier Series and Boundary Value Problems*. 4th ed. Prentice Hall, 769 pp.

Hebert, D., N. Oakey, and B. Ruddick, 1990: Evolution of a Mediterranean Salt Lens: Scalar Properties. *J. Phys. Oceanogr.*, **20** (**9**), 1468–1483, doi:10.1175/1520-0485(1990)020<1468:EOAMSL>2.0.CO;2.

Howard, S. L., J. Hyatt, and L. Padman, 2004: Mixing in the pycnocline over the western Antarctic Peninsula shelf during Southern Ocean GLOBEC. *Deep-Sea Res. Pt II*, **51** (**17**), 1965–1979, doi:10.1016/j.dsr2.2004.08.002.

Hughes, C. W., M. P. Meredith, and K. J. Heywood, 1999: Wind-Driven Transport Fluctuations through Drake Passage: A Southern Mode. *J. Phys. Oceanogr.*, **29** (**8**), 1971–1992, doi:10.1175/1520-0485(1999)029<1971:WDTFTD>2.0.CO;2.

——, P. L. Woodworth, M. P. Meredith, V. Stepanov, T. Whitworth, and A. R. Pyne, 2003: Coherence of Antarctic sea levels, Southern Hemisphere Annular Mode, and flow through Drake Passage. *Geophys. Res. Lett.*, **30** (**9**), 17.1-17.4, doi:10.1029/2003GL017240.

Huthnance, J. M., 1978: On Coastal Trapped Waves: Analysis and Numerical Calculation by Inverse Iteration. *J. Phys. Oceanogr.*, **8** (**1**), 74–92, doi:10.1175/1520-0485(1978)008<0074:OCTWAA>2.0.CO;2.

——, 1981: Waves and currents near the continental shelf edge. *Prog. Oceanogr.*, **10** (**4**), 193–226, doi:10.1016/0079-6611(81)90004-5.

Iijima, Y., S. Aoki, and K. Kutsuwada, 2009: The Southern Annular Mode and opposite-phased Basin Mode of the Southern Ocean circulation. *J. Oceanogr.*, **65** (**1**), 53–60, doi:10.1007/s10872-009-0005-0.

Isachsen, P. E., 2011: Baroclinic instability and eddy tracer transport across sloping bottom topography: How well does a modified Eady model do in primitive equation simulations? *Ocean Model.*, **39** (**1**), 183–199, doi:10.1016/j.ocemod.2010.09.007.

Jackett, D. R., and T. J. McDougall, 1997: A Neutral Density Variable for the World's Oceans. *J. Phys. Oceanogr.*, **27** (**2**), 237–263, doi:10.1175/1520-0485(1997)027<0237:ANDVFT>2.0.CO;2.

Jensen, M. F., I. Fer, and E. Darelius, 2013: Low frequency variability on the continental slope of the southern Weddell Sea. *J. Geophys. Res. - Oceans*, **118** (**9**), 4256–4272, doi:10.1002/jgrc.20309.

Joyce, T. M., 1977: A Note on the Lateral Mixing of Water Masses. *J. Phys. Oceanogr.*, **7** (**4**), 626–629, doi:10.1175/1520-0485(1977)007<0626:ANOTLM>2.0.CO;2.

Kämpf, J., 2006: Transient wind-driven upwelling in a submarine canyon: A process-oriented modeling study. *J. Geophys. Res. - Oceans*, **111** (**C11**), C11011, doi:10.1029/2006JC003497.

——, 2007: On the magnitude of upwelling fluxes in shelf-break canyons. *Cont. Shelf Res.*, **27** (**17**), 2211–2223, doi:10.1016/j.csr.2007.05.010.

Kavanaugh, M. T., F. N. Abdala, H. Ducklow, D. Glover, W. Fraser, D. Martinson, S. Stammerjohn, O. Schofield, and S. C. Doney, 2015: Effect of continental shelf canyons on phytoplankton biomass and community composition along the western Antarctic Peninsula. *Mar. Ecol. Prog. Ser.*, **524**, 11–26, doi:10.3354/meps11189.

Kiladis, G. N., and K. C. Mo, 1998: Interannual and Intraseasonal Variability in the Southern Hemisphere. *Meteorology of the Southern Hemisphere*, D.J. Karoly and D.G. Vincent, Eds., Vol. 49 of *Meteorological Monographs*, American Meteorological Society, Boston, MA, 307–336.

Kim, H., S. C. Doney, R. A. Iannuzzi, M. P. Meredith, D. G. Martinson, and H. W. Ducklow, 2016: Climate forcing for dynamics of dissolved inorganic nutrients at Palmer Station, Antarctica: An interdecadal (1993–2013) analysis. *J. Geophys. Res. - Biogeo.*, **121** (**9**), 2369–2389, doi:10.1002/2015JG003311.

Klinck, J. M., 1998: Heat and salt changes on the continental shelf west of the Antarctic Peninsula between January 1993 and January 1994. *J. Geophys. Res. - Oceans*, **103** (**C4**), 7617–7636, doi:10.1029/98JC00369.

——, E. E. Hofmann, R. C. Beardsley, B. Salihoglu, and S. Howard, 2004: Water-mass properties and circulation on the west Antarctic Peninsula Continental Shelf in Austral Fall and Winter 2001. *Deep-Sea Res. Pt II*, **51** (**17**), 1925–1946, doi:10.1016/j.dsr2.2004.08.001.

Kohut, J. T., E. Hunter, and B. Huber, 2013: Small-scale variability of the cross-shelf flow over the outer shelf of the Ross Sea. *J. Geophys. Res. - Oceans*, **118** (**4**), 1863–1876, doi:10.1002/jgrc.20090.

——, P. Winsor, H. Statscewich, M. J. Oliver, E. Fredj, N. Couto, K. Bernard, and W. Fraser, 2018: Variability in summer surface residence time within a West Antarctic Peninsula biological hotspot. *Phil. Trans. R. Soc. A*, **376** (**2122**), 20170165, doi:10.1098/rsta.2017.0165.

Kunze, E., E. Firing, J. M. Hummon, T. K. Chereskin, and A. M. Thurnherr, 2006: Global Abyssal Mixing Inferred from Lowered ADCP Shear and CTD Strain Profiles. *J. Phys. Oceanogr.*, **36** (**8**), 1553–1576, doi:10.1175/JPO2926.1.

Kusahara, K., and K. I. Ohshima, 2009: Dynamics of the Wind-Driven Sea Level Variation around Antarctica. *J. Phys. Oceanogr.*, **39** (**3**), 658–674, doi:10.1175/2008JPO3982.1.

Lecointre, A., T. Penduff, P. Cipollini, R. Tailleux, and B. Barnier, 2008: Depth dependence of westward-propagating North Atlantic features diagnosed from altimetry and a numerical 1/6 degree model. *Ocean Sci.*, **4** (**1**), 99–113, doi:https://doi.org/10.5194/os-4-99-2008.

Lefebvre, W., H. Goosse, R. Timmermann, and T. Fichefet, 2004: Influence of the Southern Annular Mode on the sea ice–ocean system. *J. Geophys. Res. - Oceans*, **109** (**C9**), C09005, doi:10.1029/2004JC002403.

Levine, M. D., 2002: A Modification of the Garrett–Munk Internal Wave Spectrum. *J. Phys. Oceanogr.*, **32** (**11**), 3166–3181, doi:10.1175/1520-0485(2002)032<3166:AMOTGM>2.0.CO;2.

Locarnini, R. A., A. V. Mishonov, O. K. Baranova, T. P. Boyer, M. M. Zweng, H. E. Garcia, J. R. Reagan, D. Seidov, K. Weathers, C. R. Paver, and I. Smolyar, 2018: World Ocean Atlas 2018, Volume 1: Temperature. NOAA Atlas NESDIS 81, 45 pp.

Mack, S. L., M. S. Dinniman, D. J. McGillicuddy, P. N. Sedwick, and J. M. Klinck, 2017: Dissolved iron transport pathways in the Ross Sea: Influence of tides and horizontal resolution in a regional ocean model. *J. Marine Syst.*, **166**, 73–86, doi:10.1016/j.jmarsys.2016.10.008.

Marshall, G. J., 2003: Trends in the Southern Annular Mode from Observations and Reanalyses. *J. Climate*, **16** (**24**), 4134–4143, doi:10.1175/1520-0442(2003)016<4134:TITSAM>2.0.CO;2.

Martinson, D. G., 1990: Evolution of the southern ocean winter mixed layer and sea ice: Open ocean deepwater formation and ventilation. *J. Geophys. Res. - Oceans*, **95** (**C7**), 11641–11654, doi:10.1029/JC095iC07p11641.

——, and R. A. Iannuzzi, 1998: Antarctic Ocean-Ice Interaction: Implications from Ocean Bulk Property Distributions in the Weddell Gyre. *Antarctic Sea Ice: Physical Processes, Interactions and Variability*, M. Jeffries, Ed., Vol. 74 of *Antarctic Research Series*, American Geophysical Union (AGU), 243–271.

——, and D. C. McKee, 2012: Transport of warm Upper Circumpolar Deep Water onto the western Antarctic Peninsula continental shelf. *Ocean Sci.*, **8** (**4**), 433–442, doi:https://doi.org/10.5194/os-8-433-2012.

——, S. E. Stammerjohn, R. A. Iannuzzi, R. C. Smith, and M. Vernet, 2008: Western Antarctic Peninsula physical oceanography and spatio–temporal variability. *Deep-Sea Res. Pt II*, **55** (**18**), 1964–1987, doi:10.1016/j.dsr2.2008.04.038.

Matthews, A. J., and M. P. Meredith, 2004: Variability of Antarctic circumpolar transport and the Southern Annular Mode associated with the Madden-Julian Oscillation. *Geophys. Res. Lett.*, **31** (**24**), L24312, doi:10.1029/2004GL021666.

McDougall, T. J., 1985a: Double-Diffusive Interleaving. Part I: Linear Stability Analysis. *J. Phys. Oceanogr.*, **15** (**11**), 1532–1541, doi:10.1175/1520-0485(1985)015<1532:DDIPIL>2.0.CO;2.

——, 1985b: Double-Diffusive Interleaving. Part II: Finite Amplitude, Steady State Interleaving. *J. Phys. Oceanogr.*, **15** (**11**), 1542–1556, doi:10.1175/1520-0485(1985)015<1542:DDIPIF>2.0.CO;2.

McKee, D. C., D. G. Martinson, and O. Schofield, 2019: Origin and attenuation of mesoscale structure in Circumpolar Deep Water intrusions to an Antarctic shelf. *J. Phys. Oceanogr.*, **49** (**5**), 1293–1318, doi:10.1175/JPO-D-18-0133.1.

Meredith, M. P., and J. C. King, 2005: Rapid climate change in the ocean west of the Antarctic Peninsula during the second half of the 20th century. *Geophys. Res. Lett.*, **32** (**19**), L19604, doi:10.1029/2005GL024042.

——, S. E. Stammerjohn, H. J. Venables, H. W. Ducklow, D. G. Martinson, R. A. Iannuzzi, M. J. Leng, J. M. van Wessem, C. H. Reijmer, and N. E. Barrand, 2017: Changing distributions of sea ice melt and meteoric water west of the Antarctic Peninsula. *Deep-Sea Res. Pt II*, **139**, 40–57, doi:10.1016/j.dsr2.2016.04.019.

Middleton, J. F., and M. Cirano, 1999: Wind-Forced Downwelling Slope Currents: A Numerical Study. *J. Phys. Oceanogr.*, **29** (**8**), 1723–1743, doi:10.1175/1520-0485(1999)029<1723:WFDSCA>2.0.CO;2.

Middleton, J. H., T. D. Foster, and A. Foldvik, 1987: Diurnal Shelf Waves in the Southern Weddell Sea. *J. Phys. Oceanogr.*, **17** (**6**), 784–791, doi:10.1175/1520-0485(1987)017<0784:DSWITS>2.0.CO;2.

Mirshak, R., and S. E. Allen, 2005: Spin-up and the effects of a submarine canyon: Applications to upwelling in Astoria Canyon. *J. Geophys. Res. - Oceans*, **110** (**C2**), C02013, doi:10.1029/2004JC002578.

Mo, K. C., and R. W. Higgins, 1998: The Pacific–South American Modes and Tropical Convection during the Southern Hemisphere Winter. *Mon. Wea. Rev.*, **126** (**6**), 1581–1596, doi:10.1175/1520-0493(1998)126<1581:TPSAMA>2.0.CO;2.

Moffat, C., and M. Meredith, 2018: Shelf–ocean exchange and hydrography west of the Antarctic Peninsula: a review. *Phil. Trans. R. Soc. A*, **376** (**2122**), 20170164, doi:10.1098/rsta.2017.0164.

——, R. C. Beardsley, B. Owens, and N. van Lipzig, 2008: A first description of the Antarctic Peninsula Coastal Current. *Deep-Sea Res. Pt II*, **55** (**3**), 277–293, doi:10.1016/j.dsr2.2007.10.003.

——, B. Owens, and R. C. Beardsley, 2009: On the characteristics of Circumpolar Deep Water intrusions to the west Antarctic Peninsula Continental Shelf. *J. Geophys. Res. - Oceans*, **114** (**C5**), C05017, doi:10.1029/2008JC004955.

National Geophysical Data Center, 1988: Digital relief of the Surface of the Earth. Data Announcement 88-MGG-02, NOAA, National Geophysical Data Center.

Naveira-Garabato, A. C., K. L. Polzin, B. A. King, K. J. Heywood, and M. Visbeck, 2004: Widespread Intense Turbulent Mixing in the Southern Ocean. *Science*, **303** (**5655**), 210–213, doi:10.1126/science.1090929.

Orsi, A. H., T. Whitworth, and W. D. Nowlin, 1995: On the meridional extent and fronts of the Antarctic Circumpolar Current. *Deep-Sea Res. Pt I*, **42** (**5**), 641–673, doi:10.1016/0967-0637(95)00021-W.

——, G. C. Johnson, and J. L. Bullister, 1999: Circulation, mixing, and production of Antarctic Bottom Water. *Prog. Oceanogr.*, **43** (**1**), 55–109, doi:10.1016/S0079-6611(99)00004-X.

Pacanowski, R. C., and S. G. H. Philander, 1981: Parameterization of Vertical Mixing in Numerical Models of Tropical Oceans. *J. Phys. Oceanogr.*, **11** (**11**), 1443–1451, doi:10.1175/1520-0485(1981)011<1443:POVMIN>2.0.CO;2.

Padman, L., H. A. Fricker, R. Coleman, S. Howard, and L. Erofeeva, 2002: A new tide model for the Antarctic ice shelves and seas. *Ann. Glaciol.*, **34**, 247–254, doi:10.3189/172756402781817752.

Pawlowicz, R., B. Beardsley, and S. Lentz, 2002: Classical tidal harmonic analysis including error estimates in MATLAB using T_TIDE. *Comput. Geosci.*, **28** (**8**), 929–937, doi:10.1016/S0098-3004(02)00013-4.

Pedlosky, J., 1987: *Geophysical Fluid Dynamics*. 2nd ed. Springer-Verlag, 710 pp.

Pelland, N. A., C. C. Eriksen, and C. M. Lee, 2013: Subthermocline Eddies over the Washington Continental Slope as Observed by Seagliders, 2003–09. *J. Phys. Oceanogr.*, **43** (**10**), 2025–2053, doi:10.1175/JPO-D-12-086.1.

Phillips, N. A., 1954: Energy Transformations and Meridional Circulations associated with simple Baroclinic Waves in a two-level, Quasi-geostrophic Model. *Tellus*, **6** (**3**), 273–286, doi:10.1111/j.2153-3490.1954.tb01123.x.

Pohl, B., N. Fauchereau, C. J. C. Reason, and M. Rouault, 2010: Relationships between the Antarctic Oscillation, the Madden–Julian Oscillation, and ENSO, and Consequences for Rainfall Analysis. *J. Climate*, **23** (**2**), 238–254, doi:10.1175/2009JCLI2443.1.

Prézelin, B. B., E. E. Hofmann, C. Mengelt, and J. M. Klinck, 2000: The linkage between Upper Circumpolar Deep Water (UCDW) and phytoplankton assemblages on the west Antarctic Peninsula continental shelf. *J. Mar. Res.*, **58** (**2**), 165–202, doi:10.1357/002224000321511133.

Rignot, E., J. L. Bamber, M. R. van den Broeke, C. Davis, Y. Li, W. J. van de Berg, and E. van Meijgaard, 2008: Recent Antarctic ice mass loss from radar interferometry and regional climate modelling. *Nat. Geosci.*, **1** (**2**), 106–110, doi:10.1038/ngeo102.

Rivas, D., 2017: Wind-driven coastal-trapped waves off southern Tamaulipas and northern Veracruz, western Gulf of Mexico, during winter 2012–2013. *Estuarine, Coastal Shelf Sci.*, **185**, 1–10, doi:10.1016/j.ecss.2016.12.002.

Ruddick, B., and D. Hebert, 1988: The Mixing of Meddy "Sharon." *Small-Scale Turbulence and Mixing in the Ocean*, J.C.J. Nihoul and B.M. Jamart, Eds., Vol. 46 of *Elsevier Oceanography Series*, Elsevier, 249–261.

Saenz, B. T., D. C. McKee, S. C. Doney, D. G. Martinson, and S. E. Stammerjohn, 2018: Influence of deep ocean heat on the sea-ice cover in the west Antarctic Peninsula. Unpublished manuscript.

Savidge, D. K., and J. A. Amft, 2009: Circulation on the West Antarctic Peninsula derived from 6 years of shipboard ADCP transects. *Deep-Sea Res. Pt I*, **56** (**10**), 1633–1655, doi:10.1016/j.dsr.2009.05.011.

Schmidtko, S., K. J. Heywood, A. F. Thompson, and S. Aoki, 2014: Multidecadal warming of Antarctic waters. *Science*, **346** (**6214**), 1227–1231, doi:10.1126/science.1256117.

Schofield, O., J. Kohut, D. Aragon, L. Creed, J. Graver, C. Haldeman, J. Kerfoot, H. Roarty, C. Jones, D. Webb, and S. Glenn, 2007: Slocum Gliders: Robust and ready. *J. Field Robot.*, **24** (**6**), 473–485, doi:10.1002/rob.20200.

——, H. Ducklow, K. Bernard, S. Doney, D. Patterson-Fraser, K. Gorman, D. Martinson, M. Meredith, G. Saba, S. Stammerjohn, D. Steinberg, and W. Fraser, 2013: Penguin Biogeography Along the West Antarctic Peninsula: Testing the Canyon Hypothesis with Palmer LTER Observations. *Oceanography*, **26** (**3**), 204–206, doi:https://doi.org/10.5670/oceanog.2013.63.

Schulz, W. J., R. P. Mied, and C. M. Snow, 2012: Continental Shelf Wave Propagation in the Mid-Atlantic Bight: A General Dispersion Relation. *J. Phys. Oceanogr.*, **42** (**4**), 558–568, doi:10.1175/JPO-D-11-098.1.

Smith, D. A., E. E. Hofmann, J. M. Klinck, and C. M. Lascara, 1999: Hydrography and circulation of the West Antarctic Peninsula Continental Shelf. *Deep-Sea Res. Pt I*, **46** (**6**), 925–949, doi:10.1016/S0967-0637(98)00103-4.

Smith, K. S., 2007: The geography of linear baroclinic instability in Earth's oceans. *J. Mar. Res.*, **65** (**5**), 655–683, doi:10.1357/002224007783649484.

——, and R. Ferrari, 2009: The Production and Dissipation of Compensated Thermohaline Variance by Mesoscale Stirring. *J. Phys. Oceanogr.*, **39** (**10**), 2477–2501, doi:10.1175/2009JPO4103.1.

Smith, R. C., K. S. Baker, W. R. Fraser, E. E. Hofmann, D. M. Karl, J. M. Klinck, L. B. Quetin, B. B. Prézelin, R. M. Ross, W. Z. Trivelpiece, and M. Vernet, 1995: The Palmer LTER: A long-term ecological research program at Palmer Station, Antarctica. *Oceanography*, **8** (**3**), 77–86, doi:10.5670/oceanog.1995.01.

Spence, P., S. M. Griffies, M. H. England, A. M. Hogg, O. A. Saenko, and N. C. Jourdain, 2014: Rapid subsurface warming and circulation changes of Antarctic coastal waters by poleward shifting winds. *Geophys. Res. Lett.*, **41** (**13**), 4601–4610, doi:10.1002/2014GL060613.

——, R. M. Holmes, A. M. Hogg, S. M. Griffies, K. D. Stewart, and M. H. England, 2017: Localized rapid warming of West Antarctic subsurface waters by remote winds. *Nat. Clim. Change*, **7** (**8**), 595–603, doi:10.1038/nclimate3335.

Stammer, D., 1998: On Eddy Characteristics, Eddy Transports, and Mean Flow Properties. *J. Phys. Oceanogr.*, **28** (**4**), 727–739, doi:10.1175/1520-0485(1998)028<0727:OECETA>2.0.CO;2.

Stammerjohn, S. E., D. G. Martinson, R. C. Smith, X. Yuan, and D. Rind, 2008: Trends in Antarctic annual sea ice retreat and advance and their relation to El Niño–Southern Oscillation and Southern Annular Mode variability. *J. Geophys. Res. - Oceans*, **113** (**C3**), C03S90, doi:10.1029/2007JC004269.

——, R. Massom, D. Rind, and D. Martinson, 2012: Regions of rapid sea ice change: An inter-hemispheric seasonal comparison. *Geophys. Res. Lett.*, **39** (**6**), L06501, doi:10.1029/2012GL050874.

Stern, A., L.-P. Nadeau, and D. Holland, 2015: Instability and Mixing of Zonal Jets along an Idealized Continental Shelf Break. *J. Phys. Oceanogr.*, **45** (**9**), 2315–2338, doi:10.1175/JPO-D-14-0213.1.

Stewart, A. L., and A. F. Thompson, 2015: Eddy-mediated transport of warm Circumpolar Deep Water across the Antarctic Shelf Break. *Geophys. Res. Lett.*, **42** (**2**), 432–440, doi:10.1002/2014GL062281.

——, A. Klocker, and D. Menemenlis, 2018: Circum-Antarctic Shoreward Heat Transport Derived From an Eddy- and Tide-Resolving Simulation. *Geophys. Res. Lett.*, **45** (**2**), 834–845, doi:10.1002/2017GL075677.

St-Laurent, P., J. M. Klinck, and M. S. Dinniman, 2013: On the Role of Coastal Troughs in the Circulation of Warm Circumpolar Deep Water on Antarctic Shelves. *J. Phys. Oceanogr.*, **43** (**1**), 51–64, doi:10.1175/JPO-D-11-0237.1.

——, P. L. Yager, R. M. Sherrell, S. E. Stammerjohn, and M. S. Dinniman, 2017: Pathways and supply of dissolved iron in the Amundsen Sea (Antarctica). *J. Geophys. Res. - Oceans*, **122** (**9**), 7135–7162, doi:10.1002/2017JC013162.

Suginohara, N., 1982: Coastal Upwelling: Onshore–Offshore Circulation, Equatorward Coastal Jet and Poleward Undercurrent over a Continental Shelf-Slope. *J. Phys. Oceanogr.*, **12** (**3**), 272–284, doi:10.1175/1520-0485(1982)012<0272:CUOCEC>2.0.CO;2.

Tamsitt, V., H. F. Drake, A. K. Morrison, L. D. Talley, C. O. Dufour, A. R. Gray, S. M. Griffies, M. R. Mazloff, J. L. Sarmiento, J. Wang, and W. Weijer, 2017: Spiraling pathways of global deep waters to the surface of the Southern Ocean. *Nat. Commun.*, **8** (**1**), 172, doi:10.1038/s41467-017-00197-0.

Tennekes, H., and J. L. Lumley, 1972: *A First Course in Turbulence*. 1st ed. MIT Press, 300 pp.

Thoma, M., A. Jenkins, D. Holland, and S. Jacobs, 2008: Modelling Circumpolar Deep Water intrusions on the Amundsen Sea continental shelf, Antarctica. *Geophys. Res. Lett.*, **35** (**18**), L18602, doi:10.1029/2008GL034939.

Thompson, A. F., S. T. Gille, J. A. MacKinnon, and J. Sprintall, 2007: Spatial and Temporal Patterns of Small-Scale Mixing in Drake Passage. *J. Phys. Oceanogr.*, **37** (**3**), 572–592, doi:10.1175/JPO3021.1.

Thompson, D. W. J., and J. M. Wallace, 2000: Annular Modes in the Extratropical Circulation. Part I: Month-to-Month Variability. *J. Climate*, **13** (**5**), 1000–1016, doi:10.1175/1520-0442(2000)013<1000:AMITEC>2.0.CO;2.

Thomson, D. J., 1982: Spectrum estimation and harmonic analysis. *Proc. IEEE*, **70** (**9**), 1055–1096, doi:10.1109/PROC.1982.12433.

Turner, J., T. Maksym, T. Phillips, G. J. Marshall, and M. P. Meredith, 2013: The impact of changes in sea ice advance on the large winter warming on the western Antarctic Peninsula. *Int. J. Climatol.*, **33** (**4**), 852–861, doi:10.1002/joc.3474.

——, H. Lu, I. White, J. C. King, T. Phillips, J. S. Hosking, T. J. Bracegirdle, G. J. Marshall, R. Mulvaney, and P. Deb, 2016: Absence of 21st century warming on Antarctic Peninsula consistent with natural variability. *Nature*, **535** (**7612**), 411–415, doi:10.1038/nature18645.

Wåhlin, A. K., R. D. Muench, L. Arneborg, G. Björk, H. K. Ha, S. H. Lee, and H. Alsén, 2012: Some Implications of Ekman Layer Dynamics for Cross-Shelf Exchange in the Amundsen Sea. *J. Phys. Oceanogr.*, **42** (**9**), 1461–1474, doi:10.1175/JPO-D-11-041.1.

——, O. Kalén, L. Arneborg, G. Björk, G. K. Carvajal, H. K. Ha, T. W. Kim, S. H. Lee, J. H. Lee, and C. Stranne, 2013: Variability of Warm Deep Water Inflow in a Submarine Trough on the Amundsen Sea Shelf. *J. Phys. Oceanogr.*, **43** (**10**), 2054–2070, doi:10.1175/JPO-D-12-0157.1.

——, ——, K. M. Assmann, E. Darelius, H. K. Ha, T. W. Kim, and S. H. Lee, 2016: Subinertial Oscillations on the Amundsen Sea Shelf, Antarctica. *J. Phys. Oceanogr.*, **46** (**9**), 2573–2582, doi:10.1175/JPO-D-14-0257.1.

Walker, D. P., M. A. Brandon, A. Jenkins, J. T. Allen, J. A. Dowdeswell, and J. Evans, 2007: Oceanic heat transport onto the Amundsen Sea shelf through a submarine glacial trough. *Geophys. Res. Lett.*, **34** (**2**), L02602, doi:10.1029/2006GL028154.

——, A. Jenkins, K. M. Assmann, D. R. Shoosmith, and M. A. Brandon, 2013: Oceanographic observations at the shelf break of the Amundsen Sea, Antarctica. *J. Geophys. Res. - Oceans*, **118** (**6**), 2906–2918, doi:10.1002/jgrc.20212.

Waterhouse, A. F., S. E. Allen, and A. W. Bowie, 2009: Upwelling flow dynamics in long canyons at low Rossby number. *J. Geophys. Res. - Oceans*, **114** (**C5**), C05004, doi:10.1029/2008JC004956.

Weijer, W., and S. T. Gille, 2005: Adjustment of the Southern Ocean to Wind Forcing on Synoptic Time Scales. *J. Phys. Oceanogr.*, **35** (**11**), 2076–2089, doi:10.1175/JPO2801.1.

Whitworth, T., A. H. Orsi, S.-J. Kim, W. D. Nowlin, and R. A. Locarnini, 1998: Water Masses and Mixing Near the Antarctic Slope Front. *Ocean, Ice, and Atmosphere: Interactions at the Antarctic Continental Margin*, S.S. Jacobs and R.F. Weiss, Eds., Vol. 75 of *Antarctic Research Series*, American Geophysical Union (AGU), 1–27.

Yuan, X., 2004: ENSO-related impacts on Antarctic sea ice: a synthesis of phenomenon and mechanisms. *Antarct. Sci.*, **16** (**4**), 415–425, doi:10.1017/S0954102004002238.

Zhou, M., P. P. Niiler, Y. Zhu, and R. D. Dorland, 2006: The western boundary current in the Bransfield Strait, Antarctica. *Deep-Sea Res. Pt I*, **53** (**7**), 1244–1252, doi:10.1016/j.dsr.2006.04.003.

Zweng, M. M., J. R. Reagan, D. Seidov, T. P. Boyer, R. A. Locarnini, H. E. Garcia, A. V. Mishonov, O. K. Baranova, K. Weathers, C. R. Paver, and I. Smolyar, 2018: World Ocean Atlas 2018, Volume 2: Salinity. NOAA Atlas NESDIS 82, 40 pp.

Appendix A: The Garrett-Munk spectrum on the WAP continental shelf

The Garrett-Munk (GM; Garrett and Munk 1975) spectrum provides an empirical description of the internal wave field in a flat-bottom open ocean away from boundaries and is frequently used to provide a statistical measure of internal wave variability in mixing parameterizations of nonlinear wave-wave interactions (e.g., G89). The GM spectrum ignores the presence of upper and lower boundaries and vertical structure in the wave field is manifested through a series of modal structures. Two fundamental parameters that scale the spectrum are a nondimensional energy E (canonically 6.3 x 10^{-5}) and a stratification depth b (canonically 1300 m). The GM shear spectrum is

$$\Phi_{\text{shear}} = \frac{3Eb^3}{2\pi j_*}\left(\frac{N_0}{N}\right)^2 \frac{\beta^2}{\left(1+\beta/\beta_*\right)^2}, \tag{A.1}$$

where β is the vertical wavenumber (in rad m^{-1}), $\beta_* = \left(\pi j_*/b\right)\left(N/N_0\right)$ is a reference wavenumber, N_0 = 0.0052 rad s^{-1} is the canonical reference stratification, and j_* = 3 is the canonical mode number. A roll-off of -1 is imposed at wavenumbers greater than β_c = 0.2π rad m^{-1}.

On the WAP continental shelf with typical bottom depths of ~400 m, the nondimensional energy E and the stratification scale b are likely quite different from canonical values (Levine 2002). Here we maintain the GM functional form (thus neglecting vertical boundaries) but adjust E and b in accordance with the environment of the WAP. One way to do so (section 4c of Levine 2002) is to first estimate the product $N_0 b$ from the observed stratification $N(z)$ and then

to estimate the energy density in the internal wave band. We estimate $N(z)$ by first computing an average density profile from all summertime (January and February) Shelf CTD casts. For all casts, the depths of a set of evenly spaced isopycnals are calculated via linear interpolation and each isopycnal is assigned its mean depth. The resulting potential density profile is then interpolated to an 8-m grid and finite-differenced in order to obtain a profile of mean $N(z)$. The product $N_0 b$, which scales the wavenumber bandwidth, is defined as

$$N_0 b = \int_{404\text{ m}}^{024\text{ m}} \overline{N(z)} dz = 1.5 \text{ m s}^{-1} \tag{A.2}$$

so that b = 288 m. The profile of mean N squared is shown in figure 2.9a. The lower integration bound is chosen as an average depth of all shelf stations and the upper integration bound is chosen as a typical seasonal mixed layer depth since overturns in the averaged density profile become apparent shallower than that (because the depth of the seasonal mixed layer varies regionally and interannually, the mean $N(z)$ profile is quasi-exponential with no apparent seasonal mixed layer). Parameters N_0 and j_* are left at their canonical values.

To estimate the nondimensional energy density, we first estimate the kinetic energy density *KE* via baroclinic energy spectra from the moored current meter data of Martinson and McKee (2012). Their current meter data generally sample once per hour, however in 2007 they have one year-long record at site 300.100 that sampled once every 20 min with two current meters spanning the permanent pycnocline (one each nominally at T_{min} and T_{max}). We define the barotropic current as the average of the two records and subtract that out. Then, the spectrum of the residual baroclinic current at each depth is calculated via squaring the Fourier transform of the complex time series, is averaged in the vertical, and is integrated over $[f, N_0]$. While the Nyquist frequency for this sampling is $0.5N_0$, the -2 roll-off in the internal wave band reveals

that most of the contribution to the integral comes from the lower portion of the band. The depth average of the two integrated spectra times 1/2 yields the kinetic energy density *KE* and the non-dimensional energy density is given by

$$E = KE \Big/ \left(N_0 b\right)^2 = 3.0 \text{ x } 10^{-4}. \tag{A.3}$$

We now consider how the modified GM spectrum translates to parameterized diffusivities. Dissipation in the G89 model is given by

$$\varepsilon = \left[1.96\left(\frac{1.67}{\pi}\right) j_*^2 b^2 N_0^2 E^2 f_0 \operatorname{acosh}\left(N_0 / f_0\right)\right]\left[\frac{N^2}{N_0^2}\right]\left[\frac{S^4}{S_{\text{GM}}^4}\right] = \varepsilon_0 \left[\frac{N^2}{N_0^2}\right]\left[\frac{S^4}{S_{\text{GM}}^4}\right] \tag{A.4}$$

where the constant ε_0 is derived from wave-wave interactions in the GM energy flux spectrum. The assumption of a steady turbulent kinetic energy balance and a constant mixing ratio yields the relation for the diffusivity

$$K_z = \frac{\Gamma \varepsilon_0}{N^2}\left[\frac{N^2}{N_0^2}\right]\left[\frac{S^4}{S_{\text{GM}}^4}\right] = K_0 \left[\frac{S^4}{S_{\text{GM}}^4}\right] \tag{A.5}$$

as presented in the text (but here without the corrections *h* and *j*; equations 2.7-2.8). Under the canonical GM spectrum, K_0 = 5.0 x 10^{-6} m^2 s^{-1} whereas for the local parameters derived above K_0 = 5.6 x 10^{-6} m^2 s^{-1}, which is a small difference. In addition, compared to shear variances using canonical GM parameters, integrated shear variances using the corrected GM parameters yield diffusivities that are generally up to a factor of 2 greater in the upper water column but almost equal near the $T_{\max}$. Given that the G89 method is demonstrated to be accurate within a factor of 2, all of this suggests that the improvements afforded by the corrected GM spectrum are small.

Appendix B: Current meter tilt analysis

B.1) Overview

Regardless of how taut, any mooring will experience some amount of blow down when subject to very strong currents. The associated tilting of sensors may degrade performance. So long as the flow speed is under 50 cm s^{-1}, the Alec Infinity EM current meters maintain an accuracy within ± 4% for tilt angles less than 15º with respect to the vertical. At tilt angles greater than 20º, the instrument compass ceases to work properly. To minimize tilting of the sensors, a large 14" float is placed immediately above each one. Nevertheless, the instruments do not have an onboard sensor to measure tilt, so we do not have knowledge of their orientations in time. All we have knowledge of is vertical deviation of the instrument as recorded by an adjacent SBE39 pressure sensor (on average, an SBE39 is situated within 11 m, 26 m, or 25 m of each shallow, pycnocline, and deep current meter, respectively).

On the other hand, two of the InterOcean S4 current meters did have an onboard tilt sensor. These were deployed in 2007 (84 dbar and 280 dbar) and in 2008 (279 dbar), allowing us to establish a relationship between tilt angle and pressure deviation. To do so, we construct 1-dbar bins of pressure deviation and obtain the mean and standard deviation of tilt angle within each bin. Then, we define a discrete function $\theta_{\text{tilt}} = f\left(\Delta p\right)$ as the tilt at two standard deviations above the bin mean for each pressure bin. This represents an approximate upper bound (97.7% level if normally distributed) of the expected tilt angle for a given pressure deviation. Finally, we find the first pressure bin for which the function exceeds 15º (and remains above 15º) to identify a threshold pressure deviation beyond which corresponding tilt is problematic. Fortunately, this relationship can be established at the two nominal depths for which most of our

sampling in subsequent years was conducted. Scatter plots for the three sensors are shown in figure B.1.

For every Alec EM current meter we have at nominal depth near these two sensors, our approach is to use the above empirical functions to determine for how many time steps the current meter was displaced vertically (and thus tilted) beyond the critical threshold. This approach assumes that the established relationship holds for all years and locations. We obviously cannot test spatial invariance, however temporal invariance at least appears to be a good assumption. The two scatter plots for site 300.100 at ~280 m depth have the same general form (figure B.1a). They also both identify the 10-11 dbar pressure bin as the threshold for critical tilt angle. The difference in the two plots is that the largest pressure deviations are smaller in year 2008 because the mooring in that year was designed with increased tension. In general, all moorings deployed in and after 2010 have more tension than these, suggesting a further restriction in large vertical displacements and sensor tilt.

B.2) Results: Deep sensors

At most mooring sites, few time steps are associated with a critical tilt angle for the deep current meters used in this study. At sites 073.108, 200.140, 300.160, 347.088, and 400.100, for all years of sampling fewer than 0.52% of time steps are affected and this number is generally far lower, being < 0.10% most of the time. At site 300.100, an average of ~4% of time steps are affected, being as low as 0.70% (2011) or as large as 7.33% (2017). As shown, this is a site with large velocity variance. At site 500.120, 3.95% - 4.87% of time steps are affected. Site 500.120 is substantially deeper than other sites sampled. We choose to tolerate these percentages. While ~4% of samples affected may seem alarming, inspection of time series of pressure deviations

reveals that most of the offending time steps are concentrated in rare high-velocity events (a few per year). A histogram of observed vertical displacements for a representative year is shown in figure B.1b.

B.3) Results: Shallow sensors

For the shallower S4 sensor in 2007, only 0.2% of time steps exceeded 15º. The function relating tilt to pressure deviation briefly exceeds 15º tilt but quickly reverts back to a stable value between 10º and 15º (figure B.1c). The brief excursions occur in bins with few samples, where estimates of bin mean and standard deviation are less reliable. Thus, there is no threshold pressure deviation to exceed and no time steps are associated with a critical tilt angle. A histogram of observed vertical displacements for a representative year is shown in figure B.1d.

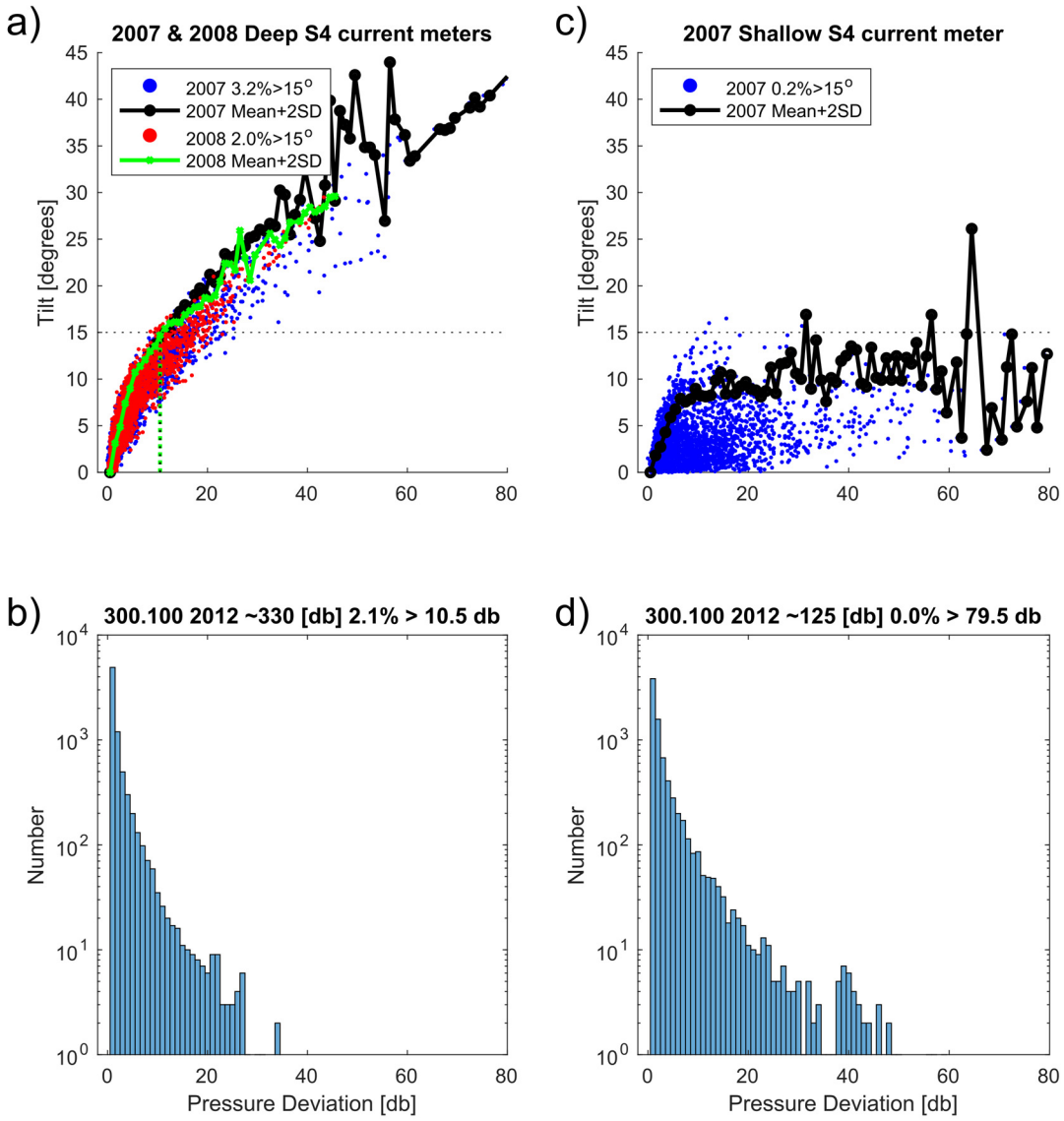

Figure B.1: Overview of current meter tilt analysis. The horizontal axes (pressure deviations) are the same in all panels. **(a)** Scatter plot of observed tilt versus associated pressure deviation for the deep S4 current meter in 2007 (blue dots) and in 2008 (red dots) along with the functional fits relating tilt to pressure deviation in those same years (black line and green line, respectively). Critical threshold of 15º is indicated as a horizontal dashed line and the bins where the functional fits intersect that threshold are indicated with vertical dashed lines. **(b)** Example histogram of the observed pressure deviations for an SBE39 sensor adjacent to an Alec Infinity EM current meter at approximately the same depth as the S4 in another year. **(c)** Exactly as in (a) for the shallow S4 in 2007. **(d)** Exactly as in (b) but for an SBE39 adjacent to a shallower Alec Infinity EM current meter in another year.

Appendix C: Bootstrap test for correlation significance

C.1) Overview

When evaluating the statistical significance of a correlation coefficient using standard methods such as the Student's *t*-test, one needs knowledge of the degrees of freedom. For time series, whose samples are by definition correlated to some degree (unless the series is white noise), the degrees of freedom are not simply DOF = N - 2, where N is the number of samples in the time series. Instead, the DOF are reduced since neighboring points are not independent from one another. One approach to remedy this is to estimate an effective DOF (EDOF), which aims to quantify the decorrelation time of the time series in order to assess how many independent samples exist. However, this strategy maintains some amount of subjectivity (for example, should the decorrelation time be the *e*-folding length of the autocorrelation function [ACF] or its first zero crossing?). An alternate strategy is to take a bootstrapping approach whereby one of the time series being compared is randomized in such a way so as to preserve its fundamental statistical moments, effectively resampling from the process that generated it and allowing the correlation to be repeated an infinite number of times. That is the approach we take, and the methodology is described here.

C.2) Methodology

Suppose we are comparing two real-valued time series y_1 and y_2, each of length N and with observed correlation coefficient r_{obs}. We compute the Fourier Transform of y_1 and express each complex harmonic in polar form

$$C_j = A_j \exp\left(i\varphi_j\right), \tag{C.1}$$

where *j* spans the positive and negative frequencies $f_j \in \left(-f_{N/2}, f_{N/2}\right]$. We then generate N_{gen} versions of y_1 by preserving the amplitude spectrum A_j while randomizing the phase spectrum φ_j. The phases are randomized by drawing $\varphi_j \in \left(-\pi, +\pi\right]$ from a random number generator for the positive frequencies and by setting $\varphi_{-j} = -\varphi_j$ for the negative frequencies so as to preserve the Hermitian symmetry of the Fourier Transform of a real-valued time series. The resulting complex spectrum can then be inverse Fourier transformed to the time domain, yielding a random time series $y_{1,n}$. Importantly, because the amplitude spectrum (and hence power spectrum) of y_1 is preserved, the two lowest order univariate moments (mean and variance) as well as the lowest order bivariate moment (the ACF) of y_1 are all preserved in each bootstrapped series. This also means that the time series generated are statistically consistent with the process that generated y_1.

With N_{gen} bootstrapped versions of y_1 calculated, we correlate each $y_{1,n}$ with the observed y_2 and plot a histogram of correlation coefficients r_n. N_{gen} should be chosen so that the distribution of r_n is smooth and we find 1,000 or 10,000 is generally sufficient. To estimate how likely it is that r_{obs} was obtained by chance, we count the number of $r_n \geq r_{\text{obs}}$ (or $r_n \leq r_{\text{obs}}$ if $r_{\text{obs}} < 0$) as N_{exceed}. Finally, a *p*-value for r_{obs} is defined as $p = N_{\text{exceed}} / N_{\text{gen}}$.

Appendix D: Barotropic shelf wave modal solution

The equation governing the BSW cross-shelf structures $F_n(y)$ and phase speeds c_n is

$$\frac{d}{dy}\left(\frac{1}{H}\frac{dF}{dy}\right)+\frac{1}{c}\frac{f}{H^2}\frac{dH}{dy}F=0 \tag{D.1}$$

subject to the boundary conditions $F(0)=0$ at the coast and $dF(L)/dy=0$ at the seaward boundary. This is a Sturm-Liouville boundary value problem with eigenvectors $F_n(y)$ and eigenvalues $\lambda_n=c_n^{-1}$. We can rewrite the equation in the standard Sturm-Liouville form (Haberman 2003) as

$$\frac{d}{dy}\left[p(y)\frac{d}{dy}F(y)\right]+q(y)F(y)=-\lambda r(y)F(y)$$

where

$$p=\frac{1}{H},\quad q=0,\quad r=\frac{f}{H^2}\frac{dH}{dy}.$$

The cross-shelf bathymetry profile $H(y)$ is that computed in the text. The equation is discretized as

$$\left[\mathbf{D}_2+\mathbf{diag}\left(p_y/p\right)\mathbf{D}_1\right]\mathbf{F}=\lambda\left[\mathbf{diag}\left(-r/p\right)\right]\mathbf{F}$$

$$\mathbf{AF}=\lambda\mathbf{BF} \tag{D.2}$$

where $\mathbf{D}_1$ and $\mathbf{D}_2$ are first and second centered-difference matrices, respectively, and p_y is the cross-shore derivative of vector *p* calculated as a centered difference. The Dirichlet condition at $x = 0$ is easily built into the first rows of **A** and **B** while the Neumann condition at $x = L$ is built into the last row as a backward difference. The generalized eigenvalues and the eigenvectors of

the matrix equation (D.2) are obtained numerically for arbitrary depth profile. We test the numerical scheme with the exponential shelf profile $H(y) = H_0 \exp(2ay)$ which has closed-form analytical expressions for its eigenvectors and eigenvalues.

Eigenfunctions of Sturm-Liouville problems are orthogonal to each other relative to a weight function. We use this property to scale the numerical eigenvectors such that

$$\int_0^L \frac{1}{H^2}\frac{dH}{dy} F_n F_m dy = \delta_{nm}\,, \tag{D.3}$$

where δ_{nm} is the Kronecker delta function. Utilizing this weighting, the modal structures form a complete basis which can explain any possible streamfunction pattern. Similar to a spatially stretched Fourier basis, each eigenfunction F_n has exactly *n*-1 zeros in the domain $y \in [0, L]$. Another useful property of Sturm-Liouville problems is that there is a smallest, but no largest, eigenvalue. This means that phase speeds decrease towards zero as mode number *n* increases.